Solar cells with photochromic organic dyes, manufacture and study of parameters influencing the photovoltaic and photochromic performances of the devices

Valid Mwalukuku

THÈSE

Pour obtenir le grade de

DOCTEUR DE L'UNIVERSITÉ GRENOBLE ALPES

École doctorale : CSV- Chimie et Sciences du Vivant
Spécialité : Chimie Physique Moléculaire et Structurale
Unité de recherche : Systèmes Moléculaires et Nano Matériaux pour l'Énergie et la Santé

Cellules solaires à colorants organiques photochromes, fabrication et étude des paramètres influençant les performances photovoltaïques et photochromiques des dispositifs

Solar cells with photochromic organic dyes, manufacture and study of parameters influencing the photovoltaic and photochromic performances of the devices

Présentée par :

Valid MWALUKUKU

Direction de thèse :

Renaud DEMADRILLE "Directeur de recherche" validé par le cea, CEA	Directeur de thèse
Pascale MALDIVI Directeur, CEA	Co-directrice de thèse

Rapporteurs :

Johann BOUCLE
MAITRE DE CONFERENCES HDR, Université de Limoges
Laurence VIGNAU
PROFESSEUR DES UNIVERSITES, Université de Bordeaux

Thèse soutenue publiquement le **26 octobre 2022**, devant le jury composé de :

Johann BOUCLE MAITRE DE CONFERENCES HDR, Université de Limoges	Rapporteur
Renaud DEMADRILLE DIRECTEUR DE RECHERCHE, CEA centre de Grenoble	Directeur de thèse
Laurence VIGNAU PROFESSEUR DES UNIVERSITES, Université de Bordeaux	Rapporteure
Juan Antonio ANTA PROFESSEUR, Universidad Pablo de Olavide	Président
Jérôme CHAUVIN MAITRE DE CONFERENCES HDR, Université Grenoble Alpes	Examinateur

Invités :

Pascale MALDIVI
INGENIEUR DE RECHERCHE, CEA Grenoble

Acknowledgments

First, I would like to thank you all the members of my jury for having accepted to take part in the evaluation of my PhD work. Indeed, I do not take it for granted and forever grateful. Special thanks go to Pr. Juan Antonio ANTA, who welcomed me in his lab « Nanostructured Solar Cells Group » in Seville, Spain. I must admit, other than the good and successful training I underwent during the 2 weeks, the ambiance of your lab and the team members has always made it memorable for me.

Many thanks to my supervisor, Dr. Renaud Demadrille whom I met during Masters courses and admired his depth of knowledge. It all started by pouring a cup of coffee on my PC during an interview with him and his post-doc, Dr. Quentin Huaulmé and at first looked like a misfortune. In return, he welcomed me to his lab and during which he acquired an ERC (European Research Council) funding. Working with you has taught me a lot and I am forever grateful. And thanks for trusting me with project PISCO.

Thanks to all our collaborators, especially the Seville team, where I had an opportunity to visit during my PhD work, I met and worked with amazing people such as Dr. Antonio Riquelme from whom I have learned a lot too. Thanks to Stéphanie Narbey and Pascal Maldivi.

During the 3 years, a team of 3 people followed my work to its entirety (Dr. Dmitry Aldakov, I hope I wrote it correctly, Dr. Frédéric Oswald and Dr. Fabrice Odobel). Thanks for taking part as my Thesis Monitoring Committee.

Thanks to the STEP and SyMMES direction for all the administrative help you accorded me. Special thanks to Rachel Mauduit and Christine Hadbi-Meunier. Thanks to all chemists (Dr. Quentin Huaulmé, Dr. Johan Liotier, Dr. José-Maria Andres Castan, Dr. Gael Heintges, Samuel Fauvel and Giroud Margaux) whom I have had an opportunity to work with, without them it could have been difficult to realize this PhD. Thanks to Dr. Cyril Aumaitre, Yann Kervella and Christian Lombard for the technical support and help you offered. Thanks to my officemate Anthonin Moinel for the discussions and the moments we had to encourage one another and all members of Demadrille's group (past and present). Thanks to Anthony Monmagnon, Dr. Olivier Bardagot, Dr. Louise Banniard, Ali Dabbous, Pawel Veyre, Dr. Lydia Cabau, Diego Mirani, Alix Haurez, Lorette Fernandez, Don Carl Abou Jaoude, Maximilian Brochnow and Dr.

Martina Sandroni. Thanks to Ranjana Yadav, Dr. Sambit Ghosh and Louis Guerin for the good times we had, the moments we shared, I will forever remember you.

Lastly, many many thanks to my family members, my dad Jones Mwalukuku, my beloved mum Esther Mwatati (thanks for your encouragement and your ever confidence and prayers to me) my brother Thomas Mwawasi, Nelson Mwatika, Hezron Mwawaza, and beautiful sister Mary Katini for your calls and support. Thanks to my uncle Mourice Mwasi, my role model and supporter, thank you for always believing in me. Thanks to my babygirl and jaber Maureen Mireri. Above all I thank the Almighty God for the good health and His support this far.

Table of Contents

Abbreviations

$A(t)$ - Absorbance of the matrix

A_∞ - residual absorbance

AC - alternating current

ACS - American Chemical Society

ADF – Amsterdam Density Functional

AM 1.5G – Air Mass 1.5 Global

a_n - amplitude of the kinetics

AVT - average visible transmittance

BIPV - Building-Integrated PhotoVoltaics

C_μ - chemical capacitance

C_0 - Prefactor

CB - conduction band

CDCA - Chenodeoxycholic acid

C_{dl} - double layer capacitance

CE - counter electrode

CF - Closed Form

$CHCl_3$ – Chloroform

CIE – Commission Internationale de l'Eclairage

CIGS – Copper Indium Gallium Diselenide

COSMO – Conductor-like Screening Model

CPE - constant-phase element

CRI - Colour Rendering index

CV - Cyclic Voltammetry

DC - direct current

DCM – Dichloromethane

DFT – Density Functional Theory

DSSC - Dye-sensitized solar cell

E_F – quasi-Fermi level

EIS - electrochemical impedance spectroscopy

EPFL - École Polytechnique Fédérale de Lausanne

E_{redox} - Redox potential

f^0 - cut-off frequencies

FTO - Flourine-doped tin oxide

g(E) - Total electron density

HOMO – Highest Occupied Molecular Orbital

IMPS - Intensity-Modulated Photoelectron Spectroscopy

IMVS - Intensity modulated photovoltage spectroscopy

j_0 - Kinetic Parameter

k_B - Boltzmann constant

k_n - Thermal decolouration kinetic constant

LiI - Lithium iodide

LiTFSI - Lithium bis(trifluoromethanesulfonyl)imide

LUMO – Lowest Unoccupied Molecular Orbital

n - total electron density

NREL – National Renewable Energy Laboratory

N_T - Total density of trap states

OF - Opened Form

PEC – PhotoElectroChemical

PEDOT - poly(3,4-ethylenedioxythiophene)

PSCs – Perovskite Solar Cells

PSS - photostationary state

PV - PhotoVoltaics

q - Elementary charge

R - resistance

R_{ct} - charge transfer or recombination resistance

R_{elec} - electronic resistance

R_{ion} - ionic resistance

R_s - bulk resistance

T - absolute temperature

TCO - transparent conductive oxide

TEMPO – (2,2,6,6-tetramethyl-1-piperidinyl)oxy

TW – TeraWatt

UV – UltraViolet

UV-Vis – UltraViolet Visible

V_0 - amplitude signal

V_F - Fermi Potential

V_{oc} - Open-circuit potential

WE - working electrode

Z - impedance

Z’ - real part

Z’’ or –Z’’ - imaginary part

α - trap distribution parameter

β - Recombination parameter

τ - electronic lifetime

ϕ - phase angle

φ - phase shift

ω - angular frequency

CHAPTER 1 : General Introduction and Methodologies

Abstract

Human race continues to advance in terms of increasing population, industrialization, and lifestyle changes. According to the late Nobel Laureate Richard Smalley, one of the critical issues is energy that needs to be affordable and reliable. The current annual worldwide electricity demand is 13 terawatts (TW) and is expected to double in the next 30 years due to factors such as technological advancement. The currently used fossil fuels, that are limited, non-renewable, and not capable of sustaining future generations are facing depletion. Notably, the recent Russian-Ukraine war has exposed the geopolitical constraints related to the use of fossil fuels resulting in escalated fuel and gas prices. Besides, they are also ecologically unfriendly and their combustion leads to emission of greenhouse gases such as carbon dioxide partially responsible for the current climatic changes referred to as global warming. For this reason, a lot of research is focusing on renewable energy sources such as biomass, wind, geothermal and solar. In comparison to the total solar power reaching the earth surface i.e. 120,000 TW, only a fraction is sufficient for our annual needs, therefore, is considered as a reliable and sustainable option. Thus, solar energy, being the most abundant energy source could be harvested or converted into different forms via photoelectrochemical (PEC), thermoelectricity and photovoltaic technologies. Harnessing energy from the sun can be attained using solar panels usually based on inorganic semiconductors such as silicon. These materials are often quite expensive and require high levels of purity. For this reason, emerging technologies based on organic materials have been developed in the past decades. This chapter focuses on the history of thin-film photovoltaic technologies, dye-sensitized solar cells, their advantages and shortcomings and hence my PhD project.

1.1 General introduction

Solar energy conversion has attracted immense interest in the last decades as a possible answer to the ever-increasing energy demands. Modern societies in the 21st century require energy that is projected to double within the next 30-40 years from the current 13 to 26 terawatt (TW) annually in the globe. This forecast was based on the increasing world's population from approximately 7 billion to 10 billion inhabitants by the year 2050 following the growth of emerging countries such as India and China. Although 26TW sounds unreachable, it is only a fraction compared to the total solar energy reaching the Earth's surface (of approximately 120000 TW) [1]. Among short-term major concerns is the constant increase in prices due to scarcity brought about by war (Russia-Ukraine war) and the constant depletion of carbon fossil fuel reserves such as coal, petroleum and gas that are considered as primary energy sources. Harnessing energy from these sources requires combustion that leads to emission of hazardous greenhouse gases such as CO_2 resulting in the controversial subject of global warming. Therefore, an increased interest in exploiting alternative and renewable energies such as wind, biomass, geothermal and solar is perceived to be a viable solution.

1.1.1 History of solar cells

The history of solar cells dates back in the 19th century when Antoine and Edmond Becquerel discovered the photo-electrochemical effect. In their work, they developed an electrochemical liquid cell that relies on light to initiate current generation known as ''photo-electrochemical solar cells''. A century later, the Bell laboratories developed solar cells based on crystalline silicon with a conversion efficiency of 6% in 1954 [2]. This formed a class of photovoltaic solar cells known as the first generation whose efficiencies have reached a record 26.6% [3]. In this work the silicon cells were fabricated through combination of interdigitated back contacts with either an amorphous silicon or crystalline silicon heterojunction. The second generation solar cells are based on group III-V direct band-gap semiconductors such as CdTe, GaAs and CIGS (copper indium gallium diselenide) that have demonstrated record efficiencies of 22.1%, 28.8% and 22.6%, respectively [4]. These multi-junction thin solar cells demonstrate comparable efficiencies to the single crystalline Si-based solar cells but the production cost has remained high owing to the high purity required of materials used.

Back in 1966, Gerischer sensitized GaAs semiconductor using a dye and demonstrated electronic injection from the dye [5]. In 1976, Amamiya *et. al* reported rose bengal dye

sensitized solar cells based on zinc oxide powder using an aqueous electrolyte. Using monochromatic light, at 563 nm, they were able to obtain solar cells with a power conversion efficiency of 1.5% [6]. Unlike the previous generations that often require high purity materials thus rendering the technologies expensive, the work of Amamiya *et. al* was revolutionized in 1991 forming third generation solar cells composed of dye-sensitized solar cells (DSSCs) and later perovskite solar cells (PSCs). DSSCs will be discussed in details hereafter but as for PSCs based on metal halides a certified power conversion efficiency of 25.2% has been reported [7].

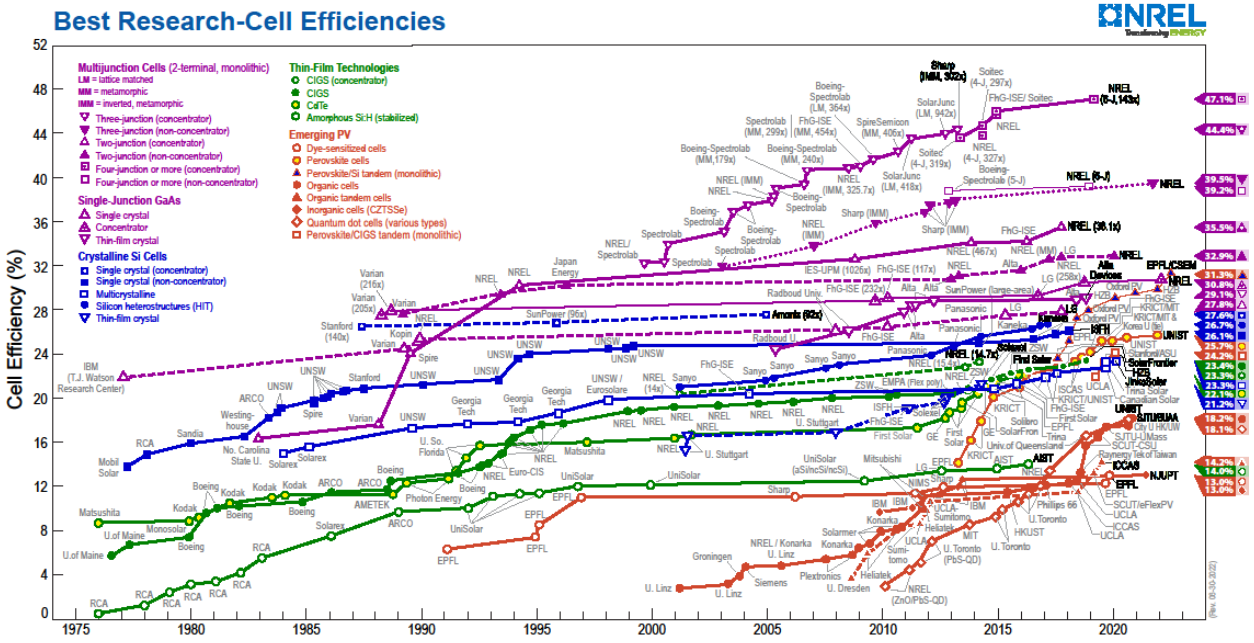

Figure 1.1 : NREL chart on solar cell technologies as extracted on 13th September 2022.

The chart above was obtained from NREL an acronym for National Renewable Energy Laboratory that documents the certified energy efficiencies of the various technologies. Preferentially, emerging photovoltaics (PV) have attracted major interests in the 21st century. The goal of these technologies is to lower the production costs i.e. <$0.5/Wp to allow for their mass production. Other than cheap components, they should be environmental friendly to facile their disposal or better recycling. Lastly, they should be stable especially under normal conditions. Among the emerging PV, dye-sensitized solar cells (DSSCs), in particular, have attracted interests owing to their appealing properties.

1.1.2 Dye-sensitized solar cells

In 1991, Grätzel revolutionized the DSSCs technology in his well-publicized work by replacing the crystalline semiconductor in Gerischer's work by a nanocrystalline semiconductor reaching and efficiency of 7.12% [8]. In this work, O'Regan and Grätzel sensitized mesoporous

TiO_2 with a Ru-based dye. The cells were made up of a 10µm thick electrodes containing nanometric sized titanium (IV) oxide particles. As a result, the surface area of the semi-conductor was greatly increased leading to an improved absorption of the incoming light. Such a device combining the nanoparticles and molecular systems mimics the photosynthetic behaviour of plants termed as artificial photosynthesis. In this technology, the nanoparticles and molecular systems are playing different roles [9] unlike in conventional silicon cells with the semiconductor assuming both functions. The clear distinction of roles in DSSCs results in lower purity demands compared to conventional silicon cells hence giving a low-cost alternative. This was a game changer and even after 31 years of intense studies, a plethora of publications is reported, aiming at improving the efficiencies further [10–17].

To understand why this topic remains hot at its ''31st birthday'', we need to look at the advantages associated with dye-sensitized solar cell as compared to other emerging PVs. First, as the title of the 1991 innovation, the solar cells are a low-cost i.e. the starting materials are cheap and abundant. The production techniques are also cheap and easy to follow i.e. from the preparation of nanocrystalline TiO_2 to the fabrication process. The other strong point is their environmental acceptability. The TiO_2 used is biodegrable which makes disposal easier [18]. Eventhough the pioneer study made use of Ru-based dyes that are rare and expensive, new studies have replaced this component with low-cost organic dyes that are environmentally friendly, easy to design and can be recycled [19,20]. DSSCs have also demonstrated higher degrees of flexibility such as shapes opening the window for many applications such as clothes [21] and scalability whereby we can have solar cells, cheaply designed mini-modules [22] and solar panels [23,24]. DSSCs based on ruthenium polypyridyl complexes opened the possibility to access a pallette of colours [25]. They have also shown the possibility to work under different environments even under low indoor light irradiation [26]. This paves way for future digital space as power sources for sensors making the Internet of Things (IoT) [27].

For all these reasons, DSSCs, among other emerging PVs, attract overwhelming interest in the scientific community despite having efficiencies half-way shy from conventional silicon based solar cells and the stunning rise of perovskites solar cells. The third decade of DSSCs was marked with strides that have rekindled the researchers' interests. They have also shown outstanding stabilities under accelerated ageing tests equivalent to up to 10 years of outdoor operation [28–30]. These strides were made by improving the dyes or electrolyte used that I will

discuss in detail in the next subsection. The current power conversion efficiencies (PCEs) of DSSCs have reached a certified value of 13.5% [10] and an uncertified one of 14.2% upon using cosensitized dyes [31].

1.2 Solar spectrum

The Sun is the power source from which the technologies listed above tap energy to generate electricity. The Sun emits light in wavelengths ranging from the ultraviolet, visible to the infrared in the electromagnetic spectrum. The spectrum peaks at the visible region characteristic of an ideal blackbody at 5760K as shown in Fig. 1.2 below.

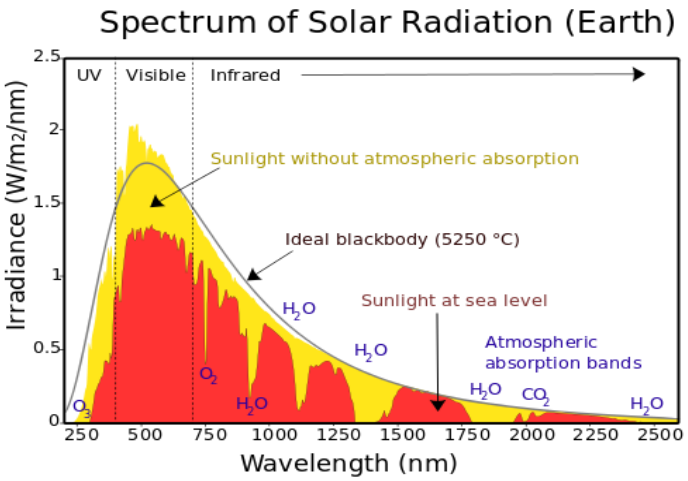

Figure 1.2 : Diagram showing the Earth's solar spectrum and the absorbing atmospheric gases. (Obtained from [9])

The atmosphere, however, is made of layers with different composition and contains several molecules such as ozone, oxygen, water, carbon dioxide that show absorption according to Figure 1.2 above. The Sun's intensity varies throughout depending on the time of the day and the geographical positioning. The position of the sun and the weather also affect the intensity of the sunlight. This would in principle mean that the intensity reaching the Earth's surface is different. For example, clear skies and time of the day (around mid-day) depending on the location allows maximum light intensity to reach the surface of the planet. Nonetheless, irrespective of the research lab location, researchers have developed a convention for standard measurements that I will discuss in the next sub-section.

1.2.1 Irradiation conditions

Depending on the position of the Sun, the path that sunlight has to travel varies and is known as air mass (AM). Calculated as,

$$A.M. = {}^{1}/_{\cos\theta}$$

Where θ is the angle of elevation of the Sun. Considering the parameters highlighted above, the standard conditions (outdoor application) employed in measurement of photovoltaic performances is AM 1.5G (global) spectrum. This makes θ = 48.2° and the irradiation energy received per unit surface to be 1000 $W.m^{-2}$ at room temperature. These standard irradiation conditions '1 Sun' can be reproduced in our STEP lab using a solar simulator.

Figure 1.3 : The solar simulator in our STEP lab connected to a Keithley digital source meter.

All the current-voltage (I-V) measurements for DSSCs reported in this manuscript were carried using this instrument and are comparable with literature data.

1.2.2 Solar Simulator

The solar simulator in our lab is (class AAA) which is a qualification with respect to the spectral match to the AM1.5G solar sepctrum. Thus, a class A solar simulator means that its non-uniformity to this spectrum is less than 2%. Very often, we scientists, crave for high performance solar cells to place the worth of the technology. Therefore, to ensure accurate and proper measurements are done hence correct data in the scientific literature, I will discuss later in the methods section how to characterize solar cells correctly.

1.2.3 Key Photovoltaic Parameters

The solar simulator explained above gives us results in form of *J(V)*-curves as shown in Fig. 1.4 from which we can extract the different parameters.

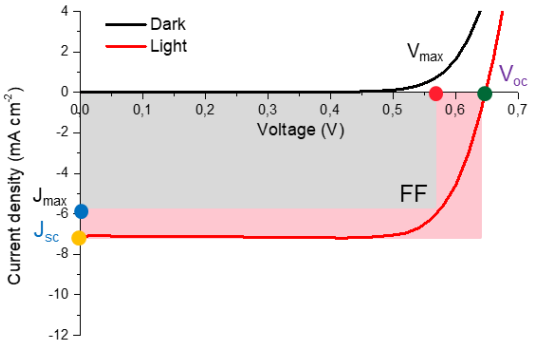

Figure 1.4 : Key photovoltaic parameters obtained from Keithley apparatus.

The utility of a solar cell technology is quantified by how efficient it is to convert the incident solar irradiance under the defined standard conditions into electrical power generated by the device. The overall sunlight-to-electric power conversion efficiency (η) is given by the equation below :

$$\eta\ (\%) = \frac{J_{sc} x\ V_{oc} x\ FF}{P_{in}} x\ 100$$

Where J_{sc} is the current density, V_{oc} is the open circuit voltage, FF is the fill factor, and P_{in} is the incident Sun's irradiation.

The photovoltage (V_{oc}) generated at open circuit under light irradiation corresponds to the energy difference between the redox potential of the electrolyte and the quasi-Fermi level of the TiO_2 semiconductor. The V_{oc} can also be impacted by the loss of charge in the device, which I shall discuss later as recombination. The photocurrent, J_{sc}, relies on the amount of light harvested (absorption properties of the dye), the number and the nature of dye molecules adsorbed on the TiO_2 surface, charged carriers movement, and injection efficiencies. The fill factor, FF, is a figure of merit that can take any value between 0 and 1 depending on the electrochemical (overvoltage) or electrical (ohmic) losses taking place in the operation of DSSC. FF is given by the equation:

$$FF = \frac{V_{max}\ x\ J_{max}}{J_{sc}\ x\ V_{oc}}$$

Thus, the (η) equation above becomes:

$$\eta(\%) = \frac{P_{max}}{P_{in}}\ x\ 100.$$

(P_{in}) as explained in sub-section (Solar Spectrum) is the universal condition adapted for standard measurements given as 1000 W.m^{-2}.

1.3 Working principle and kinetic processes in DSSCs

1.3.1 Scheme of a DSSC and working principle

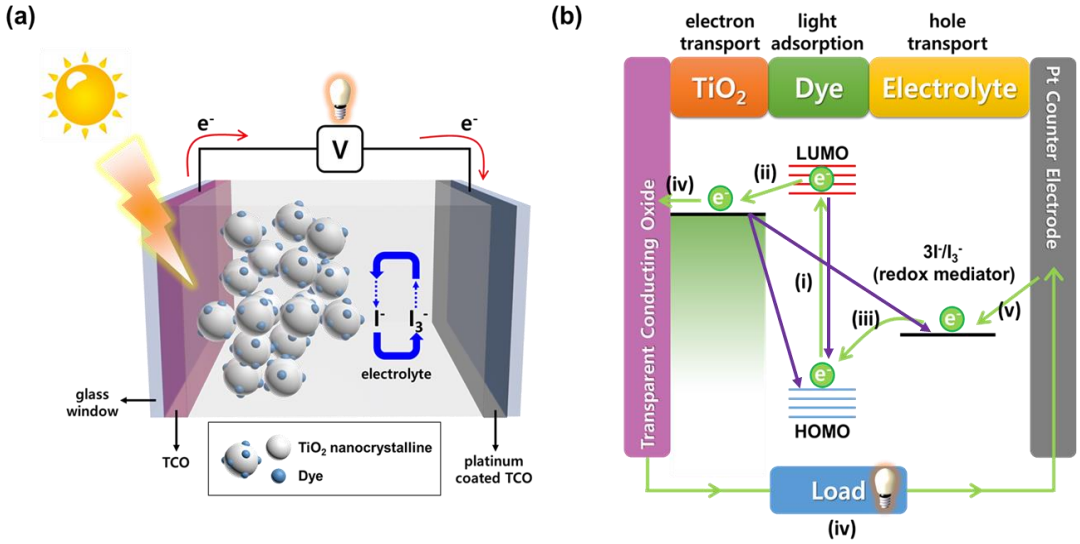

Figure 1.5 : a) Schematic representation of a dye solar cell. b) Working principle of an operational dye solar cell [17].

The operating principle of DSSCs is well known [8,17,32]. A DSSC is composed of 3 major components i.e. a photosensitizer immobilized on an inorganic semiconductor, in this case TiO_2, an electrolyte that acts as a redox couple (usually I_3^-/I^- dissolved in an appropriate organic solvent) [33] and finally the photocathode with a Pt catalyst to facilitate the electron exchange. The titanium (IV) oxide nanoparticles and the platinum are deposited on a transparent conducting oxide (TCO). There are two kinds of TCO used in the PV domain i.e. indium-doped tin(IV)oxide (ITO) and fluorine-doped tin(IV)oxide (FTO). Due to a better thermal stability, FTO is preferred for DSSCs whose manufacturing process requires high temperatures. The operational principle of a DSSC involves photoexcitation of the dye as the initiating process. The dye molecules (D) are promoted from the ground state to an excited state (D*) after absorbing photons. The excitation process involves promotion of an electron from the highest occupied molecular orbital (HOMO) to the lowest unoccupied molecular orbital (LUMO) of the dye. Then, an electron is injected from the excited dye (D*) into the conduction band (CB) of the semiconductor (usually TiO_2) thus forming an oxidized state of the dye (D^+). The electrons are then transferred to the anode via the TiO_2 mesoporous film. The electron is transported through an external circuit to the counter electrode (cathode). Meanwhile, the oxidized dye (D^+) is regenerated back to the ground state (D) by the reduced form of the redox couple (Red). This (Red) form is oxidized after donating the electron to the dye to become the oxidized form (Ox). The (Ox) form then migrates to the cathode (counter electrode) to recover the donated

electrons hence completing the circuit through an external connection. This is a perfect case scenario as other detrimental mechanisms could occur such as the back electron transfer from either TiO_2 CB or dyes' excited state to regenerate the oxidized species in the electrolyte termed as recombination [34].

1.3.2 DSSC components

In this part, I will highlight and discuss the three major components separately and show the impact of each. The discussions will lay a ground for a better understanding of why we chose the molecular design, the redox mediators and the cathode materials for the study I have undertaken in the past 3 years.

1.3.2.1 Photosensitizer

As already mentioned this is the component responsible for harvesting sunlight. Various properties are desirable in order to have efficient dyes for DSSCs. These properties include the ability to absorb in the entire visible region and the near-infrared (NIR) region of the electromagnetic spectrum to boost the device's photocurrent [35,36]. The LUMO energy level of the dye should be sufficiently high in energy compared to the conduction band of TiO_2 to allow for efficient electronic injection and the HOMO energy level lower than the redox potential of the electrolyte to allow the regeneration process [37]. Pandey *et al.* for example reported that the minimum energy barrier for efficient injection is 0.16 eV [38]. The HOMO and the LUMO levels need to have a good spatial distribution and separation to limit deactivation within the molecule and facilitate a better electronic injection into TiO_2. To graft the photosensitizer onto the TiO_2 substrate, the dye must have good anchoring groups such as sulphonic acid ($-SO_3H$), phosphoric acid ($-PO_3H$), or carboxylic acid (-COOH) groups [39]. Dye aggregation on the semiconductor surface should also be avoided that could result in formation of islands on the surface through molecular design or introducing additives for coadsorption. Lastly, the dyes should also have good thermal- and photo- stability for improved lifetime on target application.

Based on these properties, metal-based complexes were first used as DSSC photosensitizers such as ruthenium and iridium complexes (see Fig 1.6). Although not very intense, they display broad absorption spectra with an excited-state long-lived enough to transfer an electron into the TiO_2 CB [40]. This allowed Gratzel and O'Regan to attain an overall light-to-electric energy conversion yield of 7.1-7.9% under simulated light that revolutionized the field [8].

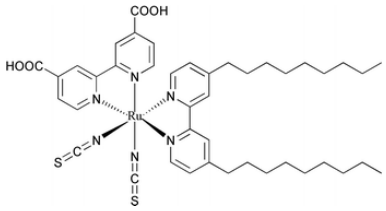

*Figure 1.6 : Chemical structure of a ruthenium-based hydrophobic **Z-907** dye [41].*

Eventhough ruthenium complexes have shown reasonably good efficiencies, they are limited in the absorption of sunlight in the NIR region of the solar spectrum. Ruthenium is a rare element making it expensive, besides its toxicity is another concern. DSSC is a low-cost technology, thus alternative photosensitizers have since been investigated such as porphyrins [42] and phthalocyanines that show absorption in the NIR [34]. Other photosensitizers are the metal-free organic dyes [43] that have shown the possibility to lower the production cost eliciting much interest into their study. Conjugated dyes have proved to be a good alternative to ruthenium photosensitizers while portraying superior traits [34,44].

A particular case are dyes with a donor-pi-conjugated bridge-acceptor configuration mainly as a strategy to decrease the HOMO-LUMO gap of the photosensitizer known as band gap engineering. The principle behind is the push-pull effect where the donor moiety has a low ionization potential (easy to donate an electron) while the electron accepting moiety is highly electronegative (more electron withdrawing/accepting) thus modulating the HOMO-LUMO gap. Other than the tunable optical properties thanks to band gap engineering, conjugated dyes have several advantages such as their ease of design and synthesis, lower cost of starting materials and building units, environmental friendliness, and higher molar extinction coefficients than the classical noble complexes [45].

1.3.2.1.1 Donor-pi-acceptor strategy

Figure 1.7 : Donor-pi-conjugated bridge-acceptor.

Among these organic dyes, triarylamine-containing dyes as the donor substituent have shown a lot of success [46,47]. Yanagida *et al.* in 2004 reported organic dyes with triphenylamine (TPA) electron donating unit with a light-to-power conversion efficiency of 6.6% that have seen its improvement in DSSCs [48]. The TPA unit is a good electron donor and its non-planar structure is believed to prevent the unfavorable dye aggregation on the TiO_2 surface [49]. This donor group

not only has an effect on the absorption spectra of the dye but also on the positioning of the LUMO levels of the photosensitizers. A good positioning of these frontier orbitals is crucial for the driving force towards charge injection and the dye's spectral response. An example of high performance DSSC based on TPA-unit type (based on Hagfeldt bulky donor [11]) is XY1b-based solar cell that has shown record 13.6% efficiency with a single dye [10]. Therefore, different donor properties of the TPA unit will be explored in this thesis.

Other interesting donor units that have been reported in literature and have been or could be interesting to implement in my project include one exhibited in ADEKA-1 dye registering up to 12.8% efficiency [50]. Carbazole-based donor units with a fused TPA donor unit have also been explored during this training.

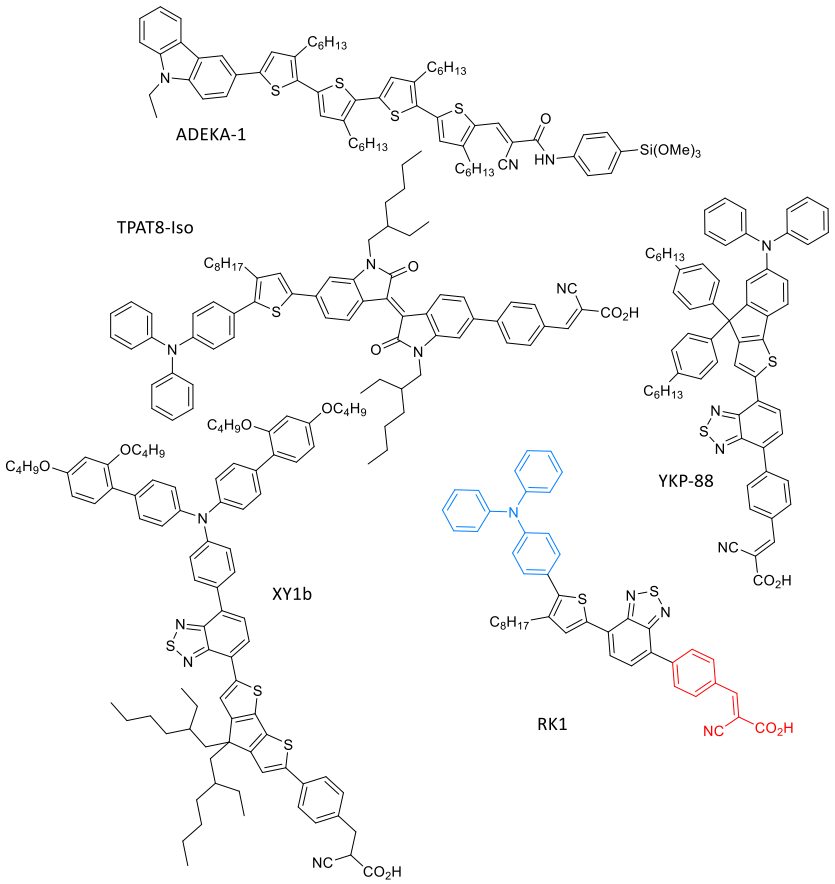

Figure 1.8 : Examples of best performing single D-pi-A based dyes reported in literature [10,51] and the others designed in our lab [22,30,52].

The π-spacer in conjugated dyes acts as a bridge that relays electrons from the donor-part to the acceptor. Chemistry developments have been focussed on the modulation of the π-conjugated bridges to improve communication within the molecule. To date more than a thousand dyes have been reported in literature and many different chromophores [14,44,47] have

been employed in the pi-conjugated bridge to modulate the final properties of the dyes, leading in some cases to efficiencies close to 13% [53]. In this work, two thiophene molecules were fused resulting in brilliant sapphire colour when sensitized with TiO_2 electrodes.

Finally, the electron-accepting moiety plays a dual role i.e. both as an electron acceptor and an anchoring function for grafting the photosensitizer onto the TiO_2 substrate. To sum up, the D- π -A structure has proved useful with not only high molar absorption coefficients and low cost in molecular design but also structural variety. The D–π–A architecture kindles the intramolecular charge transfer (ICT) from the A to the D moieties via the bridge necessary for light harnessing and hence their optoelectronic properties. In this work we shall see the effect of the different substitutions of the π-spacer with the cyanoacrylic acceptor unit. Examples of such molecules bearing the D- π –A design have been synthesized in our lab coded **RK1** [43], **YKP88** [22] among many others.

1.3.2.2 Semi-conductors

A semiconductor is simply a material whose electrical properties lie between that of a metal and an insulator. Metals have their valence band (VB) and conduction band (CB) overlaid, in semiconductors there is a gap between the VB and CB which can be overcome by thermal excitation, whereas insulators have a very huge gap that cannot be easily overcome. Different wide band-gap semiconductors have been explored as effective electron receptors in DSSCs such as ZnO [6], SnO_2 [54], Zn_2SnO_4 [55], Nb_2O_5 [56], $SrTiO_3$ [57] and TiO_2 [8]. TiO_2 is the most preferred giving highest solar conversion efficiencies with more advantages such as low cost, availability and chemical stability.

Titanium dioxide (TiO_2) exists in different crystalline forms for example, brookite, rutile, and anatase. The crystalline structure has a key role to play in light-to-power conversion efficiency. Rutile phase is known for chemical stability, high conductivity and efficient white light scattering although anatase phase is preferred for photovoltaic applications. Anatase phase on the other hand has a better surface chemistry and higher CB edge compared to rutile phase[58], more important for DSSC applications despite rutile's light diffusivity property.

During my PhD, the electrodes were fabricated with TiO_2 anatase nanoparticles. The composition of the electrodes is as shown in the figure below. A number of techniques can be used to deposit the anatase TiO_2 mesoporous (with particle size 2-50 nm) thin film on the TCO

such as spray drying, screen printing and doctor-blading. This is followed by sintering at 500°C making the photoanode. Higher solar-conversion efficiencies have been recorded with double layer structures where a scattering layer consisting of large-sized TiO_2 particles (typically 200-400 nm) is added above the mesoporous thin film. The scattering layer plays the role of diffusing light and concentrate it on the dye thereby improving absorption.

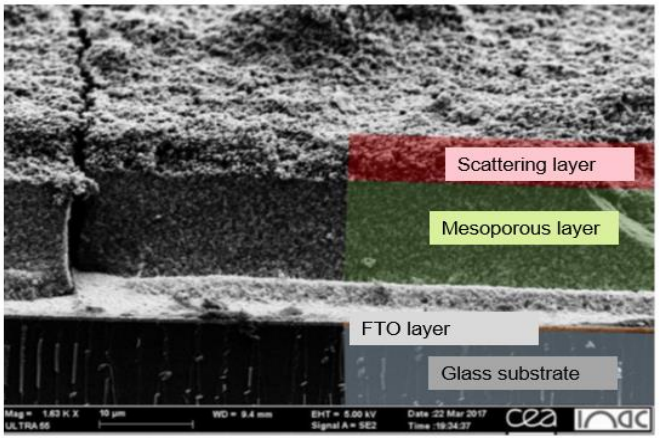

Figure 1.9 : SEM image showing the typical photoanode layout.

I have employed two types of electrodes in this work i.e. electrodes composed of mesoporous layer and scattering layer referred to as opaque whereas those containing only the mesoporous layer are transparent.

1.3.2.3 Electrolytes

An electrolyte provides a medium for ionic/charge conductance between the negative and the positive electrodes in an electrochemical cell. The electrolyte is a key component in DSSCs [8]. Electrolytes are categorized into three, quasi-solid electrolytes [33], solid-state conductors [59], and the liquid electrolytes [8] that I will focus on.

A liquid electrolyte is usually based on an organic solvent, a redox mediator (such as I_3^-/I^- redox couple), and additives. In a classical electrolyte, different ingredients are therefore added to the volatile organic solvent, acetonitrile, to gain high efficiencies. The classical liquid electrolyte is composed of, but not limited to guanidinium thiocyanate, lithium iodide, iodine, *tert*-butylpyridine, and an organic solvent -acetonitrile- as we shall see later in Chapter 2 playing different roles.

It is also responsible for charge transport in a complete solar cell and regeneration of the oxidized dye (D^+). Among other effects, the electrolyte has an influence on device's long-term operational stability, diffusion of the charge carriers (I_3^-/I^-), and light-to-electric conversion

efficiency. As already mentioned, the performance of a DSSC is determined by the three critical parameters *i.e.* J_{sc}, V_{oc}, and FF, all of which depend on the electrolyte.

For example,

J_{sc} can be influenced by the positioning of E_F of the TiO_2 and redox couple mass transport,

V_{oc} by the electrolyte's mediator redox potential with reference to the CB of TiO_2,

FF by the charge transfer resistance and the diffusion of charged species.

With this is mind, I have developed in this PhD project new electrolytes based on metal-based complexes and new additives to boost the photovoltage and charge transport diffusion and dynamics, respectively.

1.3.2.4 Cathode materials

Lastly, the photocathode takes part in the transfer and exchange of electrons between the external circuit and the electrolyte. The substrate is made up of a conducting FTO glass onto which a layer of platinum is coated to catalyze the electron transfer process. An ideal cathode for DSSCs should have traits such as high conductivity, low charge-transfer resistance, correct energy positioning, high surface area, high catalytic activity, good resistance to chemical corrosion, low cost and easy processability. The preparation process could have an impact on the particle size and morphology [60,61]. For example, small-sized particles result in increased electrode surface area hence improved catalytic activity.

Traditionally, Pt has been used to obtain high efficiencies owing to its high catalytic activity and good conductivity. Therefore, most of the work reported in this manuscript will be based on platinum to attain high efficiencies. The disadvantage with this counter material is that Pt is a rare element and expensive thus increasing the manufacturing cost of DSSCs. For this reason, several research works have attempted to replace Pt with other materials such as carbon-based ones e.g. graphene nanoplatelets that have shown high catalytic activity, increased surface area, abundant and cheap [62]. Other cathode materials based on PEDOT (poly(3,4-ethyleneedioxythiophene)) with lower processing cost and good conductivity have also been explored [63]. I have also proposed and applied the use of highly conducting polymers in my work that I will discuss in the last chapter thanks to a collaboration I made with the then PhD student in LITEN, now Dr. Amélie Schultheiss.

1.4 Interfacial processes in DSSC

When the sensitized photoanode, the electrolyte and the cathode electrode are assembled together in a sandwich format, they make a dye solar cell as shown in the image below.

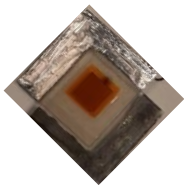

Figure 1.10 : A complete dye-sensitized solar cell.

The three components are in contact with one another thus forming interfaces in between. The TiO_2-dye-electrolyte interfaces involves processes happening at different time scales as shown in the figure below.

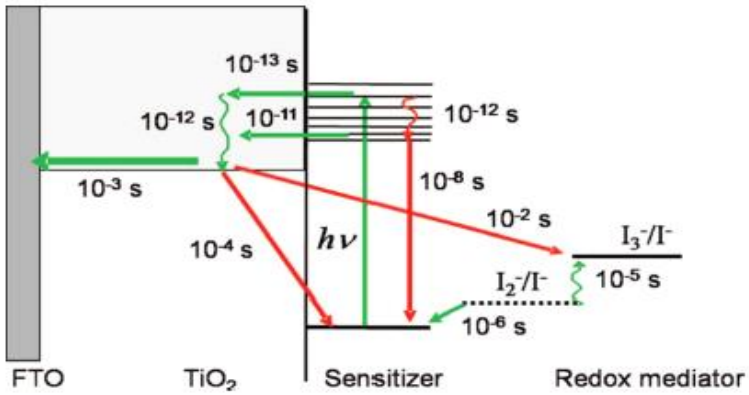

Figure 1.11 : Diagram showing the processes (forward reactions in green and recombination in red) with their time constants in a Ru-dye -based solar cell (with permission from [64]).

The processes in green are favouring the solar-to-electricity conversion. The processes in red are undesirable and will be mentioned frequently in this report as recombination. Thus, recombination refers to processes where the already injected electrons into the TiO_2 are driven back either to regenerate the oxidized dye (photosensitizer) or electron deficient redox couple (I_3^-/I^-). Consequently, these electrons are lost. Although these processes are detrimental, their negative effect is not far much pronounced due to the slow kinetics with time constants indicated in red compared to the green ones [32].

1.5 General Context

As seen, DSSCs have many advantages including ability to tune their optoelectronic properties by changing the dye and notably by replacing functional groups in the D-π-A architecture. This

opens the possibility to access a pallette of colours that are aesthetically appealing [25]. **Ru**-based dyes and **RK1** derivatives (designed and synthesized in our lab) are colourful and give rise to semi-transparent solar cells when sensitized on a mesoporous TiO_2 semiconductor can be attractive for Building-Integrated PhotoVoltaics (BIPV). The first ever example for application as architectural design was the solar façade at the École Polytechnique Fédérale de Lausanne (EPFL) Convention Centre in Switzerland [65]. This was a major step towards zero energy and zero emission buildings for the future i.e. turning buildings from energy-consuming into energy-generators with an aesthetical aspect. **RK1** was the first purely organic dye finding application in BIPV.

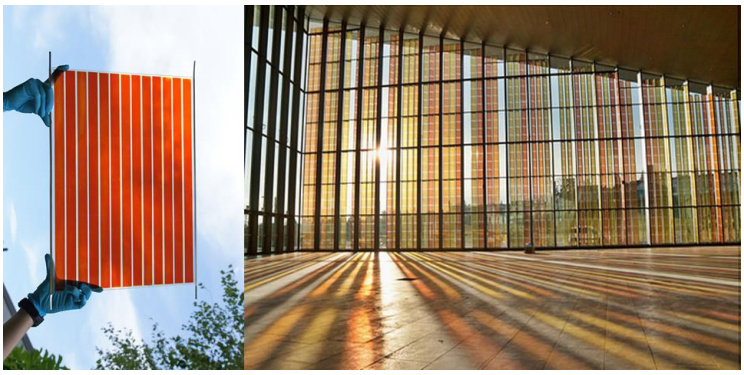

*Figure 1.12 : (On the left) A solar mini-module based on **RK1** dye and (on the right) an **RK1**-and-**Ru** (complexes) –based solar façade. (Images courtesy of Solaronix, Switzerland).*

A great advancement of this PV technology, however, several key issues need to be addressed to spread this technology further onto the market. Since highly absorbing (thus low transparency) solar devices are required to enhance the energy conversion efficiency, BIPV calls for high transparency (i.e. low absorption) meaning thinner photoactive layer. DSSCs incorporated in EPFL have encountered drawbacks, e.g. the inability to modulate their optical transmission once fixed during assembly (constant absorption). To address this, our team has introduced a new concept focusing on the replacement of classical photosensitizers (with fixed optical transmission) by photochromic photosensitizers that can self-regulate their optical transmission depending on temperature and light. In other words, a new class of dye solar cells that adapt their optical and photovoltaic properties depending on the weather conditions. The uniqueness of our work relies on the design of dyes with a “donor-pi conjugated bridge –acceptor” structure where the pi-conjugated bridge is replaced by a photochromic unit thus giving distinctive optical properties.

1.5.1 Photochromism

In this work, organic dyes have been replaced by photochromes. Therefore, it is useful to recall some basic definitions. Photochromism is a reversible change in a chemical compound induced in either one or both directions by an external stimulus that is light in this case. When the molecule absorbs electromagnetic radiation, it switches between the two forms, A and B, having different absorption spectra [66]. Other than light illumination and thermally activated photochromism, photoisomerization can induce changes in the electrical properties resulting in isomers having different ionization potentials. Electric current can also induce isomerization process and can involve some examples of electrochromism [67].

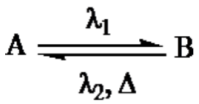

Figure 1.13 : Reversible chemical transformation using light.

When the molecules are irradiated with light, at a given temperature, a dynamic equilibrium is created. This equilibrium is known as the photo-stationary state (PSS). In the case of photochromic dyes studied here, a different wavelength or thermal deactivation could be used to return to the closed form, making them T-type photochromes (T for thermally reversible).

1.5.1.1 Examples of Photochromes and their application

Molecules that have the ability to change colour upon ultraviolet (UV) irradiation are referred to as photochromes. Molecules that are colourless in the dark (showing absorption in deep UV) and become coloured upon irradiation (with absorption in the visible) are referred to as normal photochromes otherwise reverse photochromes (with opposite behaviour). Several classes of molecules have shown photochromic effect such as spirobenzopyranes [68], azobenzenes, dihydroazulenes [69], diarylethenes [70], stilbene derivatives, and naphthopyranes. Each class is associated with a chemical process responsible for the photochromic behaviour and this process can give rise to the formation of stable or non-stable isomers. For example, in some the colouration and decolouration can be as a result of either a heterolytic bond cleavage resulting in a ring opening and closure isomerization reaction, conformational change (AZB), or an intramolecular proton transfer.

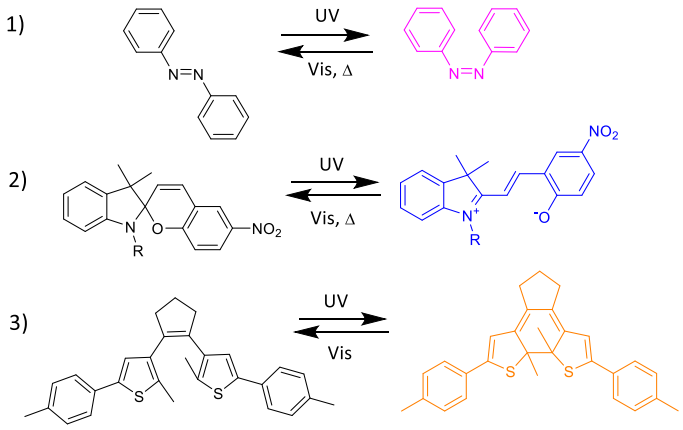

Figure 1.14 : Some examples of molecules exhibiting photochromism. 1) Azobenzene and 2) spiropyran molecules interconversion upon irradiation with ultraviolet (UV) and visible light from the colourless to coloured species. 3) Diarylethene showing two thermally stable isomers (left) colourless open-ring isomer and (right) coloured closed-ring isomer.

Such molecules have found usefulness in various fields of application such as data storage i.e. on and off from the two different states [71]. They have also been applied as molecular machines to lift a load such as in actuators [72], optical lenses [73] among many others. When looking for application of photochromic dyes in DSSCs, only very few works exist.

In 2015, Johnson *et al.* applied spirooxazines and spiropyrans in DSSCs. The TiO_2-based transparent electrodes switched their colour upon irradiation from colourless to blue but the efficiencies were rather low, 0.007% and 0.028% for spirooxazines and spiropyrans, respectively [74].

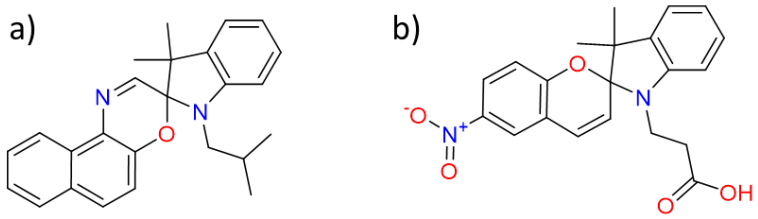

Figure 1.15 : a) 1-isobutyl-3,3-dimethylspiro[indoline-2,3'-naphtho[2,1-b][1,4]oxazine] and b) 3-(3',3'-dimethyl-6-nitrospiro[chromene-2,2'-indolin]-1'-yl)propanoic acid.

The poor PV performances were related to poor electrode sensitization due to lack of anchoring groups on their dyes. To immobilize the photochromes on the TiO_2-surface, the authors spraid a thin epoxy layer which could potentially limit the mass transport and diffusion of charged species thus limiting the regeneration process.

Another example of photochrome used in DSSC introduced the photochromic bisthienylethene (BTE) conjugated bridge in the dyes.

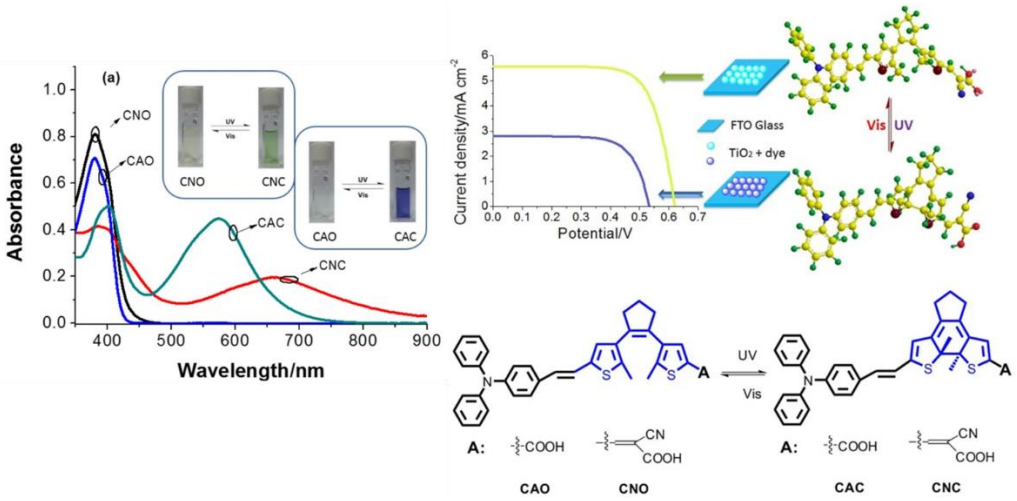

Figure 1.16 : On the left,absorption spectra of D-pi-A bisthienylethene based photochromes and on the right, their respective photoisomers and the photovoltaic performance (obtained from [75]).

The photoisomers (CNO – CNC or CAO – CAC) generated are wavelength dependent with efficiencies ranging between 0.30% - 2.00%.

The different isomers can be obtained by alternating irradiation, with UV and visible light, thus tuning the power conversion efficiency of their devices reversibly by manipulating the light source. For instance, when the devices were irradiated at 365 nm, it gave rise to absorption peaks appearing at 574 nm and 694 nm corresponding to BTE-CA and BTE-CN with colour changes from colourless to bluish-purple and yellow to green, respectively. Alternatively, upon irradiation with visible light (>500 nm), the bluish-purple or green colour switched to colourless or yellow thus recovering back the open isomers (CAO or CNO). This work was the first in its kind to regulate the PV performance of DSSC using photons of different wavelengths [75].

1.6 Building-Integrated Photovoltaics (BIPV)

Self-sustainable buildings towards zero energy and zero emissions are foreseen as a potential solution to energy problems in cities. Solar cells integration in buildings provides new aspects for architectural designs. The constant colouration of solar cells on façades or windows could create visual discomfort to inhabitants [76]. The Holy Grail is reaching high photovoltaic performance if natural light has to enter the living spaces in the building.

Different strategies could be envisioned for such BIPV applications : either the use of NIR dyes that give rise to uncoloured solar cells whatever the daylight or the use of photochromic dyes with dynamic optical properties. Baron *et. al* designed zinc phthalocyanine (coded **KMH63**)

intended for transparent and colourless solar cells. This dye shows an absorption maximum in the near-infrared at 787 nm. When applied in solar cells, a J_{sc}=1.23 mA.cm^{-2}, V_{oc}=461 mV, FF=72% and a PCE=0.41% was reported under 1 Sun. The poor performance was related to the poor electronic communication owing to lack of an overlap between LUMO and LUMO+1 leading to sluggish electronic injection [77].

Sauvage F. *et. al* have developed new sensitizers with the ability to select the wavelength through molecular engineering [78]. In their work, they estimate the maximum photocurrent density of the selective NIR absorbers to 13 mA.cm^{-2} in the 350-420 nm and 750-950 nm range. They estimated their fully optimized selective NIR-DSSCs to reach ca. 8% with high aesthetic features.

Another example is when NIR-selective heptamethine cyanine dyes coded **VG20-C$_x$** reported by Naim W. *et. al* were employed in a DSSC configuration [79].

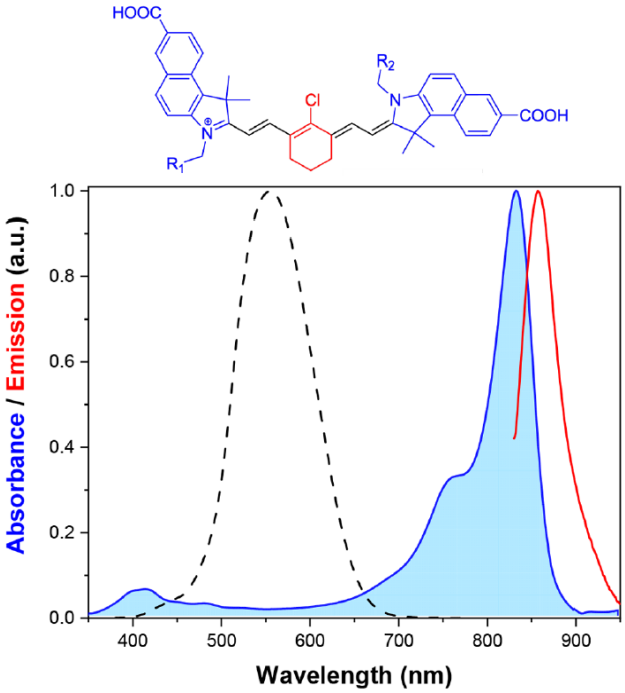

*Figure 1.17 : The chemical structure of an NIR-photosensitizer **VG20-Cx** with R_1=R_2=C_2H_5, C_8H_{17} or $C_{16}H_{33}$. In blue is the normalized absorption spectrum of **VG20-C$_{16}$** and in red the photoluminescence spectrum. The black dotted line is the human photopic response. Image extracted from [79].*

These NIR-DSSCs can show upto 3.1% power conversion efficiency with an average visible transmittance of 76%, when Co-based complex was employed as a redox mediator, a value close to that of a double glazed window at 78%.

Thus, two strategies have been envisioned for transparent photovoltaics. Either that developed by Odobel *et. al* consisting of pyrrolopyrrole cyanine as sensitizers for selective NIR-

DSSCs giving rise to uncoloured solar cells whatever is the daylight [80] or photochromic dyes with dynamic optical properties.

To overcome this challenge, our group has proposed the use of photochromic dyes with the ability to change both the colour and the PV performance upon irradiation in a reversible way hence project 'PISCO' (Photochromic Solar Cells: Towards Photovoltaic Devices with Variable and Self-Adaptable Optical Transmission).

The photochromic organic DSSCs play dual function *i.e.* they simultaneously self-adapt their transmission of light while generating electricity depending on the weather conditions. The recent introduction of photochromic DSSCs will not only help in converting energy-consuming buildings into energy generators but also "active skins". This property is valuable given that, under normal and real conditions, the Sun's intensity varies during the day.

1.7 Objectives of my PhD

The operation of DSSCs and the key parameters that determine high efficiencies are now known in the field when organic or organometallic dyes are used as sensitizers. However, photochromic dyes for organic solar cells are a new class of photosensitizers that have not been used previously in the field. Therefore, their use raises new fundamental questions such as :

- Does the device's operation follow the same rules with photochromic dyes?
- What parameters influence the efficiency when a photochromic sensitizer is employed?

The goal of this PhD is to answer these questions thus several objectives were set :

- To fabricate and characterize photochromic organic dye solar cells with decent performances.
- To optimize the best dyeing conditions for TiO_2 sensitization.
- To investigate the influence of additives in classic electrolyte and find the optimum electrolyte composition.
- To unravel the electronic processes limiting the performances.
- To establish an interplay between photochromic and photovoltaic properties and hence the balance between transparency and efficiency.

- To establish the structure-property relationships for photochromic dyes.

In this first chapter, I have discussed the general context of DSSCs, bibliography, state-of-the-art research on transparent photovoltaics and the techniques that can be employed. In Chapter 2, I will discuss the application of photochromic dyes in a DSSC configuration and an in-depth understanding of their operation. In Chapter 3, I will discuss the improvement of photochromic DSSCs performance through structure-property relationships of the dyes termed **NP**-series. In Chapter 4, I will look at the effect of donor and acceptor structural modifications based on **NPI**-backbone to attain high-performing devices. Finally, Chapter 5 shall focus on the way forward given that I understand the working with photochromic dyes.

1.8 Materials and Methods

1.8.1 Materials

During the 3 years of my PhD, I have investigated several non-photochromic and photochromic organic dyes. I have worked hand-in-hand with organic chemists in the group like Dr. Quentin Huaulmé, Dr. Johan Liotier, Dr. Gael Heintges, Dr. José-Maria Andrés Castan, PhD student Samuel Fauvel and M2 intern Margaux Giroud. With the help of Samuel Fauvel, I was able to synthesize large quantities of photochromic dyes that I needed to finish my experiments and, in collaboration with Solaronix, Switzerland, make solar mini-modules that I will detail in Chapter 2 and 3. For the photochromic dyes, I will highlight selected few. A non-photochromic dye, RK1, previously reported in the lab and commercially available at Solaronix, Switzerland was used as the reference dye [43].

Chenodeoxycholic acid (CDCA) was used as a coadsorber during TiO_2 sensitization. This molecule is known to prevent undesirable aggregation of the dyes and lead to higher performances for the devices [81].

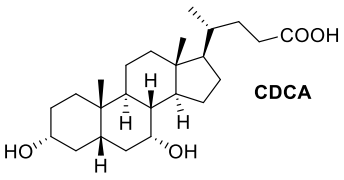

CDCA

The normal composition of a commercial electrolyte is: iodine, 4-tertbutylpyridine (TBP), guanidinium thiocyanate, lithium iodide (LiI), 1,3-dimethylimidazolium iodide (DMII) in acetonitrile (ACN). The reference DSSC based on **RK1** dye will incorporate a commercial

electrolyte known as iodolyte-HI-30 purchased from Solaronix, Switzerland. In this work, I have optimized each component to attain high performance photochromic solar cells.
The electrodes used are photoanodes and drilled counter electrodes were purchased from Solaronix, Switzerland. Some 3-4µm thick transparent photoanodes were printed in Hybriden lab, CEA-Grenoble. The counter electrodes were also prepared in the lab from the large area FTO (10cm×10cm) by cutting and drilling 0.6mm holes on the (2cm×2cm) electrodes.

Thermoplastic sealing polymer: surlyn (25 and 60 µm thick), dyeing bath bottles, hot plates, test caps and gaskets, vacuum pumps, soldering tin wire for metal contact.

The instruments used are: AM 1.5 solar simulator, UV-Vis spectrophotometer, cyclic voltammetry, electrochemical impedance spectroscopy (EIS) and intensity-modulated photocurrent spectroscopy (IMPS).

1.8.2 Preparation and Fabrication of DSSCs

Here I report the procedure that I employed for the preparation of the devices. The received electrodes have to be treated first with $TiCl_4$ before use. This treatment plays a dual function, one enhancing the bonding strength between the nanoparticles of the mesoporous TiO_2 layer [82,83]. Secondly, to improve the surface state of the TiO_2 in order to reduce defects and prevent charge recombination between injected electrons in the TiO_2 and I_3^-/I^- redox couple.
Beforehand, the electrodes are cleaned with absolute ethanol and dried under argon flux. This is mainly to remove any dust particles attached on the electrode surface. $TiCl_4$ (0.45 mL, 778 mg, 4.10 mmol) is added dropwise to cooled deionized water (100 mL) at 4°C. The solution is stirred further for 5 minutes (cooled in an ice bath). The titanium electrodes are then placed in this freshly prepared solution and heated at 70°C for 20 minutes. This is the second $TiCl_4$ treatment with the effect of improving surface roughness factor for dye adsorption thus high photocurrent [84]. The electrodes are then cooled to room temperature, rinsed with distilled water then absolute ethanol and dried under an argon flux. The electrodes are then charred under air at 500°C for 20 minutes. Once cooled to room temperature, they are immersed in a dyeing bath (of known composition) overnight. The dyeing bath is prepared in a mole ratio e.g. of 1:10 *i.e.* dye:CDCA where the dye is dissolved in chloroform and CDCA in either *tert*-butanol or ethanol.
The drilled counter electrodes are also rinsed with ethanol and dried under argon flux (to remove any dust particles). They are then coated with a thin layer of platisol (ethanolic

solution of PtH_2Cl_6) and charred under air at 500°C using the same heating procedure as the photoanodes.

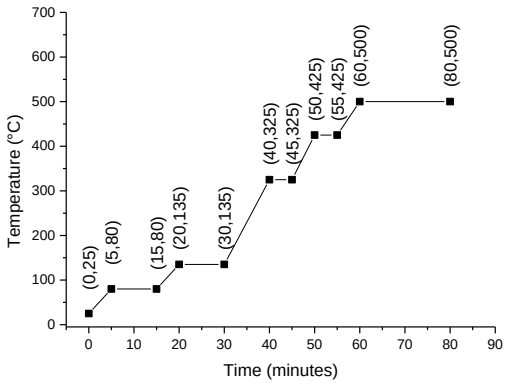

Figure 1.18 : The sintering procedure for the electrodes (photoanodes and photocathodes) preparation procedure.

After a night (approximately 16-20h) of dyeing, the photoanodes are rinsed with dichloromethane and EtOH to remove any unadsorbed dye molecules. The photoanode and the counter electrodes are sealed together using a suryln thermoglueing polymer (60 or 25 µm thick) using a heating press (T=105°C for ≈16s) while ensuring the conducting sides of the electrodes face each other in a sandwich fashion. The assembled electrodes are then filled with an appropriate electrolyte through the tiny hole on the counter electrodes using a vacuum pump. Once filled with the electrolyte, the holes are sealed with a surlyn thermo-glueing polymer and a glass cap on top to prevent the electrolyte from leaking.

A metal contact along the electrode edges is created to collect the photogenerated electrons and for easier characterization. The devices are ready for characterization.

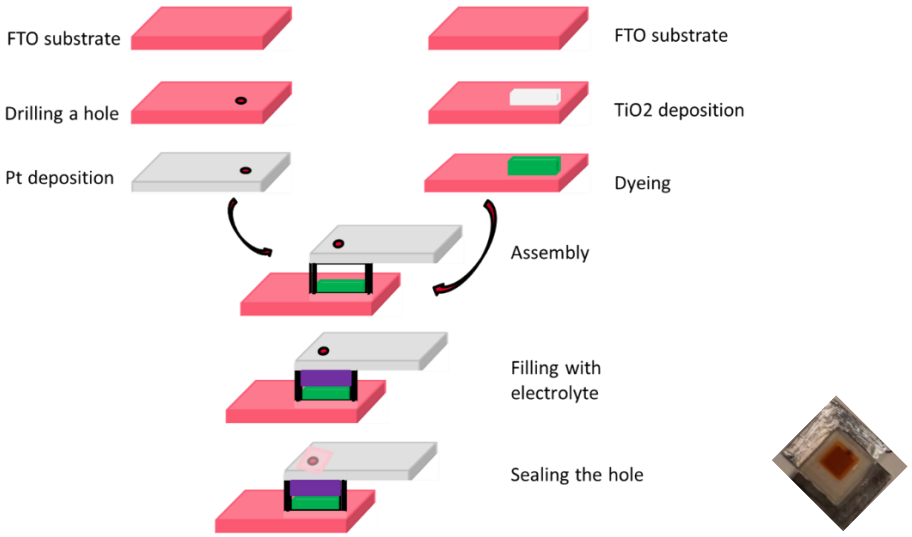

Figure 1.19 : Step-by-step DSSC manufacturing process.

1.8.3 How to measure DSSCs correctly

Before proceeding with further measurements, the AM 1.5 solar simulator emission is calibrated using a reference Si photodiode, equipped with an IR-cutoff filter (KG-3, Schott), of known mismatch and performance. There was no specific mismatch factor applied for the calibration of the simulator for each photochromic dye and the performances agree with SOLARONIX on all devices thus ensuring a relevant measurement. The error between AM 1.5 and the simulated light is reduced to less than 2% [85]. To instill a good measurement culture, the simulated sunlight was calibrated before testing DSSCs to have the standard 1 Sun (1000 $W.m^{-2}$). The solar simulator is connected to a power supply from which the power of the lamp can be adjusted to positive or negative values. The inner surfaces of the solar simulator are painted black to inhibit the reflectance of simulated sunlight leading to incorrect measurements. The reference cell has its sample holder marked, which ensures that the cell is held in position each time the calibration is done interchangeably. The test cell holder is masked with an aperture of known area to define the active area. This active area is important when changing the short-circuit current (mA) into the short-circuit current density ($mA.cm^{-2}$). Why is area definition important? I carried out an experiment with varying illuminated area and the result was as shown below.

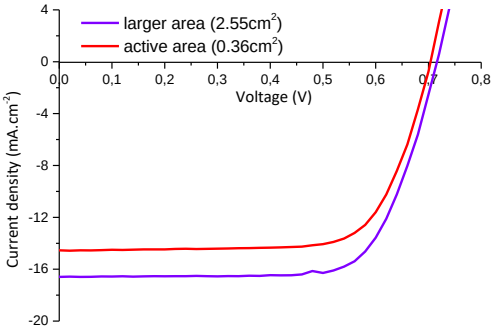

Figure 1.20 : The effect of area under illumination on the photovoltaic performances of DSSCs.

The larger area (2.55 cm^2) under illumination gave the following PV parameters : J_{sc}=16.59 $mA.cm^{-2}$, V_{oc}=0.716 V, FF=0.725 and PCE=8.62% against J_{sc}=14.55 $mA.cm^{-2}$, V_{oc}=0.704 V, FF=0.722 and PCE=7.39% when 0.36 cm^2 active area was illuminated. The most affected parameter is the photocurrent density due to the extra light from the sides. Lack of masking the inactive region of the glass substrate will result in divergent and scattered light enter the photoactive region from the sides thus increasing the registered photocurrent [86]. On the other hand, Snaith reported that if the mask is smaller than the photoactive area, the V_{oc} of the

device will be slightly decreased due to dark regions, an opposite behaviour from what I observed in Fig. 1.20 above. For this reason, all solar cells investigated in this PhD were properly masked to attain the correct active area, the indoor sun (simulated sunlight) was calibrated to have an equivalent irradiance at 1,000 $W.m^{-2}$ and a reference cell based on dye previously reported in the lab (**RK1**) was prepared and measured during each experiment.

1.8.4 Characterization

1.8.4.1 Current-Voltage measurements

The fabricated devices are analysed for the determination of power conversion efficiencies (PCE) and the electrical parameters are extracted from the current-voltage curves as shown in (Fig. 1.4) above. PCE value of a solar cell is the ratio of the maximum power to the power of incoming irradiation (Sun's). It gives information about photocurrent at zero voltage and photovoltage at zero current known as short circuit current (J_{sc}) and open circuit voltage (V_{oc}), respectively. The squareness of the curve is also determined and given as the fill factor (FF) that shows the maximum power that our devices could generate.

Incident-to-Photon conversion efficiency commonly referred to as IPCE is a related but different technique to characterize solar cells. To evaluate the photocurrent density generated and collected on an external circuit, a monochromatic light is illuminated on the solar cell and divided by the irradiated photon flux on the solar cell. This work was carried out in Pr. Juan Anta's research lab in Seville, Spain. IPCE is given by:

$$IPCE = \frac{\text{number of electrons collected}}{\text{number of incident photons}}$$

The intensity of incoming irradiation usually calibrated to 1 sun gives the P_{in} and is split into two. One beam goes through a standard silicon detector while the other goes to the sample cell. Masking of the fabricated device is crucial for this method. The current measured in IPCE is a product of the electron injection, charge collection, and light harvesting efficiencies.

1.8.4.2 Optical properties characterization

1.8.4.2.1 UV-Vis absorption spectroscopy

This technique is used to determine the state of the dye (open coloured isomer or closed uncoloured form), molar extinction coefficients (ε), dye loading, and light harvesting

efficiency. The sample's absorbance (A) is defined by a logarithmic relation of the incident light intensity and the transmitted light through a sample using the following equation.

$$A = log_{10}\left(\frac{I_O}{I_t}\right) = -log_{10}T$$

where T is the sample's transmittance. The absorption spectra are achieved by recording the light passing through a sample and that in a non-absorbing species within the same experimental set-up. From this, it is possible to find the molar extinction coefficients (ε) of the dye molecules through the Beer-Lambert's law given as:

$$A = \varepsilon C l$$

where *C* is the concentration of the species and *l* is the optical length of cuvette used, usually 1.0 cm. In order to accurately determine the epsilon values correctly, *C* should be rather low (around 10^{-5}mol.L^{-1}) to prevent aggregation and light scattering that could result in measurement errors especially when high absorbance values are recorded.

Dye loading is an important parameter when analysing the performances of DSSCs. This technique involves either dye's desorption on already sensitized electrodes using basic media [87] and measuring the absorbance of the resulting solution or measuring the dyeing bath's concentration before and after sensitization [88]. Due to higher precision, the first approach has been followed in this study. This allows the determination of the number of molecules grafted, important in understanding the photocurrent generated. Since the area of the electrode surface is known, the area occupied by a single dye molecule on the TiO_2 surface can be calculated [89] as well as the electrode's effective surface area [87].

1.8.4.2.2 Average visible transmittance (AVT)

For solar cells evaluation for BIPV application, average visible transmittance (AVT) is a valuable aspect to assess the aesthetic property. AVT is obtained by integrating the transmission spectra of the devices over the photopic response of our human eyes. It is given by the equation below :

$$AVT = \frac{\int T(\lambda)V(\lambda)S(\lambda)d(\lambda)}{\int V(\lambda)S(\lambda)d(\lambda)}$$

Where λ is the wavelength, T is transmission, V the photopic response and S the sunlight photon flux (AM 1.5G) [78].

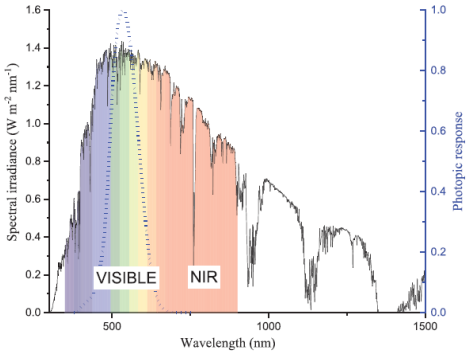

Figure 1.21: Sun's spectrum (AM 1.5G) on a clear day and the corresponding photopic response of human eye (dotted). (Image obtained from [78])

Therefore, the AVT measurements in this work shall involve finding an average transmittance between 380 nm and 740 nm. Beyond 740 nm, our eyes show no response and we perceive as completely transparent.

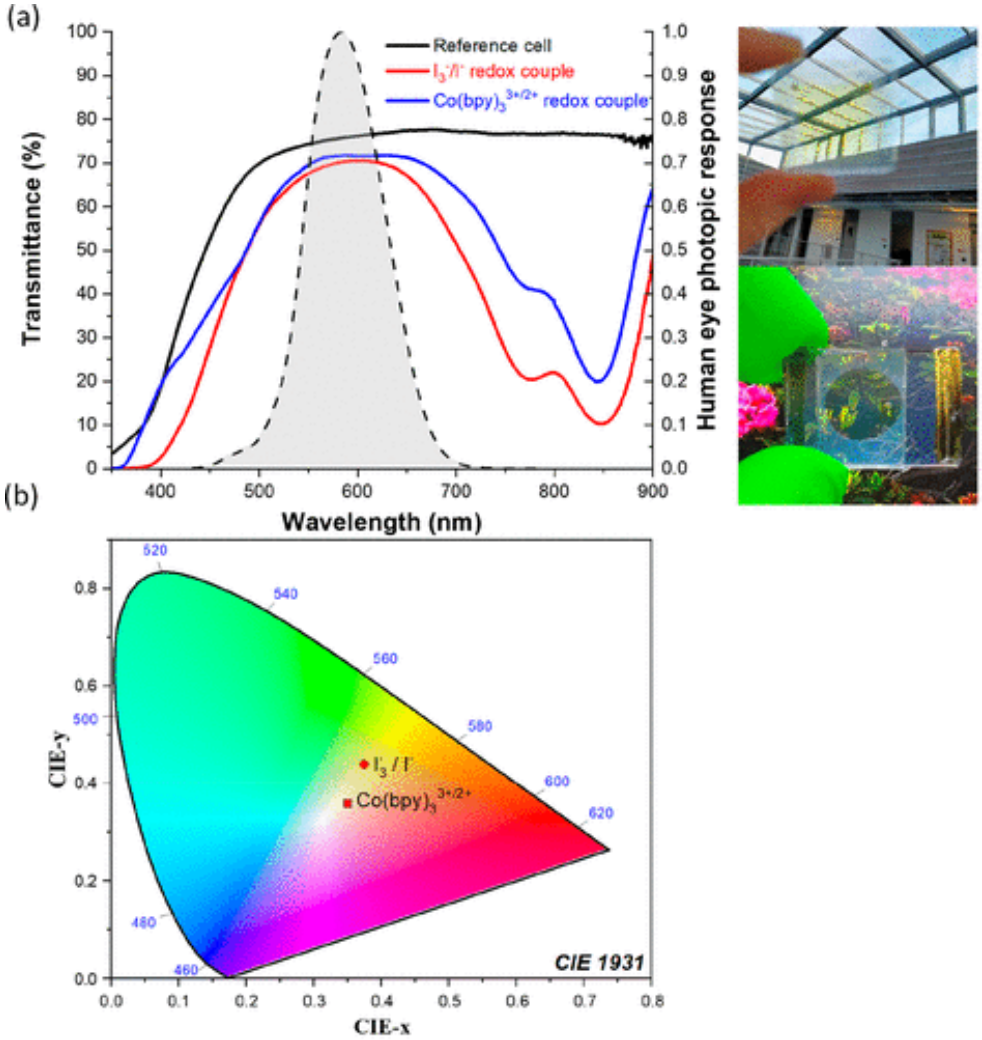

*Figure 1.22 : a) The total cell transmittance of a reference cell without dye and with an optimized electrolyte based on redox couple (black curve), with **VG20-C$_{16}$** –based device and an optimized I_3^-/I^- electrolyte (red curve) and with dye plus $Co(bpy)_3^{3+/2+}$. b) CIE 1931 colour space diagram for devices based on iodine and cobalt electrolytes. On the right-side, pictures of the semi-transparent NIR-DSSCs with iodine electrolyte (top) and with cobalt-based electrolyte (bottom).(with permission [79]).*

The AVTs of their devices are >65% and is improved further when a Cobalt-based electrolyte is applied to 76%. The other optical parameter reported in this work is the colour rendering index (CRI). The visual perception of colour varies depending on illumination source. The Commission Internationale de l'Eclairage (CIE) has set a convention to quantify how the colour of an item is rendered from the light source or via a transparent media such as transparent photovoltaics (TPV).

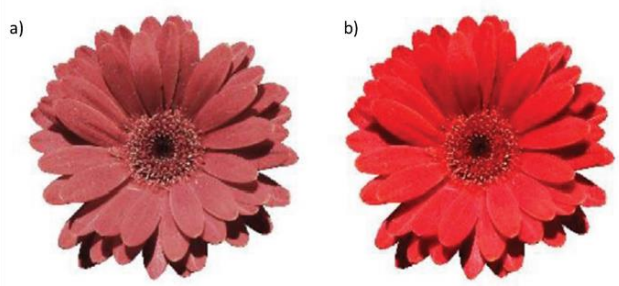

Figure 1.23 : An example showing the impact of CRI value on perception of colour. a) low CRI and b) high CRI, Image obtained from [78].

Based on this, Naim W. et al attained a high CRI value of 92.1% from their VG20-C16-based DSSCs that is greater than the required value (>85%) for integration in building façades.

1.8.4.2.3 Light Utilization Efficiency (LUE)

Very often, as explained above, the power conversion efficiency is inversely proportional to the average visible transparency. For the transparent photovoltaics (TPV), Traverse *et. al* proposed a new figure of merit known as light utilization efficiency (LUE) [90].

$$LUE = PCE \times AVT$$

A high LUE (%) value would reflect the potential of the TPV technology for application as windows without impeding natural light in the building.

1.8.4.2.4 External Quantum Efficiency

The external quantum efficiency, EQE(λ) also referred to as the incident photon-to-current efficiency (IPCE), is defined as the ratio of the incident photons at each wavelength versus the photogenerated electrons that reach the back contact in the device and is given by :

$$EQE(\lambda)[\%] = \frac{hc}{\lambda e}[eV] \times \frac{J_{ph}[mAcm^{-2}]}{\varphi[mWcm^{-2}]} \times 100$$

Where *h* is the Planck's constant, *c* the speed of light in vacuum, λ the wavelength, *e* is the elementary charge, J_{ph} is the short-circuit photocurrent density for monochromatic irradiation and φ is the intensity of the incoming monochromatic light.

The expected current density for a device configuration can be obtained by integrating the incident photon-to-current efficiency (IPCE) with the AM 1.5 terrestial solar spectrum. The IPCE can also be demonstrated as :

$$IPCE(\lambda) = LHE(\lambda) \times \phi_{inj} \times \eta_c = LHE(\lambda) \times APCE$$

Where LHE is the light harvesting efficiency at a given wavelength, ϕ_{inj} is the electron injection efficiency, η_c is the absorbed photon-to-current efficiency, APCE. In well optimized DSSCs, both ϕ_{inj} and η_c are approximately unity thus APCE~1. The LHE is, therefore, a small fraction of photons absorbed at a given wavelength which can be elaborated using Beer's law with the form,

$$LHE = 1 - 10^{-\varepsilon(\lambda)L_n C}$$

Where ε(λ) is the extinction coefficient, *C* is the concentration (determined by effective electrode roughness) and L_n is the diffusion length or electrode thickness. In most cases, the measured IPCE is limited at *ca.* 80% due to losses linked to light reflection and light absorption by the electrolyte [32]. An example of such is that reported by Graetzel with optimized **N-719** devices with an IPCE of ~80% below 650nm and decreases to <20% at longer wavelengths (>750nm) due to minimal LHE [25].

1.8.4.3 Cyclic Voltammetry

Cyclic voltammetry (CV) is a famous electrochemical technique to determine the reduction-oxidation (redox) potentials of the dyes, thus the LUMO and the HOMO energy levels of the dyes can be estimated. Using a three-electrode system, it is possible to determine the redox values of the dye in solution (our focus) or on electrode surface. The measurements are carried out in anhydrous dichloromethane (DCM) with 0.1 $mol.L^{-1}$ of $TBAPF_6$ (tetrabutylammonium hexafluorophosphate) as supporting electrolyte, $Ag/AgNO_3$ 0.01 M as the reference and Fc/Fc^+ as the internal reference. The photochromic dyes were examined in

their closed, in the dark, and the opened forms, under irradiation, in the ice for the latter to lower the discolouration kinetics and probe the opened form. The spectra are analysed with respect to ferrocene as shown in the equation below.

$$E_{(vs.\mathrm{Fc/\,Fc^{+}})} = E - E_{\mathrm{Fc/\,Fc^{+}}}$$

For consistency, our group reports frontier orbital values in eV. The following equation is applied.

$$E_{vs.vacuum} = -(E_{\mathrm{vs.Fc/Fc^{+}}} + 5.1)$$

This helps to determine if the driving force for the injection and regeneration process are sufficient to give rise to electron transfer in devices.

1.8.4.4 Small-signal Pertubation Techniques

In this section, I will highlight the techniques I applied during my PhD to understand the working of this new class of solar cells given that we understand the operation with classical photosensitizers. Thanks to our collaboration with the Nanostructured Solar Cells Group in the University of Olavide, Seville, and the help of Pr. Juan Antonio Anta and his PhD student Antonio Riquelme. During the 2-3 weeks visit in November, 2020, I was able to learn new electrochemical techniques to apply in my systems given that they have an expertise in electrochemical impedance spectroscopy (EIS) and intensity-modulated photocurrent spectroscopy (IMPS). In March 2021, Antonio Riquelme came to our lab for a 3-month exchange program until June, 2021.

Small-signal pertubation optoelectronic techniques have been applied to investigate the processes happening at different time scales in solar cells. The processes in the DSSC can be categorized into two i.e. transport resulting in electricity generation and recombination that leads to electricity loss. The main technique to extract information on transport and recombination processes is the electrochemical impedance spectroscopy [91–93] where a small voltage pertubation is superimposed on steady-state open-circuit voltage, and the resulting modulated current is registered. EIS combined with IMPS, where the modulated small light intensity is superimposed with the constant illumination, can separate transport and recombination processes. Before detailing the application of these techniques on photochromic devices, I will explain briefly what these techniques entail.

1.8.4.4.1 Electrochemical Impedance Spectroscopy (EIS)

Impedance is a measure of the ability of an electric circuit to resist the flow of current under an applied voltage. Electrochemical Impedance Spectroscopy (EIS) provides the information to distinguish two or more electrochemical reactions taking place [91]. EIS allows the identification of diffusion limited reactions, capacitive behaviour of a system, mass transport [94] and electron transfer reaction rates (kinetics) [95]. This makes it possible to differentiate between capacitive and resistive processes. The applied potential to a device is varied slightly and the resulting current response is recorded at the different frequencies. Since the objective is to understand factors impeding flow of electric current generated by the solar cells, it is important to know types of electric current. We have current flowing in only one direction known as direct current (DC) and that which flows in both directions, alternating current (AC). In DC, the ratio of voltage flowing in a circuit to the current is known as the resistance (R) given by Ohm's law.

$$R = \frac{V}{I}$$

However, in AC the same ratio is referred to as impedance, Z instead of R. The current response to the AC potential applied to a system can be understood by a small description as follows. The applied sinusoidal potential is given by:

$$V(\omega) = V_0 \sin(\omega t),$$

where V_0 is the amplitude signal, ω is the angular frequency, a function of frequency given by $\omega = 2\pi f$. The resulting current response from the perturbed sinusoidal voltage over selected DC voltage (also called applied bias) in the frequency domain is given by:

$$I(\omega) = I_0 \sin(\omega t + \varphi),$$

where φ is the phase shift representing the time delay of current with respect to voltage. The IS response comes from the AC circuit while controlling the frequency over its perturbation. Using Ohm's law equation, it is possible to find impedance as:

$$Z(\omega) = \frac{V(\omega)}{I(\omega)} = \frac{V_0 \sin(\omega t)}{I_0 \sin(\omega t + \varphi)}$$

Nevertheless, it is difficult to solve the above equation without introducing complex numbers from the Euler's relation given as:

$$e^{i\theta} = cos\theta + i\, sin\theta,$$

that results in

$$V(\omega) = V_0.e^{i\omega t} \; and \; I(\omega) = I_0.e^{(i\omega t+\varphi)}$$

That makes our work easier to solve for impedance, Z. Thus,

$$Z = \frac{V_0}{I_0}\, e^{-i\phi} = Z_0 e^{-i\phi}$$

which shows that impedance measurements are dependent of the phase shift, φ, that also depends on the specific circuit's element. The size of the shift determines the phase angle, ϕ. Therefore,

$$Z_0\, e^{-i\varphi} = Z_0 \cos(\varphi) - Z_0\, isin(\varphi),$$

having the real part in the equation termed Z' and the other imaginary as Z" or –Z''. This gives us the equation:

$$Z(\omega) = Z'(\omega) + iZ''(\omega),$$

that will be useful in explaining and interpreting the impedance response of the solar cell once an external potential is applied. For reliable interpretation, the frequency applied should cover a wide range such as 1/0.1 MHz to 1 mHz in our case.

Impedance measurements can be performed under different illumination conditions as shown in the figure below. This data can be presented in two different forms, Bode and Nyquist plots.

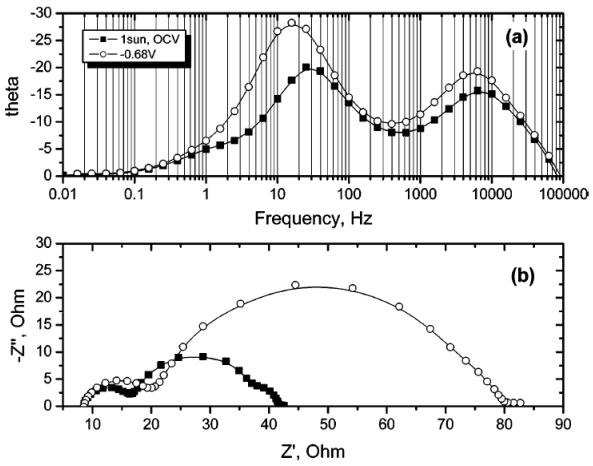

*Figure 1.24 : Impedance spectra of a **Ru**-based dye (**Z907**) solar cell performed at the open-circuit (-0.68V) in the dark and under light (1 Sun). (a) Bode and Nyquists plots (with permission from [92]).*

The differences between them are how they are presented and the information we can extract. For example, Nyquist plots are made up of imaginary (Z'') against real (Z') axes whereas Bode plots comprise of phase (φ) or magnitude (|Z|) versus frequency. Therefore, information obtained is different. For instance, capacitance can be calculated from the Bode plots simply because they give information about cut-off frequencies (f^0) making it possible to use the relation:

$$RC\omega = RC2\pi f^0 = 1$$

All these terms, resistance and capacitance, are used in electrical appliances and typical AC circuit elements. Consequently, the photoelectrochemical process in solar cells can be represented with an equivalent electrical circuit known as Randles circuit (that will be expounded in the results section). The existence, evolution and magnitude of these circuit elements give specific information on the photoelectrochemical cells. In a complete solar cell, the resistances could be electronic (R_{elec}), ionic (R_{ion}), bulk (R_s), and the charge transfer or recombination resistance (R_{ct}) [96]. R_{elec} and R_{ion} take into account the electronic and ionic motions within the electrode structure. R_s accounts for resistance between the WE and the CE and lastly the R_{ct} is the electron transfer resistance between the electrode-electrolyte interface. On the other hand, the capacitance or double layer capacitance (C_{dl}) or sometimes substituted with a constant-phase element (CPE) at the electrolyte-electrode interface is faradaic meaning the process involves charge transfer at the interface because of redox reactions i.e. electrons can either be taken away or injected into the electrode. Otherwise an ideal circuit with no faradaic process. Below is an example of a circuit to fit the EIS spectra.

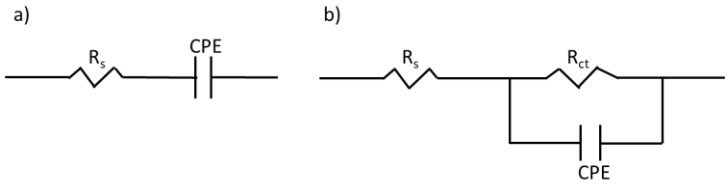

Figure 1.25 : An equivalent circuit a) without faradaic processes and b) with faradaic processes.

The EIS spectra give information on both the resistive and capacitive nature of an electric circuit. The resistance unveils the electron transfer or transport events whereas the capacitance tell us about the electronic carrier accumulation and distribution in the solar cell.

Electrochemical impedance spectroscopy can be performed in the dark or under irradiation at a voltage corresponding to the open circuit voltage conditions. To model the spectrum, the user has to fit an equivalent circuit model, such as in (Fig. 1.25 b) in a dedicated software (ZView or NOVA), to attain the best correlation possible from the instrument's data points and the fitted curve from the software by evaluating the accuracy through the error distribution and chi-squares against the frequency [97]. The equivalent circuit elements combination has to be in accordance with the Kirchoff circuit laws for correct interpretation and quantification of circuit elements.

In the dark, the quasi-Fermi level of electrons in TiO_2 is in equilibrium with the redox potential of the couple (dark current). Under irradiation, the impedance is performed under a voltage equal to the open-circuit condition. The voltage is usually varied by simply varying the light intensity. Upon illumination, an electron is promoted into the excited state of the dye followed by injection into the TiO_2 conduction band (CB). Upon injection, the electron is transported via the mesoporous framework either by hopping or by multiple-trapping until its collection in the FTO. There are two types of capacitances that can be observed in solar cells : the geometrical capacitance and the chemical capacitance. The difference between the two is that the former is independent of voltage and the later increases with voltage. The differential chemical capacitance, C_μ, is often used to describe the density of electron stored in the mesoporous film, which is known to increase exponentially as a function of the open-circuit voltage. This behaviour is as a result of an exponential distribution of the traps below the CB edge, *g(E)*, as shown below.

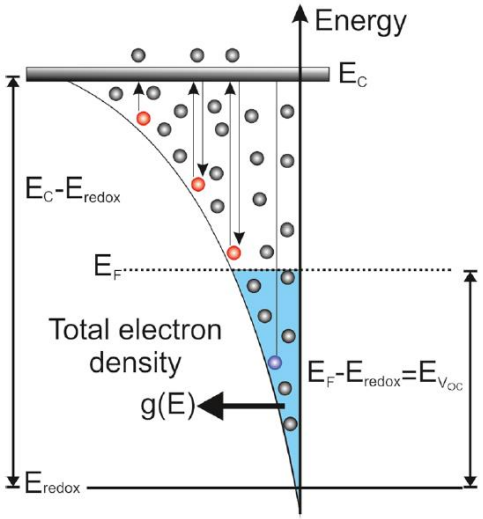

Figure 1.26 : A diagram showing distribution of traps obtained with Permission from ACS [98].

$$g(E) = \frac{\alpha NT}{k_B T} \exp[-\frac{\alpha(Ec - E)}{k_B T}]$$

The trap-state distribution, *g(E)*, is defined by the total density of trap states, N_T, α explains the trap depth, E_C is the energy of the conduction band, k_B the Boltzmann constant and *T* the absolute temperature. The total electron density, *n*, in the traps as a function of quasi-Fermi level, E_F, of electrons in the CB can be found by integrating density in the equation above with right boundary conditions i.e.

$$n(E_F) = \int_{-\infty}^{EF} g(E)\ dE = \int_{-\infty}^{E_{redox}} g(E)\ dE + \int_{E_{redox}}^{E_F} g(E)\ dE = N_T exp(-\frac{\alpha(E_C - E_F)}{k_B T})$$

The first part of the integral from minus infinity to E_{redox} describes the charge stored under dark conditions known as the dark current. Upon irradiation of the solar cell, the energetics change and the E_F of the TiO_2 is in equilibrium with the TCO Fermi level. On the other hand, the Fermi of CE balances with the redox potential. The photovoltage generated depends on the CB positioning with respect to the redox i.e. $qV_{oc} = (E_F - E_{redox})$. During impedance measurement, a voltage perturbation is applied corresponding to $qdV_{oc} = d(E_F - E_{redox}) = d\,E_F$.

For photochromic dyes, the dyes undergo change in conformation when applied in TiO_2-based solar cells. Therefore, it will be of essence to understand the chemical capacitance, C_μ, and where it comes from.

$$C_\mu = \frac{qdn}{dV_{oc}} = q^2 \frac{dn}{dE_F} = \frac{q^2 N_T \alpha}{k_B T} \exp\left(-\frac{\alpha(E_C - E_F)}{k_B T}\right)$$
$$= \frac{q^2 N_T \alpha}{k_B T} \exp\left(-\frac{\alpha(E_C - E_{redox})}{k_B T}\right) \exp\left(\frac{\alpha q V_{oc}}{k_B T}\right) = C_0 \exp\left(\frac{\alpha q V_{oc}}{k_B T}\right)$$

Simply,

$$C_\mu = C_0 \exp\left(\frac{\alpha q V_{oc}}{k_B T}\right)$$

Where C_0 is the prefactor, α is the trap distribution parameter that could help us define the depth of trap states and hence CB allignment, k_B is the Boltzmann constant, and *T* the absolute temperature. The equation above demonstrates the exponential dependence of the chemical capacitance with the open-circuit voltage.

EIS separates and differentiates the capacitive from the resistive behaviour of an electrochemical cell. The interpretation of charge transfer resistance from the Nyquists plots is as shown :

$$R_{rec} = \frac{k_B T}{q\beta j_0} \exp -\frac{q\beta V_F}{k_B T} = R_0 \exp\left(-\frac{\beta q V}{k_B T}\right)$$

The charge transfer resistance is also known to vary with the open-circuit voltage and decreases exponentially.

1.9 Molecular Orbital Calculation

Density Functional Theory (DFT) calculations were used to compliment the spectroelectrochemical information mainly by giving orbital energy information and the physical location of the HOMO and LUMO orbitals. Theoretical calculations of the frontier orbitals reported here were carried out using Amsterdam Density Functional (ADF) program [99]. The calculations in this document were carried out using B3LYP functional (a 3-parameter hybrid functional that applies the Hartree-Fock exchange term, Becke 88 exchange functional [100], and the Lee, Yang, and Parr correlation) [101]. Triple-zeta basis sets with polarization functions were used for these calculations. The true minima ground state calculations of several dyes were performed and orbital information extracted. The result was considered at the optimized geometry for the particular dyes (either in their opened or closed forms). For molecules in solution, single point calculations were done using Conductor like Screening Model (COSMO) to take into account of the solvation effects.

1.10 References

1. *Solar energy conversion and storage: photochemical modes*. (CRC Press, Taylor & Francis Group, 2016).
2. Chapin, D. M., Fuller, C. S. & Pearson, G. L. A New Silicon *p-n* Junction Photocell for Converting Solar Radiation into Electrical Power. *Journal of Applied Physics* **25**, 676–677 (1954).
3. Yoshikawa, K. *et al.* Silicon heterojunction solar cell with interdigitated back contacts for a photoconversion efficiency over 26. *Nat Energy* 2, 17032 (2017).
4. Green, M. A. *et al.* Solar cell efficiency tables (version 49). *Prog. Photovolt: Res. Appl.* **25**, 3–13 (2017).
5. Genscher, H. Electrochemical Behavior of Semiconductors under Illumination. *J. Electrochem. Soc.* **113**, 1174 (1966).
6. Tsubomura, H., Matsumura, M., Nomura, Y. & Amamiya, T. Dye sensitised zinc oxide: aqueous electrolyte: platinum photocell. *Nature* **261**, 402–403 (1976).
7. Jeong, J. *et al.* Pseudo-halide anion engineering for α-FAPbI3 perovskite solar cells. *Nature* **592**, 381–385 (2021).
8. O'Regan, B. & Grätzel, M. A low-cost, high-efficiency solar cell based on dye-sensitized colloidal TiO2 films. *Nature* **353**, 737–740 (1991).
9. Wu, J. *et al.* Electrolytes in Dye-Sensitized Solar Cells. *Chem. Rev.* **115**, 2136–2173 (2015).
10. Zhang, D. *et al.* A molecular photosensitizer achieves a Voc of 1.24 V enabling highly efficient and stable dye-sensitized solar cells with copper(II/I)-based electrolyte. *Nat Commun* **12**, 1777 (2021).
11. Feldt, S. M. *et al.* Design of Organic Dyes and Cobalt Polypyridine Redox Mediators for High-Efficiency Dye-Sensitized Solar Cells. *J. Am. Chem. Soc.* **132**, 16714–16724 (2010).
12. Tsao, H. N. *et al.* Cyclopentadithiophene Bridged Donor-Acceptor Dyes Achieve High Power Conversion Efficiencies in Dye-Sensitized Solar Cells Based on the tris-Cobalt Bipyridine Redox Couple. *ChemSusChem* **4**, 591–594 (2011).
13. Yum, J.-H. *et al.* A cobalt complex redox shuttle for dye-sensitized solar cells with high open-circuit potentials. *Nat Commun* **3**, 631 (2012).
14. Zhang, W. *et al.* Comprehensive control of voltage loss enables 11.7% efficient solid-state dye-sensitized solar cells. *Energy Environ. Sci.* **11**, 1779–1787 (2018).

15. Han, M.-L. *et al.* The improved photovoltaic performance of phenothiazine-dithienopyrrole based dyes with auxiliary acceptors. *Journal of Power Sources* **387**, 117–125 (2018).
16. Yang, J. *et al.* Influence of the Donor Size in D–π–A Organic Dyes for Dye-Sensitized Solar Cells. *J. Am. Chem. Soc.* **136**, 5722–5730 (2014).
17. Ning, Z., Fu, Y. & Tian, H. Improvement of dye-sensitized solar cells: what we know and what we need to know. *Energy Environ. Sci.* **3**, 1170 (2010).
18. Tu-morn, M., Pairoh, N., Sutapun, W. & Trongsatitkul, T. Effects of titanium dioxide nanoparticle on enhancing degradation of polylactic acid/low density polyethylene blend films. *Materials Today: Proceedings* **17**, 2048–2061 (2019).
19. Schoden, F. *et al.* Investigating the Recycling Potential of Glass Based Dye-Sensitized Solar Cells—Melting Experiment. *Materials* **14**, 6622 (2021).
20. Schoden, F., Detzmeier, J., Schnatmann, A. K., Blachowicz, T. & Schwenzfeier-Hellkamp, E. Investigating the Remanufacturing Potential of Dye-Sensitized Solar Cells. *Sustainability* **14**, 5670 (2022).
21. Bandara, T. M. W. J., Hansadi, J. M. C. & Bella, F. A review of textile dye-sensitized solar cells for wearable electronics. *Ionics* **28**, 2563–2583 (2022).
22. Godfroy, M. *et al.* Benzothiadiazole-based photosensitizers for efficient and stable dye-sensitized solar cells and 8.7% efficiency semi-transparent mini-modules. *Sustainable Energy Fuels* **5**, 144–153 (2021).
23. Hinsch, A. *et al.* Worldwide first fully up-scaled fabrication of 60 × 100 cm ^{2} dye solar module prototypes: Worldwide first fully up-scaled fabrication of 60 cm × 100 cm dye solar module prototypes. *Prog. Photovolt: Res. Appl.* **20**, 698–710 (2012).
24. Toyoda, T. *et al.* Outdoor performance of large scale DSC modules. *J. Photochem. Photobiol. A: Chem.* **164**, 203–207 (2004).
25. Grätzel, M. Solar Energy Conversion by Dye-Sensitized Photovoltaic Cells. *Inorg. Chem.* **44**, 6841–6851 (2005).
26. Yella, A. *et al.* Porphyrin-Sensitized Solar Cells with Cobalt (II/III)–Based Redox Electrolyte Exceed 12 Percent Efficiency. *Science*, 629-634 (2011).
27. Aslam, A. *et al.* Dye-sensitized solar cells (DSSCs) as a potential photovoltaic technology for the self-powered internet of things (IoTs) applications. *Solar Energy* **207**, 874–892 (2020).

28. Katoh, R. *et al.* Highly stable sensitizer dyes for dye-sensitized solar cells: role of the oligothiophene moiety. *Energy Environ. Sci.* **2**, 542 (2009).
29. Wang, Z.-S. *et al.* Molecular Design of Coumarin Dyes for Stable and Efficient Organic Dye-Sensitized Solar Cells. *J. Phys. Chem. C* **112**, 17011–17017 (2008).
30. Joly, D. *et al.* A Robust Organic Dye for Dye Sensitized Solar Cells Based on Iodine/Iodide Electrolytes Combining High Efficiency and Outstanding Stability. *Sci Rep* **4**, 4033 (2015).
31. Ji, J., Zhou, H., Eom, Y. K., Kim, C. H. & Kim, H. K. 14.2% Efficiency Dye-Sensitized Solar Cells by Co-sensitizing Novel Thieno[3,2- *b*]indole-Based Organic Dyes with a Promising Porphyrin Sensitizer. *Adv. Energy Mater.* **10**, 2000124 (2020).
32. Hamann, T. W., Jensen, R. A., Martinson, A. B. F., Ryswyk, H. V. & Hupp, J. T. Advancing beyond current generation dye-sensitized solar cells. *Energy Environ. Sci.* **1**, 66-78 (2008).
33. Wu, J. *et al.* Progress on the electrolytes for dye-sensitized solar cells. *Pure and Applied Chemistry* **80**, 2241–2258 (2008).
34. Hagfeldt, A., Boschloo, G., Licheng Sun, Lars Kloo & Henrik Pettersson. Dye-Sensitized Solar Cells. *Chem. Rev.* **110**, 6595–6663 (2010).
35. Cheema, H., Watson, J., Peddapuram, A. & Delcamp, J. H. A 25 mA cm $^{-2}$ dye-sensitized solar cell based on a near-infrared-absorbing organic dye and application of the device in SSM-DSCs. *Chem. Commun.* **56**, 1741–1744 (2020).
36. Kinoshita, T. *et al.* Spectral splitting photovoltaics using perovskite and wideband dye-sensitized solar cells. *Nat Commun* **6**, 8834 (2015).
37. Mann, J. R., Gannon, M. K., Fitzgibbons, T. C., Detty, M. R. & Watson, D. F. Optimizing the Photocurrent Efficiency of Dye-Sensitized Solar Cells through the Controlled Aggregation of Chalcogenoxanthylium Dyes on Nanocrystalline Titania Films. *J. Phys. Chem. C* **112**, 13057–13061 (2008).
38. Pandey, S. S., Morimoto, T., Fujikawa, N. & Hayase, S. Combined theoretical and experimental approaches for development of squaraine dyes with small energy barrier for electron injection. *Solar Energy Materials and Solar Cells* **159**, 625–632 (2017).
39. Zhang, L. & Cole, J. M. Anchoring Groups for Dye-Sensitized Solar Cells. *ACS Appl. Mater. Interfaces* **7**, 3427–3455 (2015).
40. Kuang, D. *et al.* High Molar Extinction Coefficient Heteroleptic Ruthenium Complexes for Thin Film Dye-Sensitized Solar Cells. *J. Am. Chem. Soc.* **128**, 4146–4154 (2006).

41. Wang, P., Zakeeruddin, S. M., Exnar, I. & Grätzel, M. High efficiency dye-sensitized nanocrystalline solar cells based on ionic liquid polymer gel electrolyte. *Chem. Commun.* 2972–2973 (2002).
42. Cherian, S. & Wamser, C. C. Adsorption and Photoactivity of Tetra(4-carboxyphenyl)porphyrin (TCPP) on Nanoparticulate TiO_2. *J. Phys. Chem. B*, **104**, 3624–3629 (2000).
43. Joly, D. *et al.* Metal-free organic sensitizers with narrow absorption in the visible for solar cells exceeding 10% efficiency. *Energy Environ. Sci.* **8**, 2010–2018 (2015).
44. Muñoz-García, A. B. *et al.* Dye-sensitized solar cells strike back. *Chem. Soc. Rev.* **50**, 12450–12550 (2021).
45. Liu, X. *et al.* An Efficient Organic-Dye-Sensitized Solar Cell with in situ Polymerized Poly(3,4-ethylenedioxythiophene) as a Hole-Transporting Material. *Adv. Mater.* **22**, E150–E155 (2010).
46. Agarwala, P. & Kabra, D. A review on triphenylamine (TPA) based organic hole transport materials (HTMs) for dye sensitized solar cells (DSSCs) and perovskite solar cells (PSCs): evolution and molecular engineering. *J. Mater. Chem. A* **5**, 1348–1373 (2017).
47. Liang, M. & Chen, J. Arylamine organic dyes for dye-sensitized solar cells. *Chem. Soc. Rev.* **42**, 3453 (2013).
48. Kitamura, T. *et al.* Phenyl-Conjugated Oligoene Sensitizers for TiO_2 Solar Cells. *Chem. Mater.* **16**, 1806–1812 (2004).
49. Liang, M. Arylamine organic dyes for dye-sensitized solar cells. *Chem Soc Rev* 36 (2013).
50. Kakiage, K. *et al.* Fabrication of a high-performance dye-sensitized solar cell with 12.8% conversion efficiency using organic silyl-anchor dyes. *Chem. Commun.* **51**, 6315–6317 (2015).
51. Kakiage, K. *et al.* Highly-efficient dye-sensitized solar cells with collaborative sensitization by silyl-anchor and carboxy-anchor dyes. *Chem. Commun.* **51**, 15894–15897 (2015).
52. Aumaitre, C. *et al.* Visible and Near-infrared Organic photosensitizers comprising isoindigo derivatives as chromophores: synthesis, optoelectronic properties and factors limiting their efficiency in dye solar cells. *J. Mater. Chem. A,* **6**, 10074-10084 (2018).
53. Ren, Y. *et al.* A Stable Blue Photosensitizer for Color Palette of Dye-Sensitized Solar Cells Reaching 12.6% Efficiency. *J. Am. Chem. Soc.* **140**, 2405–2408 (2018).

54. Bedja, I., Hotchandani, S. & Kamat, P. V. Preparation and Photoelectrochemical Characterization of Thin SnO_2 Nanocrystalline Semiconductor Films and Their Sensitization with Bis(2,2'-bipyridine)(2,2'-bipyridine-4,4'-dicarboxylic acid)ruthenium(II) Complex. *J. Phys. Chem.* **98**, 4133–4140 (1994).
55. Choi, S.-H. *et al.* Solar Cells: Amorphous Zinc Stannate (Zn_2SnO_4) Nanofibers Networks as Photoelectrodes for Organic Dye-Sensitized Solar Cells. *Adv. Funct. Mater.* **23**, 3133–3133 (2013).
56. Sayama, K., Sugihara, H. & Arakawa, H. Photoelectrochemical Properties of a Porous Nb_2O_5 Electrode Sensitized by a Ruthenium Dye. *Chem. Mater.* **10**, 3825–3832 (1998).
57. Elzayat, M. Photoelectrochemical properties of dye sensitized Zr-doped $SrTiO_3$ electrodes. *International Journal of Hydrogen Energy* **23**, 259–266 (1998).
58. Wold, A. Photocatalytic properties of titanium dioxide (TiO_2). *Chem. Mater.* **5**, 280–283 (1993).
59. Hu, Q., Wang, J., Zhao, Y. & Li, D. A light-trapping structure based on Bi_2O_3 nano-islands with highly crystallized sputtered silicon for thin-film solar cells. *Opt. Express* **19**, A20 (2011).
60. Siriroj, S. *et al.* High performance dye-sensitized solar cell based on hydrothermally deposited multiwall carbon nanotube counter electrode. *Appl. Phys. Lett.* **100**, 243303 (2012).
61. Briscoe, J. & Dunn, S. Dye-Sensitized Solar Cells: The Future of Using Earth-Abundant Elements in Counter Electrodes for Dye-Sensitized Solar Cells. *Adv. Mater.* **28**, 3976–3976 (2016).
62. Kim, C. K. *et al.* Comparative study of edge-functionalized graphene nanoplatelets as metal-free counter electrodes for highly efficient dye-sensitized solar cells. *Materials Today Energy* **9**, 67–73 (2018).
63. Saito, Y., Kitamura, T., Wada, Y. & Yanagida, S. Poly(3,4-ethylenedioxythiophene) as a hole conductor in solid state dye sensitized solar cells. *Synthetic Metals* **131**, 185–187 (2002).
64. Boschloo, G. & Hagfeldt, A. Characteristics of the Iodide/Triiodide Redox Mediator in Dye-Sensitized Solar Cells. *Acc. Chem. Res.* **42**, 1819–1826 (2009).
65. EPFL's campus has the world's first solar window. https://actu.epfl.ch/news/epfl-s-campus-has-the-world-s-first-solar-window (2013).

66. *Photochromism: molecules and systems* (eds Durr, H. & Bouas-Laurent, H.) 314-466 (Elsevier, 1990).
67. Tsujioka, T. & Irie, M. Electrical functions of photochromic molecules. *J. Photochem. Photobiol. C: Photochem. Rev.* **11**, 1–14 (2010).
68. Keum, S.-R., Hur, M.-S., Kazmaier, P. M. & Buncel, E. Thermo- and photochromic dyes: indolino-benzospiropyrans. Part 1. UV–VIS spectroscopic studies of 1,3,3-spiro(2 *H* -1-benzopyran-2,2′-indolines) and the open-chain merocyanine forms; solvatochromism and medium effects on spiro ring formation. *Can. J. Chem.* **69**, 1940–1947 (1991).
69. Mengots, A. *et al.* Dihydroazulene-Azobenzene-Dihydroazulene Triad Photoswitches. *Chem. Eur. J.* **27**, 12437–12446 (2021).
70. Irie, M. Photochromism of diarylethene single molecules and single crystals. *Photochem. Photobiol. Sci.* **9**, 1535 (2010).
71. Berkovic, G., Krongauz, V. & Weiss, V. Spiropyrans and Spirooxazines for Memories and Switches. *Chem. Rev.* **100**, 1741–1754 (2000).
72. Irie, M., Fukaminato, T., Matsuda, K. & Kobatake, S. Photochromism of Diarylethene Molecules and Crystals: Memories, Switches, and Actuators. *Chem. Rev.* **114**, 12174–12277 (2014).
73. Evans, R. A. *et al.* The generic enhancement of photochromic dye switching speeds in a rigid polymer matrix. *Nature Mater* **4**, 249–253 (2005).
74. M. Johnson, N. *et al.* Photochromic dye-sensitized solar cells. *AIMS Materials Science* **2**, 503–509 (2015).
75. Wu, W. *et al.* A strategy to design novel structure photochromic sensitizers for dye-sensitized solar cells. *Sci Rep* **5**, 8592 (2015).
76. Ru, T., de Kort, Y. A. W., Smolders, K. C. H. J., Chen, Q. & Zhou, G. Non-image forming effects of illuminance and correlated color temperature of office light on alertness, mood, and performance across cognitive domains. *Building and Environment* **149**, 253–263 (2019).
77. Baron, T. *et al.* Zinc phthalocyanine absorbance in the near-infrared with application for transparent and colorless dye-sensitized solar cells. *Comptes Rendus. Chimie* **24**, 157–170 (2021).

78. Grifoni, F. *et al.* Toward Sustainable, Colorless, and Transparent Photovoltaics: State of the Art and Perspectives for the Development of Selective Near-Infrared Dye-Sensitized Solar Cells. *Adv. Energy Mater.* **11**, 2101598 (2021).
79. Naim, W. *et al.* Transparent and Colorless Dye-Sensitized Solar Cells Exceeding 75% Average Visible Transmittance. *JACS Au* **1**, 409–426 (2021).
80. Baron, T. *et al.* Transparent and Colorless Dye-Sensitized Solar Cells Based on Pyrrolopyrrole Cyanine Sensitizers. *Angew Chem Int Ed* **61**, (2022).
81. Hara, K. *et al.* Effect of Additives on the Photovoltaic Performance of Coumarin-Dye-Sensitized Nanocrystalline TiO $_2$ Solar Cells. *Langmuir* **20**, 4205–4210 (2004).
82. Sedghi, A. & Miankushki, H. N. Influence of $TiCl_4$ Treatment on Structure and Performance of Dye-Sensitized Solar Cells. *Jpn. J. Appl. Phys.* **52**, 075002 (2013).
83. Xu, Y. *et al.* Comprehensive understanding of $TiCl_4$ treatment on the compact TiO_2 layer in planar perovskite solar cells with efficiencies over 20%. *Journal of Alloys and Compounds* **787**, 1082–1088 (2019).
84. Ito, S. *et al.* Control of dark current in photoelectrochemical (TiO_2/I^-–I_3^-) and dye-sensitized solar cells. *Chem. Commun.* 4351 (2005) doi:10.1039/b505718c.
85. Nazeeruddin, M. K. *et al.* Engineering of Efficient Panchromatic Sensitizers for Nanocrystalline TiO_2 -Based Solar Cells. *J. Am. Chem. Soc.* **123**, 1613–1624 (2001).
86. Snaith, H. J. The perils of solar cell efficiency measurements. *nature photonics* **6**, 4 (2012).
87. Pazoki, M. *et al.* CVD-grown TiO_2 particles as light scattering structures in dye-sensitized solar cells{. 8 (2012).
88. Edvinsson, T. *et al.* Intramolecular Charge-Transfer Tuning of Perylenes: Spectroscopic Features and Performance in Dye-Sensitized Solar Cells. *J. Phys. Chem. C* **111**, 15137–15140 (2007).
89. Pazoki, M., Lohse, P. W., Taghavinia, N., Hagfeldt, A. & Boschloo, G. The effect of dye coverage on the performance of dye-sensitized solar cells with a cobalt-based electrolyte. *Phys. Chem. Chem. Phys.*, **16**, 8503-8508 (2014).
90. Traverse, C. J., Pandey, R., Barr, M. C. & Lunt, R. R. Emergence of highly transparent photovoltaics for distributed applications. *Nat Energy* **2**, 849–860 (2017).
91. Kern, R., Sastrawan, R., Ferber, J., Stangl, R. & Luther, J. Modeling and interpretation of electrical impedance spectra of dye solar cells operated under open-circuit conditions. *Electrochimica Acta* **47**, 4213–4225 (2002).

92. Wang, Q., Moser, J.-E. & Grätzel, M. Electrochemical Impedance Spectroscopic Analysis of Dye-Sensitized Solar Cells. *J. Phys. Chem. B* **109**, 14945–14953 (2005).
93. Bisquert, J. & Garcia-Belmonte, G. Interpretation of AC Conductivity of Lightly Doped Conducting Polymers in Terms of Hopping Conduction. *Russian J. Electrochem.* **40**, 352-358 (2004).
94. Wang, J. *et al.* Systematic investigation on determining chemical diffusion coefficients of lithium ion in Li1 + xVPO4F (0 ≤ x ≤ 2). *J Solid State Electrochem* **19**, 153–160 (2015).
95. Giannuzzi, R. *et al.* Ultrathin TiO_2(B) Nanorods with Superior Lithium-Ion Storage Performance. *ACS Appl. Mater. Interfaces* **6**, 1933–1943 (2014).
96. Laschuk, N. O., Easton, E. B. & Zenkina, O. V. Reducing the resistance for the use of electrochemical impedance spectroscopy analysis in materials chemistry. *RSC Adv.* **11**, 27925–27936 (2021).
97. Simi, V. S. & Rajendran, N. Influence of tunable diameter on the electrochemical behavior and antibacterial activity of titania nanotube arrays for biomedical applications. *Materials Characterization* **129**, 67–79 (2017).
98. Pourjafari, D. *et al.* Brookite-Based Dye-Sensitized Solar Cells: Influence of Morphology and Surface Chemistry on Cell Performance. *J. Phys. Chem. C* **122**, 14277–14288 (2018).
99. te Velde, G. *et al.* Chemistry with ADF. *J. Comput. Chem.* **22**, 931–967 (2001).
100. Becke, A. D. Density-functional exchange-energy approximation with correct asymptotic behavior. *Phys. Rev. A* **38**, 3098–3100 (1988).
101. Lee, C., Yang, W. & Parr, R. G. Development of the Colle-Salvetti correlation-energy formula into a functional of the electron density. *Phys. Rev. B* **37**, 785–789 (1988).

CHAPTER 2 : First Generation Photochromic Solar Cells

Abstract

In Chapter 1, we have seen how dye-sensitized solar cells (DSSCs) among other thin film technologies has made progress owing to its affordability, environmentally benign and optically tunable properties. The latter opens the possibility of integration in buildings and cars as windows. For such integrations, fixed optical properties established during manufacturing is a challenge. Our group has proposed solutions to this via multifunctional solar cells capable of generating electricity and adapting their colour in sync termed photochromic solar cells surmounting 4% in efficiency. These solar cells with variable optical transmission and colours are based on photochromic dyes as sensitizers instead of the classical organic dyes. In this chapter, I will focus on the impact of chemistry, the optimization of the fabrication parameters, and the effect of the photochromic behaviour on photovoltaic (PV) properties given that we understand the working with classical dyes.

2.1 Introduction

As previously highlighted in Chapter 1, photochromism has been defined as a reversible colour change with response to light illumination. Besides colour change, other properties could change such as the magnetic property[1], refractive index[2], hydrophobicity[3], surface morphology[4] and fluorescence[5] as a result of photoisomerization. These additional properties have opened the window for application of photochromic molecules in areas such as information storage, opto-controlled optical switches, photoinduced reversible surface water repellency, photodriven nanometric-scale actuators and imaging, respectively.

However, these molecules have found little application in the photovoltaic (PV) industry. In principle, application of photochromes in solar cells should display the two different forms thus smart PVs. However, the few examples applied so far, for instance with bis-thienylethene, also highlighted in Chapter 1, the interconversion between its photo-isomers was achieved via light manipulation of ultraviolet (UV) and visible wavelenths [6]. Another example employing photochromic spiropyran and spirooxazine dyes in DSSCs, also highlighted in Chapter 1, shows photochemically and thermally activated bleaching process resulted in a power conversion efficiency (PCE) around 0.2% after 30 minutes under UV irradiation. In this latter example, the

dyes were poorly colourable and their anchoring function was not conjugated with the photochromic core hence bad sensitization of their photoanodes and lacked reversibility.

To tackle these challenges, our group has proposed new photochromic sensitizers based on the integration of diphenyl-naphthopyran core into push-pull architectures. While following the classic donor-π-conjugated bridge-acceptor –type architecture with the acceptor part acting as the anchoring fuction, we have replaced the π-conjugated bridge with a photochromic unit.

2.2 First generation photochromic solar cells

Current state-of-the art of semi-transparent solar cells only allow for the fabrication of solar devices showing an optical transmission that is fixed during the manufacturing process [7–10]. For the development of smart photovoltaics as windows and their massive integration in buildings, variable and self-adapatable optical properties are desirable. The ultimate goal would be that the solar cells, transparent under low light conditions, could tune their absorption under more intense illumination to generate energy without any external manipulation. To address this challenge, a strategy based on photochromic dyes emerged where upon irradiation, they can undergo a reversible chemical change between two forms exhibiting different absorption spectra [11]. Normally, the uncoloured isomer is observed in the dark and the coloured one is generated under irradiation.

2.2.1 Presentation of NPL, NPB and NPI

This generation is composed of 3 photochromic dyes based on naphthopyran (NP) that differ in the photochromic moiety. The diphenyl-naphthopyran moiety was chosen due to its desirable characteristics for photovoltaic (PV) applications. For such application, the photochromic unit needs to show good stability, high turn over frequency (good photoswitchability), high turn over number to have good colourability, fatigue resistance and quick decolouration. All these are essential for application in solar cells that were found in a naphthopyran unit.

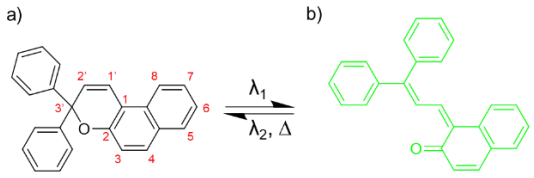

Figure 2.1: An example of the photoisomerization process based on a 3,3-diphenyl-3H-naphtho[2,1-b]pyran core and an equilibrium reaction between the closed form (a) with one of its opened coloured form isomer (b).

The closed colourless form (a), absorbs light in the UV and undergoes a ring opening reaction to generate the opened coloured form (b) with different absorption spectra [11,12]. The photoisomerization reaction that generates the coloured isomer(s) is as a result of photoinduced $C_{3'}$ - O bond cleavage. The naphthalenone and butadiene motifs (b) can reversibly transform to the initial closed form through a back-reaction (ring closure) thermally (Δ) or photochemically (λ_2) [13]. A state of equilibrium between the closed form (CF) (a) and the opened form (OF) (b) is known as the photostationary state (PSS). The ring-opening reaction gives rise to various photoisomeric products depending on the position of the phenyl rings with respect to this ketone group.

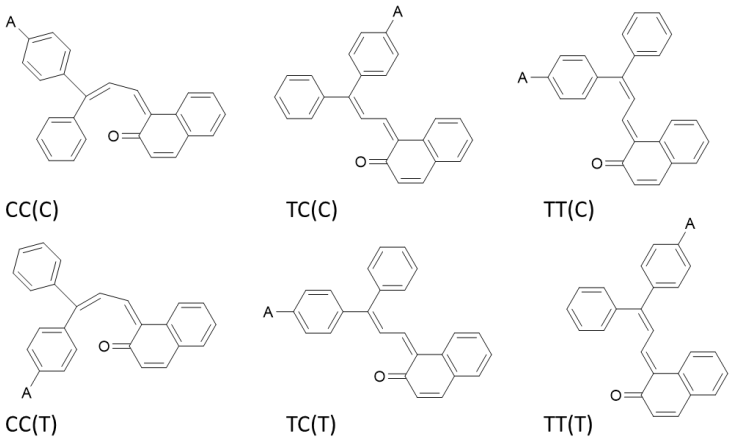

Figure 2.2 : Showing the different possible photoisomers that can be generated by the photoisomerization process of the diphenyl-naphthopyran. The (T) and (C) notations are referred to with reference to A, an acceptor group for trans and cis configurations, respectively.

This class of photochromes is known for its high fatigue resistance that allows for numerous switchability between the opened coloured forms and the closed colourless ones. They possess good photocolourability [14] and relatively good colouration quantum yield (ϕ_r = 0.8) of the [15], a good trait for our target application. The photochromic naphthalene unit above is non-symmetrical.

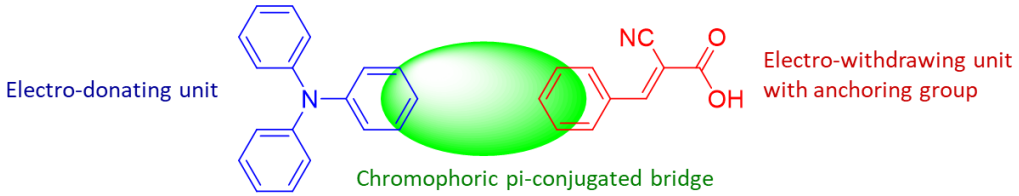

Figure 2.3 : The general donor-photochrome-acceptor architecture.

Due to the non-symmetrical nature of the photochromic unit, it is critical to choose the donor (D) and acceptor (A) functional groups positions to control the spatial localisation of the frontier orbitals as well as their energy level positions. For application of this photochromic unit in a DSSC configuration, controlled spatial localization of the HOMO and LUMO levels helps to facilitate a good TiO_2 sensitization and regeneration by the redox couple. Thanks to DFT calculations and modelling that were performed to identify the favourable orientation of this unit in a donor-pi-conjugated-acceptor structure.

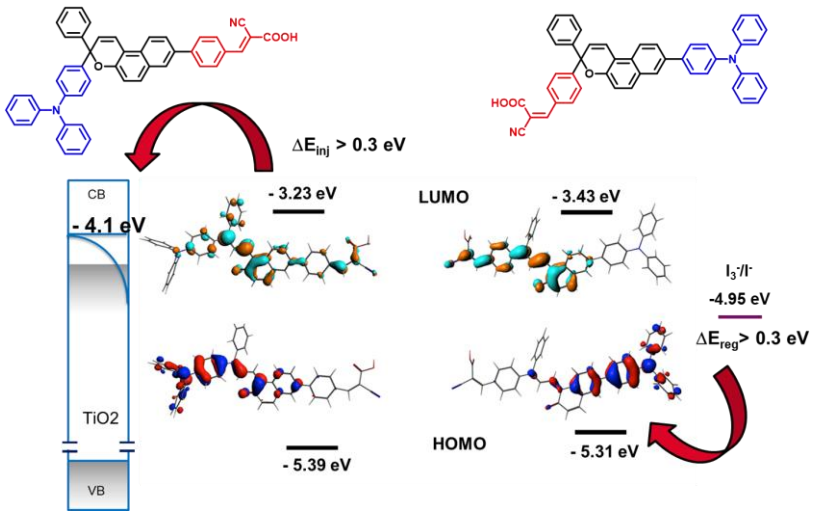

*Figure 2.4 : HOMO-LUMO energy levels and orbital distributionaccording to the direction of functionalization of **NPL** photochromic molecule. Calculation : optimization (PBE/TZ2P) followed by single point B3LYP/TZ2P. Closed forms structural representation are included at the top for clarity.*

Both the closed and opened forms could work as photosensitizers in a DSSC configuration. The substitution direction has a small impact on the HOMO energy level with a difference of less than 0.1 eV but a significant impact on the positioning of the LUMO level (0.2 eV) but remains compatible with our solar cells. However, considerable differences are observed on the orbital spatial distribution where functionalization of the electron-withdrawing part on the naphthalene part (on the left side of Fig. 2.4), results in delocalization of the LUMO on nearly the entire molecule. This is unfavourable for effective electronic injection into the metal oxide thus the other (on the right side of Fig. 2.4) was preferred.

The acceptor part (A) was functionalized with a phenyl-cyanoacrylic acid and the opposite part was attached to a donor moiety based on a triphenylamine (TPA) discussed in Chapter 1. We synthesized a new series of molecules based on a 3,3-diphenyl-3*H*-naphtho[2,1-b]pyran core, coded **NPL** (L for Linear), the second on a 2,2-diphenyl-2*H*-naphtho[1,2-b]pyran core, coded **NPB** (B for Bend) and the third on a 2,2-diphenyl-2*H*-indeno[2,1-*f*]naphtho[1,2-*b*]pyran core coded **NPI** (Indeno-fused). The first two i.e. **NPL** and **NPB** are quite easy to synthesize involving 5 steps whereas NPI is a little longer due to fusion of an indene group at the bridge terminal (between photochromic core and TPA donor unit) to the (*f*-face) whose impact we shall investigate. The dyes that make-up the first generation are as listed below :

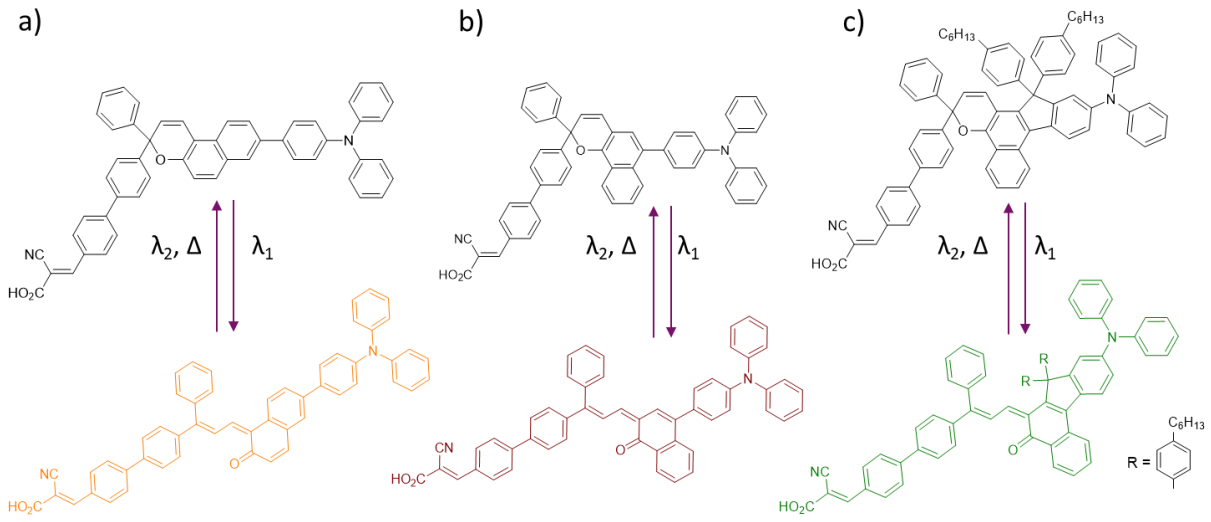

*Figure 2.5 : First generation photochromic dyes based on a diphenyl-naphthopyran pi-system showing the reversible photochemical transformation between the closed forms (top) and the opened coloured forms (bottom) of a) **NPL**, b) **NPB** and c) **NPI**.*

2.2.2 Synthesis of NPI

As demonstrated in Chapter 1, among the best performing photosensitizers in DSSC technology embed the donor- π spacer – acceptor architecture. In our case the π-bridge is replaced by a photochromic unit. I also had an opportunity to carry out some synthetic chemistry for preparing the dyes thanks to Samuel Fauvel, a 2nd year PhD student, by replacing the π-spacer with a photochromic naphthopyran core. The synthetic route followed to obtain **NPI** is as shown below.

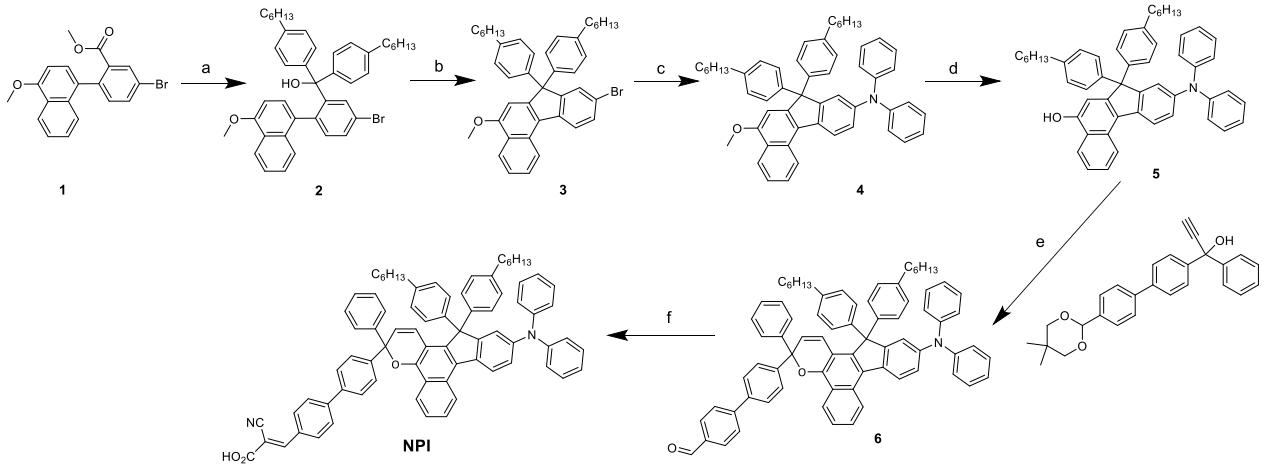

*Figure 2.6 : Synthetic route to access **NPI** dye. The experimental conditions for steps : a) bromo-hexylphenyl, n-BuLi, THF, -95°C b) $BF_3.OEt_2$, DCM, 0°C-RT c) diphenylamine, $Pd_2(dba)_3$, HP^tBuBF_4 (phosphine), tBuOK, toluene, 110°C d) BBr_3, DCM, 0°C-RT e) PPTS, trimethylorthoformate, DCE, 70°C, $TBAPF_6$ f) cyanoacetic acid, NH_4OAc, Toluene, 90°C.*

The starting material, brominated naphth-2-ol ester derivative (**1**), has a methoxy group protection to prevent the formation of a naphthoquinone and allow use of *n*-BuLi. Step(a) involves a double nucleophilic attack of the lithiated phenyl-hexyl groups on the ester derivative to give a tertiary alcohol (**2**) (yield=85%). Step (b) is an intramolecular Friedel Craft reaction (yield=81%). Step (c) involves the insertion of the electron-donating diphenylamine (DPA) unit via a Buchwald cross-coupling reaction (yield=93%). Step (d) is a demethylation reaction to obtain the alcohol through deprotection reaction (yield=100%). Step (*e*) is the most critical step is one that involves the formation of the photochromic naphthopyran ring through chromenisation reaction (yield=56%). This is achieved via a coupling between the 2-naphthol derivative and a propargylic acid catalyzed by pyridinium para-toluene sulfonate (PPTS) [16,17] in slightly acidic conditions to decrease the degradation of propargylic alcohol. It is a 3-step reaction that involves dehydration, addition and finally C-C coupling via a Claisen condensation reaction then a proton shift leading to the formation of the photochromic unit. Lastly, step (f) involves a Knoevenagel reaction that attaches the anchoring group to give **NPI** (yield=62%).

2.2.3 Optical characterization

The 3 dyes above were characterized optically under ambient conditions by a UV-Vis spectrophotometer. The UV-Vis equipment used is an Agilent Cary60 spectrophotometer in the 300-800 nm wavelength range. The dye solutions with a molar concentration (10^{-5} M) were prepared for all dyes and measured in a quartz cuvette with a pathlength of 1 cm. To ensure that similar environmental conditions for the measurements, the sample cuvette

holder temperature is controlled and performed at 25°C, thanks to the Agilent Peltier temperature controller. The dyes were studied in their two states i.e. closed and opened form. The closed form (CF) was performed in the dark whereas the open form was accessed through irradiation (300-600 nm) with filtered light (350-425 nm) using an Asahi Spectra MAX-303 Xenon light source. The thermal discolouration kinetics were also registered by cutting the irradiation source and shall be discussed here.

2.2.3.1 UV-Vis absorption

All the 3 dyes presented above undergo a reversible photochemical reaction that involves the cleavage of the C-O bond on the pyran moiety to generate the open coloured forms according to their naming colour codes. **NPL** photoisomerizes to give orange coloured open form dyes, **NPB** gives reddish and **NPI** gives a green colouration. Their absorption spectra are as presented below,

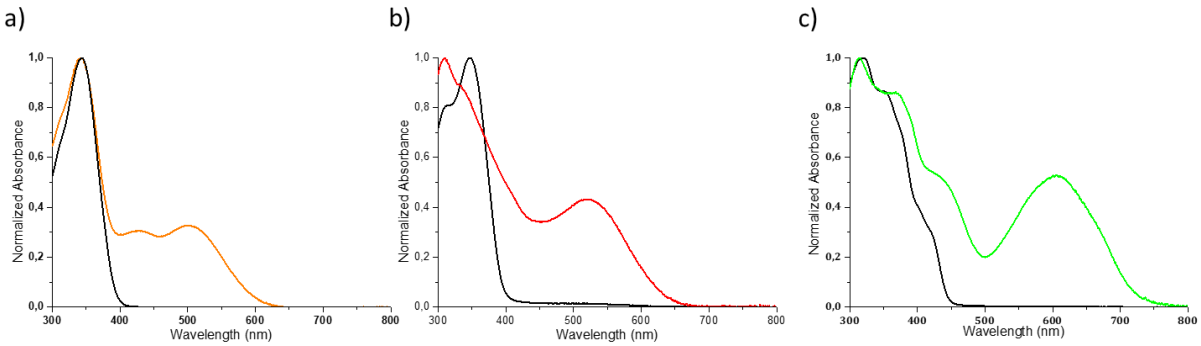

*Figure 2.7 : Absorption spectra of (a) **NPL** in its closed form (black curve) and open form (orange curve) (b) **NPB** in its closed form (black curve) and open form (reddish-brown curve) and (c) **NPI** in its closed form (black curve) and open form (green curve) at 25°C, 10^{-5} M (irradiation conditions : 200W Xenon lamp, 350-425 nm filter) in toluene.*

The optical parameters of the 3 dyes are as shown in the table below,

Dye	λ_{max} CF (nm)	λ_{onset} CF (nm)	ε CF ($mol.L^{-1}.cm^{-1}$)	λ_{max} OF (nm)	λ_{onset} OF (nm)	ΔE_{opt} OF (eV)
NPL	345	400	53,000	502	610	2.03
NPB	347	400	45,100	519	636	1.95
NPI	318	450	41,800	605	728	1.70

For all dyes, the closed forms (in the dark) show an intense absorption peak in the UV part of electromagnetic spectrum. Both **NPL** and **NPB** show relatively similar absorption spectra in their closed form with their closed forms with a maxima around 346 nm. However, the molar absorption coefficients in the UV region of **NPL** (5.30×10^4 $M^{-1}.cm^{-1}$) dye is slightly higher than **NPB** (4.51×10^4 $M^{-1}.cm^{-1}$) but their λ_{onset} remains at 400 nm. **NPI** on the other hand has

comparable high molar extinction coefficient (4.18×10^4 $M^{-1}.cm^{-1}$) with an absorption maximum at 318 nm and several shoulders. Distinctively, **NPI** that shows a difference from **NPB** by the indeno-fused naphthalene and DPA electron-donating unit, shows a 50 nm red-shift in the λ_{onset} of its closed form. This shift is important for application of these dyes in solar cells made up of FTO glass substrate and TiO_2 film absorbing until 400 nm. Indeed, it will help to improve the light absorption above 400nm, by the uncolored form, and will give rise to a larger quantity of coloured isomers. The photoactivated solar cells will be activated with lower energy photons once grafted on TiO_2 substrate and prevent the screening effect of the oxide (<400 nm) [18].

Consequently, upon UV irradiation of the ring-closed forms, the molecules undergo a heterolytic cleavage of the C-O bond in the pyran cycle to generate the open forms. The molecule undergoes a rearrangement of the heterocyclic pyran unit showing absorption in the visible range, different from the CF ones. As a result, the molecules exhibit an instant change of colour from colourless (as in **NPL**), slightly reddish (as in **NPB**) or yellowish (as in **NPI**) to yellowish-orange in **NPL**, intense reddish in **NPB** and an intense green colouration in **NPI**, respectively. **NPL** and **NPB** portray show an absorption that peaks at 502 and 519 nm and a λ_{onset} at 610 and 636 nm, respectively. The change in the position of the phenyl in the photochromic core from a linear position in **NPL** to a bend in **NPB** results in a 17 nm red-shift in the absorption maximum and hence colour. On the other hand, **NPI** shows an 86 nm red-shift in its OF with respect to **NPB** and an intense internal charge transfer (ICT) transition which would in principle mean more harvesting of low-energy photons (with maximum at 605 nm). This absorption in the red translates to a complementary green colouration, one of a kind in this family of naphthopyran photochromes. The λ_{onset} of **NPI** is 728 nm thus demonstrating the lowest optical HOMO-LUMO gap when the equation ($\Delta E_{opt} = 1241/ \lambda_{onset}$) is considered. The molar extinction coefficients of the opened forms are hard to determine given that different PSSs and conformers can be accessed.

2.2.3.2 Discolouration kinetics in solution

The speed/rate at which these photochromic molecules revert back to their initial state was also investigated by UV-Vis spectroscopy. This is achieved through continuous irradiation of the dye dissolved in toluene in a cuvette. After the PSS is reached, the irradiation source is stopped and the thermal bleaching to the initial closed form is registered by following the

disappearance of the absorption maximum (λ_{max}) peak of the opened forms and modelled into the following equation :

$$A(t) = a_1 e^{-k_1 t} + a_2 e^{-k_2 t} + A_\infty$$

$$A(t) = a_1 e^{-k_0 t} + A_\infty \ (mono\ exponential)$$

Where *A(t)* is the absorbance at a given time, k_1 and k_2 are the first and second thermal discolouration kinetic discolouration constants (the former being faster than the later), a_1 and a_2 being the amplitudes of the kinetic constants of k_1 and k_2, respectively, and finally A_∞ is the residual absorbance.

The discolouration curves for the 3 dyes were registered in the dark at controlled temperatures (25°C). The normalized absorbance as a function of time was plotted to make comparison.

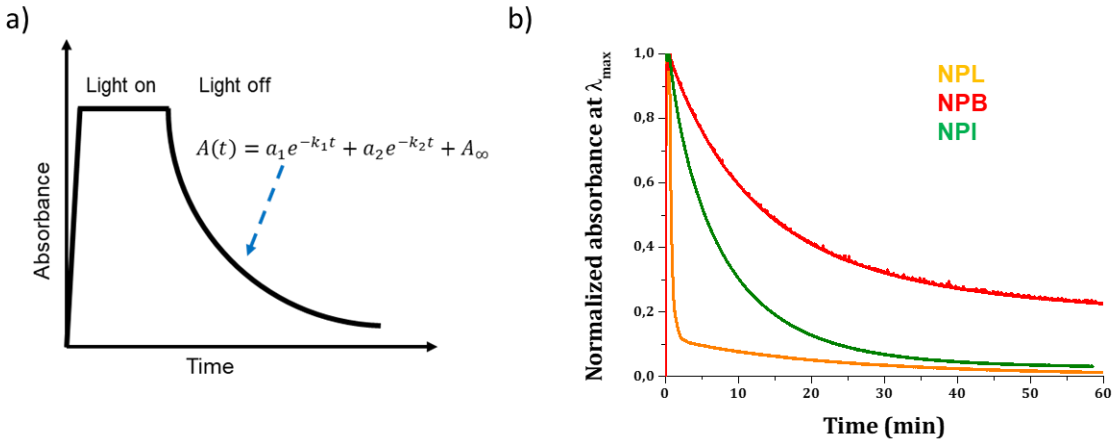

*Figure 2.8 : a) Illustration of how the discolouration kinetics are registered with plateau known as the photo-stationary state. b) the discolouration kinetics of the 3 photochromic dyes **NPL**, **NPB** and **NPI** that make the first generation, studied in solution (toluene, 25°C, 10^{-5} M).*

The obtained discolouration kinetic constants are as shown in the table below,

Dyes	k_1 at 25°C (s^{-1})	k_2 at 25°C (s^{-1})
NPL	9.8×10^{-2}	1.1×10^{-3}
NPB	1.4×10^{-3}	2.0×10^{-4}
NPI	2.1×10^{-3}	-

Table 2.1 : Showing the thermal discolouration kinetic constants (in s^{-1}) for the n^{th} kinetic process.

First, it should be noted that the PSS is obtained after few tens of seconds in all cases. **NPL** shows the fastest 1st discolouration constant (k_1) of 9.8×10^{-2} s^{-1} followed by a slower 1.1×10^{-3} s^{-1} k_2 constant in solution. **NPB** has the slowest ring-closure kinetics in the dark with k_1 of 1.4×10^{-3} s^{-1} followed by a slower 2.0×10^{-4} s^{-1} k_2 constant in solution. The residual absorbance in

NPB is way higher than that of **NPL**. Indeed, **NPB** solution remains coloured for a long time after exposure to light due to the formation of stable and long-lived TT isomers [19,20]. Surprisingly, **NPI** discolouration decay curve could fit to a monoexponential equation i.e. $A(t) = a_1 e^{-k_0 t} + A_\infty$ instead of the bi-exponential one presented above. The kinetic constant is rather high and equates to 2.1×10^{-3} s^{-1} in solution at 25°C. Both **NPB** and **NPI** are based on a 2,2-diphenyl-2*H*-naphtho[1,2-b]pyran core which demonstrates that the insertion of an indene group possessing the bulky *para*-phenylhexyl substituents is a good strategy to limit the formation of stable and long-lived TT isomers, all thanks to the steric hinderance. As a result, the generated OF isomers are much more unstable in the absence of light thus fastening their ring-closure towards stable CF. This was confirmed through an NMR spectroscopy study carried out by Dr. Johan Liotier during his PhD work.

Earlier, I had mentioned that the PSS is dependant on the experimental conditions such as temperature.

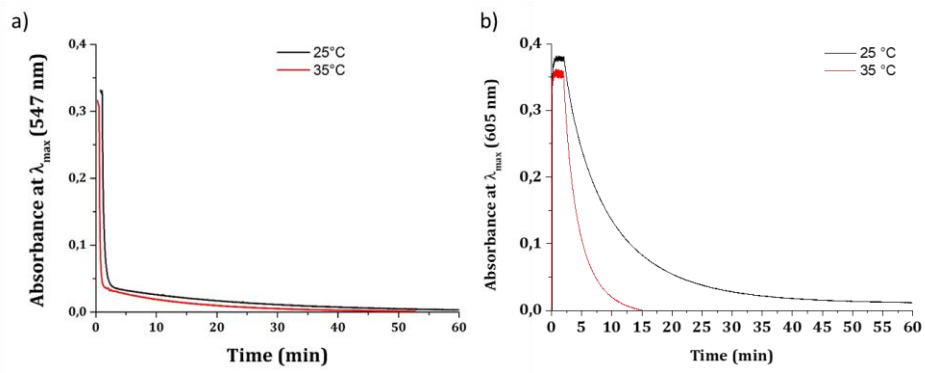

*Figure 2.9 : Absorbance measured during irradiation until the photo-stationary state (PSS) and registered over time when the irradiation is stopped at the wavelength maximum of the coloured opened form, a) **NPL** (547 nm) and b) **NPI** (605 nm). Conditions (toluene, 10^{-5} M, at 25°C (black curve) and at 35°C (red curve)).*

Fig. 2.9 above demonstrates that a higher PSS is reached at a lower temperature (25°C) as compared to higher temperatures (35°C). This proves the impact of temperature on the photochemical reaction and that the equilibrium is attained faster at high temperatures leading to low light absorption.

2.2.4 Energy levels determination

For incorporation of these dyes in a DSSC configuration, it is crucial to know if they match the energy levels for an effective charge extraction and generate electricity. This helps to determine if the driving for injection into TiO_2 and dye regeneration are sufficient to give rise to electron transfer in complete devices.

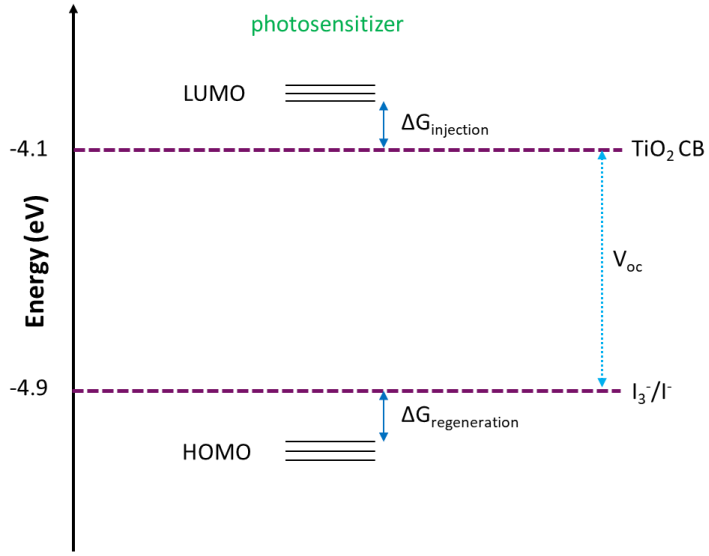

Figure 2.10 : An energy level diagram of a complete DSSC configuration.

Therefore, optoelectronic properties of the dyes (both closed and opened forms) were unravelled theoretically and experimentally by CV (see an example of CV trace in Figure 2.12) to determine their frontier orbitals positioning. The diagram below illustrates the energy levels,

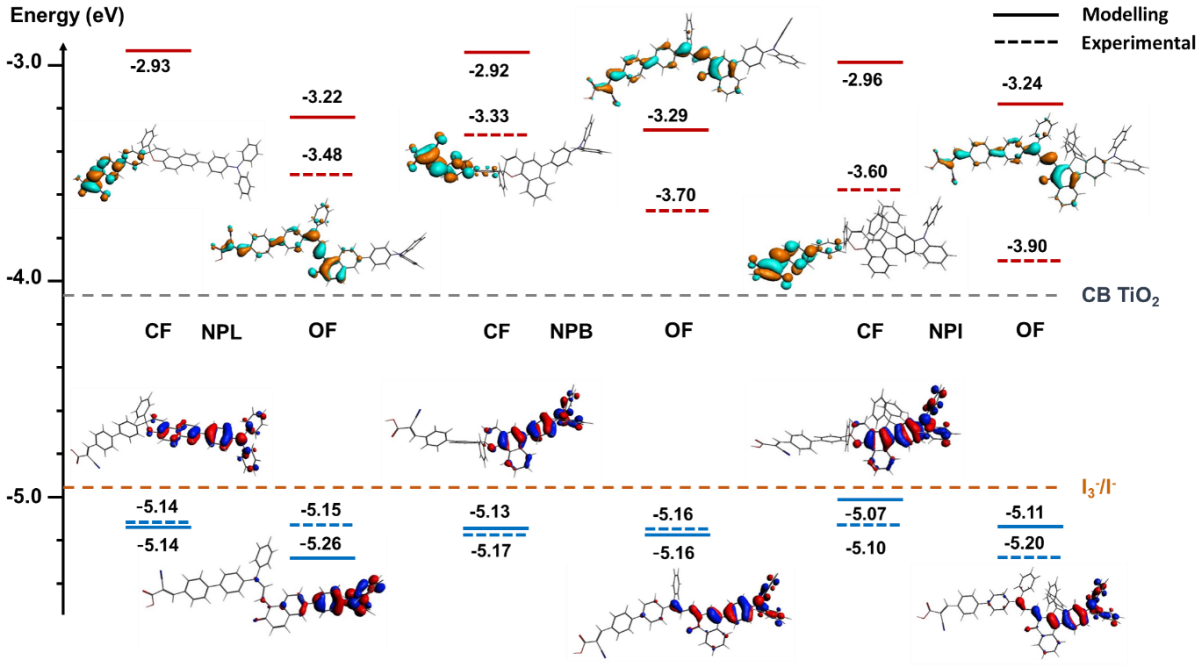

Figure 2.11 : Theoretical and experimental determination of frontier molecular orbitals of the photosensitizers in their closed and open forms. The metal oxide conduction band edge and the redox potential have been included for quick comparison.

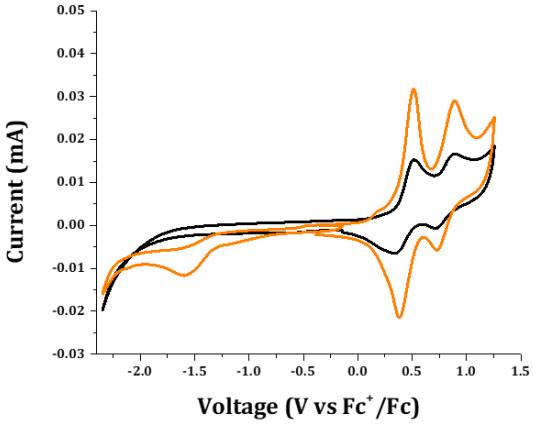

*Figure 2.12 : An example of cyclic voltammogram of photochromic **NPL** dye in the dark, black curve, and under irradiation, orange curve. These measurements were performed during the PhD work of Johan Liotier.*

Both the closed and opened forms of all dyes can sensitize TiO_2 and allow for efficient injection of electrons due to the correctly positioned LUMO levels. Pandey *et al.* for example reported that the minimum energy barrier for efficient injection is 0.16 eV [21]. All dyes, irrespective of their state, can allow the regeneration process, thanks to their well-positioned HOMO levels (between -5.1 to -5.2 eV experimental) allowing a sufficient driving force for the process ($\Delta G_{regeneration}$ = >0.15 eV) [22,23]. From the DFT calculation at the B3LYP level of theory, the spatial distribution of the electron cloud density is well suited for DSSC application. For instance, the HOMO is homogeneously localized on the electron-donating (TPA) part to facilitate the regeneration process by the redox couple whereas the LUMO is situated close to the anchoring function to make the electron injection easier. This distribution is important to create a clearly separated charged states under exposure to solar irradiation. At this point, we have designed, synthesized and characterized optoelectronically the three photochromic dyes and consider them practical in a DSSC configuration.

2.2.5 Optimization of photochromic solar cells

In this sub-section, I will focus on the integration of photochromic dyes in solar cells by anchoring them on a TiO_2 substrate. It also contains the efforts made to achieve record efficiencies with the new class of dyes given that I understand the working with classical dyes. Solar cells are assessed by their power conversion efficiencies (PCE) obtained from the device's current-voltage spectrum. A reminder, J_{sc}, V_{oc}, FF and PCE are important photovoltaic parameters. The electrolyte and the photoanode were identified as vital components.

First, it is worth to mention that the adsorbed photochromic photosensitizers on the TiO_2 surface undergo a photochemical transformation as in solution. The closed forms of the dyes are yellowish or slightly coloured whereas their opened form counterparts are strongly coloured. The colours observed vary depending on the wavelengths in which the dyes absorb in the UV-visible region of the electromagnetic spectrum.

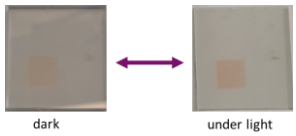

Figure 2.13 : An example of colour change after the dye is anchored on the TiO_2 surface.

The first time I applied photochromic dyes in solar cells, I used **NPI** dye with a commercially available Iodolyte-HI-30 electrolyte. It contains additives that play different roles [24–29]. This electrolyte is composed of 0.5M 1-butyl-3-methylimidazolium iodide (BMII), 0.03M I_2, 0.5M LiI, 0.5M guanidinium thiocyanate and 0.5M 4-*tert*-butylpyridine (tBP) in acetonitrile. The solar cells fabrication conditions applied were those reported with the best dye in the lab (**RK1**) i.e. dye:10CDCA.

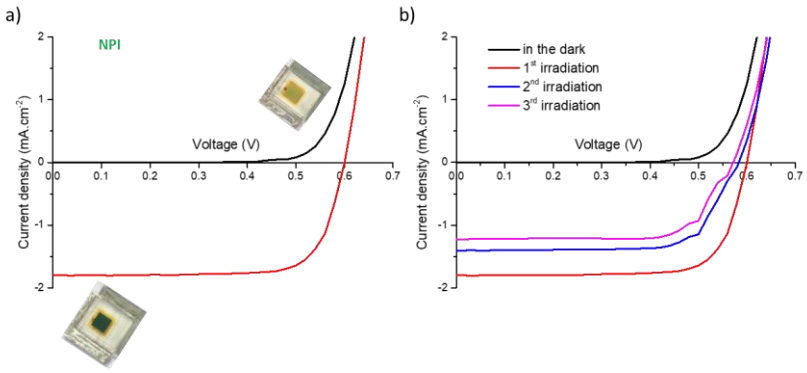

Figure 2.14 : First test of photochromic solar cells based on NPI a) J(V) curve after 15s irradiation and b) after subsequent irradiations amounting to 120s (magenta curve).

From Fig. 2.14 above, the complete solar cells are photochromic i.e. they change their colour from yellowish (in their closed form) to a dark green (in their opened form) under irradiation. The PV parameters after 15s of irradiation (red curve) are J_{sc} = 1.67 mA.cm^{-2}, V_{oc} = 600 mV, FF = 81.7% and a PCE = 0.82%. When the cell was left under 1 Sun, as shown in (b), both the J_{sc} and the V_{oc} diminished. The PV parameters of the magenta curve (plot b) are J_{sc} = 1.22 mA.cm^{-2}, V_{oc} = 577 mV, FF = 72.6% and a PCE = 0.51%. All these parameters are very low that call for optimization and understanding their loss as a function of irradiation time to achieve record efficiencies for photochromic DSSCs (see Chapter 1).

To further understand the effect of the different components in the electrolyte, I carried out a study aiming at optimizing the performances.

2.2.5.1 Impact of iodine concentration

Mathew *et.* al and related work have reported increased photocurrent density (J_{sc}) with iodine concentration in the electrolyte [30]. A hypothesis built is that, by increasing I_2 concentration the J_{sc} will increase and hence the performance. To test it, while maintaining nearly the same electrolyte composition as Iodolyte-HI-30, I screened the iodine composition from 0.03M (as in commercial electrolyte) to 0.11M. The devices' electrical parameters as a function of iodine concentration are as reported below at the photostationary state (PSS).

Table 2.2 : Showing the optimization of the J_{sc} as a function of the iodine concentration at the photostationary state (PSS).

Iodine concentration (M)	**J_{sc} (mA.cm^{-2})**	**V_{oc} (V)**	**FF**	**η (%)**
0.03	2.68	0.56	0.72	1.08
0.05	2.82	0.57	0.73	1.17
0.07	2.91	0.58	0.72	1.22
0.09	3.23	0.62	0.75	1.48
0.11	2.89	0.57	0.69	1.14

The J_{sc} and power conversion efficiencies as a function of concentration and irradiation time were plotted in a bar graph to see their evolution as shown in the figure below. The first bar corresponds to the parameters registered after 15s of irradiation; the PSS corresponds to the parameters obtained when the I-V curves do not vary anymore upon illumination.

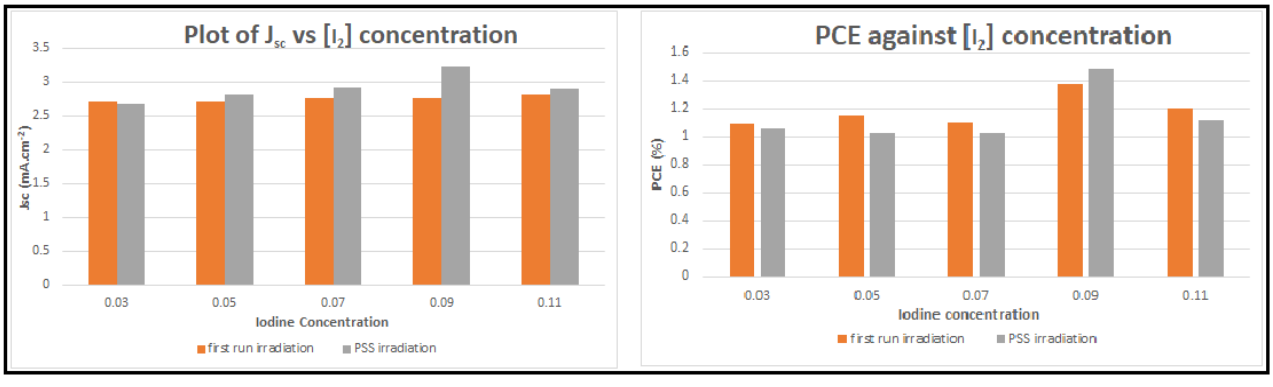

Figure 2.15 : A bar graph showing the evolution of the generated photocurrent and the power conversion efficiency as a function of iodine concentration.

The J_{sc} increases progressively to reach a maximum value at the PSS with 0.09M I_2 concentration. Contrarily, the PCE decreases between the first irradiation and that at PSS, for

all concentrations, except for the 0.09M [I_2] value. The V_{oc} was also highest (620 mV) at this concentration bearing in mind that we have additives such as *t*BP. This was an encouraging result reaching a PCE of 1.48% but still low compared to the state-of-the-art.

2.2.5.2 Optimization of the 4-*tert*-butylpyridine concentration.

The 4-*tert*-butylpyridine (*t*BP) is a widely used additive in electrolytes for DSSCs. This additive is known to play a crucial role on the V_{oc} of the solar cells. In 2005, Ruhle *et al.* reported that organic molecules attached on the TiO_2 substrate can modify the electronic properties in a DSSC configuration as shown in their work in Fig. 2.16 [31].

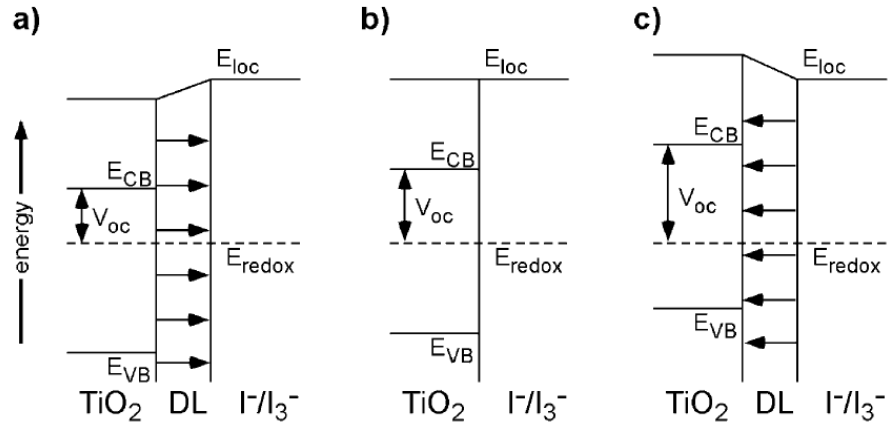

Figure 2.16 : Effect of organic molecules dipole on the TiO_2/electrolyte interface. (Image extracted from [31])

In case **a)**, the dipole layer (DL) consists of molecules having positive dipole moments at the TiO_2/redox couple interface, arrows pointing away from TiO_2 surface, results in a decrease of the V_{oc}. **b)** is a case without a DL at the interface and V_{oc} is ruled out by TiO_2 CB and I_3^-/I^- positioning. In **c)** with a negative dipole moment at the interface results in V_{oc} increase.

The 4-*tert*-butylpyridine is known to have a positive shift on TiO_2 CB towards the vacuum level (case c) [32–34]. This CB shift to higher energies can have two different impacts: first, increasing the V_{oc} and second, decreasing the current density, J_{sc}, by decreasing the efficiency for electronic injection into TiO_2 CB. However, I needed to find a compromise between these two PV parameters to win high performance photochromic solar cells.

Therefore, I made a hypothesis that *t*BP will shift TiO_2 CB towards the vacuum level (E_{loc}) thus increase the V_{oc}. Starting from the concentration of the commercial Iodolyte-HI-30 (0.5M [*t*BP]), I varied this concentration to 0.0M[*t*BP] to find the optimum.

*Table 2.3 : Key electrical parameters after first run irradiation (**at 15s**).*

***t*BP concentration (M)**	**J_{sc} ($mA.cm^{-2}$)**	**V_{oc} (V)**	**FF**	**PCE (%)**
0	8.62	0.59	0.71	3.25
0.1	4.79	0.63	0.76	2.23
0.5	3.26	0.66	0.80	1.72

*Table 2.4 : Key electrical parameters after first run irradiation (**at PSS**).*

***t*BP concentration (M)**	**J_{sc} ($mA.cm^{-2}$)**	**V_{oc} (V)**	**FF**	**PCE (%)**
0	10.44	0.58	0.74	3.69
0.1	4.45	0.58	0.71	1.82
0.5	2.76	0.58	0.75	1.17

The hypothesis on *t*BP is true as there is a considerable increase in the V_{oc} with increasing *t*BP concentration simply due to shifting of TiO_2 CB towards vacuum level for the first run irradiations and remains similar at the PSS. The PV parameters are presented in a bar graph to make comparison.

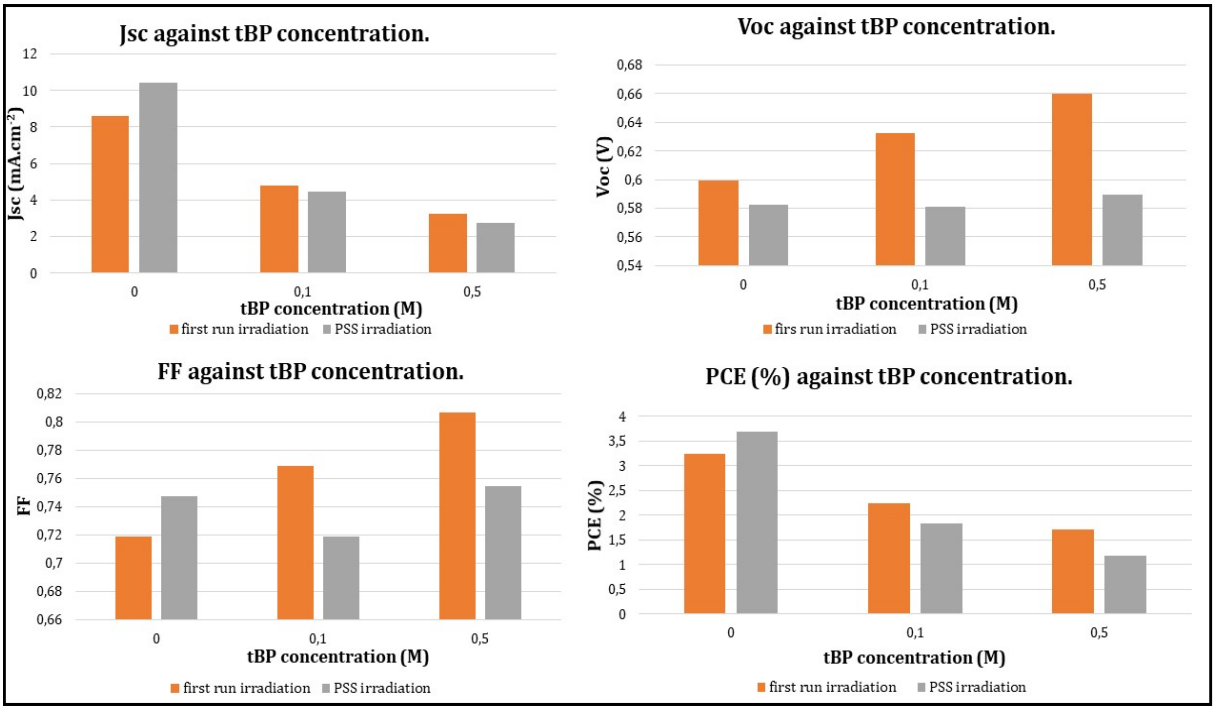

Figure 2.17 : Effect of tBP concentration.

The J_{sc} is inversely related to the V_{oc}. The J_{sc}, V_{oc}, FF and PCE decreases between 1st irradiation to PSS with *t*BP. The low J_{sc} is likely due to the lowly positioned **NPI** LUMO (around -3.9 eV from CV above) that decreases the electron injection driving force as we generate more

opened forms with irradiation time. The opposite effect is observed on J_{sc}, FF and PCE with 0 *t*BP. An incredible 4-fold J_{sc} increase was observed from 2.76 up to 10.44 mA.cm^{-2}.

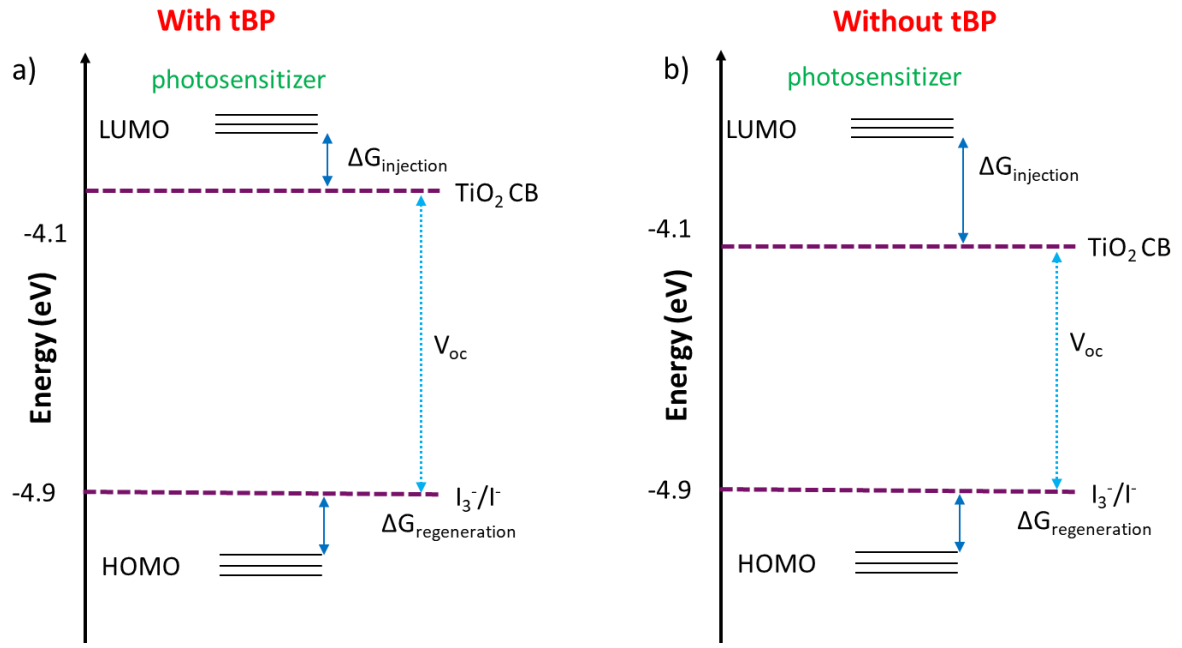

Figure 2.18 : Demonstration of the tBP additive impact on our photochromic solar cells.

The J_{sc} increased by ~3 mA.cm^{-2} between irradiations (1st and at the PSS) leading to the highest performance of 3.69% efficiency. Consequently, *t*BP was eliminated because any slight addition was accompanied by poor driving force for electronic injection into TiO_2 CB hence lowering the J_{sc}. The electrodes used to obtain these results were opaque (12µm (mesoporous) + 4µm (scattering layer)). The other component in iodolyte-HI-30 i.e. guanidinium thiocyanate was omitted in the composition because it has similar effect as *t*BP [35] to simply 0.09M I_2 and 0.5M LiI in acetonitrile was chosen as the **optimized electrolyte** (**OE**) for photochromic solar cells.

2.2.5.3 Electrode thickness

The thickness of the mesoporous layer is known to affect the amount of the dye adsorbed and hence the J_{sc} [36–38]. In this section, I investigated the film thickness that was varied from 8 to 13µm. Note that we used a 4µm-thick scattering layer to optimize the diffusion of light in the mesoporous film, thus improving the light harvesting efficiency of the devices.

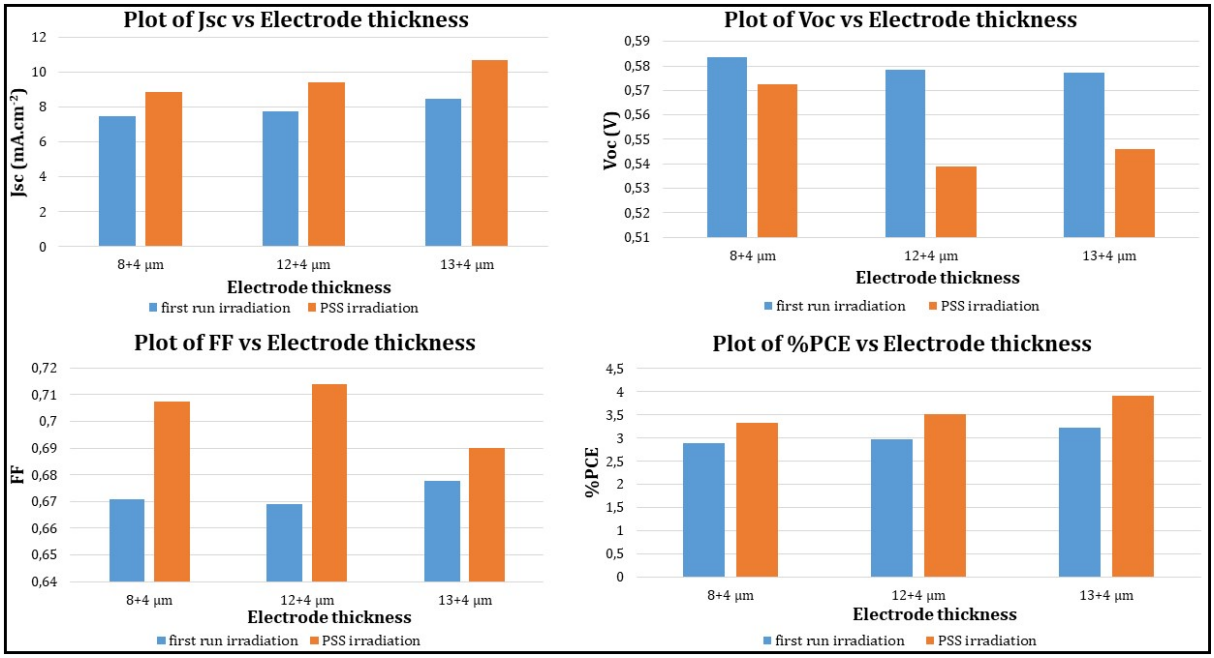

Figure 2.19 : Effect of electrode thickness.

The plot above establishes the dependence of photovoltaic properties of photochromic DSSCs on the film thickness. There is an increase in J_{sc} associated with an increased number of dye molecules adsorbed on the mesoporous layer as a function of film thickness [39]. Compared to thinner film, larger films exhibit lower V_{oc}'s linked to higher charge recombination and restrained mass transport with increased surface area [40,41]. Overall, the photovoltaic conversion efficiency is enhanced with increasing the thickness from 8µm to 13µm. To this point, a J_{sc} of around 10.6 mA.cm^{-2} and a V_{oc} of 540 mV giving a PCE of 3.90% was attained with our home-made electrolyte at the PSS. This led to the conclusion that 13µm+4µm opaque electrodes are optimum for high performance photochromic solar cells. Beyond this thickness, electrodes are more likely to crack during preparation.

To confirm reliability of our protocol and measurements at this time, an independent collaborative company, Solaronix (Switzerland) repeated the experiments with our optimized electrolyte and device preparation parameters. The experiments were done by Stéphanie Narbey and obtained the following results,

*Table 2.5 : The average performances of **NPI**-based dye solar cells prepared with optimum conditions using opaque electrodes.*

Solaronix	3.52 ± 0.042 %
Our Lab (CEA-Grenoble)	3.71 ± 0.186 %

These optimizations were done using **NPI** photochromic dye. The optimized conditions were transferred to the other dyes, **NPL** and **NPB,** to extract structure-property relationships making the first-generation reversible photochromic DSSCs family.

2.2.6 Optimized photochromic DSSCs devices

After testing three different thicknesses, I finally decided to work without *t*BP in the electrolyte composition with thicker electrodes (13µm + 4µm) while maintaining the optimized iodine content (0.09 M). The resulting PV parameters obtained are as reported in the table below :

*Table 2.6 : Showing the PV performances of **NPL**, **NPB** and **NPI**-based solar cells with statistics done on atleast 3 solar cells for **NPL** and **NPB** using 13µm transparent cells and 13µm + 4µm scattering opaque cells. For **NPI**, statistics are based on atleast 3 solar cells for transparent devices and 21 solar cells for opaque ones. On the extreme right column, the amount of each dye grafted on the TiO_2 surface.*

Dyes	Electrode	Jsc ($mA.cm^{-2}$)	Voc (V)	FF	PCE (%)	Dye Loading ($moles.cm^{-2}$)
NPL	Transparent	3.27 (3.07 ± 0.26)	0.513 (0.508 ± 0.004)	0.706 (0.702 ± 0.003)	1.16 (1.09 ± 0.09)	5.56×10^{-7}
	Opaque	4.11 (3.90 ± 0.16)	0.487 (0.493 ± 0.013)	0.732 (0.732 ± 0.008)	1.43 (1.40 ± 0.02)	5.93×10^{-7}
NPB	Transparent	5.62 (5.50 ± 0.13)	0.515 (0.514 ± 0.005)	0.742 (0.739 ± 0.002)	2.15 (2.09 ± 0.04)	4.04×10^{-7}
	Opaque	6.94 (6.62 ± 0.22)	0.513 (0.508 ± 0.003)	0.757 (0.752 ± 0.007)	2.63 (2.53 ± 0.05)	3.95×10^{-7}
NPI	Transparent	10.74 (9.85 ± 1.10)	0.521 (0.515 ± 0.016)	0.658 (0.676 ± 0.029)	3.68 (3.41 ± 0.20)	2.03×10^{-7}
	Opaque	12.59 (10.60 ± 0.95)	0.505 (0.519 ± 0.016)	0.656 (0.692 ± 0.029)	4.17 (3.78 ± 0.18)	2.60×10^{-7}

The statistical distribution of power conversion efficiencies for the 3 photochromic dyes is as shown below.

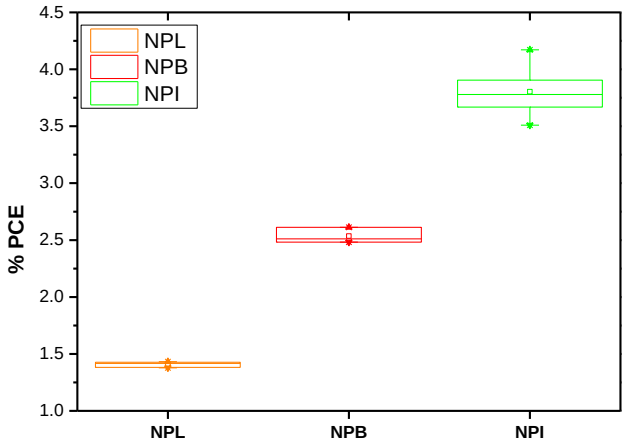

*Figure 2.20 : Box plot for **NPL**, **NPB** and **NPI** – based photochromic solar cells with their colour codes.*

The distribution is good and a bit larger with **NPI**. Therefore, **NPI** data was analysed separately as shown below.

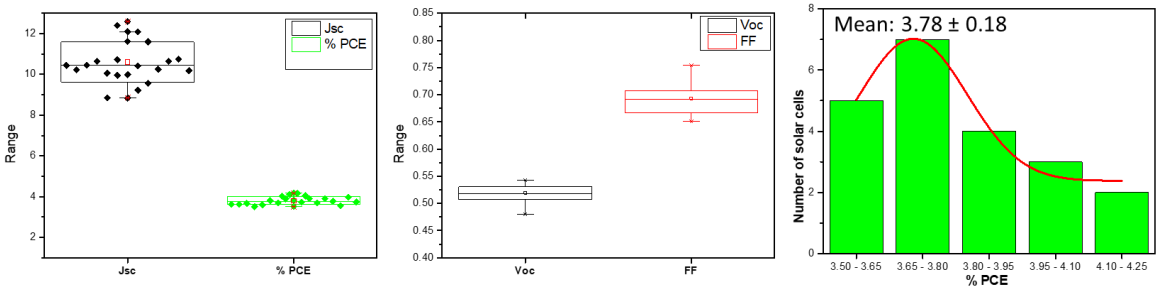

*Figure 2.21: Distribution of the photovoltaic parameters of **NPI**-based cells around the mean value.*

The J_{sc} shows a few outliers resulting in a central tendency in the photocurrent conversion efficiency. This analysis was done to confirm our results, demonstrate the reliability and reproducibility of our findings and methodologies. The statistics on **NPI** with 21 devices, opaque solar cells, has an average value of 3.78 ± 0.18%.

Thus, the best performing solar cells are as reported in Table 2.6 above with the performances increasing from 1.43% with **NPL**, 2.63% with **NPB** to a remarkable 4.17% using **NPI** while displaying an orange, reddish-brown to a deep green colouration, respectively, as seen in their *J(V)* curves below.

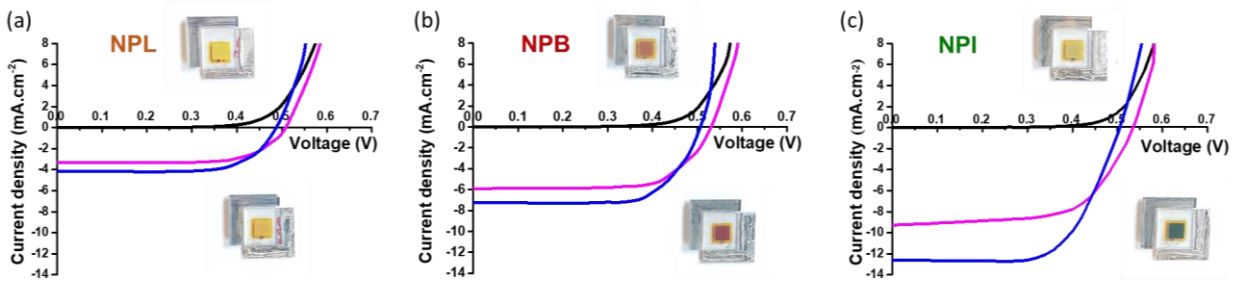

*Figure 2.22 : J(V) curves of the best **NPL**, **NPB** and **NPI**-based cells with the corresponding pictures. Top images in the dark (yellowish or brownish as in **NPB**) and below under light (orange for **NPL**, reddish-brown for **NPB** and green for **NPI**) (extracted from [42]).*

NPL and **NPI** devices are yellowish in dark with nearly the same colour as the electrolyte unlike **NPB** ones that shows slight colouration suggesting the presence of stable opened form isomers. From the curves above, the photovoltages of the 3 photochromic dyes –based devices are quasi-similar. They also have the same tendency where the V_{oc} decreases between the first irradiation ~15s (pink curve) and that at the PSS. However, visible differences are seen in the J_{sc} that increases drastically from 4.1 mA.cm^{-2} in **NPL**, to 6.9 mA.cm^{-2} in **NPB** and finally

to 12.6 mA.cm^{-2} in **NPI** resulting in world record efficiency for photochromic solar cells (**4.17%**) at the PSS.

The evolution of the PV parameters and the maximum powerpoint was tracked from the initial exposure to 1 Sun to the PSS as shown below.

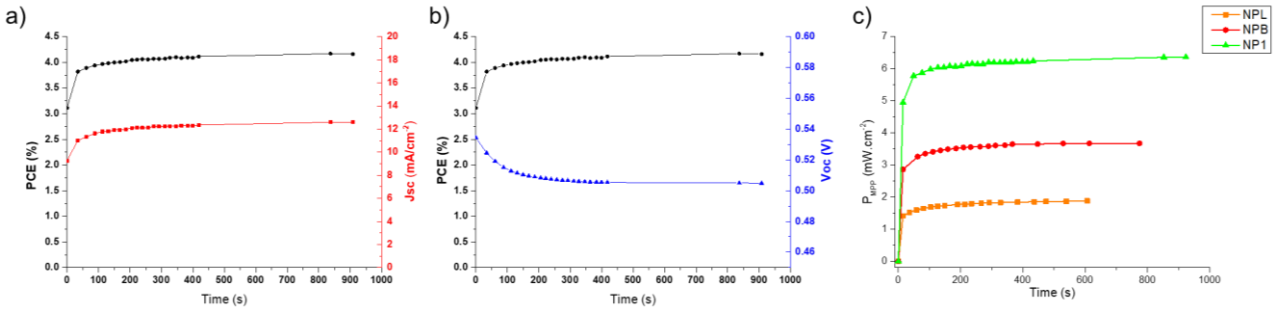

*Figure 2.23 : a) and b) The evolution of the J_{sc} and V_{oc} with the PCE as a function of irradiation time for **NPI**-based solar cell. c) The evolution of power at maximum power point (MPP) as a function of the irradiation time for **NPL**, **NPB** and **NPI**.*

The PCE increases due to increased J_{sc} to reach the PSS in around 5 minutes. The V_{oc} on the other hand decreases progressively to a constant value at the PSS within the same period of time. The maximum power also increases to reach a plateau in 5 minutes due to increased J_{sc}.

2.2.7 Source of V_{oc} loss

Conspicuously, the V_{oc} decreases as a function of irradiation time i.e. between the first irradiation (magenta curve) and that at the PSS (blue curve) as shown in Fig. 2.22 above. This behaviour is unusual and is not observed with classical organic photosensitizers such as **RK1**. The magnitude of the decrease (20-50 mV) to a constant at the PSS is notable in addition to the moderate V_{oc}'s of the solar cells. This is detrimental and limits us from attaining high performance photochromic solar cells.

From the basic working principles of DSSCs, we developed two hypotheses to explain this V_{oc} loss :

1) either a downward shift of the metal oxide quasi-fermi level or
2) an increased recombination rate (red arrows) as shown in the figure below.

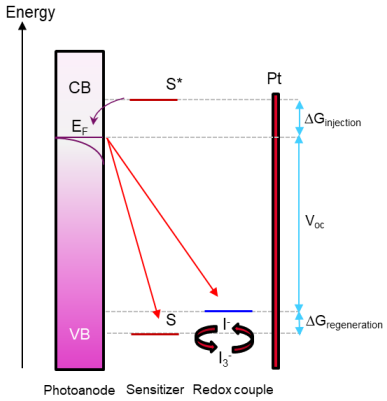

Figure 2.24 : An energy diagram showing the origin of photovoltage.

To verify which hypothesis is true we carried out a theoretical and experimental study using DFT calculation and impedance spectroscopy measurements.

Pandey *et. al* in 2009 reported how organic sensitizing dyes used in DSSCs could create band offsets after attachment onto TiO_2 surface thus affecting the V_{oc} [43]. The change in the conformation between the non-activated (close configuration) to the activated state (open configuration) could induce a change of the dipole moment thus have an impact on the CB of TiO_2. In this view, with the help of Dr. Pascale Maldivi, we calculated the components of the dipole moments, μ, of the **NPI**'s dye closed and open forms relative to the TiO_2 surface plane. The optimized geometry of **NPI** was adsorbed onto an anatase model using ADF program. The adsorption was achieved by deprotonating the acrylic group giving a carboxylate that can bind two Ti atoms in a bridging way [44] as shown below.

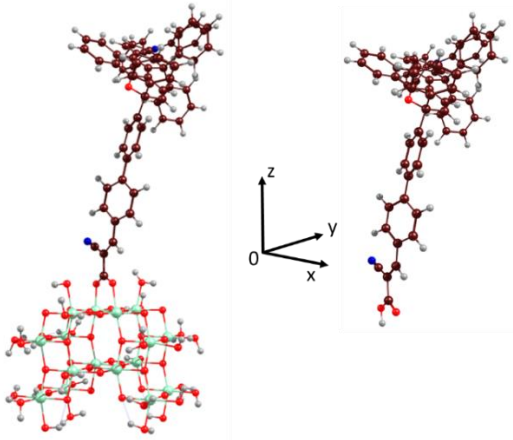

*Figure 2.25 : TiO_2 model with **NPI** dye anchored (extracted from [42]).*

The entire system (dye + TiO_2 model) were optimized through molecular relaxation while keeping the TiO_2 fragment fixed. This calculation helped us identify the molecular orientation of **NPI** in the *z* direction perpendicular to the surface. This calculation was performed for **NPI**'s

closed form (CF) and open isomers (OF) in its TC(T) and TT(C) isomers and the obtained dipole moments are as listed in the table below.

Table 2.7 : Calculated dipole moments (in Debye) at the B3LYP/TZ2P/COSMO level as per the reference frame with z perpendicular to TiO_2 surface as shown in Fig. 2.25 above.

NPI (on TiO_2)	Isomer	μ_x	μ_y	μ_z	μ
	CF	-4.9	-0.9	1.0	5.1
	OF TC(T)	-9.3	-0.6	5.1	10.6
	OF TT (C)	-7.9	-3.1	5.6	10.2

From Table 2.7 above, the total surface dipole moment of the **NPI** dye increases from 5.1 D in the CF to 10 D in the OF forms. This increase has been associated with an upward offset of the conduction band leading to increased V_{oc} [44,45]. Contrarily, a loss in the V_{oc} is observed in photochromic DSSCs after isomerization.

To unravel such detrimental mechanisms, impedance spectroscopy measurements were carried out, thanks to the collaboration with Pr. Juan A. Anta's group at the University Pablo de Olavide, Seville, Spain. The measurements were done before and after irradiation at the open-circuit voltage using red (λ_{red} = 635 nm), blue (λ_{blue} = 465 nm) and white illuminations under varying light intensities.

These measurements were carried out by applying a 10 mV voltage pertubation in the $10^6/10^5$-10^{-1} Hz frequency range as described in **Chapter 1**. I have investigated three dyes i.e **NPB** and **NPI** to deduce the impact of chemistry on the interfacial processes and a non-photochromic reference dye **RK1** for comparison purposes.

2.2.7.1 Impedance on **RK1**-based DSSCs

The electrochemical impedance spectroscopy measurements were performed on a complete **RK1**-based DSSC and the result is as shown below. These measurements were carried out at an applied voltage in the dark and under 1 Sun illumination at a voltage equal to the open-circuit voltage of around 0.7 V.

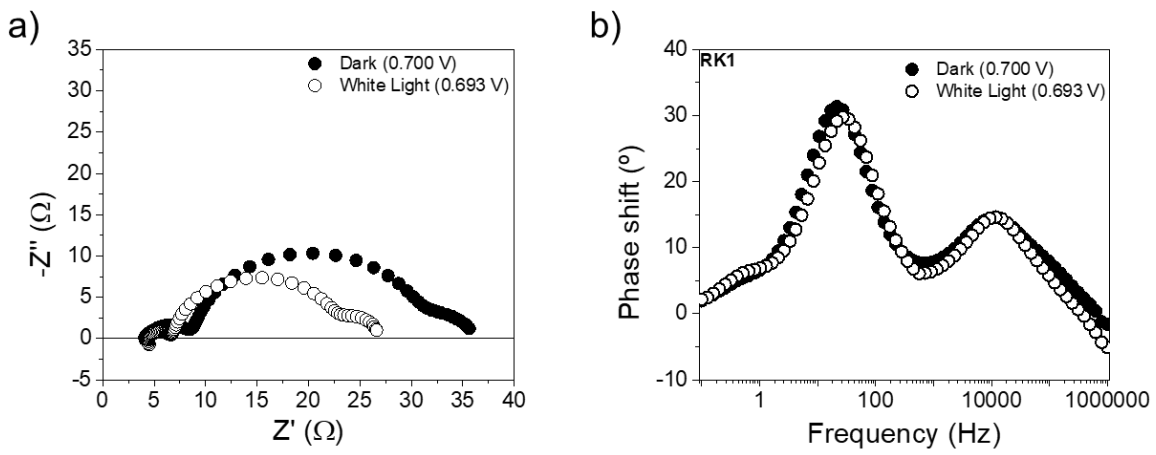

*Figure 2.26: Impedance measurements a) Nyquists plots and b) Bode plots of an **RK1**-based DSSC under different light conditions.*

The Nyquist plots in Fig. 2.26 a) show three semicircles on the real axis under the different irradiation conditions with their characteristic frequency peaks in the Bode plot [46]. These three arcs appear at 1-100 kHz, 5-500 Hz and 0.1-1 Hz frequency regimes. Each semi-circle corresponds to a physical process happening at the interface. The start of the arc relates to series resistance of the device. The first semi-circle, below 10 ohms, is observed at high frequencies and is related to platinum [47,48]. This is confirmed because when I performed impedance measurements based on an **RK1** device using a PEDOT-based counter electrode, this high frequency feature disappeared as shown in the Bode plot below [48].

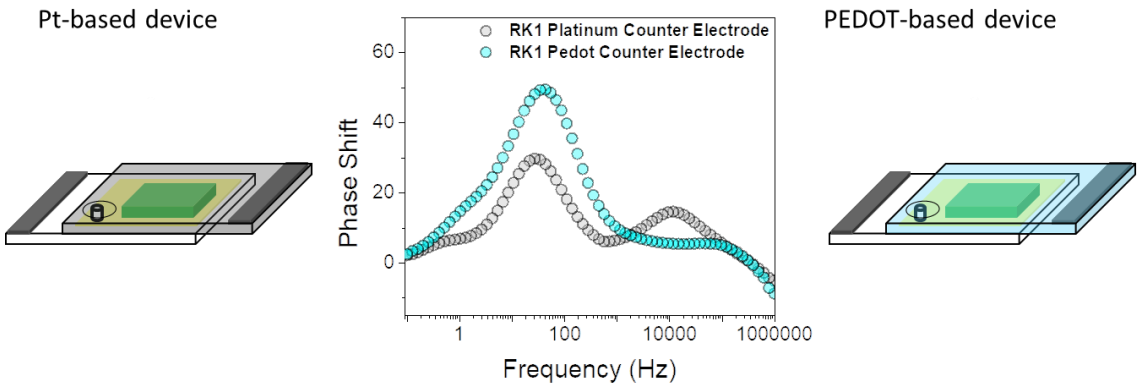

Figure 2.27 : Comparison between Bode plots of an RK1-based devices using platinum or PEDOT-based cathodes. The spectra were obtained (0.7 V applied voltage) under white illumination equal to voltage attained under 1 Sun illumination.

The arc at low frequencies (below 1 Hz) relates to the diffusion of charged species in the electrolyte (Nernst diffusion impedance at the Pt/electrolyte interface) [49,50]. Lastly, the mid-frequency arc between 5-500 Hz is linked to the electron transfer and recombination processes at the TiO_2/electrolyte interface [46]. The diameter of this arc on the real part of the

Nyquist plot can give information on the recombination resistance at a glance. From the dark to white light illumination, this mid-frequency arc (recombination arc) shrinks in a similar fashion as observed with the classical **Z907**-based cell presented in chapter 1.

Indeed, the impedance to electron transfer between the mesoporous TiO_2 and the triiodide ions in the electrolyte decreases under light compared to under dark conditions at similar potential. This behaviour is common in DSSCs and can be related to the increased concentration of the triiodide species close to the photoanode to regenerate the oxidized dye leading to increased recombination [51,52]. However, no remarkable differences are observed in the Bode plots.

The recombination arcs from the Nyquists plots were fit to an equivalent circuit (see Chapter 1) to assess the capacitative and the resistive behaviour of the **RK1**-based DSSC. Unfortunately, the classical Bisquert and co-workers transmission line model [46,53] could not fit the recombination arc of our solar cells. This major arc was fit to a parallel –RC– element and the extracted resistance values were related to either the charge transfer resistance (under dark conditions) or the recombination resistance (R_{CT}) of the device under operation whereas the capacitance values were linked to the chemical capacitance (C_μ). Both the resistance and the capacitance are known to vary with voltage and show an exponential dependence [54]. I will remind you the two equations from chapter 1 applied :

$$R_{ct} \sim exp\left(-\frac{\beta q V}{k_B T}\right) \qquad \text{(Equation 1)}$$

$$C_\mu \sim exp\left(\frac{\alpha q V}{k_B T}\right) \qquad \text{(Equation 2)}$$

A wide range of voltage was applied in the dark and under light where the applied voltage under illumination equals to the open circuit voltage achieved at specific light intensity. The data was plotted as shown below.

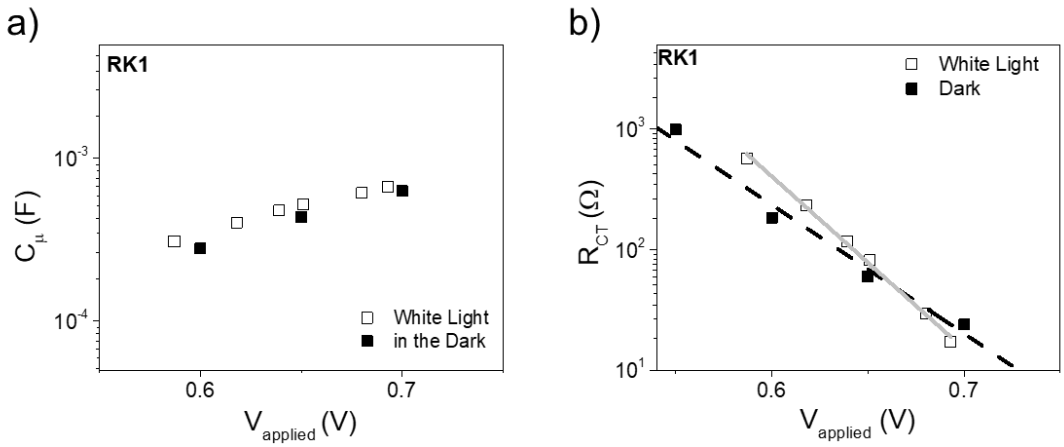

*Figure 2.28 : The capacitance and resistance values over the applied voltages of **RK1**-based device under dark and white light conditions. The data was obtained from fitting the recombination arc of the Nyquist plot to a parallel -RC- element.*

From the plots in the figure above, both the resistance and the capacitance show an exponential dependence according to the 2 equations (in chapter 1 and above : reminder). In Fig. 2.28a), the capacitance values are independent of the illumination conditions i.e. the capacitance values in the dark and under illumination lie on the same line. Such a behaviour suggests that there is no TiO_2 conduction band shift with irradiation conditions [55,56].

2.2.7.2 Impedance on photochromic DSSCs

This technique was transferred to photochromic dyes to understand the origin of the V_{oc} loss of their devices between irradiations i.e. at 15 s and at the PSS.

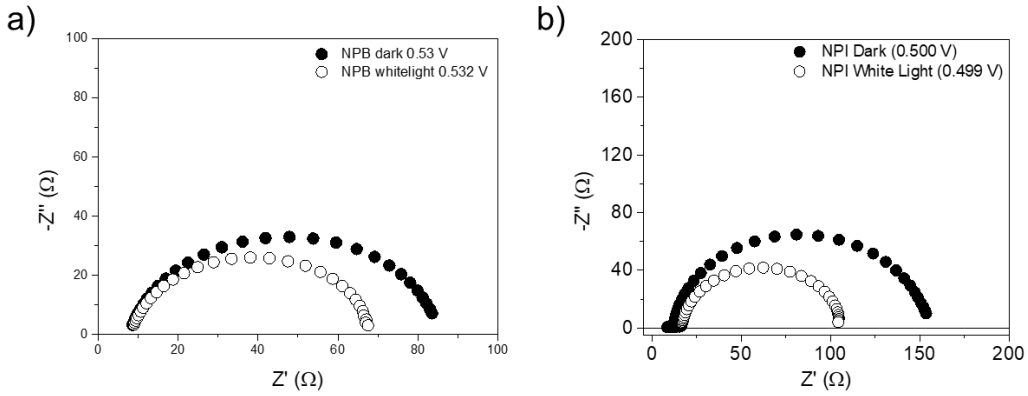

*Figure 2.29 : Nyquists plots of a) **NPB**- and b) **NPI**-based photochromic devices.*

The Nyquists plots of photochromic DSSCs shows two semi-circles on the real axis i.e. in the high and low frequency domains. The high frequency arc, similar to **RK1**-based device, is due to platinum counter electrode. The major semi-circle is related to the recombination of electrons between the CB of TiO_2 with the oxidized species in the electrolyte [46]. In my opinion, the third arc as a result of electrolyte diffusion is not observed in photochromic DSSCs because

a home-made electrolyte is used (with higher iodine concentration) compared to iodolyte-HI-30 (with lower iodine concentration) used in **RK1** cell. The main focus shall be on this semi-circle to understand what is happening at the TiO_2/electrolyte interface. To a first approximation, the diameter of this arc can give information on the recombination resistance. This arc also shrinks meaning the recombination resistance lowers as a function of irradiation [52].

The Nyquist plots above were analyzed and modelled by fitting them into an equivalent circuit. Given that the classical transmission line model developed by Bisquert [46] could not fit this spectrum, an –RC– element (a resistor and a capacitor in parallel) used for **RK1** was applied too. From the fitting, the chemical capacitance and the charge transfer were obtained by applying equations 1 and 2 above. The chemical capacitance, C_μ, is derived from the electron density versus voltage for the exponentially distributed trap states. The extracted C_μ values were plotted as shown below.

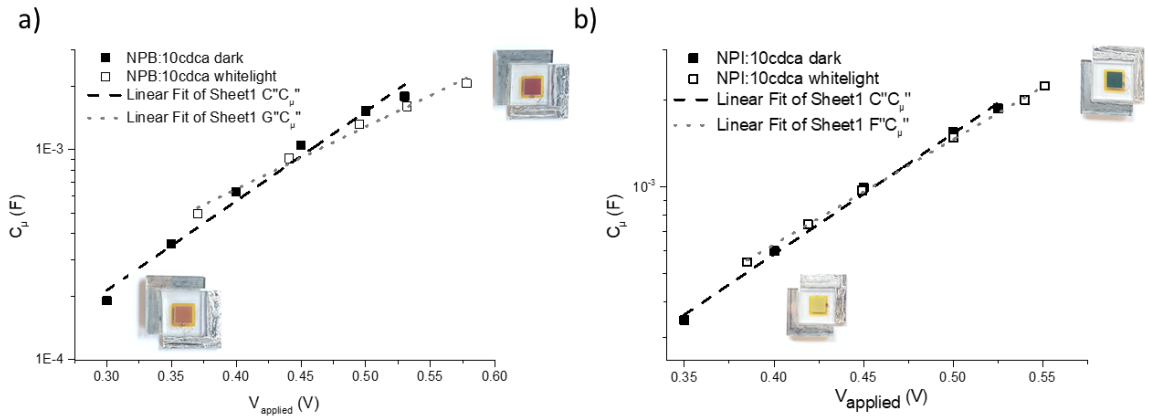

*Figure 2.30 : Comparison of the extracted chemical capacitance plots as a function of the voltage performed in the dark and under illumination for a) **NPB** and b) **NPI**.*

From the plots above, the chemical capacitance values of the recombination arc show an exponential voltage dependence as described in equation 2 above. The chemical capacitance values show independence on illumination conditions as seen with classical **RK1** dyes suggesting that the conduction band edges do not shift [55,56].

By plotting these C_μ values, the trap distribution parameters, α, can be obtained that are known to lie within the 0.15-0.35 range [55].

Table 2.8 : Showing the al and be values under dark and white illumination conditions after fitting the recombination arc of the Nyquist plot to an -RC- element using the two equations above.

DSSC	α		β	
	Dark	White light	Dark	White light
NPB	0.26	0.18	0.48	0.68
NPI	0.30	0.21	0.50	0.83
RK1	0.24	0.19	0.66	0.88

On the other hand, the β parameter is the recombination parameter that lies within 0.5 – 0.8 range [55,57–59]. In comparison to **RK1**, the evolution of this parameter is much more important in **NPI** devices than **NPB** ones. For the various **NPI**-based cells, the β values could approach unity and is unusual in DSSCs.

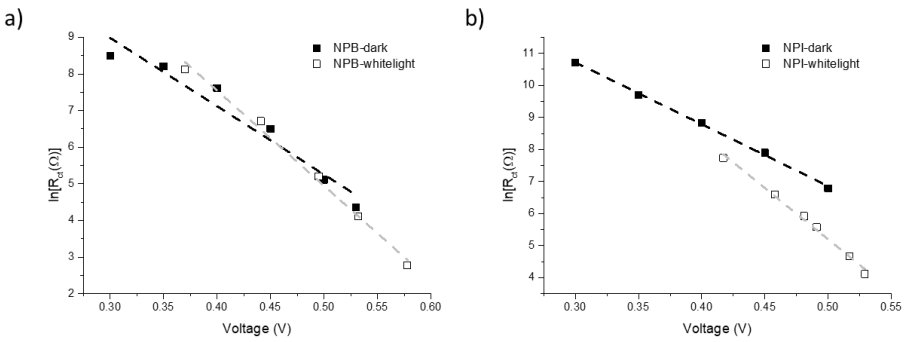

*Figure 2.31 : Recombination resistance as a function of the d.c. voltage (in the dark) and Voc (under light) of a) **NPB** and b) **NPI**-based devices. The dotted lines show linear fits to the equation (2) above.*

From Fig. 2.31 above, the recombination resistance shows an exponential dependence on voltage according to equation 1 above. The small change in the recombination slope of **NPB** device could be due to the presence of stable open form isomers in the dark. Consequently, the large difference in the β values observed for the **NPI**-based devices reflects the rapid drop in the recombination resistance under illumination with respect to dark resistance, especially with higher voltages. This signified an accelerated recombination rate between the dark (with CF of the dyes) and under illumination (to generate the OF of the dyes) thus explaining the decrease in the V_{oc} of the cells with irradiation time as demonstrated in Fig. 2.32 below.

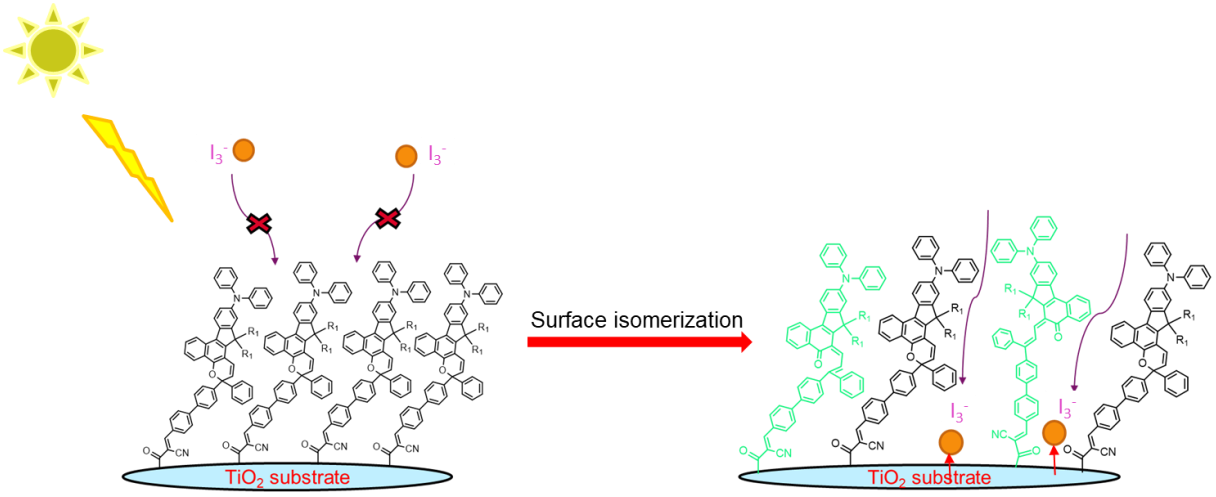

Figure 2.32 : The functioning and the effect of surface isomerization in photochromic dye solar cells.

To understand the impact of the indeno-fused bridge connecting the photochrome unit to the TPA-based donor on the performance of photochromic dyes in DSSCs, I made a comparison between **NPB** and **NPI** by impedance spectroscopy and the result is as follows.

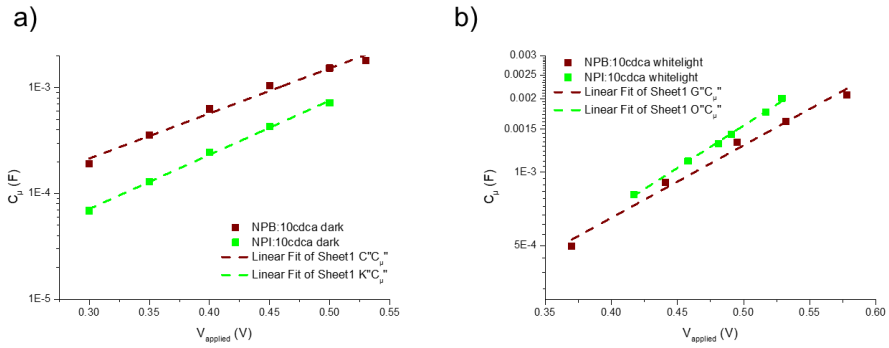

*Figure 2.33 : Chemical capacitances of **NPB** and **NPI** in the dark and under white illumination.*

In the dark, the capacitance plots are parallel to one another meaning there is a band shift in between the dyes with **NPB** showing slightly higher CB. However, upon irradiation the concentration of electrons is higher in **NPI**-based devices than in **NPB** ones. Very often, these structure-property differences can be ellucidated but by ensuring that the devices are at similar electron density at the quasi-Fermi level [60–62]. Therefore, a voltage correction was applied thus shifting the capacitances plots and the recombination resistances with corresponding Nyquists plotted.

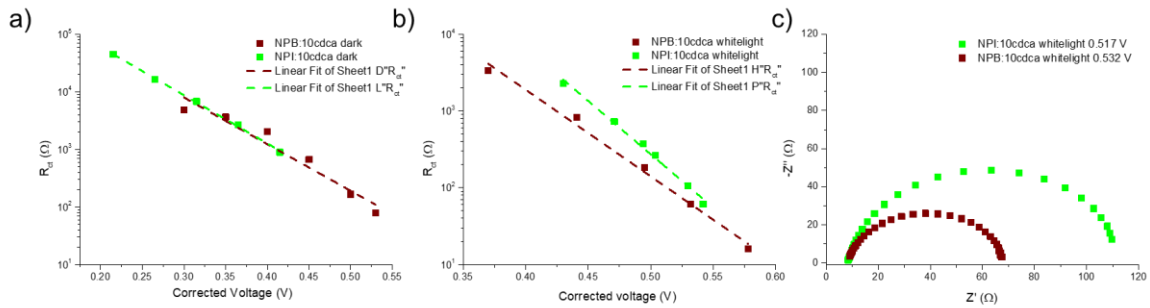

Figure 2.34 : Recombination resistance at the corrected voltages and the corresponding Nyquist plot under illumination (at the corrected voltage).

Indeed, an -85 mV and +13 mV bandshifts in **NPI**-based cell are observed in the dark and under illumination, respectively with respect to **NPB**. In Fig. 2.34b **NPI** shows a higher recombination resistance compared to **NPB**-based devices meaning lower recombination. This demonstrates that the fusion of the indeno moiety on the bridge is not only useful to red-shift the absorption spectra and improve absorptivity, but also in cutting the recombination mechanisms. This is observed in the Nyquist plot at the corrected voltages where the recombination arc of **NPI**-device is larger than that of **NPB**-device.

2.2.7.3 Impact of photochromism on recombination and electron transport

In the previous impedance section, we have seen that **NPI**-based cells show a comparable behaviour to classic dye solar cells where a shrink in the recombination arc is observed with irradiation. Thanks to EIS, we have unravelled that the surface activation of photochromic dyes accelerates the recombination kinetics in devices leading to loss of charges. Thus, surface isomerization of the dyes creates pathways for triiodide scavengers to reach the TiO_2 surface leading to enhanced recombination and hence lowering the charge collection efficiency. To unravel the impact of photochromism on the recombination, we performed the impedance measurements under different illumination sources i.e. dark, red, blue and then white illumination, in this order, to prevent the activation of the devices in the first two sets of measurements. We considered the **NPI**- and **RK1**-reference devices for this study as shown below.

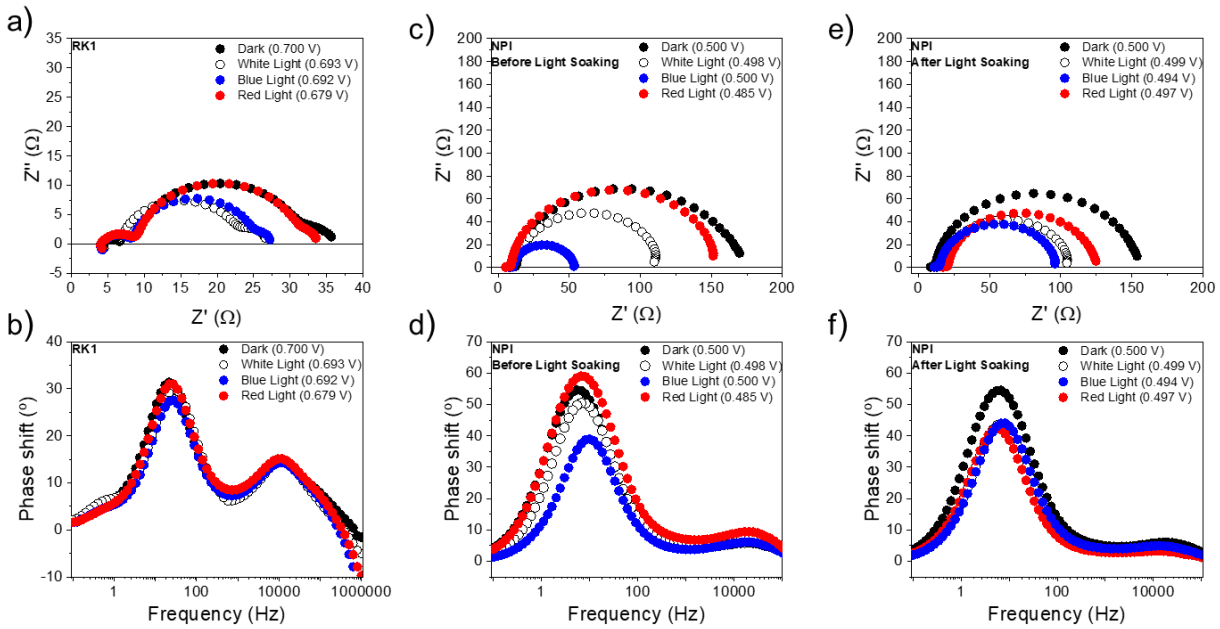

*Figure 2.35 : Nyquists and Bode plots of **RK1** and **NPI**-based cells before and after activation.*

In classical **RK1**-devices, the recombination resistances under different illuminations is as shown in Fig. 2.35 above. The size of the recombination arcs is roughly the recombination resistance. The dark and red illumination show similar diameters. This is so because according to the absorption spectra of **RK1** in solution, the absorbance is zero in the red. This translates to a lower recombination current at the V_{oc} hence lower I_3^- generation. The Bode plots apexes of **RK1**-based cell are similar and do not seem to show dependence on the illumination. This suggests that the wavelength of illumination does not influence the recombination rate.

On the other hand, **NPI**-based cells show closely related behaviour. The recombination arc shrinks in the dark>red>white>blue order. The recombination resistances are more dramatic under blue (465 nm) and white illumination. Blue and white illuminations 'before light soaking – inactive dye' were seen to activate the photochromic cells because the closed **NPI**-dye form absorbs within these wavelengths resulting in a slight to deep green colouration during the measurement, respectively. The impedance under red illumination decreases further when the **NPI**-cell was irradiated to reach a PSS using 1 Sun irradiation under the solar simulator termed 'after light soaking'. This makes it rather cumbersome to compare between the non-activated and activated photochromic devices using a light excitation wavelength where the dye molecules absorb. The impact is more pronounced where blue light impedance apex of the Bode plot is slightly shifted to larger frequencies as compared to dark and red impedance. To understand the impact of blue illumination, we performed impedance restricting ourselves

in the 1-100 Hz frequency range in 5 minutes where the recombination arc appears as shown below.

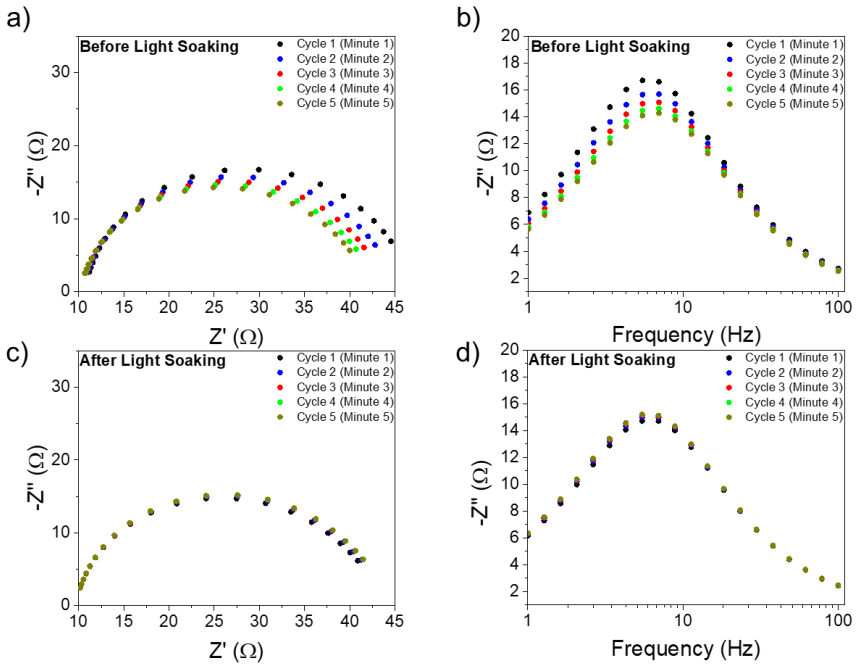

Figure 2.36 : Nyquists plots and Cole-Cole plots of impedance measurements under blue light illumination before (a,b) and after light soaking (c,d) restricted in the 1-100 Hz (extracted from [48]).

In Fig. 2.36 a) we observe that, as a function of time, there is an acceleration of recombination showing how fast the device can be activated. This is so because a shrink in the recombination arc is observed meaning recombination increases. Consequently, a shift to higher frequencies is observed in the Cole-Cole plot (Fig. 2.36 b).

In brief, impedance has demonstrated that in both **RK1** and **NPI** –based devices the chemical capacitances do not depend on the illumination conditions indicating that conduction band edges do not shift. Thus, the activation of the **NPI** dye does not induce a CB shift. Rather, as seen with blue light impedance, the shift to higher frequencies is because of an increased recombination rate. Thus, the drop of the V_{oc} observed for the photochromic dyes devices (see *J(V)* curves) is a kinetic effect, rather as the photochromes under surface isomerization from the closed to the open forms, the triiodide scavengers approximate the TiO_2 surface hence accelerating the recombination rate.

2.2.8 Semi-transparent photochromic solar cells

Semi-transparent solar cells are important for BIPV and their transparency level are vital for the application envisioned. In addition, the interplay between optical and photovoltaic

properties for this new class of dyes with dynamic optical properties is crucial. The self-adaptation of photochromic solar cells' optical properties upon irradiation was analyzed by average visible transmittance (AVT) studies in complete transparent solar cells. The incident photon-to-electron conversion efficiency of the best photochromic dye was also studied as will be shown.

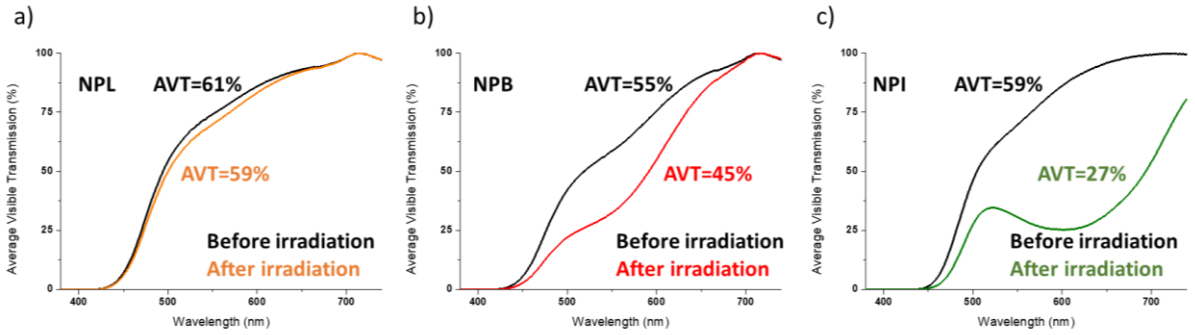

*Figure 2.37 : Transmission spectrum of a complete a) **NPL**, b) **NPB** and c) **NPI**-based 13 µm transparent solar cells in the dark (black curve) with corresponding averaged transmittance (AVT) and after reaching PSS under irradiation.*

The AVTs were calculated within the 380 – 740nm range [63]. The AVTs in the dark for all dyes lie within 55% - 61%. Upon irradiation, **NPL** generates the opened forms but the transmission is less impacted. For example, the AVT between the closed and opened forms varies by 2% in **NPL** (little colour change), 10% in **NPB** and largely in **NPI** by 32% to reach 27% at the PSS (more colouration). The transmission at the absorption maximum for **NPI** could reach <25%. This experiment demonstrates the potential applicability of photochromic DSSCs as they show high visible light transmission of ~60% when the light is off and under light, the solar cells act as protective screens to mitigate the light passing through (shading with up to 27% averaged transmittance at PSS). The photochromic-photovoltaic properties were investigated further to understand the relationship between AVT and PCE as shown below.

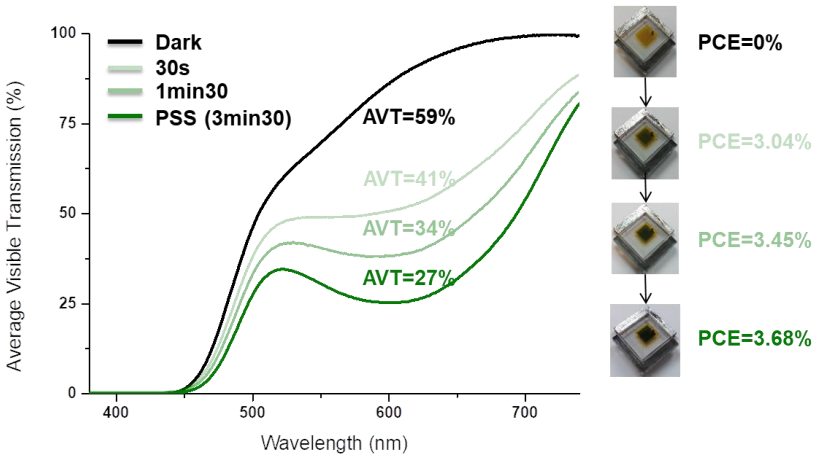

*Figure 2.38 : Transmission spectrum of a complete **NPI**-based 13 µm transparent solar cell in the dark (black curve) with corresponding averaged transmittance (AVT) and the evolution of power conversion efficiencies with irradiation.*

The **NPI**-based device shows a 59% transparency without electricity generation and the cell takes the colour of the iodine-based electrolyte. Upon irradiation, the cells become coloured and the AVT decreases progressively. At the PSS, a PCE of 3.7% is observed marked with deep colouration. This is a proof of concept meaning new photochromic solar cells that can self-adapt their power conversion efficiency and average visible transparency, simultaneously, as a function of irradiation time.

2.2.9 Incident to photon conversion efficiency (IPCE)

These measurements were carried out at the Pablo Olavide University in Seville in Pr. Juan Anta's group by Antonio Riquelme. They were performed under two different states i.e. in the dyes' closed form and opened form using opaque solar cells. To measure the IPCE of the dyes in their closed states, the cells were stored in the dark before measurements. The IPCE was scanned from 800 nm to 300 nm, in this order, to avoid activating the dye and probe the closed configuration only with a 10 nm step. After the dark measurements, the cells were irradiated continuously for 15 minutes under AM 1.5G conditions to ensure that the dyes attain their PSS. The solar cells were placed in position with a 530 nm light beam. The IPCE spectra are as shown below.

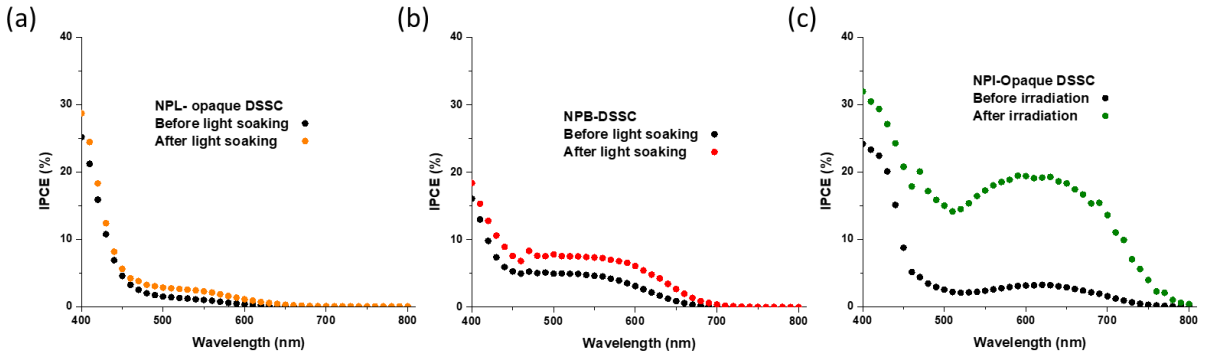

*Figure 2.39 : The incident-to-photon conversion efficiency spectra of the 3 first generation photochromic dyes **NPL**, **NPB** and **NPI** –based solar cells in the closed and opened form configurations.*

From the figure above, the dark measurements curves do not resemble the closed form absorption spectra of the dyes. Rather, an absorption shoulder is observed in the visible that is absent in the spectra in solution. Given that a longer wavelength was used to position the cell, the small activation of the dye could have come from the measurement process itself whereby the instrument scans through the entire UV-Vis range before starting the measurement. As a result, the cells appeared slightly coloured after the wavelength scan in the dark.

After irradiation at the PSS, **NPL** shows the smallest change in the spectra due to poor colouration.

2.2.10 Kinetics in devices

For application of photochromic dyes in solar cells, colouration-discolouration kinetics need to be fast enough to improve the average transparency in the absence of light. Of interest, the ring-closure kinetics were investigated for **NPI**-based devices using transparent 13 µm photoanodes as shown below.

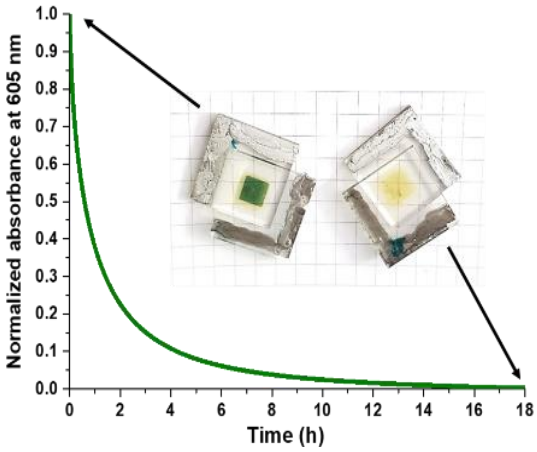

*Figure 2.40 : Themal discolouration kinetics of a complete **NPI**-based device (13 µm thick TiO_2 electrode) registered at the maximum absorption of the opened form.*

The normalized absorption shows that **NPI**-based cell loses 80% and 90% in 2 and 4 hours, respectively, and the remaining stable opened molecules take longer to close leading to nearly complete discolouration in 18 hours.

2.2.11 Device Stability Tests

We applied the ISOS-D1 standard protocol [64,65] to access the stability of photochromic solar cells based on **NPI**. The solar cell was stored in the dark after I-V characterization at the PSS by covering it in an aluminium foil and stored under ambient conditions.

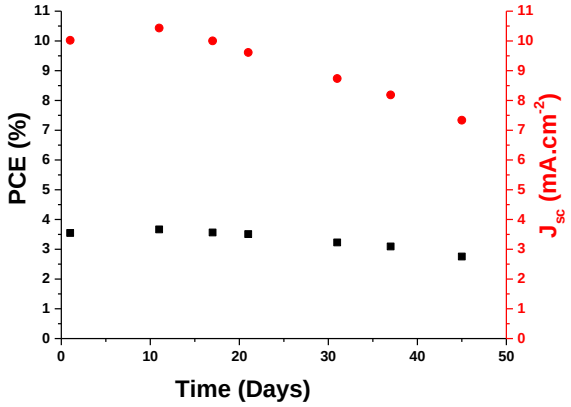

Figure 2.41: Variation of the current density and the power conversion efficiency registered over time from the fabrication up to almost 2 months later.

From the figure above, we observe an increase in the PCE between the first two measurements associated with an increased J_{sc}. This could be due to improved electrolyte penetration in the thick mesoporous TiO_2 via percolation resulting in an improved electrode activation [66]. Thereafter, a seemingly 'linear' decrease in the Jsc was observed followed by a decrease in the PCE to a T_{80} (time for the cell to lose 20% of its initial PCE) of approximately

1080 hours (45 hours). The decreased performances over time was linked to a fading J_{sc} due to evaporation of the volatile electrolyte [67–69] and lack of stabilizers.

2.2.12 Photochromic solar cells degradation

I preserved the photochromic solar cells and re-measured their performances after several months and the images are as shown below.

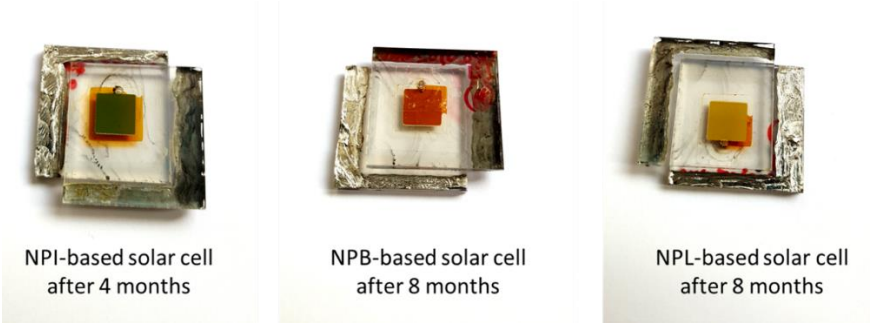

Figure 2.42: First generation degraded photochromic solar cells.

Indeed, the liquid electrolyte evaporation is an issue that is lost either through leakage and/or solvent evaporation despite proper sealing of the cells with the surlyn. The iodide/triiodide electrolyte is known for its corrosive nature hindering long-term stabilities of DSSCs [69]. I took images of a freshly-made and an aged **NPI**-device and the images are as shown below.

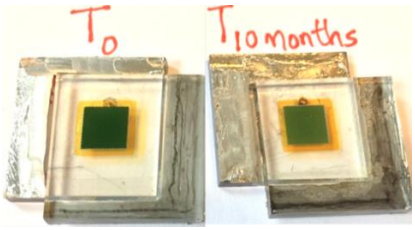

*Figure 2.43 : Images of a freshly-made **NPI**-based opaque solar cell (on the left) and a 10-month old one (right) taken when the cells attained their photostationary state.*

At T_0, the electrolyte is slightly yellowish and darker at T_{10}. The solar cell at T_0 shows a deep green colouration of the dye whereas at T_{10} the cell shows faint green colouration on the photoanode. Eventhough the electrolyte looks darker at T_{10}, it does not change colour with irradiation time thus ruling out the desorption hypothesis. The PCE at T_0 is 4.04% and at T_{10} is 0.80%. Therefore, the diminished colouration and hence efficiency could be as a result of the naphthopyran-based dyes' degradation which was reported previously by Demadrille *et. al* undergoing various degradation pathways in solvents [70]. This is so because opening and refilling the T_{10} cell with a freshly prepared electrolyte could not improve the overall

performance. The best refilled old cell gave a PCE of 0.84% after 15s that kept on decreasing as a function of irradiation time.

2.2.13 Application of NPI in solar mini-modules

In the upscaling from lab solar cells to solar modules, patterning is usually done to mitigate sheet resistance [71]. The different patterning strategies to prevent resistive losses results in different module architectures such as parallel, series monolithic, series Z-type and series W-type connections. The parallel connections suffers from low working potential associated with high generated current hence high power losses. The series connections on the other hand are linked to high photovoltages and reliable power outputs in large area devices under different temperatures and illumination conditions [72].

The best photochromic dye (**NPI**) was applied in large area semi-transparent device to assess their potential for application. Thanks to a collaboration with an industrial partner, Solaronix, Stéphanie Narbey fabricated mini-modules with an overall surface area of 23 cm^2 with an active area of 14.08 cm^2. The electrodes were printed in a five rectangular-shaped single cells interconnected in series via a W-type design as shown below.

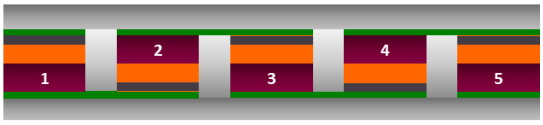

"W" type

Figure 2.44 : Five stripes used in the W-type module architecture. (Maroon: TiO_2+dye, orange: electrolyte, dark grey: platinum, green: TCO)

An 8 um thick mesoporous TiO_2 without a scattering layer was used to allow for good transparency. The optimized home-made electrolyte for photochromic DSSCs was applied to achieve high performance mini-modules.

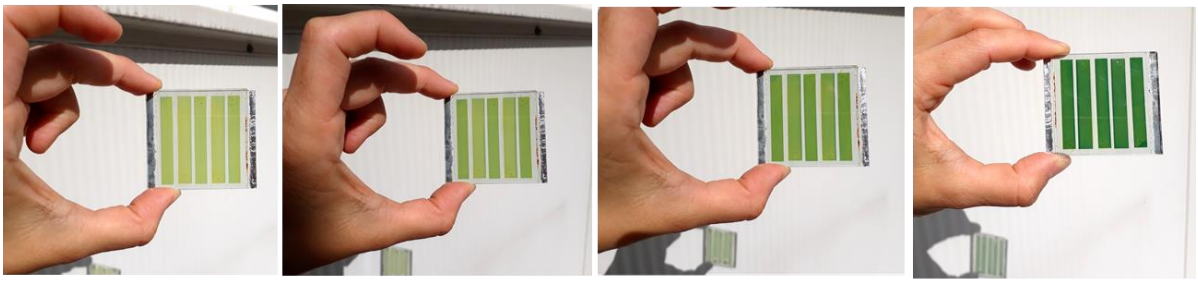

*Figure 2.45 : Progressive colouration of an **NPI**-based mini-module with an active area of 14.08 cm^2 under exposure to Sun at different times.*

The I-V curve registered at 1 Sun is as shown below.

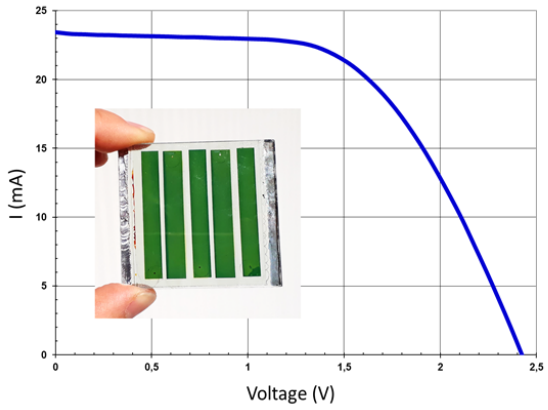

V_{oc}	2.43	[V]
I_{sc}	23.62	[mA]
P_{max}	32.52	[mW]
V_{mpp}	1.608	[V]
I_{mpp}	20.22	[mA]
FF	56.65	[%]
J_{sc}	1.68	[mA.cm^{-2}]
Efficiency	2.31	[%]

*Figure 2.46 : I(V) curve an **NPI**-based mini-module with the corresponding photovoltaic parameters registered at the photostationary state (PSS) under standard illumination conditions AM 1.5G 1000W.m^{-2}, 25°C.*

At the PSS, this mini-module shows a V_{oc} of 2.43 V, an I_{sc} of 23.62 mA and a FF of 56.7 resulting in a maximum power output of 32.5 mW. In comparison to the state-of-the-art mini-modules such as that reported with **YKP88** showing an aesthetic burgundy red tint demonstrates a V_{oc} of 3.63 V, I_{sc} of 58.1 mA, a FF of 58.3 and a power output of 122.9 mW [73], **NPI** is promising in large area surfaces in addition to multifunctional solar cells that can self-regulate their transparency and efficiency.

2.3 Conclusion

In this chapter, we have studied three photochromic dyes denoted **NPL**, **NPB** and **NPI**. Both **NPL** and **NPB** show relatively similar absorption in their closed forms with a maxima around 346 nm. However, upon illumination, these two dyes display different absorption spectra showing orange and reddish colouration, respectively. The absorption spectrum of **NPB** extends a little further in the red compared to **NPL**, absorbing lower-energy photons.

All the three dyes conserved their photochromic properties once incorporated in solar cells.

NPB-based cells are more coloured than **NPL** and due to slower discolouration, they absorb more photons leading to better performance. More chemistry in **NPB** through fusion of the photochromic core to the donor unit via an indeno-fused unit yielded **NPI**. **NPI** emerged the champion dye in this chapter portraying amazing performance due to better activation of the dye's closed form, > 400 nm, generating open forms that show intense and red-shifted

absorption giving deep green colouration. The kinetics of **NPI** are slower than the one of **NPL** and faster than for **NPB** thanks to the bulky indeno-fused moiety. When incorporated in a DSSC configuration, these dyes show an increase in the photocurrent density followed by an intense colouration as a function of irradiation time. Meaning, a new class of dye solar cells capable to self-adapt their transparency levels and energy production as a function of daytime. This was the first example ever of dye solar cells that can self-adapt these properties simultaneously.

But, we identified a challenge where the V_{oc} is lost with irradiation time hindering us from attaining high performance photochromic solar cells. Thanks to impedance spectroscopy, we are able to understand the resistive and capacitive of our system. The chemical capacitances, C_{μ}, of the activated and non-activated **NPI**-based cell remained constant, meaning the V_{oc} loss we observe in the J(V) curves does not come from a shift in the TiO_2 band edge. Rather, from the EIS analysis, the recombination resistances change dramatically when the cell is activated. Thus, the V_{oc} with irradiation time is because of accelerated recombination upon surface isomerization, a kinetic effect. Lastly, we have demonstrated that our photochromic dyes can be applied over a large surface area. This work has been published in a peer review journal ' Huaulmé, Q., Mwalukuku, V.M., Joly, D. *et al.* Photochromic dye-sensitized solar cells with light-driven adjustable optical transmission and power conversion efficiency. *Nat Energy* **5,** 468–477 (2020). https://doi.org/10.1038/s41560-020-0624-7 ' and in 'Riquelme *et al.* Characterization of Photochromic Dye Solar Cells Using Small-signal Perturbation Techniques. *ACS Appl. Energy Mater.* 2021, 4, 9, 8941–8952. https://doi.org/10.1021/acsaem.1c01204 '.

2.4 References

1. Matsuda, K. & Irie, M. Diarylethene as a photoswitching unit. *J. Photochem. Photobiol. C: Photochem. Rev.* **5**, 169–182 (2004).
2. Kim, E., Choi, Y.-K. & Lee, M.-H. Photoinduced Refractive Index Change of a Photochromic Diarylethene Polymer. *Macromolecules* **32**, 4855–4860 (1999).
3. Uchida, K. *et al.* Photoinduced Reversible Formation of Microfibrils on a Photochromic Diarylethene Microcrystalline Surface. *Angew. Chem. Int. Ed.* **45**, 6470–6473 (2006).
4. Irie, M., Kobatake, S. & Horichi, M. Reversible Surface Morphology Changes of a Photochromic Diarylethene Single Crystal by Photoirradiation. *Science* **291**, 1769–1772 (2001).
5. Fukaminato, T., Sasaki, T., Kawai, T., Tamai, N. & Irie, M. Digital Photoswitching of Fluorescence Based on the Photochromism of Diarylethene Derivatives at a Single-Molecule Level. *J. Am. Chem. Soc.* **126**, 14843–14849 (2004).
6. Wu, W. *et al.* A strategy to design novel structure photochromic sensitizers for dye-sensitized solar cells. *Sci Rep* **5**, 8592 (2015).
7. Li, Y., Xu, G., Cui, C. & Li, Y. Flexible and Semitransparent Organic Solar Cells. *Adv. Energy Mater.* **8**, 1701791 (2018).
8. Della Gaspera, E. *et al.* Ultra-thin high efficiency semitransparent perovskite solar cells. *Nano Energy* **13**, 249–257 (2015).
9. Rahmany, S. & Etgar, L. Semitransparent Perovskite Solar Cells. *ACS Energy Lett.* **5**, 1519–1531 (2020).
10. Sun, J. & Jasieniak, J. J. Semi-transparent solar cells. *J. Phys. D: Appl. Phys.* **50**, 093001 (2017).
11. Fihey, A., Perrier, A., Browne, W. R. & Jacquemin, D. Multiphotochromic molecular systems. *Chem. Soc. Rev.* **44**, 3719–3759 (2015).
12. Heinz Durr, Henri Bouas-Laurent. *Photochromism: Molecules and Systems*. (Elsevier, 2003).
13. Barry Van GEMERT. *Organic Photochromic and Thermochromic Compounds*. vol. 1 (John C. Crano, Robert J. Guglielmetti, 1999).
14. N.Y.C. Chu, R. Guglielmetti, Heinz Durr, Henri Bouas-Laurent. *Photochromism: Molecules and Systems: Molecules and Systems*. (Elsevier, 2003).

15. Görner, H. & Chibisov, A. K. Photoprocesses in 2,2-diphenyl-5,6-benzo(2H)chromene. *J. Photochem. Photobiol. A: Chem.* **149**, 83–89 (2002).
16. Zhao, W. & Carreira, E. M. Facile One-Pot Synthesis of Photochromic Pyrans. *Org. Lett.* **5**, 4153–4154 (2003).
17. Frigoli, M., Moustrou, C., Samat, A. & Guglielmetti, R. Synthesis of New Thiophene-Substituted 3,3-Diphenyl-3H-naphtho[2,1-b]pyrans by Cross-Coupling Reactions, Precursors of Photomodulated Materials. *Eur. J. Org. Chem.* **2003**, 2799–2812 (2003).
18. He, D. *et al.* Micro fiber with cladding of titanium dioxide (TiO_2) nanoparticles and its violet light sensing. *Opt. Mater. Express* **7**, 264 (2017).
19. Delbaere, S. *et al.* Kinetic and structural studies of the photochromic process of 3H-naphthopyrans by UV and NMR spectroscopy. *J. Chem. Soc., Perkin Trans. 2* 1153–1158 (1998).
20. Demadrille, R., Rabourdin, A., Campredon, M. & Giusti, G. Spectroscopic characterisation and photodegradation studies of photochromic spiro[fluorene-9,3'-[3'H]-naphtho[2,1-b]pyrans]. *J. Photochem. Photobiol. A: Chem.* **168**, 143–152 (2004).
21. Pandey, S. S., Morimoto, T., Fujikawa, N. & Hayase, S. Combined theoretical and experimental approaches for development of squaraine dyes with small energy barrier for electron injection. *Solar Energy Materials and Solar Cells* **159**, 625–632 (2017).
22. Hamann, T. W., Jensen, R. A., Martinson, A. B. F., Ryswyk, H. V. & Hupp, J. T. Advancing beyond current generation dye-sensitized solar cells. *Eneygy Environ. Sci.*, **1**, 66-78 (2008).
23. Mann, J. R., Gannon, M. K., Fitzgibbons, T. C., Detty, M. R. & Watson, D. F. Optimizing the Photocurrent Efficiency of Dye-Sensitized Solar Cells through the Controlled Aggregation of Chalcogenoxanthylium Dyes on Nanocrystalline Titania Films. *J. Phys. Chem. C* **112**, 13057–13061 (2008).
24. Liu, Y., Hagfeldt, A., Xiao, X.-R. & Lindquist, S.-E. Investigation of influence of redox species on the interfacial energetics of a dye-sensitized nanoporous TiO2 solar cell. *Solar Energy Materials and Solar Cells* **55**, 267–281 (1998).
25. Pelet, S., Moser, J.-E. & Grätzel, M. Cooperative Effect of Adsorbed Cations and Iodide on the Interception of Back Electron Transfer in the Dye Sensitization of Nanocrystalline TiO_2. *J. Phys. Chem. B* **104**, 1791–1795 (2000).

26. Nakade, S. *et al.* Role of Electrolytes on Charge Recombination in Dye-Sensitized TiO_2 Solar Cell (1): The Case of Solar Cells Using the I^-/I_3^- Redox Couple. *J. Phys. Chem. B* **109**, 3480–3487 (2005).
27. Fukui, A., Komiya, R., Yamanaka, R., Islam, A. & Han, L. Effect of a redox electrolyte in mixed solvents on the photovoltaic performance of a dye-sensitized solar cell. *Solar Energy Materials and Solar Cells* **90**, 649–658 (2006).
28. Boschloo, G., Häggman, L. & Hagfeldt, A. Quantification of the Effect of 4-*tert*-Butylpyridine Addition to I^-/I_3^- Redox Electrolytes in Dye-Sensitized Nanostructured TiO_2 Solar Cells. *J. Phys. Chem. B* **110**, 13144–13150 (2006).
29. Boschloo, G. & Hagfeldt, A. Characteristics of the Iodide/Triiodide Redox Mediator in Dye-Sensitized Solar Cells. *Acc. Chem. Res.* **42**, 1819–1826 (2009).
30. Mathew, A. Effect of iodine concentration on the photovoltaic properties of dye sensitized solar cells for various I_2/LiI ratios. *Electrochimica Acta* 5 (2013).
31. Rühle, S. *et al.* Molecular Adjustment of the Electronic Properties of Nanoporous Electrodes in Dye-Sensitized Solar Cells. *J. Phys. Chem. B* **109**, 18907–18913 (2005).
32. Hara, K. *et al.* Effect of Additives on the Photovoltaic Performance of Coumarin-Dye-Sensitized Nanocrystalline TiO_2 Solar Cells. *Langmuir* **20**, 4205–4210 (2004).
33. Gao, J., Prajapati, G. K., Hao, Y. & Kloo, L. Exploring Lewis-Base Effects to Improve the Efficiency of $[Co(bpy)_3]^{2+/3+}$ -Mediated Dye-Sensitized Solar Cells. *ACS Appl. Energy Mater.* **3**, 5705–5711 (2020).
34. Katoh, R. *et al.* Effects of 4- *tert* -Butylpyridine and Li Ions on Photoinduced Electron Injection Efficiency in Black-Dye-Sensitized Nanocrystalline TiO_2 Films. *J. Phys. Chem. C* **113**, 20738–20744 (2009).
35. Zhang, C., Huang, Y., Huo, Z., Chen, S. & Dai, S. Photoelectrochemical Effects of Guanidinium Thiocyanate on Dye-Sensitized Solar Cell Performance and Stability. *J. Phys. Chem. C* **113**, 21779–21783 (2009).
36. Ruhane, T. A. *et al.* Impact of photo electrode thickness and annealing temperature on natural dye sensitized solar cell. *Sustainable Energy Technologies and Assessments* **20**, 72–77 (2017).
37. Ni, M., Leung, M. K. H. & Leung, D. Y. C. Theoretical modelling of the electrode thickness effect on maximum power point of dye-sensitized solar cell. *Can. J. Chem. Eng.* **86**, 35–42 (2008).

38. Mathew, A., Rao, G. M. & Munichandraiah, N. Effect of TiO_2 electrode thickness on photovoltaic properties of dye sensitized solar cell based on randomly oriented Titania nanotubes. *Materials Chemistry and Physics* **127**, 95–101 (2011).
39. Ito, S. *et al.* High-Efficiency Organic-Dye- Sensitized Solar Cells Controlled by Nanocrystalline-TiO2 Electrode Thickness. *Adv. Mater.* **18**, 1202–1205 (2006).
40. Wang, Z.-S., Kawauchi, H., Kashima, T. & Arakawa, H. Significant influence of TiO_2 photoelectrode morphology on the energy conversion efficiency of N719 dye-sensitized solar cell. *Coord. Chem. Rev.,* **248**, 1381–1389 (2004).
41. Katoh, R., Furube, A., Barzykin, A. V., Arakawa, H. & Tachiya, M. Kinetics and mechanism of electron injection and charge recombination in dye-sensitized nanocrystalline semiconductors. *Coord. Chem. Rev.,* **248**, 1195–1213 (2004).
42. Huaulmé, Q. *et al.* Photochromic dye-sensitized solar cells with light-driven adjustable optical transmission and power conversion efficiency. *Nat Energy* **5**, 468–477 (2020).
43. Pandey, S. S., Sakaguchi, S., Yamaguchi, Y. & Hayase, S. Influence of nature of surface dipoles on observed photovoltage in dye-sensitized solar cells as probed by surface potential measurement. *Organic Electronics* **11**, 419–426 (2010).
44. Chen, P. *et al.* High Open-Circuit Voltage Solid-State Dye-Sensitized Solar Cells with Organic Dye. *Nano Lett.* **9**, 2487–2492 (2009).
45. Liu, B. *et al.* Photovoltaic performance of solid-state DSSCs sensitized with organic isophorone dyes: Effect of dye-loaded amount and dipole moment. *Dyes and Pigments* **94**, 23–27 (2012).
46. Fabregat-Santiago, F., Garcia-Belmonte, G., Mora-Seró, I. & Bisquert, J. Characterization of nanostructured hybrid and organic solar cells by impedance spectroscopy. *Phys. Chem. Chem. Phys.* **13**, 9083–9118 (2011).
47. Idígoras, J. *et al.* Highly efficient flexible cathodes for dye sensitized solar cells to complement Pt@TCO coatings. *J. Mater. Chem. A* **2**, 3175–3181 (2014).
48. Riquelme, A. J. *et al.* Characterization of Photochromic Dye Solar Cells Using Small-Signal Perturbation Techniques. *ACS Appl. Energy Mater.* **4**, 8941–8952 (2021).
49. Xie, Y. *et al.* Electrolyte Effects on Electron Transport and Recombination at ZnO Nanorods for Dye-Sensitized Solar Cells. *J. Phys. Chem. C* **114**, 17880–17888 (2010).

50. Hoshikawa, T., Ikebe, T., Kikuchi, R. & Eguchi, K. Effects of electrolyte in dye-sensitized solar cells and evaluation by impedance spectroscopy. *Electrochimica Acta* **51**, 5286–5294 (2006).
51. Wang, Q., Moser, J.-E. & Grätzel, M. Electrochemical Impedance Spectroscopic Analysis of Dye-Sensitized Solar Cells. *J. Phys. Chem. B* **109**, 14945–14953 (2005).
52. Wang, Q. *et al.* Characteristics of High Efficiency Dye-Sensitized Solar Cells. *J. Phys. Chem. B* **110**, 25210–25221 (2006).
53. Bisquert, J. Theory of the Impedance of Electron Diffusion and Recombination in a Thin Layer. *J. Phys. Chem. B* **106**, 325–333 (2002).
54. Anta, J. A. *et al.* A continuity equation for the simulation of the current–voltage curve and the time-dependent properties of dye-sensitized solar cells. *Phys. Chem. Chem. Phys.* **14**, 10285 (2012).
55. Guillén, E., Peter, L. M. & Anta, J. A. Electron Transport and Recombination in ZnO-Based Dye-Sensitized Solar Cells. *J. Phys. Chem. C* **115**, 22622–22632 (2011).
56. Raga, S. R., Barea, E. M. & Fabregat-Santiago, F. Analysis of the Origin of Open Circuit Voltage in Dye Solar Cells. *J. Phys. Chem. Lett.* **3**, 1629–1634 (2012).
57. Bisquert, J., Zaban, A. & Salvador, P. Analysis of the Mechanisms of Electron Recombination in Nanoporous TiO_2 Dye-Sensitized Solar Cells. Nonequilibrium Steady-State Statistics and Interfacial Electron Transfer via Surface States. *J. Phys. Chem. B* **106**, 8774–8782 (2002).
58. Bisquert, J. & Mora-Seró, I. Simulation of Steady-State Characteristics of Dye-Sensitized Solar Cells and the Interpretation of the Diffusion Length. *J. Phys. Chem. Lett.* **1**, 450–456 (2010).
59. Bisquert, J. Chemical capacitance of nanostructured semiconductors: its origin and significance for nanocomposite solar cells. *Phys. Chem. Chem. Phys.* **5**, 5360 (2003).
60. Fisher, A. C., Peter, L. M., Ponomarev, E. A., Walker, A. B. & Wijayantha, K. G. U. Intensity Dependence of the Back Reaction and Transport of Electrons in Dye-Sensitized Nanocrystalline TiO_2 Solar Cells. *J. Phys. Chem. B* **104**, 949–958 (2000).
61. Walker, A. B., Peter, L. M., Lobato, K. & Cameron, P. J. Analysis of Photovoltage Decay Transients in Dye-Sensitized Solar Cells. *J. Phys. Chem. B* **110**, 25504–25507 (2006).

62. Villanueva-Cab, J., Wang, H., Oskam, G. & Peter, L. M. Electron Diffusion and Back Reaction in Dye-Sensitized Solar Cells: The Effect of Nonlinear Recombination Kinetics. *J. Phys. Chem. Lett.* **1**, 748–751 (2010).
63. Ma, X. *et al.* Simultaneously improved efficiency and average visible transmittance of semitransparent polymer solar cells with two ultra-narrow bandgap nonfullerene acceptors. *J. Mater. Chem. A* **6**, 21485–21492 (2018).
64. Khenkin, M. V. *et al.* Consensus statement for stability assessment and reporting for perovskite photovoltaics based on ISOS procedures. *Nat Energy* **5**, 35–49 (2020).
65. Reese, M. O. *et al.* Consensus stability testing protocols for organic photovoltaic materials and devices. *Solar Energy Materials and Solar Cells* **95**, 1253–1267 (2011).
66. Zhang, Z., Ito, S., Moser, J.-E., Zakeeruddin, S. M. & Grätzel, M. Influence of Iodide Concentration on the Efficiency and Stability of Dye-Sensitized Solar Cell Containing Non-Volatile Electrolyte. *ChemPhysChem.* **10**, 1834–1838 (2009).
67. Kim, J. H. *et al.* 6.16% Efficiency of Solid-State Fiber Dye-Sensitized Solar Cells Based on LiTFSI Electrolytes with Novel TEMPOL Derivatives. *ACS Sustainable Chem. Eng.* **8**, 15065–15071 (2020).
68. Raut, P., Kishnani, V., Mondal, K., Gupta, A. & Jana, S. C. A Review on Gel Polymer Electrolytes for Dye-Sensitized Solar Cells. *Micromachines* **13**, 680 (2022).
69. Toivola, M., Ahlskog, F. & Lund, P. Industrial sheet metals for nanocrystalline dye-sensitized solar cell structures. *Solar Energy Materials and Solar Cells* **90**, 2881–2893 (2006).
70. Demadrille, R., Rabourdin, A., Campredon, M. & Giusti, G. Spectroscopic characterisation and photodegradation studies of photochromic spiro[fluorene-9,3'-[3'H]-naphtho[2,1-b]pyrans]. *J. Photochem. Photobiol. A: Chem.* **168**, 143–152 (2004).
71. Mariani, P. *et al.* Graphene-Based Interconnects for Stable Dye-Sensitized Solar Modules. *ACS Appl. Energy Mater.* **4**, 98–110 (2021).
72. Barichello, J. *et al.* Stable Semi-Transparent Dye-Sensitized Solar Modules and Panels for Greenhouse Application. *Energies* **14**, 6393 (2021).
73. Godfroy, M. *et al.* Benzothiadiazole-based photosensitizers for efficient and stable dye-sensitized solar cells and 8.7% efficiency semi-transparent mini-modules. *Sustainable Energy Fuels* **5**, 144–153 (2021).

CHAPTER 3 : Chemical Structure-Property Relationships (NPseries)

Abstract

Thanks to my work on the first generation of photochromic dyes, photochromic solar cells have made progress surpassing the 4% barrier. Among the best performing devices, are those based on **NPI** photochrome. In this chapter, based on the understanding with the first generation photochromic dye solar cells, I explore modifications of **NPI**'s molecular structure via molecular engineering to establish structure-property relationships for this new family of molecules. Cosensitization approach is also explored and photoanode chemical treatment and surface functionalization have been applied. Small signal perturbation techniques such as impedance spectroscopy is employed to understand the operation in devices.

3.1 NPseries photochromes family

3.1.1 Introduction and Objectives

In Chapter 2, I synthesized a dye, characterized and optimized the fabrication conditions of the photochromic dyes in solar cells. The champion **NPI** dye registered a power conversion efficiency (PCE) of 4.17% translating to the highest efficiency ever obtained for photochromic solar cells at that time [1]. From its skeleton, thanks to chemists I worked with Dr. Johan Liotier, Dr. Quentin Huaulmé and PhD student Samuel Fauvel, we have proposed and made different structural modifications based on **NPI** backbone thus forming a generational terminology called **NPseries**.

NPI, as already seen, has an extended pi-conjugated photochromic unit via the indeno-fused moiety fusion, essential to shift the absorption spectrum of the closed form above 400 nm. This resulted in an intense and red-shifted absorption of the open form giving a deep green colouration hence better photosensitization of the photoanode at the photostationary state (PSS). Shifting the closed form spectra > 400 nm also limited the screening effect from TiO_2 thus activating photochromism with low energy photons hence improving closed form (CF) absorption. However, the first generation photochromic solar cells were associated with low photovoltages and a V_{oc} loss linked to the recombination kinetics reason. The devices were also characterized with a retarded discolouration due to a rather slow ring closure kinetic of the dye [1].

In the literature, Koumura N. *et. al* reported alkyl-functionalized organic dyes through structural engineering of the donor, linker and acceptor building units independently. In their

dyes (**MK-1** and **MK-2**), they substituted n-hexyl groups at the oligothiophene linker with the goal to prevent the acceptors (I_3^-) from approaching either the dye cation or the TiO_2 surface. When they incorporated these dyes in a DSSC layout, higher V_{oc}s were reported with longer alkyl chains as compared to without. They associated this observation to increased electronic lifetime in the TiO_2 conduction band (CB) due to reduced recombination [2]. **YC** sensitizers possessing long alkyl chains on all the building block units, have also been reported to attain efficiencies up to 10.5% linked to decreased dye aggregation thus improving electronic injection [3].

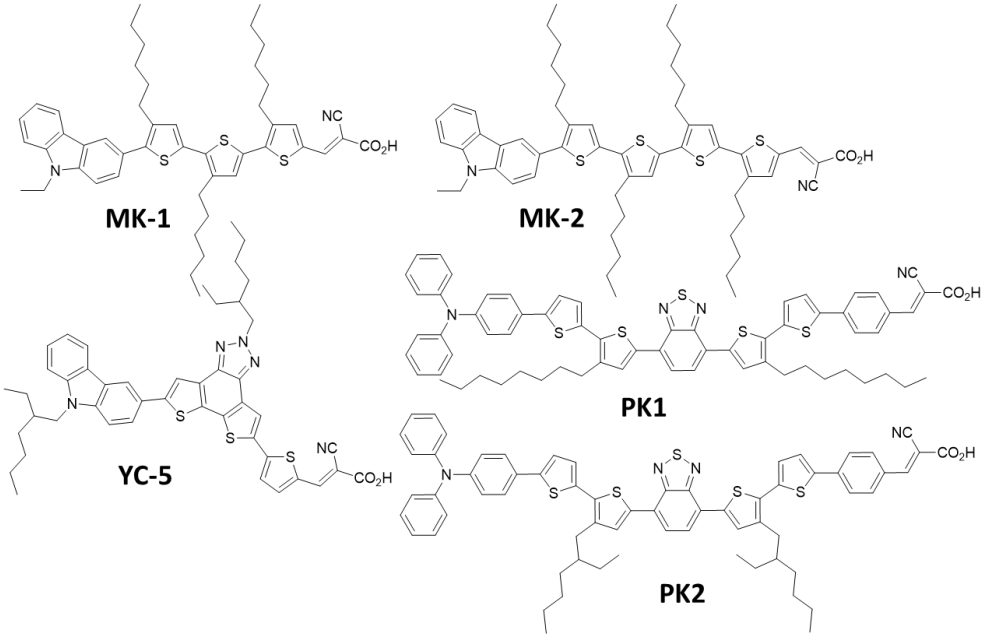

*Figure 3.1 : Molecular structures of **MK-1**, **MK-2**, **YC-5**, **PK1** and **PK2** sensitizers.*

Our group has also reported on side chain engineering of classic organic sensitizers for dye-sensitized solar cells as a strategy to boost the perfomances and stabilities. Dyes **PK1** and **PK2** do not only have improved solubility in solution but also good photovoltaic performances thanks to the bulky substituents that helped boost performances upto 9.05% using a liquid electrolyte. The improvement in the performances was explained from the charge extraction and transient photovoltage measurements as a result of increased electron lifetimes [4–6].

Concerning photochromism, Malic N. *et. al* developed a novel conjugate architecture consisting a photochromic dye covalently linked to a hetero-functionalized Y-branching linker with the goal to increase both the colouration and the discolouration kinetics within the rigid

polymer lens matrix. In this work, they covalently attached soft polymers on spirooxazine and naphthopyran compounds to allow fast photochromic switching.

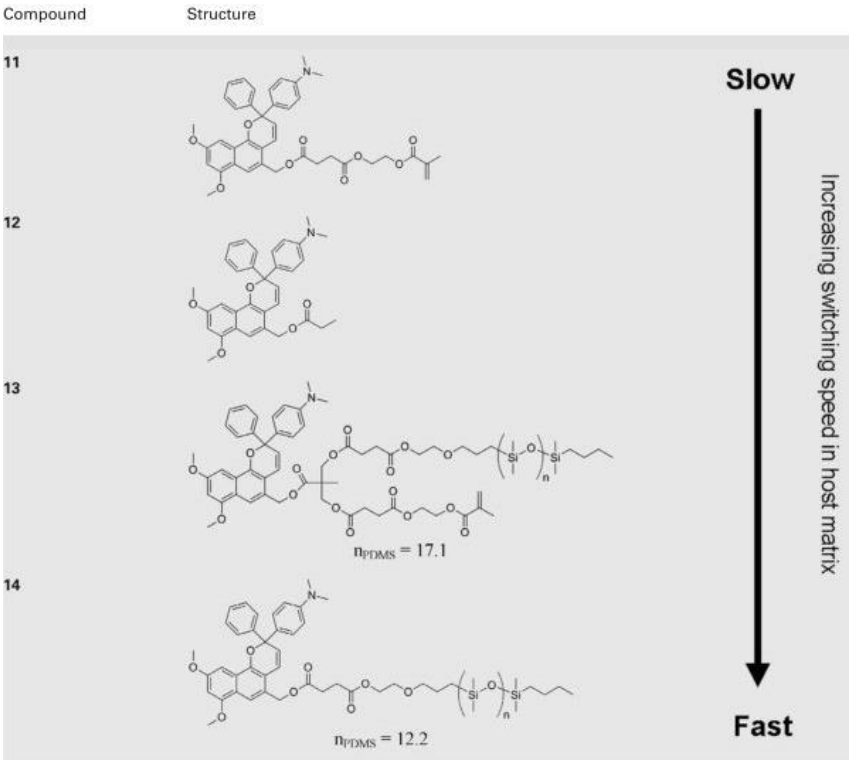

Figure 3.2 : Naphthopyran-functionalized conjugates and control compounds (with permission from [7]).

The result of this work was an increased switching speed in the host matrix as a function of the polymer length. The spectrokinetic data was fit to an empirical biexponential equation (presented in **Chapter 2**). From the fitting, the k_1 and k_2 rate constants for the fast and slow processes, respectively, followed an increasing trend. The corresponding absorbances at a given time, A_1 increased as A_2 decreased demonstrating that the decolouration process was moving towards a monoexponential decay fashion as the fading speed inceased with polymer length [7].

In this respect, with an understanding of the interfacial processes i.e. semiconductor/dye/electrolyte interface, bulky substituents employed in classical photosensitizers were added onto the **NPI** skeleton. Thanks to impedance spectroscopy performed on the 1st generation, the limiting process to high performance cells is due to an accelerated recombination due to dye's isomerization on the TiO_2 surface as demonstrated in the previous Chapter. Therefore, to decrease the recombination rate, we have employed our group's expertise in chemical engineering by introducing bulky substituents and/or long

hydrophobic alkyl chains either on the photochromic core or on the TPA-based donor with the goal to cushion the TiO_2 from I_3^- that is responsible for an increase in recombination [8,9]. I also ventured into the murky synthetic world of designing new photochromic molecules with other chemists that I have already mentioned to either slow recombination and improve photovoltaic (PV) performance and/or improve the kinetics for application leading to **NP1**-**NP6** series as listed in the next sub-section.

Thus, the objectives of this chapter are :

- To prevent the V_{oc} loss by passivating the TiO_2 surface to decrease recombination.
- To improve the PV performances of photochromic solar cells
- To improve the discolouration kinetics of devices.
- To understand how the modifications of the chemical structure impact the interfacial electronic processes at the TiO_2/dye/electrolyte interface.

We have tried to answer these objectives through chemistry on **NPI** as shown below :

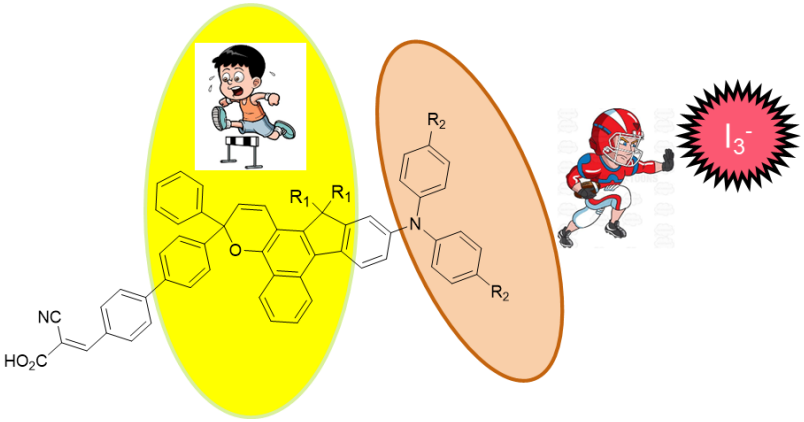

*Figure 3.3 : Possible structural modification on champion **NPI** dye.*

By adding bulky substituents either on the photochromic core or the electron-rich unit, **NP**series is born. Chemistries on the photochrome core is expected to affect the discolouration kinetics whereas that on the electron-donating part to act as a shield.

3.1.2 Presentation of NPseries dyes

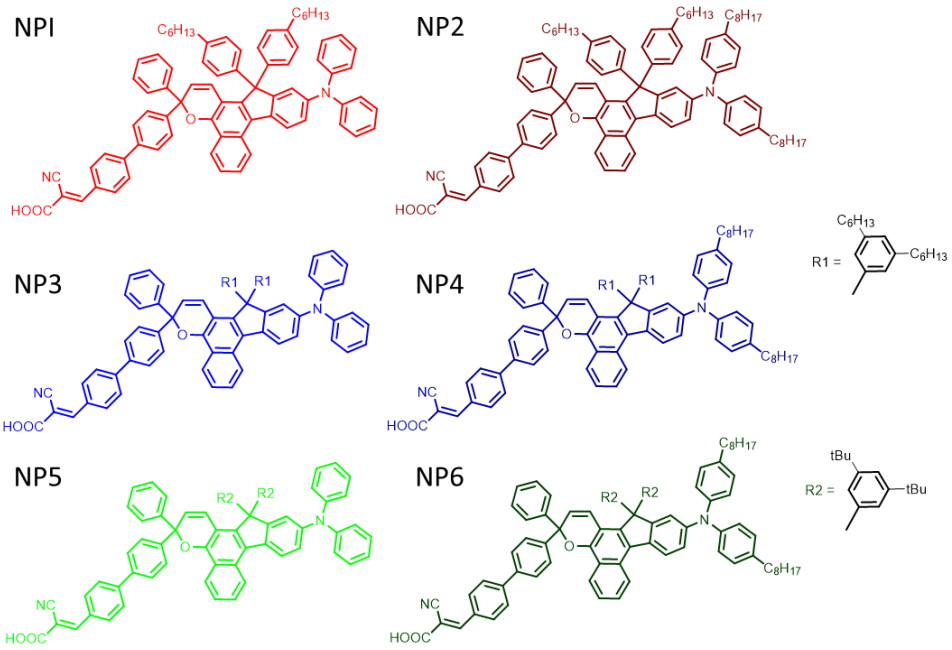

*Figure 3.4 : Chemical structures of the **NP**series dyes in their closed form configurations.*

As shown above, **NP2** was inspired by **NPI** dye. The only difference being the introduction of C_8 chains at the periphery of DPA donor unit. The purpose of the chains has been reported in normal dyes to cushion the TiO_2 from the oxidized species in the electrolyte [10]. **NP3** and **NP5** with an additional C_6 and *t*-Bu chain on the π-spacer, respectively, with reference to **NPI** was intended to improve on the discolouration kinetics. **NP4** and **NP6** bearing alkyl chains as **NP3** and **NP5**, respectively, with additional C_8 chain on the donating part to improve both the kinetics and cut recombination routes. To sum up, this chapter focuses on the investigation of similar alkyl chain length effects at the terminal or within the molecule on the photovoltaic performance and photochromic properties of devices under same processing conditions.

3.1.3 Synthesis of NP2

Among these **NP**series dyes, I was able to synthesize **NP2** in a similar fashion as **NPI** in chapter 2. The synthetic route is the same with a slight difference in the reactants.

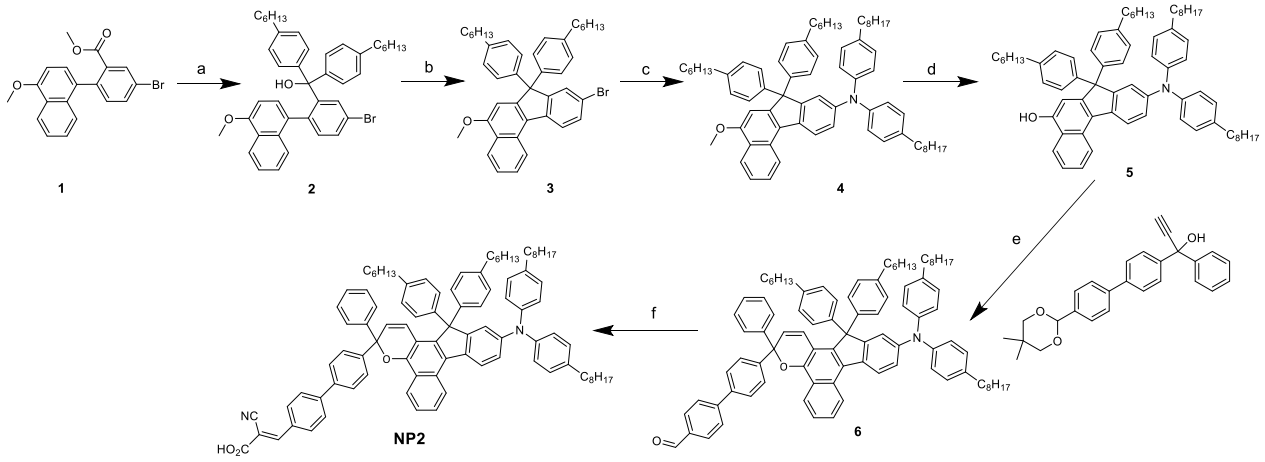

*Figure 3.5 : Synthetic pathway of **NP2** dye. The experimental conditions for steps : a) bromo-hexylphenyl, n-BuLi, THF, -95°C b) $BF_3.OEt_2$, DCM, 0°C-RT c) bis-alkylated diphenylamine, $Pd_2(dba)_3$, HP^tBuBF_4 (phosphine), tBuOK, toluene, 110°C d) BBr_3, DCM, 0°C-RT e) PPTS, trimethylorthoformate, DCE, 70°C, $TBAPF_6$ f) cyanoacetic acid, NH_4OAc, Toluene, 90°C.*

The starting material, brominated naphth-2-ol ester derivative (**1**), has a methoxy group protection to prevent the formation of a naphthoquinone and allow use of n-BuLi. Step(a) involves a double nucleophilic attack on the ester derivative to give a tertiary alcohol (**2**) (yield= 85%). Step (b) is an intramolecular Friedel Craft reaction (yield=81%). Step (c) involves the insertion of the electron-donating bis-alkylated diphenylamine (DPA) unit via a Buchwald cross-coupling reaction (yield=78%). Step (d) is a demethylation reaction to obtain the alcohol by reaction with BBr_3 (yield=88%). Step (*e*) is the most critical step is one that involves the formation of the photochromic naphthopyran ring through chromenisation reaction (yield=53%). This is achieved via a coupling between the 2-naphthol derivative and a propargylic alcohol catalyzed by pyridinium para-toluene sulfonate (PPTS) in slightly acidic conditions to decrease the degradation of propargylic alcohol. A 3-step reaction that involves dehydration, addition and finally C-C coupling via a Claisen condensation reaction then a proton shift leading to the formation of the photochromic unit. Lastly, step (f) involves a Knoevenagel reaction that attaches the anchoring group to give **NP2** (yield=63%).

3.1.4 Optoelectronic Characterization

3.1.4.1 UV-Vis absorption

All the 6 **NP** dyes demonstrate a reversible chemical transformation between the closed form (yellowish) in the dark and the open forms (greenish) under illumination via the C-O bond breaking.

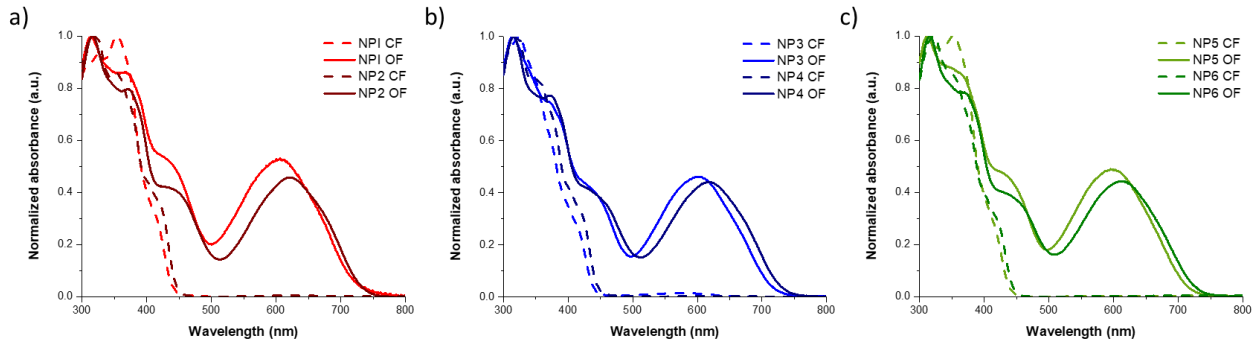

*Figure 3.6 : Absorption spectra of a) **NPI** and **NP2**, b) **NP3** and **NP4** and c) **NP5** and **NP6** in their closed forms (dotted curves) and open forms (solid curves) at 25°C, 10^{-5} M (irradiation conditions : 200W Xenon lamp, 350-425 nm filter) in toluene.*

The optical parameters of the 6 dyes are as listed in the table below,

Dye	λ_{max} CF (nm)	λ_{onset} CF (nm)	ε CF ($mol.L^{-1}.cm^{-1}$)	λ_{max} OF (nm)	λ_{onset} OF (nm)	ΔE_{opt} OF (eV)
NPI	318	450	41,800	605	728	1.70
NP2	320	450	43,790	620	730	1.70
NP3	324	450	35,320	603	716	1.73
NP4	319	450	38,760	617	730	1.70
NP5	323	450	42,310	597	716	1.73
NP6	322	450	40,270	614	729	1.70

The closed form spectra of all dyes are comparable. Fig. 3.6 above shows shifted absorption of the **NP**s closed forms (CF) (>400 nm) making it possible to induce photochromism using low energy photons, thus evading the screening effect of TiO_2. From the absorption spectra of the CF of the dyes in solution, it can be concluded that the introduction of alkyl groups on various positions of the photochromic dye have a minor influence on their absorption. The absorption edge is around 450 nm for all dyes. The introduction of C_8 alkyl chains on the periphery shifts the absorption edge a bit. **NP2** shows the highest molar absorption coefficient of 43,790 $mol.L^{-1}.cm^{-1}$ in the dark.

When the dyes are irradiated, the absorption spectra of the opened forms (OF) reveal two types of transitions. The peaks <500 nm likely correspond to π- π* transitions arising from conjugation within the molecule. The intense bands >500 nm translate to the internal charge transfer (ICT) transitions in the opened forms. Minor variations are observed corresponding to electronic or steric effects of the OF. The absorption onsets of all dyes are within the 716 – 730 nm range. Thus, the optical bandgaps of the OFs are quasi-similar around 1.70 eV.

3.1.4.2 Kinetics in solution

The closed forms of the dye molecules were irradiated until the photostationary state was attained and the decolouration kinetics were registered in solution (in the dark) and modelled using the equation below.

$$A(t) = a_1 e^{-k_0 t} + A_\infty$$

$$A(t) = a_1 e^{-k_1 t} + a_2 e^{-k_2 t} + A_\infty$$

The discolouration spectra are as shown below,

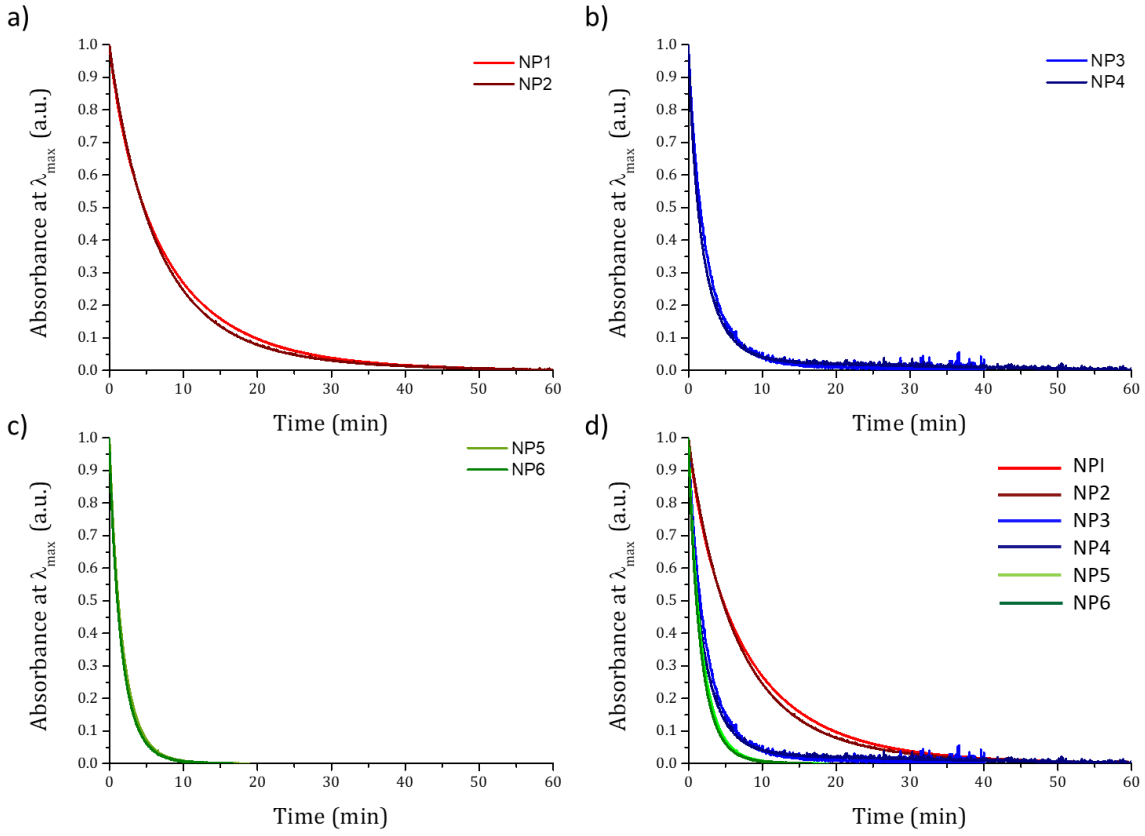

Figure 3.7 : Normalized discolouration kinetics of NPI-NP6 with comparisons. Conditions 25°C, PhMe and 10^{-5} M.

These spectra were modelled using the above equation where, $A(t)$ is the absorbance of the matrix, k_n is the thermal decolouration kinetic constant (in s^{-1}) of the n^{th} kinetic process, a_n the amplitude of the kinetics of this process, and A_∞ the residual absorbance. The extracted values are as shown below.

Table 3.1 : Extracted values from discolouration curve after fitting to equation above.

Dye	A_0	k (s^{-1})
NPI	0.38	2.1×10^{-3}
NP2	0.38	2.3×10^{-3}
NP3	0.38	6.3×10^{-3}
NP4	0.38	7.3×10^{-3}
NP5	0.38	8.9×10^{-3}
NP6	0.38	9.7×10^{-3}

The effect of the substitution with alkyl groups on the thermal kinetics of decolouration is more significant than on the absorption spectra. All the discolouration curves were fit to a monoexponential decay. First, comparing **NPI** and **NP2** we can see that the C_8 alkyl chains on the periphery accelerate a bit the thermal decolouration. **NP3** and **NP4** show comparable discolouration kinetics suggesting that the addition of bulky groups on the photochromic core contribute more on the fading than on the electron-donating TPA unit. More strikingly, the kinetics are accelerated with increasing the bulkiness of the substituents on the indene group as shown in Fig. 3.7d. Indeed, **NPI** and **NP2** have comparable first discolouration constant, **NP3** and **NP4** discolour three times faster compared to **NPI** and finally between 4-5 times faster in **NP5** and **NP6** dyes. These results prove that the strategy to increase the bulkiness of the substituents attached on the indeno units is powerful and efficient to control the kinetics of decolouration.

3.1.5 Energetic level determination for NPseries

Next, the HOMO-LUMO levels of the **NP**series dyes were estimated in solution to check whether their positioning match DSSC components for electron transfers. The cyclic voltammetry carried out gave values as shown in the figure below.

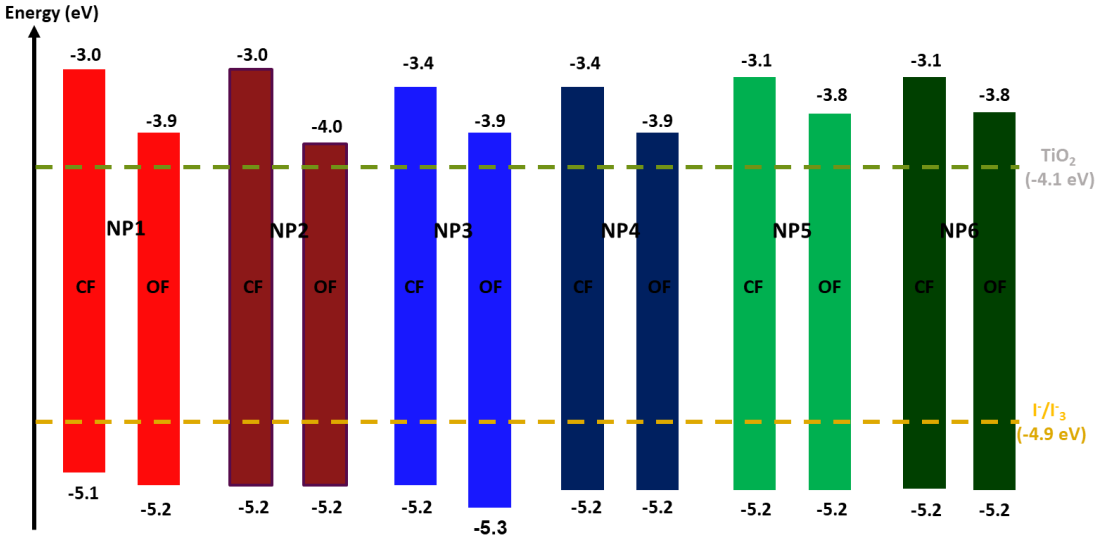

*Figure 3.8 : Frontier orbitals of **NPI-NP6** dyes showing their positions with reference to the vacuum level (0 eV) of both the open and the closed forms. TiO_2 conduction band and the redox couple potential have been included to check whether they match.*

The HOMO values of these dyes lie between -5.1 eV and -5.3 eV which are sufficiently high enough to allow for the dyes regeneration process by the I_3^-/I^- redox couple (-4.9 eV). The LUMO levels are slightly higher, sufficiently high enough to allow the electronic transfer into the conduction band energy level of TiO_2 metal oxide (-4.1 eV). For all the **NP**series dyes, the LUMO levels of the opened forms are more lowly positioned with respect to the closed form. The injection efficiency is expected to slow with isomerization and their HOMO levels remain quasi identical after isomerization. Nevertheless, their energetic positions in all conformations remain favorable to work in a DSSC configuration.

Hereafter, having understood the optoelectronic properties, I will report the optimizations done, the effect of these bulky substituents and thereafter, the different approaches investigated to decrease the back electron transfer (BET) and improving the electron injection into the TiO_2 CB to win high efficiencies.

3.1.6 Chemical structure-property relationship

3.1.6.1 I-V characterization - CDCA optimization of **NP**series

As already mentioned in Chapter 1, dye adsorption on DSSCs alone could result in unfavourable aggregation on TiO_2 surface leading to the formation of aggregates prone to quench the excited state thus lowering the performance [11–13]. Thus, CDCA co-adsorbant is useful to prevent undesirable aggregation. The amount of CDCA in the dyeing bath is equally

important. For instance, the more CDCA there is, the less photosensitizing dye molecules will be anchored and vice-versa is true but an optimum ratio is best.

Despite the bulkiness of the new dyes, I thought important to optimize the amount of chenodeoxycholic acid used as a coadsorber in device manufacturing. The results are as reported below.

*Table 3.2 : Effect of varying CDCA concentration in the dyeing bath on the photovoltaic parameters using **NPI-NP6** dyes. Opaque electrodes (13 + 4 µm) of the same batch were used for optimization. The values in red are the optimum values.*

Dye	CDCA ratio	Jsc ($mA.cm^{-2}$)	Voc (V)	FF	PCE (%)
NPI	0	8.40	0.564	0.74	3.54
	5	11.04	0.535	0.65	3.89
	10	**12.59**	**0.505**	**0.65**	**4.17**
NP2	0	10.79	0.480	0.64	3.36
	5	**12.74**	**0.502**	**0.64**	**4.16**
	10	11.21	0.480	0.67	3.65
NP3	0	3.43	0.530	0.68	1.25
	5	**5.67**	**0.561**	**0.72**	**2.32**
	10	4.60	0.483	0.66	1.49
NP4	0	9.38	0.531	0.69	3.44
	5	**9.77**	**0.546**	**0.71**	**3.82**
	10	9.44	0.544	0.72	3.73
NP5	0	6.02	0.545	0.71	2.36
	5	**6.23**	**0.550**	**0.73**	**2.50**
	10	3.82	0.609	0.78	1.81
NP6	0	4.83	0.554	0.72	1.95
	5	4.71	0.592	0.77	2.17
	10	**6.13**	**0.579**	**0.77**	**2.75**

The table above shows the role played by chenodeoxycholic acid (CDCA) on the PV performances of photochromic DSSCs. When electrodes are sensitized without CDCA, the dyes tend to aggregate on the TiO_2 surface leading to low performances due to a lower J_{sc}.

Chenodeoxycholic acid (CDCA) has been used to mitigate dyes' aggregation in solar cells. Such is manifested when **NPI** dye is employed in solar cells. With a ratio of 10 CDCA, the current density is slightly higher by 1 mA/cm^2 as compared to when the content ration was decreased to 5. This suggests that by decreasing CDCA concentration, the dyes encroach towards each other during anchorage leading to unfavourable aggregation thus lowering the J_{sc}.

NP5-based solar cells with 0 CDCA show comparable performances with respect to one with **NP5**:10 CDCA suggesting that the two side tert-butyl chains on the π-spacer help to prevent the formation of aggregates while not being completely efficient.

For dyes **NP2**-**NP5**, the optimal dye:CDCA ratio obtained is dye:5 CDCA whereas that of **NP6** is surprisingly high (dye:10 CDCA). Even though the amount of dye adsorbed on TiO_2 decreases with CDCA adsorption, better photocurrents and photovoltages of solar cells were recorded. The better V_{oc}'s with CDCA could be as a result of better protection of TiO_2 surface from the oxidized redox couple in the electrolyte by occupying the vacant sites in between dyes hence passivation [14,15]. As the amount of CDCA was increased beyond the optimized ratio, a decrease in the photocurrent was observed accompanied by low conversion efficiencies due to probably more sites occupied by the CDCA, instead of the photosensitizing dye, that is not a light harvester in the visible range. On the other side, V_{oc} increased with higher CDCA ratios due to better surface passivation of TiO_2 surface [16]. The **NP**series results presented hereafter are those with the best CDCA conditions and the varying CDCA in **NPI** and **NP6** are reported for comparison.

3.1.6.2 Optimized **NP**series – Photovoltaic Characterization

The PV performance of **NP**series was evaluated after incorporation in a DSSC layout. Using the best dyeing conditions obtained above coupled with the already optimized electrolyte composition as reported in previous work [1] and chapter 2, i.e. 90 mM I_2 and 0.5M LiI in a low viscosity acetonitrile, were used to obtain highly efficient photochromic DSSCs. The current-voltage characteristics were registered in the dark and at different time intervals and the PV parameters extracted from the *I(V)* curves. The results with the dyes are as reported below where the first column for each dye, either based on opaque or transparent cells, presents the best device followed by their statistics in parentheses done on at least 3 devices. The table below summarizes the PV performances for **NPI**-**NP6**.

*Table 3.3 : Solar cell characterizations of opaque (13 µm mesoporous + 3 µm scattering layer) and transparent (13 µm mesoporous) for **NP**series-based cells with their respective amounts of dye adsorbed.*

Dyes : CDCA ratio	Electrode	Jsc ($mA.cm^{-2}$)	Voc (V)	FF	PCE (%)	Dye Loading ($moles.cm^{-2}$)
NP1 :10	Transparent	10.74 (9.85 ± 1.10)	0.521 (0.515 ± 0.016)	0.658 (0.676 ± 0.029)	3.68 (3.41 ± 0.20)	2.03×10^{-7}
:10	Opaque	12.59 (10.60 ± 0.95)	0.505 (0.519 ± 0.016)	0.656 (0.692 ± 0.029)	4.17 (3.78 ± 0.18)	2.60×10^{-7}
NP1 :5	Transparent	10.45 (10.27 ± 0.29)	0.522 (0.525 ± 0.003)	0.660 (0.652 ± 0.019)	3.59 (3.52 ± 0.05)	1.83×10^{-7}
:5	Opaque	11.04 (10.74 ± 0.21)	0.535 (0.531 ± 0.008)	0.657 (0.677 ± 0.014)	3.89 (3.83 ± 0.04)	1.98×10^{-7}
NP2 :5	Transparent	12.90 (12.62 ± 0.52)	0.492 (0.484 ± 0.012)	0.615 (0.612 ± 0.016)	3.90 (3.73 ± 0.17)	1.47×10^{-7}
:5	Opaque	12.74 (13.55 ± 0.67)	0.503 (0.491 ± 0.009)	0.649 (0.620 ± 0.020)	4.16 (4.12 ± 0.04)	2.15×10^{-7}
NP3 :5	Transparent	7.44 (6.85 ± 0.66)	0.555 (0.544 ± 0.007)	0.712 (0.711 ± 0.004)	2.94 (2.65 ± 0.28)	1.61×10^{-7}
:5	Opaque	8.85 (8.39 ± 0.40)	0.548 (0.555 ± 0.007)	0.699 (0.704 ± 0.004)	3.39 (3.27 ± 0.09)	1.74×10^{-7}
NP4 :5	Transparent	9.17 (9.01 ± 0.15)	0.529 (0.532 ± 0.004)	0.670 (0.673 ± 0.003)	3.26 (3.22 ± 0.02)	1.35×10^{-7}
:5	Opaque	9.77 (9.51 ± 0.26)	0.546 (0.545 ± 0.003)	0.716 (0.721 ± 0.008)	3.82 (3.74 ± 0.05)	$1.37x\ 10^{-7}$
NP5 :5	Transparent	5.78 (5.50 ± 0.24)	0.544 (0.548 ± 0.002)	0.734 (0.736 ± 0.004)	2.31 (2.22 ± 0.07)	1.30×10^{-7}
:5	Opaque	6.23 (5.97 ± 0.24)	0.550 (0.554 ± 0.008)	0.731 (0.732 ± 0.000)	2.50 (2.42 ± 0.06)	1.28×10^{-7}
NP6 :10	Transparent	6.53 (6.46 ± 0.13)	0.533 (0.521 ± 0.008)	0.724 (0.728 ± 0.003)	2.52 (2.45 ± 0.07)	1.44×10^{-7}
:10	Opaque	7.53 (7.54 ± 0.08)	0.534 (0.524 ± 0.009)	0.724 (0.720 ± 0.006)	2.91 (2.85 ± 0.05)	1.33×10^{-7}
NP6 :5	Transparent	8.31 (7.69 ± 0.70)	0.482 (0.496 ± 0.014)	0.676 (0.691 ± 0.018)	2.70 (2.62 ± 0.10)	1.14×10^{-7}
:5	Opaque	9.61 (9.27 ± 0.37)	0.500 (0.506 ± 0.008)	0.674 (0.685 ± 0.010)	3.24 (3.21 ± 0.03)	1.13×10^{-7}

For all cells, a spectacular colour adaptation is observed from yellow to green hued cells (as shall be seen in Fig. 3.9). This demonstrates photochromism of our dyes upon anchorage on a semi-conductor. From the table above, under similar conditions, **NP2** shows the highest performance. Conversely, **NP6** has increased J_{sc} hence PCE with decreasing CDCA content. This can be purely accounted for by the hydrophobic lateral alkyl chains both on the spacer and on the donor unit that prevent the aggregation.

With **NP2,** we wanted to demonstrate that the introduction of alkyl chains could prevent the I_3^- from reaching the TiO_2 and thus improve the photo-voltage. **NPI-** and **NP2-**based solar cells show slightly improved overall PV performances. For example, with reference to transparent solar cells, **NP2-**based devices show higher J_{sc}=12.90 $mA.cm^{-2}$ compared to 10.74 $mA.cm^{-2}$ with **NPI**. However, the V_{oc} does not seem impacted.

NP3 and **NP5** dyes, with bis C_6 and tert-butyl chains on the indene bridge respectively, were synthesized to study the effect of kinetics on the PV performance of photochromic DSSCs. **NP3-**opaque cell has a J_{sc}=8.85 $mA.cm^{-2}$ and that of **NP5-**opaque cell J_{sc}=6.23 $mA.cm^{-2}$ with comparable photo-voltages thus giving PCEs of 3.39% and 2.50%, respectively. Therefore, it seems that the decolouration speed (see Fig. 3.7d) plays a role on the performance. The dyes with a higher tendency to revert back to the initial state recorded lower efficiencies.

The discolouration kinetics of **NP3** and **NP4** are comparable. With inclusion of C_8 chains on **NP3** gave rise to **NP4** that red-shifted a bit the absorption spectrum thus reaping more photons giving a J_{sc}=9.17 mA.cm^{-2}, slightly higher than **NP3**'s. Therefore, **NP4** recorded 3.82% PCE compared to **NP3**'s of 3.39%.

Introduction of C_8 alkyl chains onto **NP5** brought forth **NP6** again with slightly red-shifted open-form absorption spectrum but commensurate kinetics. As a result, we harvest more photons with **NP6** giving a J_{sc}=7.53 mA.cm^{-2} and a PCE=2.91% marking a 16% improvement compared to **NP5**.

From the dye loading experiments, we can reveal the detrimental effect of the peripheral C_8 chains on the number of dye molecules adsorbed. For instance, **NPI**-opaque cells adsorb 2.60x10^{-7} moles/cm^2 whereas **NP2**-opaque cell has 2.15x10^{-7} moles/cm^2. This is also reflected in **NP3** and **NP4** with 1.74x10^{-7} moles/cm^2 and 1.37x10^{-7} moles/cm^2, respectively. Overally, the number of molecules attached on the surface is decreased by 17-20% when the donating group is substituted with peripheral C_8 chains.

Surprisingly, the different structural modifications led to varying photovoltaic parameters. To reveal the impact of light exposure, the *J(V)* curves were registered at the beginning and when the cells attained their photostationary state (PSS), i.e. a state of equilibrium between the closed and open forms of the dye molecules. The curves are as shown below :

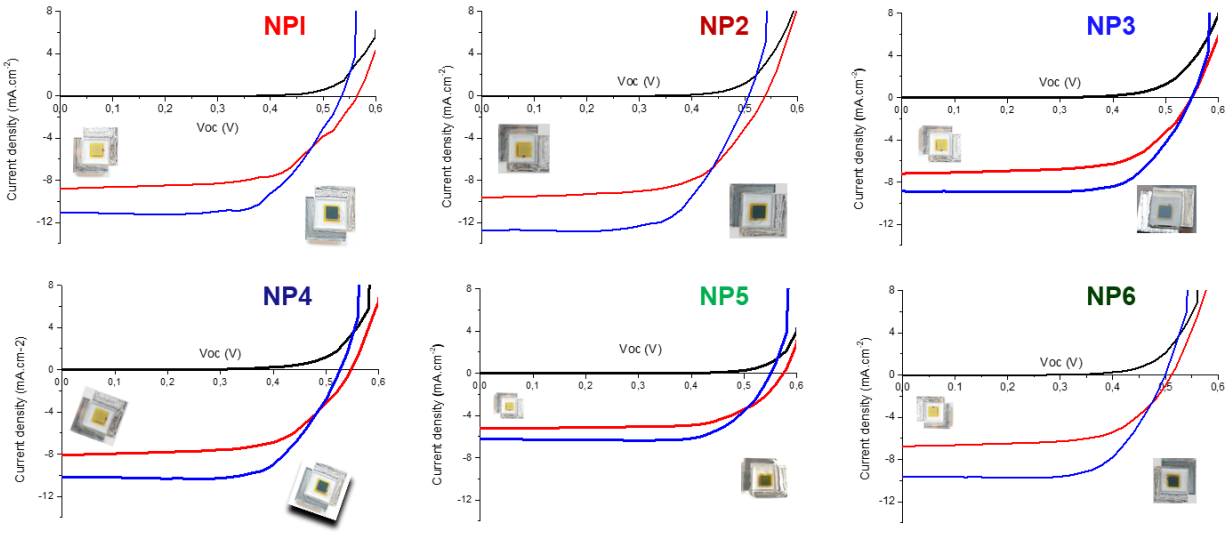

*Figure 3.9 : J(V) curves of the **NP**series-based cells fabricated under dye :5CDCA conditions. The red curve is registered after 15 s irradiation and the blue curve after attaining the photostationary state.*

From the figure above, all the dyes in this family have similarities including moderate photovoltages and the increase in J_{sc} with irradiation time. The V_{oc} loss with increasing the time of irradiation was already observed in the first generation photochromic cells and reported in our previous work. It is linked to accelerated recombination kinetics upon isomerization and not a CB shift. In comparison with **NPI-**based *J(V)* curve, the V_{oc} difference between the first irradiation and that at the PSS is 30 mV whereas in **NP2** (see Fig. 3.9) is 26 mV. This is comparable and the effect of the C_8 chains on recombination to improve V_{oc} cannot be proved. **NP4**, **NP5** and **NP6** have a V_{oc} drop magnitude of 21 mV, 24 mV and 19 mV respectively, as presented above.

Distinctively, with **NP3-**based solar cells, this drop in the V_{oc} is not observed and remains constant (or even sometimes increases slightly) with irradiation time. Therefore, the differences in V_{oc} drop magnitude between dyes and lack thereof (as in **NP3**-devices) raises important questions.

- Can we draw structure-property relationships ?
- What is happening in the case of **NP3** ?

To answer these questions, I have done complete study using small-signal perturbations technique as shown below.

3.1.7 Electrochemical Impedance measurements for NPseries

The impedance spectra obtained from measurements (as explained in chapter 1) were fit to an equivalent –RC- circuit and the recombination resistances and the chemical capacitances extracted. The dark condition measurements were done after fabricating the cells in nearly dark conditions and storing the cells overnight to ensure that they were completely deactivated and only the closed form exists. On the other hand, measurements done under illumination were taken after 15 minutes of continuous light soaking while carrying out the *J(V)* curves to a constant efficiency value, under 1 Sun, to ensure open forms are generated and the PSS is reached. For comparison between the different dyes, the voltages were corrected taking into account band shifts due to structural differences.

The Nyquist plots in the dark and under irradiation were registered using transparent solar cells. After fitting the curves into equivalent circuits using the 2 equations exposed in chapter

1, the recombination resistance and chemical capacitance values were extracted and their slopes at different applied voltages is as shown in the table below.

Table 3.4 : The α and β values under dark and white illumination conditions after fitting the recombination arc of the impedance spectra to an –RC- elements using appropriate equations.

DSSC	α // β			
	Dark	White Light	Dark	White Light
NP1:5cdca	0.23	0.22	0.66	0.88
NP1:10cdca	0.25	0.23	0.50	0.83
NP2:5cdca	0.23	0.22	0.70	0.86
NP3:5cdca	0.23	0.23	0.61	0.82
NP4:5cdca	0.21	0.20	0.60	0.85
NP5:5cdca	0.22	0.22	0.48	0.74
NP6:5cdca	0.21	0.21	0.47	0.60
NP6:10cdca	0.27	0.24	0.48	0.89
RK1	0.24	0.19	0.65	0.88

For all dyes, irrespective of the amount of CDCA coadsorbant, the α values have remained within the 0.15-0.35 range reported for DSSCs [17,18]. On the other hand, the recombination parameter in **NPI**-based devices with 5 CDCA and 10 CDCA changes more rapidly in the later than the former as a function of irradiation conditions. Similar effect is observed when **NP6** dye is employed, the recombination resistance slope is higher with increasing CDCA amount (see table 3.4 above). Literally, this could mean that the recombination kinetics are accelerated with increased CDCA concentration.

However, these symmetry values can neither deduce structure-property relationships nor explain recombination and photochromism interplay. Therefore, the fitted chemical capacitances values under the different illumination conditions can be meaningful as follows,

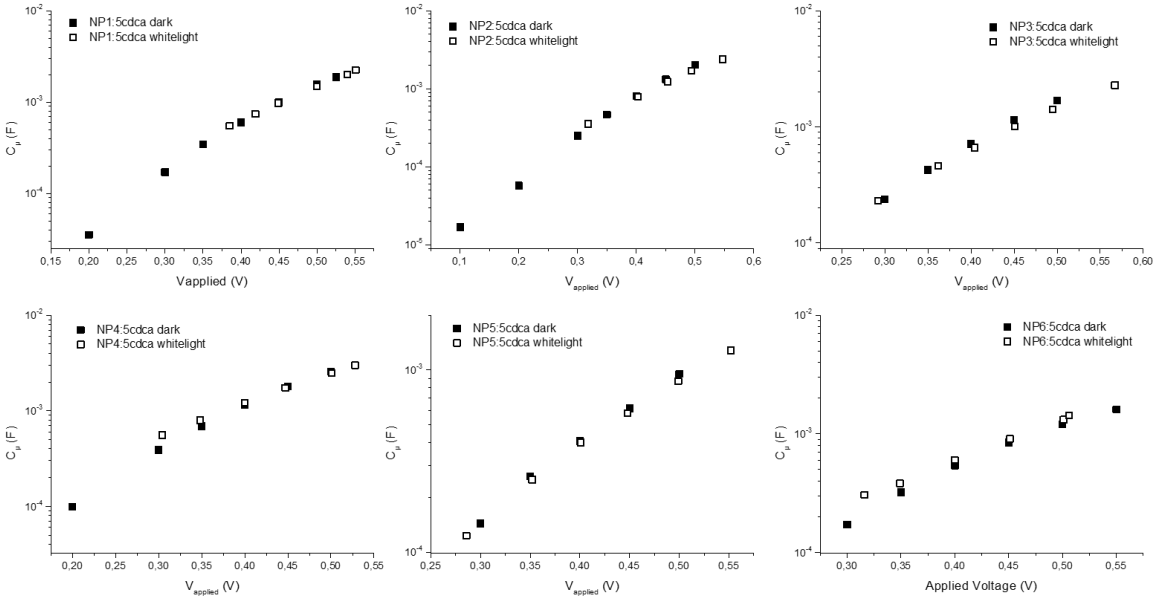

*Figure 3.10 : Chemical capacitances of the **NP**series after fitting to an equivalent -RC-circuit under dark and light conditions.*

For all **NP**series dyes, the capacitance is exponentially dependent on the open-circuit voltage in accordance with the exponential trap states distribution. Although there are differences on the slopes, one thing is clear that the capacitances at the different applied voltages lie on the same straight line and they seem to overlap. The slopes depend on the trap distribution parameter, α, therefore, the changes we observe are a result of structural differences. The C_μ, for a given voltage, relies on the positioning of the TiO_2 CB with respect to the electrochemical potential of the redox couple. Therefore, this observation is important because its physical meaning confirms lack of CB shift for this series when dyes isomerizes from the closed isomer, in the dark, to an open isomer, under light. Eventhough the fitted chemical capacitances values under different illumination conditions give information about the energetic shifts, they are insufficient to explain the structure-property relationship. Below are the Nyquist plots, already explained above, under similar conditions from where the chemical capacitances comparisons were derived.

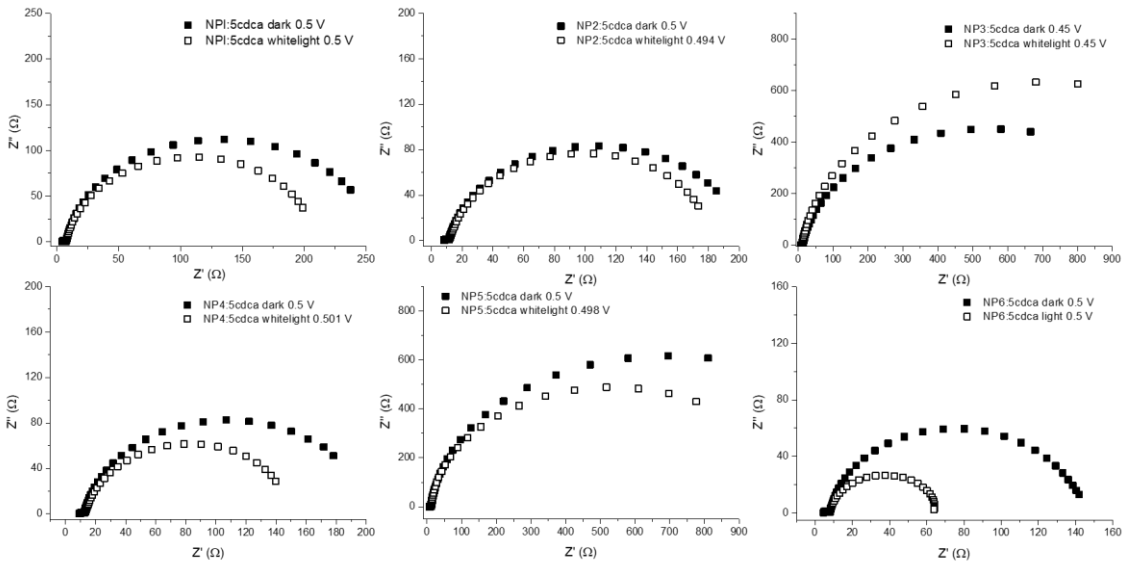

*Figure 3.11 : Nyquist plots of the **NP**series under dark and under white light illumination conditions.*

There are two evident semi-circles, the first appearing at high frequencies and the other at low frequencies. The first one is as a result of platinum counter electrodes [19,20] and the second, that we shall focus on, is due to the charge transfer resistance at the electrode-electrolyte interface. The diameter of this semicircle (real axis) gives the recombination resistance at a glance i.e. electron transfer from TiO_2 to the I_3^- in the electrolyte. From Fig. 3.11 above, for all photochromic dye-based cells except **NP3**, the semi-circle in the dark shrinks upon exposure to irradiation at the same voltage typical in classical DSSCs [21,22] and observed in **RK1**-based cell [19]. Such shrinks correspond to the local [I_3^-] concentration increase upon illumination due to dye's regeneration hence fastening recombination [21,22] accompanied with the dyes' surface isomerization that creates recombination routes. On the contrary, **NP3**-based cell shows an increase in the recombination resistance upon illumination. This corroborates the lack of V_{oc} loss as opposed to other family members and in some cases a slight V_{oc} increase of up to 4 mV in transparent solar cells was observed. From this observation, we can conclude that eventhough the activation of the photochromic dye accelerates recombination kinetics, substitution on the correct position of the dye helps to decelarate recombination. Thus, the surface opening fashion of **NP3** dye helps to cut the local [I_3^-] concentration by limiting their approach on the TiO_2 to seize useful electrons hence lower recombination. Since same electrodes were used, any decrease/increase in charge transfer resistance is excluded to photochromism.

We have thus far observed that the chemical capacitances do not change and thus no CB shift. In addition, we have understood the nature of recombination for **NP**series. To make comparison in between the dyes i.e. structure-property relationship, oftenly, the capacitance plots are displaced to overlay hence correcting the shifts in the band edges. This is vital for comparison but we need to ensure that all the cells are at the same electron quasi-Fermi level and ensuring that the electron density in the photoanode is equal [23–25]. However, this is only possible in systems with similar traps density and distribution parameter thus similar electrodes were employed in this study [26–28]. Such corrections are done to compare recombination kinetics at the same electron density thus giving a way to distinguish themodynamics from kinetics. Since similar electrodes were applied, an assumption taken is that the N_T and α are comparable hence no need for capacitance integration [25] and that the slight differences are as a result of dyes' structural differences. Similar fabrication conditions were also considered i.e. a dyeing bath with dye: CDCA ratio of 1:5.

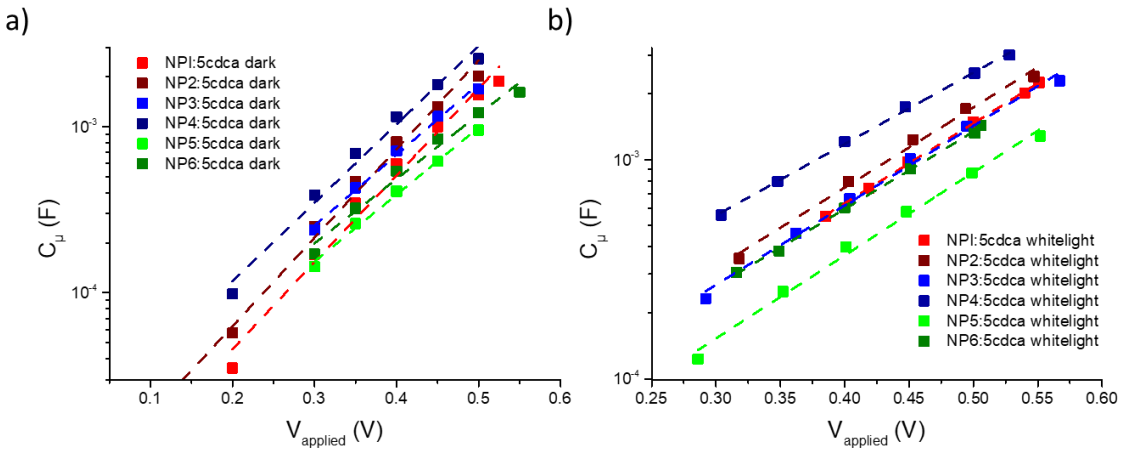

*Figure 3.12 : Chemical capacitances plots of the **NP**series devices a) in the dark and b) under whitelight after reaching the photostationary state under 1 Sun.*

In the dark, the capacitance plots are parallel to each other indicating the differences in the electron densities within the metal oxide. The same trend is observed when cells were irradiated and the dyes attained the PSS. This suggests that the conduction band edges of TiO_2 shifts in between the dyes. For comparison, I chose **NPI** whose properties are well understood from the previous chapter and from which the **NP**series inspiration was born. Therefore, voltage corrections were performed with reference to **NPI**.

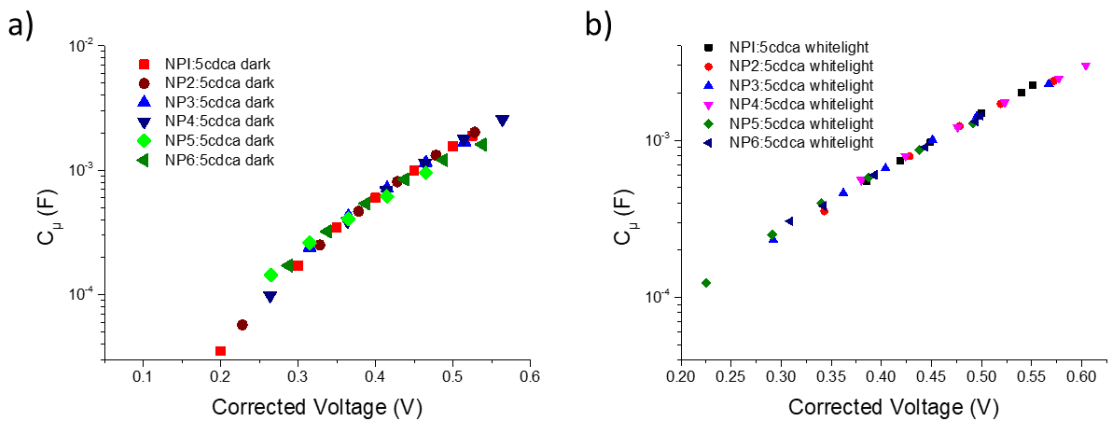

*Figure 3.13 : Corrected chemical capacitances with respect to **NPI**.*

At similar electron densities, it is now possible to make comparisons on the nature of recombination in between the dyes as follows.

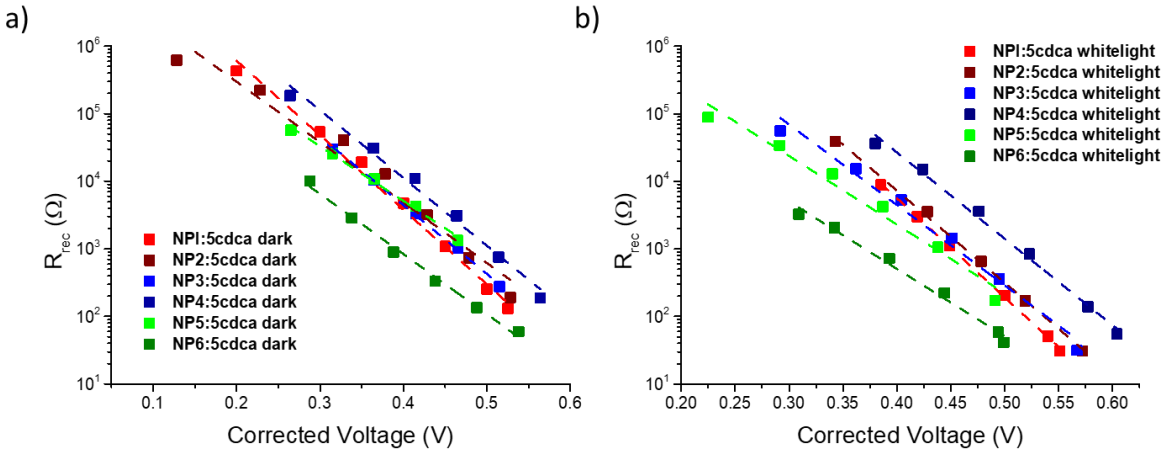

*Figure 3.14 : Structure-property relationships on the NPseries with respect to champion **NPI**.*

At the same electron concentration, I am able to extract information crucial for comparison. From Fig. 3.14 above, **NP4**, the dye bearing 6 long hydrophobic alkyl chains, shows the highest recombination resistance under both illumination conditions. **NP2** and **NP3** show higher recombination resistance compared to **NPI** especially at open-circuit potential above 500 mV. **NP6** shows the lowest recombination resistances both in the dark and under illumination in the same experimental conditions which is concurrent with the lower V_{oc} of its cells (<500 mV) at the PSS. This indicates that linear alkyl chains attached to the core of the dye have a higher passivation effect compared to branched ones.

From EIS, the effective electronic lifetime was determined from $\tau_n = R_{rec}C_\mu$ [29] as shown below.

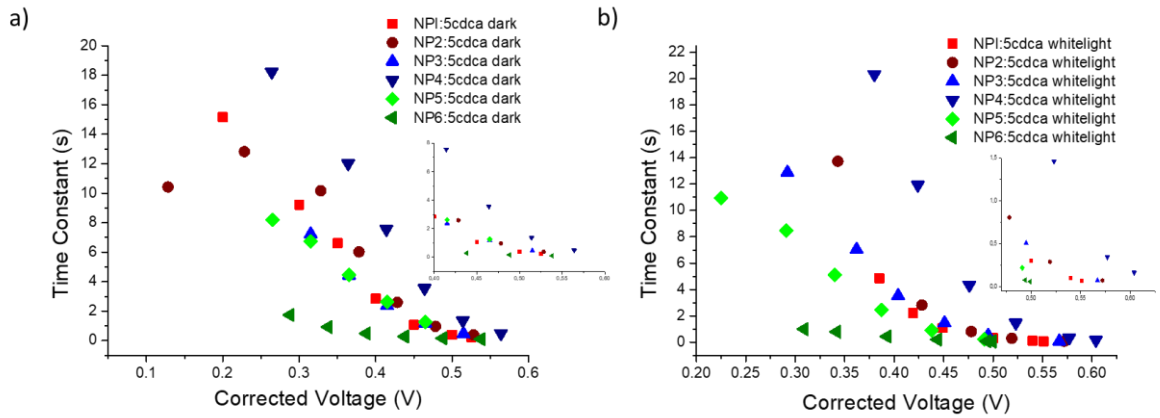

*Figure 3.15 : Time constant comparison in between the dyes in the **NP**series.*

The effective electron lifetime decreases as a function of both the irradiation intensity and the open-circuit voltage. The trends are similar irrespective of the irradiation conditions. The time constant mimics the recombination resistances evolution with the applied voltage which implies that, the decreased R_{rec} values result in increased recombination and the charge carriers recombine at higher rate hence decreasing their lifetime. Lastly, eventhough **NP5** and **NP6** have shown to have the lowest recombination resistance and the lowest electronic lifetimes, they have impressive V_{oc} of (at least or ~530 mV as shown in table 3.3) which could be due to the large band shift (in between the dyes). Under operating conditions, the band shifts of the **NP**series i.e. **NP2**, **NP3**, **NP4**, **NP5** and **NP6** with respect to **NPI** are +25 mV, +3 mV, +76 mV, -61 mV, and -7 mV respectively. We can notice from this that the more bulky dyes, after grafting on the electrodes, induce a negative bandshift.

Thus far I have demonstrated the impact of bulky substituents on the **NPI** skeleton either on the photochromic core or on the periphery. I have also made comparison in between the **NP**series dyes i.e. **NPI**-**NP2**, **NP3**-**NP4**, **NP5**-**NP6** and others that I will not mention here.

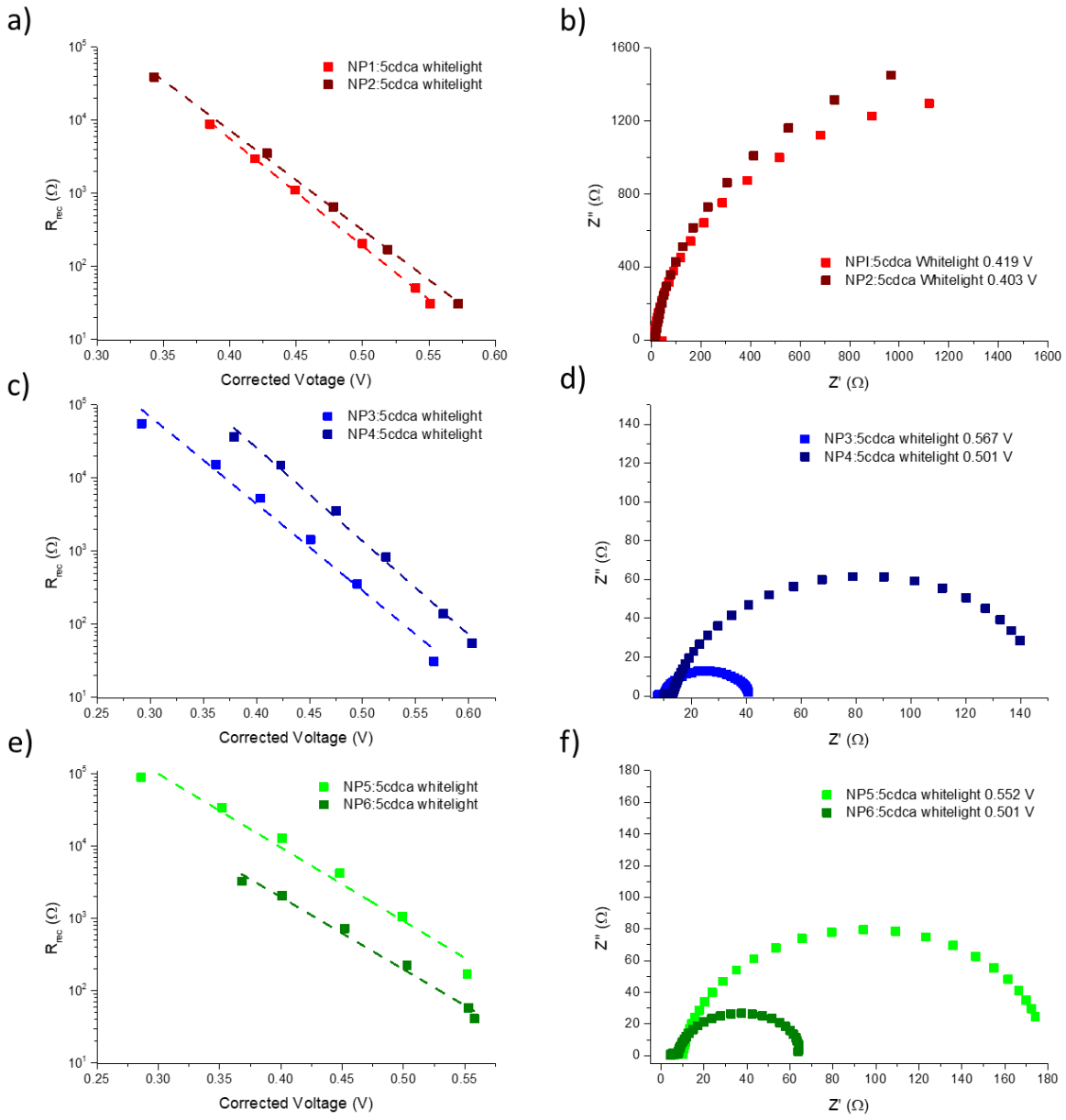

*Figure 3.16 : Comparison between **NPI-NP2**, **NP3-NP4** and **NP5-NP6** –based devices to uncover structure-property relationships after irradiation at the PSS using whitelight illumination.*

Fig. 3.16 a) and b) shows comparison between **NPI** and **NP2** devices under operating conditions. At the PSS, the hydrophobic C_8 alkyl chains introduced on the periphery of **NP2** play the role of surface passivation from I_3^- thus increasing the recombination resistance hence lower recombination. As a result, improved PV performance is reported for **NP2** compared to **NPI** under similar fabrication conditions. Similar effect is seen (see Fig. 3.16 c) and d)) when alkyl chains are added in **NP3** thus forming **NP4**. However, an opposite behaviour is observed when long alkyl chains are added in **NP5** to form **NP6**. This suggests that the bulky

substituents on the photochromic core alone are sufficient to not only fasten discolouration kinetics, but also to reduce recombination.

3.1.8 Comparison of optical properties in complete DSSCs

3.1.8.1 Kinetics in devices

Having understood the optoelectrical properties in solution of **NP**series, tested them in a device configuration and finally deduced structure-properties relationship, I investigated the optical properties of complete devices for application. I introduced these molecules in devices, irradiated and characterized them at the PSS. The thermal discolouration kinetics to the stable closed forms were registered in a complete cell and modelled using the equations above. The discolouration curves are as shown below.

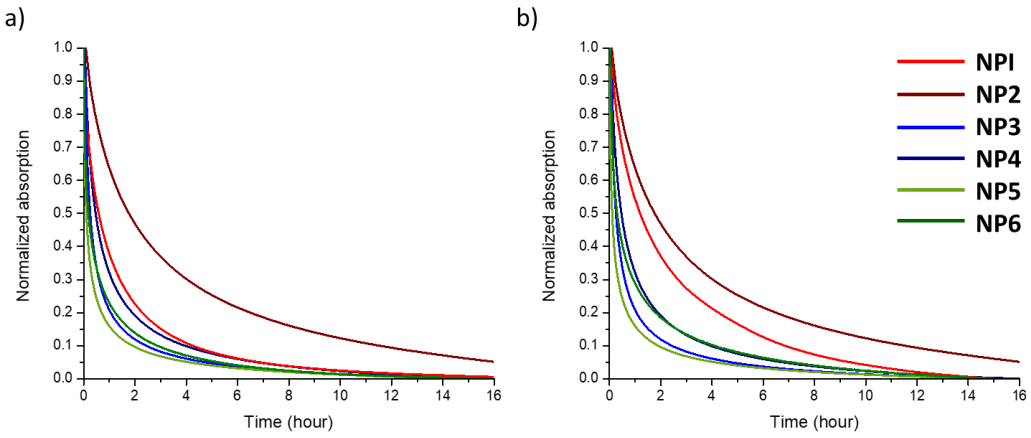

*Figure 3.17 : Normalized decolouration kinetics curves of **NP**series after reaching the photostationary state under irradiation, a) in complete cells under optimized conditions where **NPI** and **NP6** have a ratio of dye:10 CDCA and the rest with 5 CDCA, b) all under similar conditions with dye: 5 CDCA ratio. (Conditions at 25°C).*

Whereas discolouration kinetics in solution could fit in a monoexponential decay with **NP5** and **NP6** portraying highest first order kinetic constants, all NPseries in complete devices were fit to a biexponential decay bearing two kinetic constants. For nearly all dyes, the behaviour in solution was transferred onto solar cells except for **NP2**. On the TiO_2 surface, the decolouration constant are far less compared to **NPI** despite being comparable in solution. The table below shows the calculated discolouration constants.

Table 3.5 : The discolouration constants in complete cells of NPseries with varying CDCA concentration.

Dye	5 CDCA	5 CDCA	10 CDCA	10 CDCA
	k_1 (s^{-1})	k_2 (s^{-1})	k_1 (s^{-1})	k_2 (s^{-1})
NP1	$4.5x10^{-4}$	$6.7x10^{-5}$	$5.1x10^{-4}$	$8.9x10^{-5}$
NP2	$2.4x10^{-4}$	$3.3x10^{-5}$	n/a	n/a
NP3	$1.3x10^{-3}$	$1.2x10^{-4}$	n/a	n/a
NP4	$7.6x10^{-4}$	$8.9x10^{-5}$	n/a	n/a
NP5	$2.3x10^{-3}$	$1.3x10^{-4}$	n/a	n/a
NP6	$1.2x10^{-3}$	$9.0x10^{-5}$	$1.2x10^{-3}$	$1.1x10^{-4}$

NP3 and **NP6** show relatively fast initial constant with **NP4** the slowest. Overally, **NP2** shows the slowest kinetics when employed in solar cells. The anti-aggregating agent, CDCA, has an impact on the decolouration of photochromic devices. For example, in **NPI**-based cells, the first-order kinetics constant increases with increasing CDCA concentration where 80% of initial colouration, after PSS, is lost in 2 hours for cells having 10 CDCA ratio as compared to 60% with 5 CDCA under same duration. However, this effect is not observed with **NP6** as CDCA does not have much impact and the kinetics have remained almost unaltered. This is probably due to the fact that with **NP6**, the aggregation of the dye is strongly reduced by the lateral bulky substituents.

3.1.8.2 Average visible transmittance (AVT) studies

Using complete devices based on 13 µm thick photoanodes, I investigated the interplay between photochromism and photovoltaic properties for application as see-through windows.

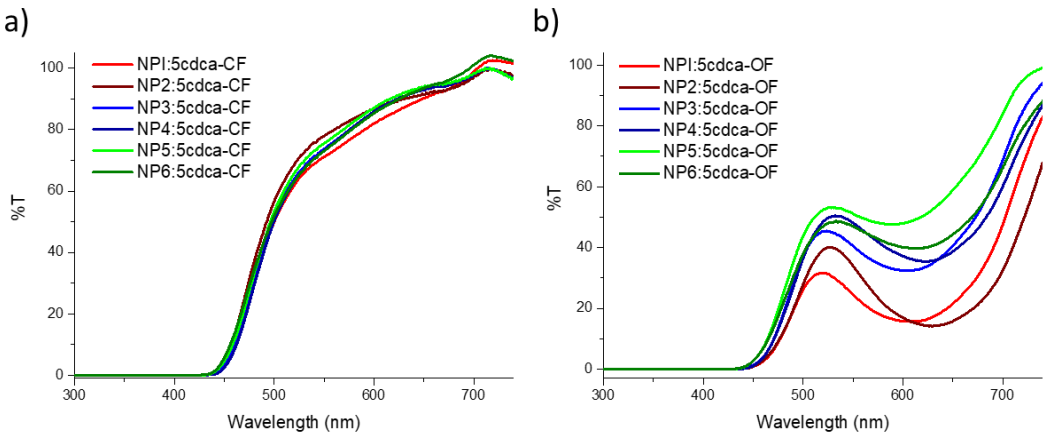

*Figure 3.18 : Average visible transmittance of the **NP**series a) in the dark and b) after irradiation at the PSS. (Conditions 25°C).*

The average values were calculated in the 380 – 740 nm and the values at the PSS are as listed in the table below.

*Table 3.6 : Percent average visible transmittance of the **NP**series in their closed and open configuration in complete DSSCs (13µm electrodes) with dye:5cdca ratio.*

Dyes	AVT in the dark (%)	AVT under light at PSS (%)
NPI	59.3	22.4
NP2	61.8	20.6
NP3	60.3	34.5
NP4	60	34.4
NP5	61.4	44.2
NP6	61.3	36.8

For all dyes, the AVT in the dark is comparable lying between 59 - 61%. However, upon irradiation at the PSS, we observe variations ranging from 20 - 44%. The huge differences can be explained from the dye-loading experiments and hence the size of the individual molecules. Indeed, **NP5** and **NP6** possessing bulky substituents show high levels of transparency.

3.1.8.3 Light Utilization Efficiency (LUE)

Finally, I investigated this new parameter as explained in chapter 1 relating the performance and the optical properties given they have an inverse relationship.

*Table 3.7 : Light utilization efficiency values of the **NP**series. The solar cells are based on 6 µm and 13 µm photoanodes where the photovoltaic and optical parameters were registered at the photostationary state (PSS).*

Dye (6 µm)	AVT (%)	PCE (%)	**LUE** (%)	Dye (13 µm)	AVT (%)	PCE (%)	**LUE** (%)
NPI :5cdca	n/a	n/a	n/a	**NPI** :5cdca	22.4	3.59	0.80
NPI :10cdca	22.4	2.23	0.50	**NPI** :10cdca	27	3.68	0.99
NP2 :5cdca	23.3	2.85	0.66	**NP2** :5cdca	20.6	3.90	0.80
NP3 :5cdca	n/a	n/a	n/a	**NP3** :5cdca	34.5	2.94	1.01
NP4 :5cdca	32.2	2.20	0.71	**NP4** :5cdca	34.4	3.26	1.12
NP5 :5cdca	35.2	0.86	0.30	**NP5** :5cdca	44.2	2.31	1.02
NP6 :5cdca	38.5	1.32	0.51	**NP6** :5cdca	36.8	2.70	0.99
NP6 :10cdca	43	1.90	0.82	**NP6** :10cdca	44.5	2.52	1.12

The light utilization efficiency (LUE) values are lower (<1%) with thin photoactive layer. When the thickness is increased to 13µm, we achieve slightly higher values, except a few, >1%. Keeping in mind that I do not use an antireflective coating that is often used to boost the LUE [30]. According to Traverse *et. al*, transparent PVs demonstrating LUE>1% have the potential to self-empower smart windows thus giving our **NP**series dyes an entry-level to the application threshold [31].

3.1.9 Cosensitization

Among the requirements for high performance DSSCs, as explained in chapter 1, the dye should absorb largely in the visible and/or in the near infrared (NIR) regions. Finding sensitizers capable of mimicking the solar emission spectrum is rare. Amidst strategies to achieve panchromatic absorption, different techniques have been applied such as cosensitization. Therefore, multiple harvesters (cocktail dyes) have been reported to boost performances of DSSCs mainly due to the extension of the absorption spectra in the visible region [32–34]. Thanks to this technique, the dye molecules are able to provide synergetic effect through connotation thus high performing solar cells. Therefore, using the cosensitization technique, I have blended two best performing **NP**series dyes **NPI** and **NP2**. Before I delve into the cocktail result of **NP**series, I investigated the impact of 1st generation photochromic cells blends i.e. **NPB** and **NPI** and the preliminary result is as shown below.

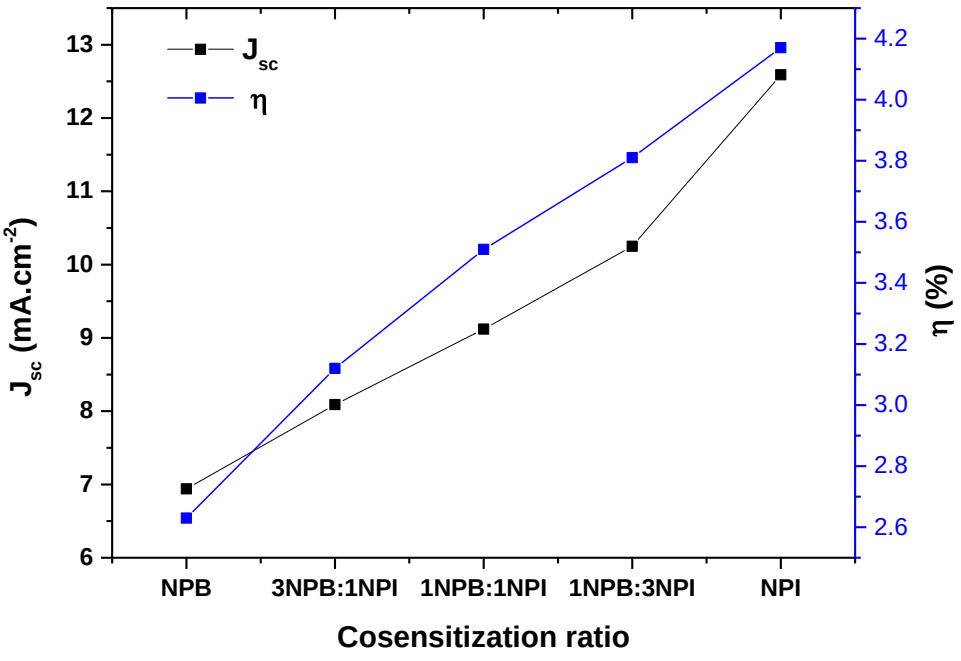

*Figure 3.19 : Impact of **NPB** and **NPI** cografting on the photovoltaic performance.*

NPB (a reddish-brown dye at the PSS) has a maximum absorption at 519 nm gave an efficiency of 2.63%. **NPI** (a dark green dye at the PSS) with a maximum absorption at 605 nm has an efficiency of 4.17%. I developed a hypothesis that mixing the dyes will result in complementary absorption thus improve the overall efficiency. As shown in Fig. 3.19 above, the PV performance was not improved. For example, at 0.25**NPB** :0.75**NPI** the J_{sc}=10.25 mA.cm^{-2}, V_{oc}=517 mV, FF=0.72 and a PCE=3.81%. Despite a lower PCE obtained, a neutral grey colour was observed. This is an interesting result since neutral hue are more desirable for application in windows. This would add more visual comfort for the users by improving the colour-rendering index of the solar cells.

Therefore, using the same approach, I have blended **NPI** and **NP2** and the cocktail result is as shown below.

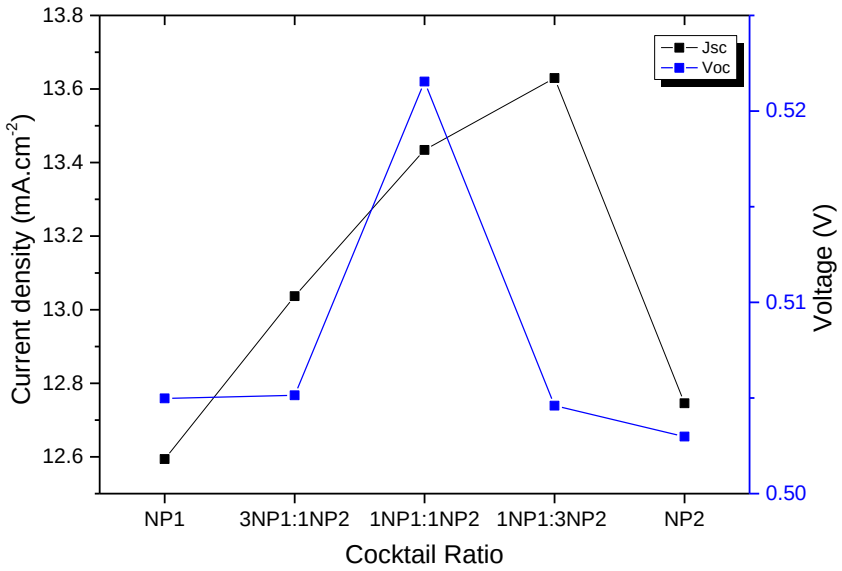

*Figure 3.20 : Effect of **NPI** and **NP2** cosensitization of the PV performance.*

From Fig. 3.20 above, the photocurrent increases linearly from pure **NPI** up to 0.25 :0.75 **NPI** :**NP2** due to the synergistic effect. On the other hand, the photovoltage remains nearly constant for all ratios except a spike with the 1:1 ratio possibly due to better surface passivation and organization of the dyes. As a result, this optimum ratio yields a J_{sc}=13.43 mA.cm^{-2}, V_{oc}=0.521 V, FF=0.62 leading to a power conversion efficiency of 4.34% while portraying a green colouration. The statistics performed on three opaque cells and the *J(V)* characteristics are as shown below.

*Table 3.8 : The PV performance and the statistics of opaque (13+4) µm of cosensitized **NPI/NP2** : 5cdca devices.*

Dye	J_{sc} (mA.cm^{-2})	V_{oc} (V)	FF	PCE (%)
NPI/**NP2** :5cdca	13.43 (13.34 ± 0.35)	0.521 (0.515 ± 0.011)	0.62 (0.62 ± 0.00)	4.34 (4.26 ± 0.06)

The J(V) curves of the corresponding devices with comparison is as shown below.

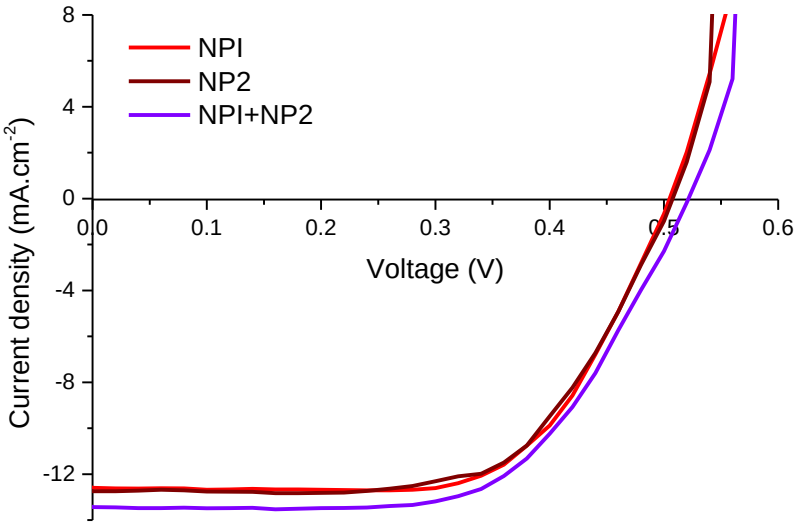

*Figure 3.21 : The J(V) curves of **NPI, NP2** and a 1:1 **NPI:NP2** cocktail in the best conditions for each.*

Indeed, the current density and the photovoltage are slightly increased as compared to individual dyes due to synergetic effect and improved surface passivation, respectively. The energy conversion efficiency attained at this point (PCE = 4.34%) is the highest value reported for photochromic solar cells.

These slightly improved PV parameters were investigated further by small-signal perturbation to understand the impact of the cocktail mixture. The impedance measurements were performed and the Nyquists spectra fit to an equivalent circuit and the capacitance and recombination resistance values extracted.

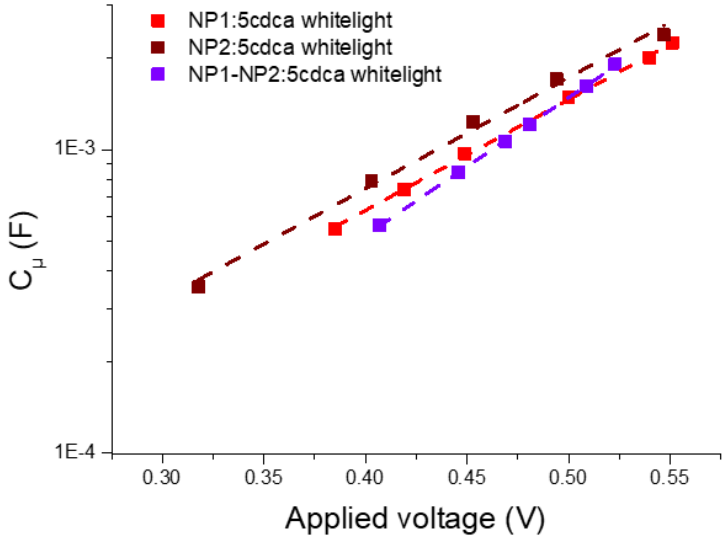

Figure 3.22 : Chemical capacitances values after fitting the impedance data to an equivalent circuit with the devices under operating conditions.

The chemical capacitance plots above are parallel to each other. This suggests that there is a band edge shift in between the devices with the concentration of electrons being higher in **NP2**-based cells. To extract information on the recombination while using cocktail dyes, I corrected the voltage with reference to individual dyes and the following was deduced.

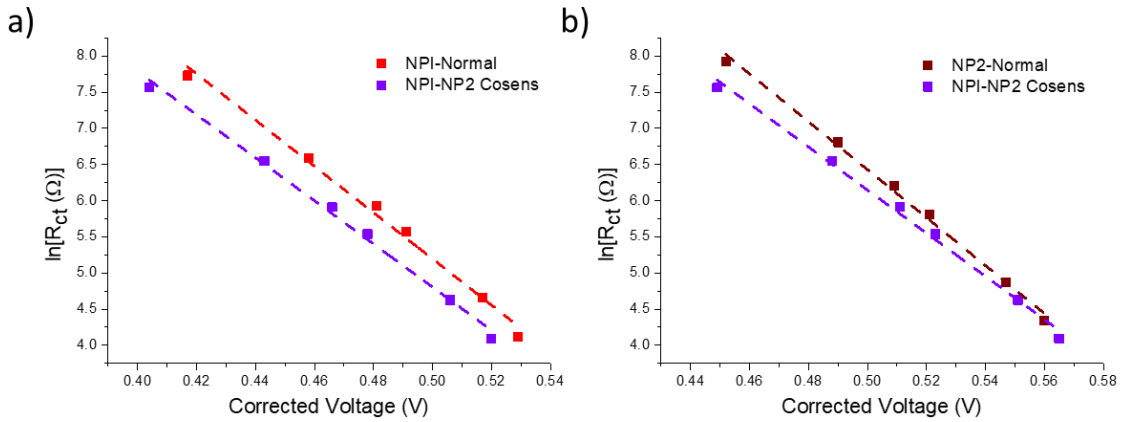

*Figure 3.23 : Comparison of recombination resistance as a function of corrected d.c. voltage under operating conditions for cells based on **NPI** :5cdca versus **NPI/NP2** :5cdca and **NP2** :5cdca versus **NPI/NP2** :5cdca.*

From Fig. 3.23 above, the **NPI**/**NP2** cosensitized devices with respect to individual dyes based devices is not conclusive to what we observe in their PV performance. The recombination resistance with cocktail devices is lower in all cases but approaches that of **NP2**-based device with larger voltages.

3.2 Electrode treatments / Photoanode modification

3.2.1 Hydrazine treatment

Various studies have demonstrated the significance of the TiO_2/dye/electrolyte interface to the PV performance of DSSCs [35,36]. The back electron transfer (BET) to reduce the oxidized species in the device termed as recombination, has a detrimental effect towards the performance of photochromic solar cells. To cut or reduce this tendency, two approaches have been applied i.e. chemical and structural engineering (**NP**series) and the cosensitization approach but efficiencies are relatively low. Among challenges identified and known in DSSCs, is the high density of electron traps in the mesoporous TiO_2 [37–40]. Their existence pose a negative effect as they act as potential recombination sites. Traps are due to oxygen vacancies, meaning, injected electrons are lost while filling them under operation. Trap states can be estimated either through charge-extraction or infrared transmittance. Therefore, by charge-extraction where Ti^{4+} is reduced to a low valence metal ion such as Ti^{3+} fills these vacancies prior to device fabrication, is a promising approach towards high performance photochromic DSSCs. In addition, this method has been reported to enhance electron transfer from TiO_2 to fluorine-doped tin oxide (FTO) through formation of excitons in TiO_2 [41].

Hydrazine is a well-known reducing agent [42–44]. Thus, I have used this chemical to treat photoanodes i.e. before the $TiCl_4$ treatment for 20 minutes at 70°C and then evaporated the excess hydrazine. I fabricated solar cells based on **NP2** dye with N_2H_4-treated photoanodes and the photovoltaic values registered are as shown below.

*Table 3.9 : Comparison between the normal untreated and N_2H_4 treated **NP2**-based solar cells with statistics performed on at least 3 opaque devices.*

Dyes	Electrode	Jsc ($mA.cm^{-2}$)	Voc (V)	FF	PCE (%)
NP2	Opaque	12.74 (13.55 ± 0.67)	0.503 (0.491 ± 0.009)	0.649 (0.620 ± 0.020)	4.16 (4.12 ± 0.04)
NP2 (N_2H_4 Treated)	Opaque	11.69 (11.20 ± 0.34)	0.527 (0.524 ± 0.003)	0.652 (0.692 ± 0.010)	3.94 (3.83 ± 0.07)

The J_{sc} of the devices is negatively affected and I lost nearly 1 $mA.cm^{-2}$. The photovoltage of our best performing **NP2**-based device shows a V_{oc}=503 mV. After hydrazine treatment, we have a slight improvement of the V_{oc} (by 20 mV) reaching 527 mV. Unfortunately, due to a lower J_{sc}, the overall performance is lower. This result is interesting because a V_{oc} improvement and a decreased J_{sc} could suggest that there is either an upward shift of the TiO_2 with reference to the redox potential of the I_3^-/I^- couple or a decrease in the recombination

processes. The later could be possible because the aim was to fill traps implying that fewer electrons are lost filling oxygen vacancies. This brings up several vital questions such as : is there a change in the chemical capacitance, C_μ, with more electrons in the TiO_2 CB? Is the lower J_{sc} due to poor electron injection because of a positive CB shift?

To answer these questions, I applied a small signal perturbation technique *i.e.* impedance spectroscopy and x-ray photoelectron spectroscopy (XPS) tools are used to unravel the impact of hydrazine. The obtained Nyquists plots were fit to an equivalent –RC– elements in parallel and the capacitive and resistive behaviour defined as shown below.

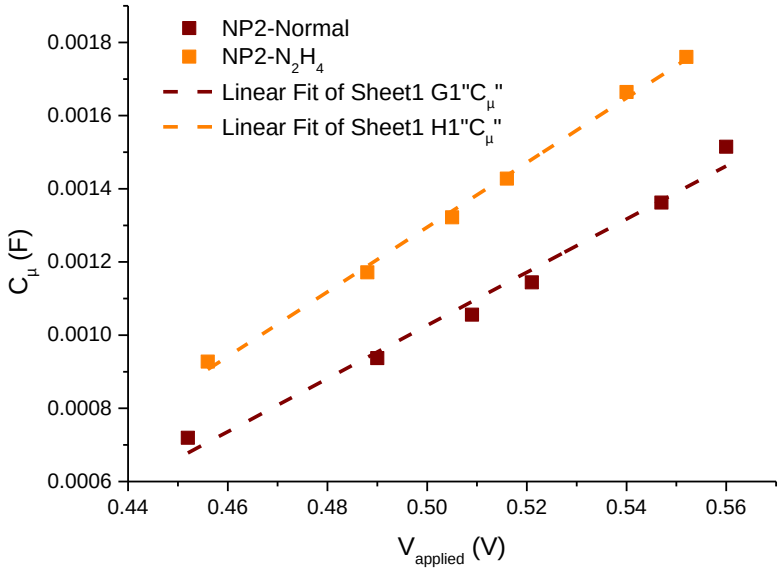

*Figure 3.24 : Chemical capacitance values of **NP2** :5cdca based cell versus hydrazine treated **NP2** :5cdca cell after fitting the recombination part of the Nyquist plot to an equivalent circuit.*

From Fig. 3.24 above, the chemical capacitances of **NP2**-based device are parallel to the **NP2**-hydrazine pre-treated electrodes. This suggests that there is a possible band edge shift with hydrazine treatment corroborating that indeed the initially presumed role to fill the traps in the metal oxide was successful as the concentration of electrons increased. For comparison and to discuss the nature of recombination between these sets of solar cells, I corrected the voltage at the quasi-Fermi level at the operating conditions as shown below.

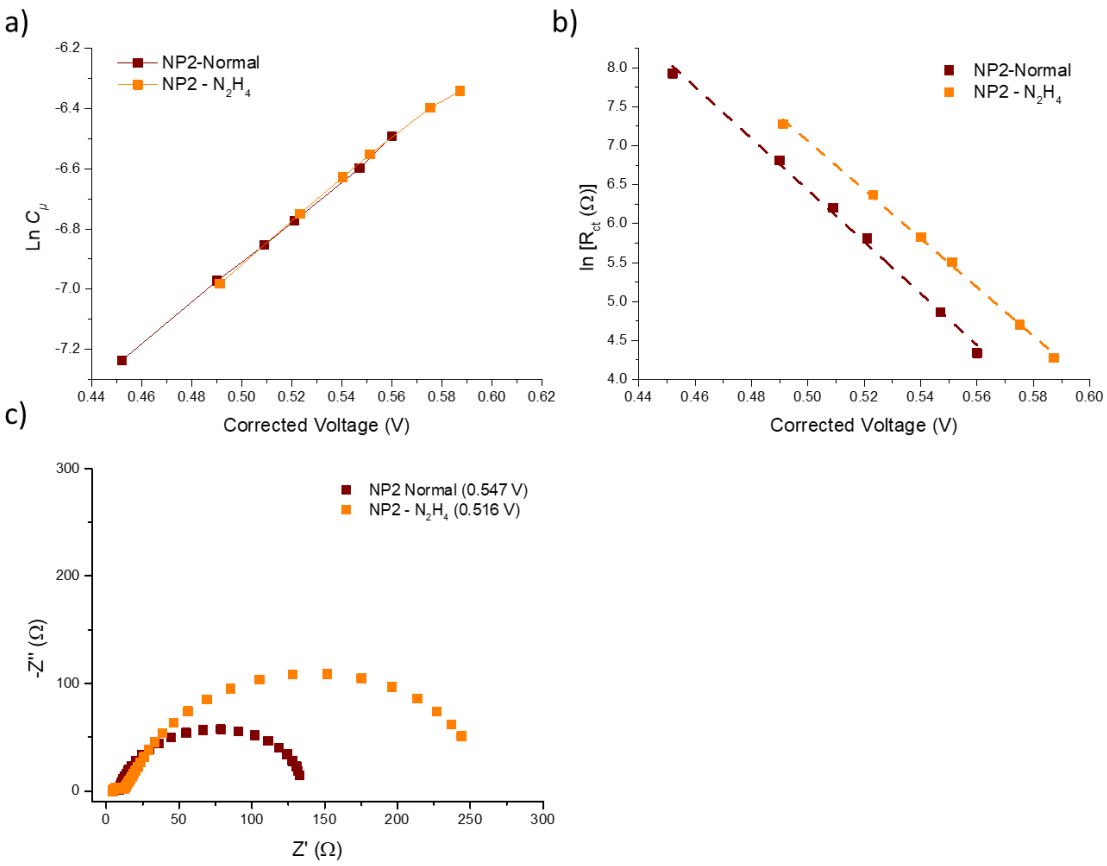

*Figure 3.25 : Comparison between **NP2**-based devices under illumination with and without hydrazine treatment with a) showing the voltage correction, b) the recombination resistances and c) the Nyquists plots at the corrected voltages.*

The figure above shows, at similar electron concentration, the recombination resistance in hydrazine-treated devices is higher than in classic **NP2** devices. From the Nyquists plots, the recombination arc diameter in **NP2**-N_2H_4 cells is larger means the recombination is lower. From the correction as seen in Fig 3.25 a), the hydrazine treatment induces an upward CB shift of +35.4 mV thus explaining the improved photovoltages followed by a slight J_{sc} loss.

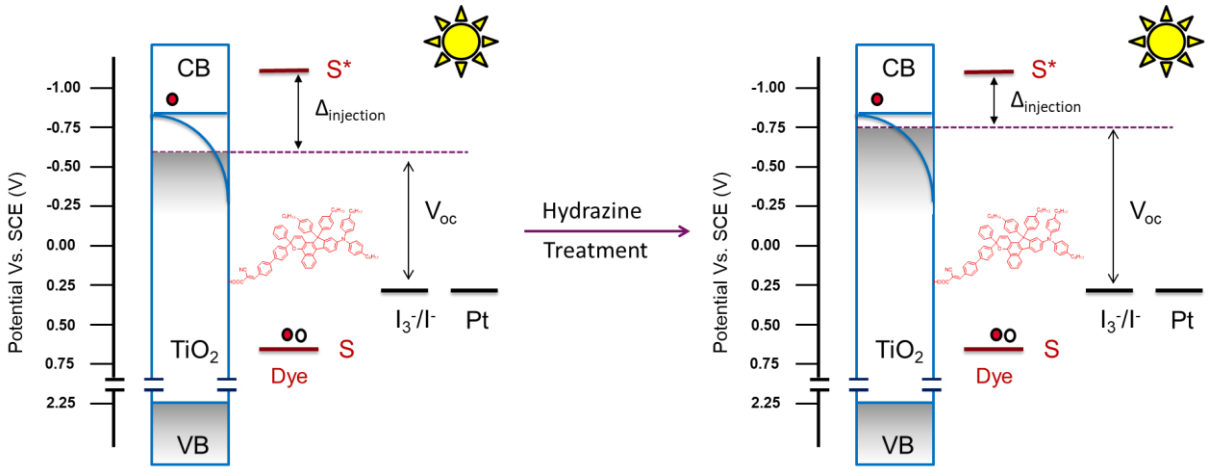

*Figure 3.26 : Effect of hydrazine pre-treatment on the PV performance of **NP2** photochromic dye cells.*

The illustration above demonstrates the impact of hydrazine on the performance of photochromic dyes. There is an upward shift of the band edge with more electrons leading to a poorer driving force for electronic injection. The question is, how then can we simultaneously improve electronic injection and avoid electron loss in traps while either conserving the generated photocurrent or even improve it?

3.2.2 Oleic Acid Post-sensitization

In the previous sub-section, we have seen that it is possible to improve the photovoltage of photochromic solar cells through filling traps in TiO_2. However, the challenge was a poor driving force for electron injection after the hydrazine treatment thus limiting the generated photocurrent. I came across some work in the literature reporting on the presence of potential active sites that remain after sensitization of the TiO_2 photoanode. Anantharaj *et. al* reported highly efficient devices with eradication of remaining active sites on the TiO_2 surface after dyes' sensitization using oleic acid (**OA**) [45]. The hypothesis is, by diminishing active sites present on the TiO_2 surface modifies the dye/TiO_2/electrolyte interface and the dynamics hence improved device performance.

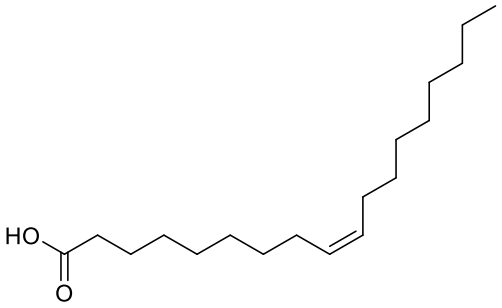

Figure 3.27 : Chemical structure of the monosaturated oleic acid (OA).

While following the same fabrication procedure as reported in chapter 1, I combined the pre-hydrazine photoanode treatment, then $TiCl_4$ treatment, dye sensitization then followed by an **OA** post-sensitization step (0.5 mM solution of OA in $CHCl_3$/t-BuOH 1/1, v/v, for 45 minutes) then finally assembled the cells and sealed. The cells were filled with the home-based electrolyte specifically designed for photochromic DSSCs and the *J(V)* characterization curves for the best device is as shown below.

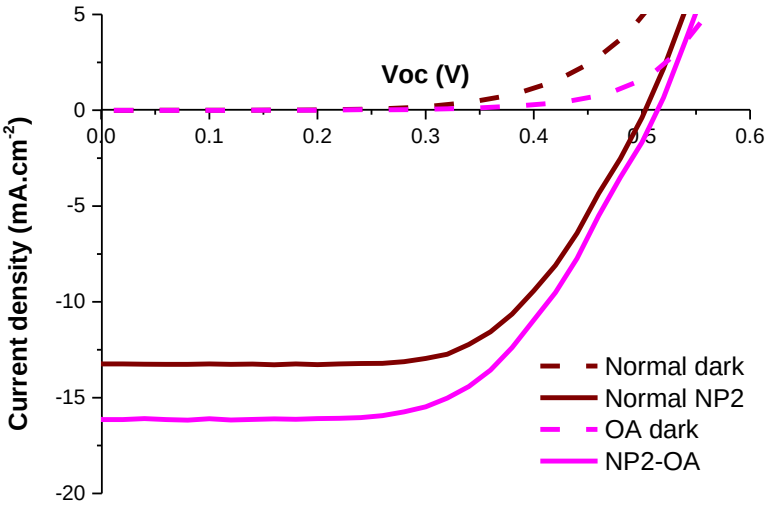

*Figure 3.28 : Comparison between normal **NP2**-based cells and the hydrazine+oleic acid treated device using **NP2** dye showing up to 4.90% efficiency at the PSS.*

The result above marks the best performance so far with photochromic DSSCs. There is a remarkable increase in the J_{sc} from 12.74 mA.cm^{-2} with an untreated device, 11.69 mA.cm^{-2} with hydrazine-treated one, and upto 15.35 mA.cm^{-2} with hydrazine-oleic acid-treated electrode. This allowed us to obtain a record efficiency of 4.90% corresponding to a 17% increase from the previously untreated cells. Interestingly, the V_{oc} was averaged to 514 mV i.e. between 502 mV without treatment and 527 mV in hydrazine-treated cell. One of the roles of OA depicted is the downward shift of TiO_2 CB thus facilitating better electronic driving force for injection coupled with filled traps [45]. The decrease in V_{oc} between the first irradiation to that at the PSS is still evident that suggests the TiO_2 surface is not fully passivated.

I transferred these treatments i.e. hydrazine + **OA** post-sensitization to **NPI** photochromic dye and the effect on the PV parameters is as shown in the table below.

*Table 3.10 : Photovoltaic parameters of the **NPI** and **NP2** based devices with hydrazine pre-treated and oleic acid post-sensitized photoanodes. The statistics of **NPI** are based on 3 devices whereas **NP2** are based on 10 devices.*

Dyes	Electrode	J_{sc} (mA.cm^{-2})	V_{oc} (V)	FF	PCE (%)
NPI	Opaque	13.76 (13.88 ± 0.08)	0.527 (0.510 ± 0.012)	0.627 (0.628 ± 0.003)	4.55 (4.45 ± 0.07)
NP2	Opaque	15.35 (16.32 ± 0.56)	0.514 (0.487 ± 0.015)	0.621 (0.593 ± 0.018)	4.90 (4.71 ± 0.10)

NPI :10cdca normal devices recorded a J_{sc}=12.59 mA.cm^{-2}, V_{oc}=0.505 V, FF=0.656 leading to a PCE=4.17%. When N_2H_4 and **OA** treatments were applied the J_{sc} increased by more than 1 mA.cm^{-2} to reach 13.76 mA.cm^{-2} with a V_{oc}=0.527 V, FF=0.627 and a PCE=4.55%. In this case, the V_{oc} was slightly improved due to better surface passivation.

On the other hand, the treated **NP2**-based devices show a larger improvement on the photocurrent density compared to the normal untreated devices. An increase in the J_{sc} can be as a result of increased number of adsorbed dye molecules. For this reason, I investigated the amount of dye on the TiO_2 of the treated electrodes. Surprisingly, after desorption, the amount of dye loading in **NP2**-N_2H_4-**OA** treated electrodes is 1.29x10^{-7} moles.cm^{-2} versus 2.15x10^{-7} moles.cm^{-2} in the **NP2**-normal counterpart. This equals to ~50% less dye compared to normal-**NP2** cell configuration. Therefore, the increased J_{sc} does not come from the number of adsorbed dye molecules.

To understand the source of increased J_{sc}, I studied the optical properties of the **NP2**-dye on a bare photoanode and in a complete **NP2**-based devices with and without the treatments and the result is as shown below.

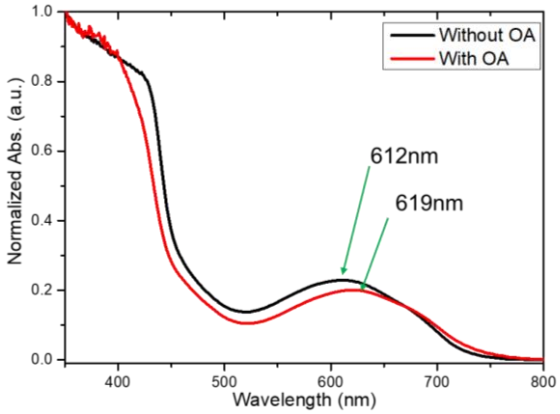

*Figure 3.29 : Absorption spectrum of a bare untreated electrode and a hydrazine-oleic acid treated transparent **NP2**-based electrode after irradiation at the photostationary state.*

In a complete device with the electrolyte, the spectra is as shown below.

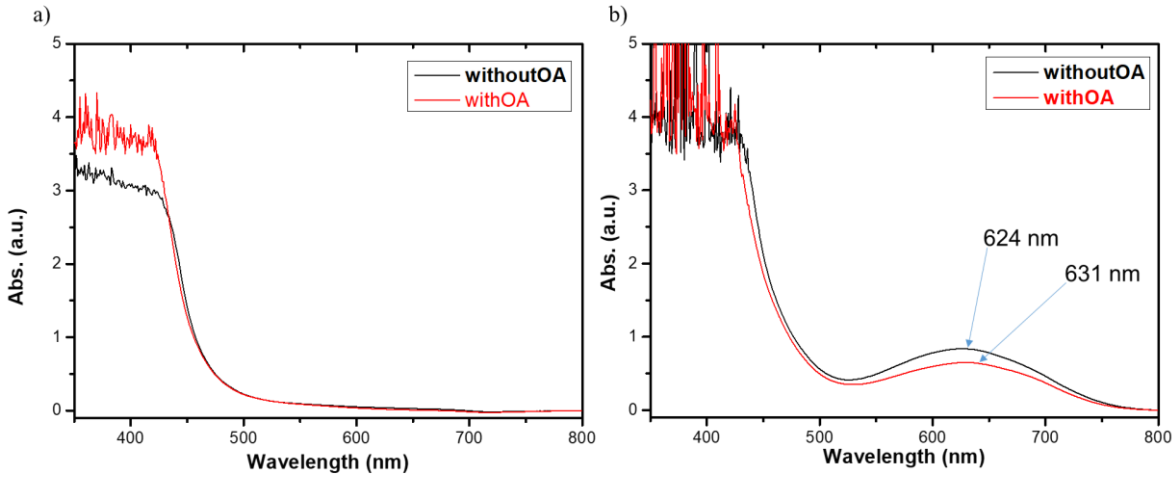

*Figure 3.30 : Absorption spectra of a complete **NP2**-based cell hydrazine and oleic acid treated with a) the spectrum of the device in the dark and b) when the cell reaches the photostationary state.*

In the dark, as seen in Fig. 3.30, there are no remarkable differences between the normal and treated devices. However, upon irradiation, the **OA** anchorage with **NP2** both on the photoanode and in complete devices, induces a slight red shift (magnitude = 7 nm) of the absorption peak of the internal charge transfer (ICT) band of the OF spectrum. This could explain the contribution to the J_{sc} in addition to the filled traps making transport in the device more efficient [42] despite the lower dye adsorption.

3.2.3 X-ray Photoelectron Spectroscopy (XPS)

From the hydrazine treatments we have established by impedance spectroscopy that a band edge shift is observed leading to a slight increase in the V_{oc}. In addition, **OA** post-sensitization leads to improved photocurrent related to a bathochromic shift the absorption spectrum of the OF. Hydrazine treatment is believed to alter the composition of the metal oxide acting as both a nitrogen source and a reducing agent thus enhancing visible light absorption [42,46,47]. Therefore, I carried out X-ray photoelectron spectroscopy (XPS) studies to investigate surface chemical compositions. To accomplish this, I studied bare TiO_2, TiO_2-hydrazine treated

electrodes and TiO_2-hydrazine treated-**NP2** dye sensitized+**OA** electrodes. The XPS spectra obtained is as shown below.

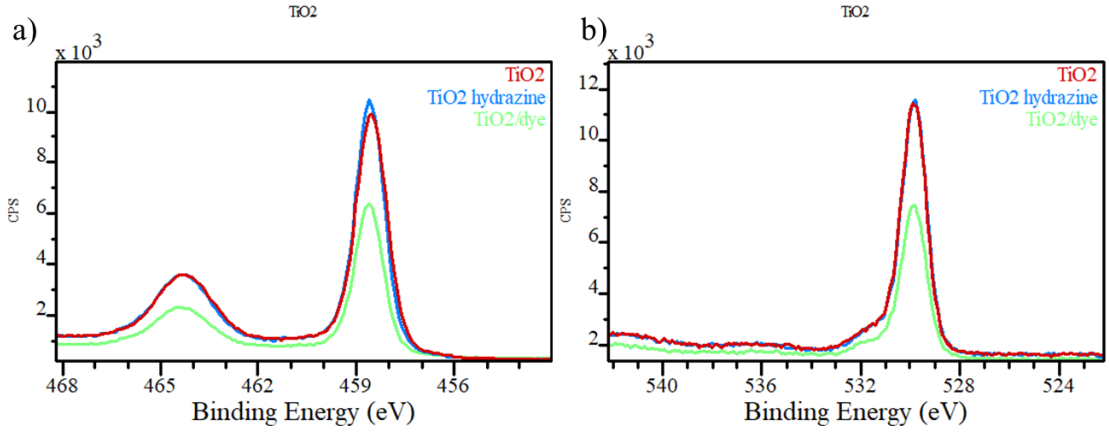

*Figure 3.31 : Position of the Ti 2p peaks b) positions of O 1s orbital peaks for the untreated TiO_2 sample (red curve), hydrazine treated (blue curve), and hydrazine-dye adsorbed-then **OA** treated TiO_2 substrates (green curve).*

The nitrogen atom was also analyzed and characterized as shown below.

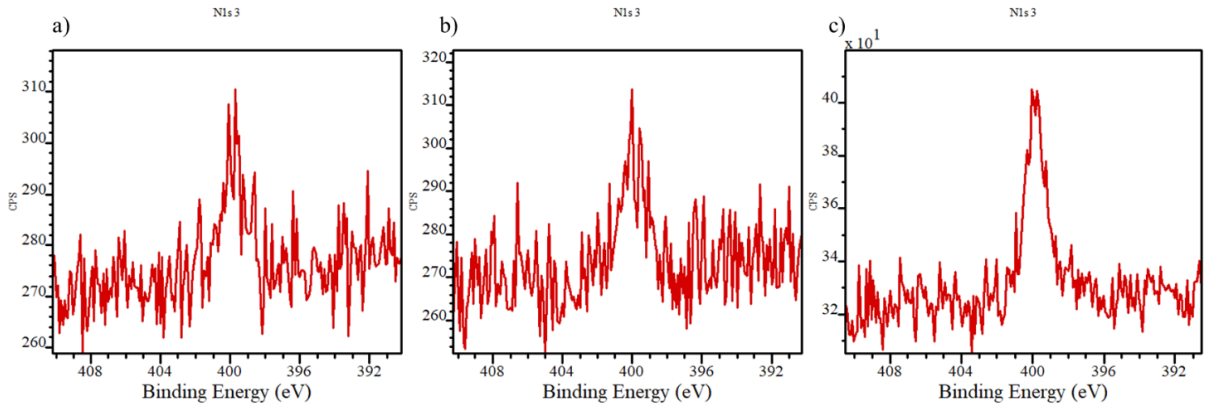

Figure 3.32 : The nitrogen composition in a) untreated TiO_2 substrate b) hydrazine-treated TiO_2 sample and c) hydrazine-treated-then, dye sensitized then oleic acid post-treated sample.

The untreated and hydrazine-treated samples in Fig. 3.31(a) show similar Ti chemical composition with differences in the peak intensity. The Ti 2p peaks at 458.6 and 464.3 eV can be attributed to Ti^{4+} $2p_{3/2}$ and Ti^{4+} $2p_{1/2}$ states, respectively. This implies that the photoanode consists of only titanium (IV) oxide and that low oxidation Ti suboxides such as TiO and Ti_2O_3 do not exist at the photoanode surface. The difference in the intensity with oleic acid treated electrodes suggests oleic acid adsorption. The same applies for the O 1s orbitals where there seem to be no chemical modification. From the spectra above, we could not tell any change in the oxidation state of the Ti. From Fig. 3.32, the results is surprising because the blank sample contains N. The mesoporous TiO_2 paste contains cellulose and terpenol into which

nitric acid is added in the process to help in the transition from semi-aqueous to semi-organic. Even after rinsing, traces of HNO_3 remain thus explaining the N source. In Fig. 3.32(c), the intensity peak of N is far pronounced because the photochromic dyes used has N atoms.

Table 3.11 : Films compositions as determined by XPS.

Atomic %	Ti	O	C	N
TiO_2 blank	24.1	52.4	23.1	0.42
TiO_2/hydrazine	24.3	53.3	22.1	0.26
TiO_2/dye/OA	18.3	40.6	40.5	0.55

Other information obtained from the XPS spectra was the valence band positioning of the semi-conductor. The result is as shown below,

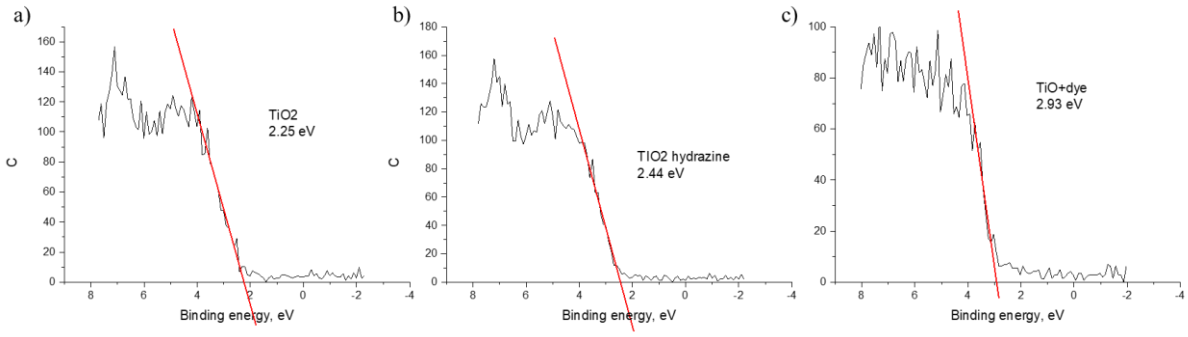

*Figure 3.33 : Valence band positioning of a) blank sample (13 µm electrode) b) hydrazine-treated 13 µm electrode and c) 13 µm hydrazine treated-**NP2** dye adsorbed and oleic acid treated.*

Fig. 3.33 above shows a positive shift of the TiO_2 valence band from the blank to hydrazine and finally with the hydrazine-dye-oleic acid substrate. The shift in the band edge observed after hydrazine treatment has already been demonstrated by impedance spectroscopy studies above.

3.2.4 Impedance studies on NP2-N_2H_4-OA treated cells

From the hydrazine-only treated **NP2**-based electrodes, we observed a positive band edge shift thus improving the photovoltage of the devices, thanks to impedance and XPS spectroscopies. Combining the N_2H_4 and **OA** post-sensitization treatments, we observe a slightly improved photovoltage compared to the normal counterpart. The slight V_{oc} improvement and huge J_{sc} increase led to a record 4.90% efficiency. I carried out an impedance study on the **NP2**-N_2H_4-OA treated cells and the result is as shown below.

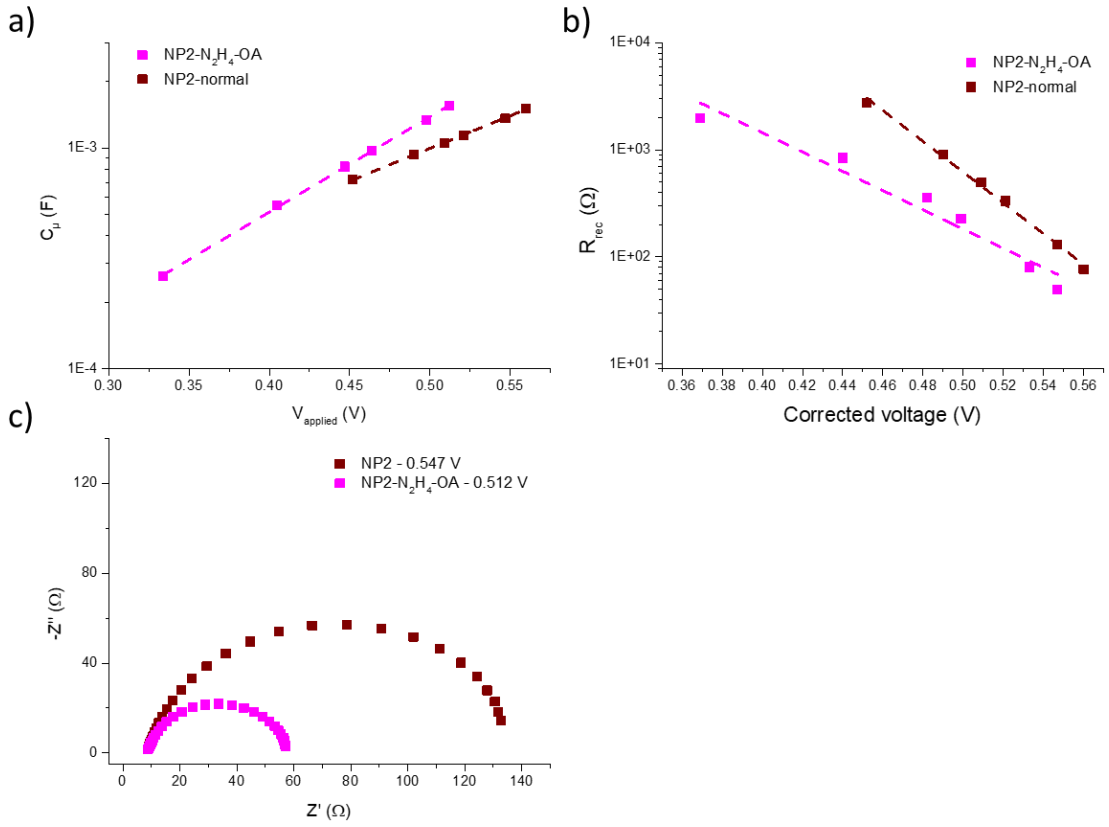

*Figure 3.34 : Shows impedance studies on **NP2**-N2H4-OA treated devices with comparison of a) chemical capacitances, b) recombination resistance at the quasi-Fermi level and c) the Nyquists plots at the corrected voltages.*

In Fig. 3.34 a), we observe a higher chemical capacitance and different slope with the N_2H_4-OA treated **NP2** devices. This suggests that the concentration of electrons in the TiO_2 CB is higher and that the TiO_2 surface has been altered. A +35mV band shift is observed with respect to the normal **NP2** devices. The recombination resistance plot at the corrected voltage in Fig. 3.34b) indicates that the recombination resistance in the treated electrodes is lower than the untreated ones. This means that the recombination is higher in treated cells, which suggests that OA did not decrease recombination but increased. This result agrees with the dye-loading experiments proving the desorptive nature of OA thus creating even more vacant spaces for I_3^- to reach the TiO_2 surface.

Finally, I applied these treatments to the cocktail dyes (**NPI** + **NP2** mixture). In most cases, the N_2H_4-**OA** treatments did not work and ended up with power conversion efficiencies lower than 4.35%. Sauvage F. *et al.* reported on the beneficial effect of decreasing the temperature during dye adsorption on the mesoporous titanium. They found out that by decreasing the grafting temperature from 60°C to 4°C, the recombination resistance increased related to increased structural order of the self-assembled dye monolayer [48]. In this connection, I performed the

hydrazine treatment on the photoanodes, followed by TiO_2 sensitization in the freezer (at -20°C) and finally post-sensitized with **OA**. The preliminary results with statistics are as shown below.

*Table 3.12 : The effect of sensitization temperature on the photovoltaic performance of **NPI** :**NP2** (1 :1) cosensitized dye solar cells at -20°C. The statistics were performed on 3 opaque cells of (13+4) µm thick photoanodes.*

DSSC	J_{sc}	V_{oc}	FF	η
NPI + **NP2** :5cdca	16.01 (15.34 ± 0.49)	0.461 (0.469 ± 0.008)	0.606 (0.609 ± 0.007)	4.47 (4.38 ± 0.08)

From the table above, we have a slightly increased J_{sc} and a lower V_{oc}. The increased photocurrent can be linked to the effect of adsorption temperature since N_2H_4 and **OA** treatments had no impact on the **NPI**/**NP2** cosensitized devices. The low V_{oc} could be as a result of desorption as observed in **NP2**-N_2H_4-**OA** based cells because dye-loading experiments could not be performed on the cocktail mixture.

3.2.5 Optical and Stability measurements of NP2-N_2H_4-OA treated devices

I have managed to obtain high performance photochromic solar cells registering up to 4.90% efficiency. I then studied their optical properties relevant for building integrated photovoltaics. The average visible transmittance of complete devices were determined and compared with normal **NP2**-based devices. The AVT of normal **NP2**-based devices is 20.6% whereas that of **NP2**-N_2H_4-**OA** devices is 30.6%. This marks a 50% increase compared to the untreated conterpart. Unexpectedly, other than improved photocurrent generation and transparency, the discolouration kinetics were greatly enhanced which is important for the transparent photovoltaics. The thermal fading kinetics were registered for complete devices in the dark as shown below.

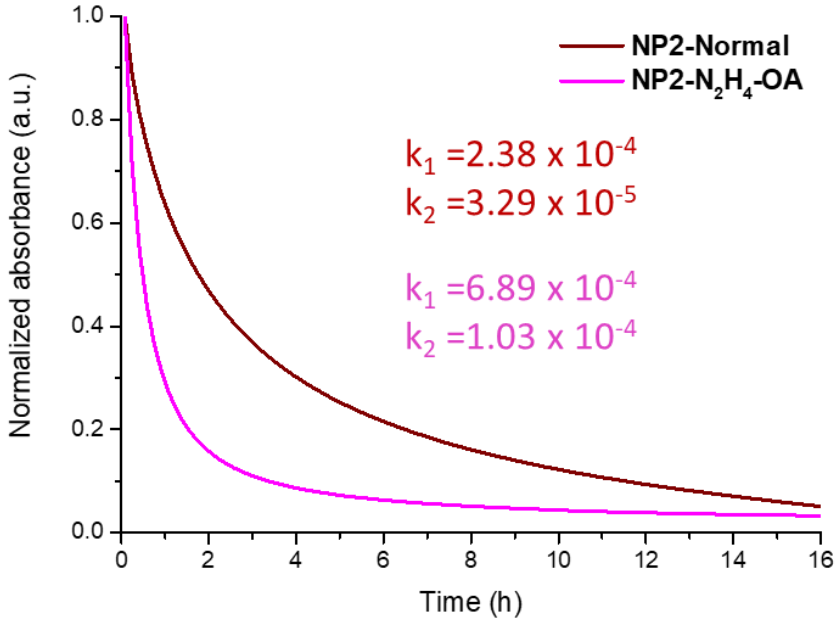

*Figure 3.35 : Dicolouration kinetics of **NP2**-normal versus **NP2**-N_2H_4-**OA** based devices with their discolouration constants in complete devices.*

For a better comparison, I normalized the spectra, as shown above, with varying absorption intensities due to the competition of oleic acid with the dye for the active sites (in good agreement with the dye loading values reported). With **OA** coadsorption, the treated solar cell loses 80% of its colouration (after attaining PSS) in an hour of storage in the darkness. This marks a huge improvement in kinetics compared to the untreated counterpart that loses 80% of its initial transparency after 7 hours of storage in the darK. The discolouration kinetics spectra were fit to a biexponential equation previously exposed in chapter 1 and 2 and the discolouration constants extracted. As evidenced in Fig. 3.35 above, the first discolouration constant, k_1, for the treated device is 3-times faster as compared to the untreated ones whereas the second one, k_2, is one order of magnitude faster. The desorption by **OA** is believed to improve the organization of the dyes on the TiO_2 surface giving them more space to undergo the isomerization process thus leading to improved ring-closure kinetics and lower residual absorbance. This unexpected result offers a new path to improve the speed for the photoresponse of the cells. **OA** plays an important role as a coadsorbant on the TiO_2 surface thus eliminating possible interactions between photochromes and sticking/entrapment in their open form isomers.

3.2.5.1 Device stability test

Finally, the stability of the devices was evaluated by performing several *J(V)* measurements consecutively. In between measurements, the devices were stored in the dark to allow them to discolour at 20°C following the laid standard ISOS-D1 protocol. The PV parameters registered are as shown below.

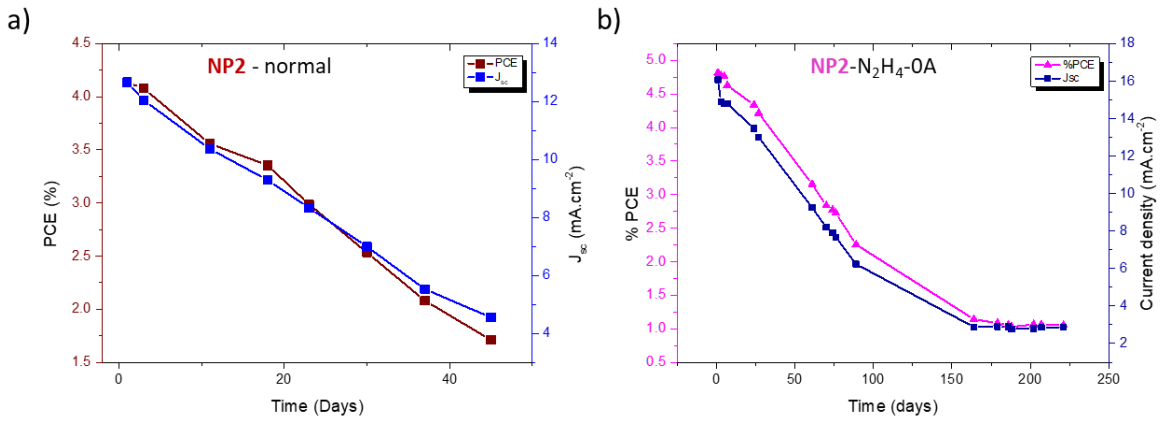

*Figure 3.36 : Stability measurements according to the ISOS-D1 protocol for a) **NP2**–normal device and b) **NP2**-N_2H_4-**OA** devices.*

Both devices preserve their photochromic behaviour during the tests but the power conversion efficiencies keep on diminishing due to a loss in the J_{sc}. The PCEs and the J_{sc} as a function of time shows that the photocurrent is most affected. Where normal **NP2**-based devices loss 50% of their initial efficiencies in 40 days, the hydrazine-OA **NP2** devices reach their half-life in 90 days (around 3 months). This demonstrates that the adopted photoanode treatments are useful to increase the shelf-life of our solar cells.

3.3 Conclusion

To conclude this chapter, I have optimized the fabrication conditions for photochromic DSSCs. A series of molecules that involves different substitutions on the champion **NPI** dye was developed and studied in detail. The addition of hydrophobic chains on the DPA unit leads to improvement in the photovoltage. Addition of alkyl chains on the photochromic unit improves the kinetics for the ring closure. **NP3**-based cells, for instance, show no V_{oc} drop which suggests that probably the addition of alkyl chains on the bridge is a good strategy to protect the metal oxide semiconductor from I_3^- hence "decent" V_{oc}s. Nevertheless, this strategy cannot be extended when alkyl chains are present on the donating unit. Cosensitization method that involves cocktail dye mixtures provide a synergetic effect leading to efficiencies up to **4.35%** based on photochromic dyes only. The pre- and post-treatment modifications of the photoanodes have proved useful to obtain highly efficient photochromic solar cells registering up to **4.90%** record efficiency with a 3-fold improvement on fading kinetics. Although the effects of electrode treatments could not be replicated in cocktail dyes, combined with low sensitization temperature, leads to high performance photochromic devices reaching **4.47%**. Thanks to impedance spectroscopy studies, we understand better the effect of chemistry and electrode treatments to the performance of photochromic DSSCs. This chapter defines a clear roadmap on structure-property relationships towards the realization of highly efficient photochromic devices in the future. The findings of this chapter allows us the opportunity to explore different possibilities through chemistry either on the electron donating or withdrawing part that I will detail in the next chapter.

3.4 References

1. Huaulmé, Q. *et al.* Photochromic dye-sensitized solar cells with light-driven adjustable optical transmission and power conversion efficiency. *Nat Energy* **5**, 468–477 (2020).
2. Koumura, N. *et al.* Alkyl-Functionalized Organic Dyes for Efficient Molecular Photovoltaics. *J. Am. Chem. Soc.* **128**, 14256–14257 (2006).
3. Ni, J.-S., Yen, Y.-C. & Lin, J. T. Organic sensitizers with a rigid dithienobenzotriazole-based spacer for high-performance dye-sensitized solar cells. *J. Mater. Chem. A* **4**, 6553–6560 (2016).
4. Joly, D. *et al.* Side chain engineering of organic sensitizers for dye-sensitized solar cells: a strategy to improve performances and stability. *J. Mater. Chem. A* **5**, 6122–6130 (2017).
5. Xu, M. *et al.* Energy-Level and Molecular Engineering of Organic D-π-A Sensitizers in Dye-Sensitized Solar Cells. *J. Phys. Chem. C* **112**, 19770–19776 (2008).
6. Jiang, X. *et al.* Structural Modification of Organic Dyes for Efficient Coadsorbent-Free Dye-Sensitized Solar Cells. *J. Phys. Chem. C* **114**, 2799–2805 (2010).
7. Malic, N., Campbell, J. A., Ali, A. S., Francis, C. L. & Evans, R. A. Fast switching immobilized photochromic dyes: Fast Switching Immobilized Photochromic Dyes. *J. Polym. Sci. A Polym. Chem.* **49**, 476–486 (2011).
8. Song, H., Li, X., Ågren, H. & Xie, Y. Branched and linear alkoxy chains-wrapped push-pull porphyrins for developing efficient dye-sensitized solar cells. *Dyes and Pigments* **137**, 421–429 (2017).
9. Lu, F. *et al.* Novel D–π–A porphyrin dyes with different alkoxy chains for use in dye-sensitized solar cells. *Dyes and Pigments* **125**, 116–123 (2016).
10. Chen, H. *et al.* Improving the photovoltaic performance by employing alkyl chains perpendicular to the π-conjugated plane of an organic dye in dye-sensitized solar cells. *J. Mater. Chem. C* **7**, 7249–7258 (2019).
11. Sobuś, J., Karolczak, J., Komar, D., Anta, J. A. & Ziółek, M. Transient states and the role of excited state self-quenching of indoline dyes in complete dye-sensitized solar cells. *Dyes and Pigments* **113**, 692–701 (2015).
12. Zhang, L. & Cole, J. M. Dye aggregation in dye-sensitized solar cells. *J. Mater. Chem. A* **5**, 19541–19559 (2017).

13. El-Zohry, A., Orthaber, A. & Zietz, B. Isomerization and Aggregation of the Solar Cell Dye D149. *J. Phys. Chem. C* **116**, 26144–26153 (2012).
14. Horiuchi, T., Miura, H., Sumioka, K. & Uchida, S. High Efficiency of Dye-Sensitized Solar Cells Based on Metal-Free Indoline Dyes. *J. Am. Chem. Soc.* **126**, 12218–12219 (2004).
15. Lee, Y.-G. *et al.* Effective Passivation of Nanostructured TiO_2 Interfaces with PEG-Based Oligomeric Coadsorbents To Improve the Performance of Dye-Sensitized Solar Cells. *J. Phys. Chem. C* **116**, 6770–6777 (2012).
16. Hara, K. *et al.* Effect of Additives on the Photovoltaic Performance of Coumarin-Dye-Sensitized Nanocrystalline TiO_2 Solar Cells. *Langmuir* **20**, 4205–4210 (2004).
17. Bisquert, J., Zaban, A. & Salvador, P. Analysis of the Mechanisms of Electron Recombination in Nanoporous TiO_2 Dye-Sensitized Solar Cells. Nonequilibrium Steady-State Statistics and Interfacial Electron Transfer via Surface States. *J. Phys. Chem. B* **106**, 8774–8782 (2002).
18. Bisquert, J. Chemical capacitance of nanostructured semiconductors: its origin and significance for nanocomposite solar cells. *Phys. Chem. Chem. Phys.* **5**, 5360 (2003).
19. Riquelme, A. J. *et al.* Characterization of Photochromic Dye Solar Cells Using Small-Signal Perturbation Techniques. *ACS Appl. Energy Mater.* **4**, 8941–8952 (2021).
20. Idígoras, J. *et al.* Highly efficient flexible cathodes for dye sensitized solar cells to complement Pt@TCO coatings. *J. Mater. Chem. A* **2**, 3175–3181 (2014).
21. Wang, Q. *et al.* Characteristics of High Efficiency Dye-Sensitized Solar Cells. *J. Phys. Chem. B* **110**, 25210–25221 (2006).
22. Wang, Q., Moser, J.-E. & Grätzel, M. Electrochemical Impedance Spectroscopic Analysis of Dye-Sensitized Solar Cells. *J. Phys. Chem. B* **109**, 14945–14953 (2005).
23. Fabregat-Santiago, F., Garcia-Belmonte, G., Mora-Seró, I. & Bisquert, J. Characterization of nanostructured hybrid and organic solar cells by impedance spectroscopy. *Phys. Chem. Chem. Phys.* **13**, 9083–9118 (2011).
24. Peter, L. M. Characterization and Modeling of Dye-Sensitized Solar Cells. *J. Phys. Chem. C* **111**, 6601–6612 (2007).
25. Pourjafari, D. *et al.* Brookite-Based Dye-Sensitized Solar Cells: Influence of Morphology and Surface Chemistry on Cell Performance. *J. Phys. Chem. C* **122**, 14277–14288 (2018).

26. Kern, R., Sastrawan, R., Ferber, J., Stangl, R. & Luther, J. Modeling and interpretation of electrical impedance spectra of dye solar cells operated under open-circuit conditions. *Electrochimica Acta* **47**, 4213–4225 (2002).
27. Idígoras, J., Pellejà, L., Palomares, E. & Anta, J. A. The Redox Pair Chemical Environment Influence on the Recombination Loss in Dye-Sensitized Solar Cells. *J. Phys. Chem. C* **118**, 3878–3889 (2014).
28. Kusumawati, Y., Hosni, M., Martoprawiro, M. A., Cassaignon, S. & Pauporté, Th. Charge Transport and Recombination in TiO2 Brookite-Based Photoelectrodes. *J. Phys. Chem. C* **118**, 23459–23467 (2014).
29. Bisquert, J., Fabregat-Santiago, F., Mora-Seró, I., Garcia-Belmonte, G. & Giménez, S. Electron Lifetime in Dye-Sensitized Solar Cells: Theory and Interpretation of Measurements. *J. Phys. Chem. C* **113**, 17278–17290 (2009).
30. Naim, W. *et al.* Transparent and Colorless Dye-Sensitized Solar Cells Exceeding 75% Average Visible Transmittance. *JACS Au* **1**, 409–426 (2021).
31. Traverse, C. J., Pandey, R., Barr, M. C. & Lunt, R. R. Emergence of highly transparent photovoltaics for distributed applications. *Nat Energy* **2**, 849–860 (2017).
32. Cole, J. M., Pepe, G., Al Bahri, O. K. & Cooper, C. B. Cosensitization in Dye-Sensitized Solar Cells. *Chem. Rev.* **119**, 7279–7327 (2019).
33. Kakiage, K. *et al.* Highly-efficient dye-sensitized solar cells with collaborative sensitization by silyl-anchor and carboxy-anchor dyes. *Chem. Commun.* **51**, 15894–15897 (2015).
34. Yang, J. *et al.* Understanding the effects of the co-sensitizing ratio on the surface potential, electron injection efficiency, and Förster resonance energy transfer. *Phys. Chem. Chem. Phys.* **22**, 5568–5576 (2020).
35. Palomares, E., Clifford, J. N., Haque, S. A., Lutz, T. & Durrant, J. R. Control of Charge Recombination Dynamics in Dye Sensitized Solar Cells by the Use of Conformally Deposited Metal Oxide Blocking Layers. *J. Am. Chem. Soc.* **125**, 475–482 (2003).
36. Son, H.-J. *et al.* Glass-Encapsulated Light Harvesters: More Efficient Dye-Sensitized Solar Cells by Deposition of Self-Aligned, Conformal, and Self-Limited Silica Layers. *J. Am. Chem. Soc.* **134**, 9537–9540 (2012).
37. Gong, J., Sumathy, K., Qiao, Q. & Zhou, Z. Review on dye-sensitized solar cells (DSSCs): Advanced techniques and research trends. *Renewable and Sustainable Energy Reviews* **68**, 234–246 (2017).

38. Nelson, J., Haque, S. A., Klug, D. R. & Durrant, J. R. Trap-limited recombination in dye-sensitized nanocrystalline metal oxide electrodes. *Phys. Rev. B* **63**, 205321 (2001).
39. Villanueva-Cab, J., Jang, S.-R., Halverson, A. F., Zhu, K. & Frank, A. J. Trap-Free Transport in Ordered and Disordered TiO_2 Nanostructures. *Nano Lett.* **14**, 2305–2309 (2014).
40. Kopidakis, N., Neale, N. R., Zhu, K., van de Lagemaat, J. & Frank, A. J. Spatial location of transport-limiting traps in TiO2 nanoparticle films in dye-sensitized solar cells. *Appl. Phys. Lett.* **87**, 202106 (2005).
41. Sudhakar, V. & Krishnamoorthy, K. Enhancing the device efficiency by filling the traps in photoanodes. *J. Mater. Chem. C* **7**, 14632–14638 (2019).
42. Islam, S. Z. & Rankin, S. E. Hydrazine-based synergistic Ti(III)/N doping of surfactant-templated TiO2 thin films for enhanced visible light photocatalysis. *Materials Chemistry and Physics* **182**, 382–393 (2016).
43. Mao, C., Zuo, F., Hou, Y., Bu, X. & Feng, P. In Situ Preparation of a Ti^{3+} Self-Doped TiO_2 Film with Enhanced Activity as Photoanode by N_2H_4 Reduction. *Angew. Chem. Int. Ed.* **53**, 10485–10489 (2014).
44. Aman, N., Mishra, T., Sahu, R. K. & Tiwari, J. P. Facile synthesis of mesoporous N doped zirconium titanium mixed oxide nanomaterial with enhanced photocatalytic activity under visible light. *J. Mater. Chem.* **20**, 10876 (2010).
45. Anantharaj, G. & Lakshminarasimhan, N. Interfacial Modification of Photoanode|Electrolyte Interface Using Oleic Acid Enhancing the Efficiency of Dye-Sensitized Solar Cells. *ACS Omega* **3**, 18285–18294 (2018).
46. Li, D. *et al.* New synthesis of excellent visible-light TiO2−xNx photocatalyst using a very simple method. *Journal of Solid State Chemistry* **180**, 2630–2634 (2007).
47. Selvam, K., Balachandran, S., Velmurugan, R. & Swaminathan, M. Mesoporous nitrogen doped nano titania—A green photocatalyst for the effective reductive cleavage of azoxybenzenes to amines or 2-phenyl indazoles in methanol. *Applied Catalysis A: General* **413–414**, 213–222 (2012).
48. Sauvage, F. *et al.* Effect of Sensitizer Adsorption Temperature on the Performance of Dye-Sensitized Solar Cells. *J. Am. Chem. Soc.* **133**, 9304–9310 (2011).

CHAPTER 4 : Impacts of Donor-Acceptor Modifications on the performance of Photochromic DSSCs.

Abstract

This far we have developed an entire family of dyes termed **NP**series from which structure-property relationships were established. The photochromic dyes presented absorb a photon causing isomerization. The open form isomers demonstrate a push-pull effect with a strong absorption in the visible range. The generated opened form molecules are excited and donate an electron from donor part that travels through a π-bridge towards the electron accepting and anchoring part. This chapter shall focus on the design and modification of the donor and acceptor moieties for high performance photochromic dye-sensitized solar cells (pDSSCs) with iodide-, metal-based and TEMPO-based electrolytes.

4.1 Effect of Donor-Acceptor architecture on Photochromic DSSCs

4.1.1 Introduction

To this point, photochromic dyes have been applied in solar cells using iodine-based electrolyte and a platinum counter electrode [1]. For the application of new electrolytes in a photochromic dye-sensitized solar cell (pDSSCs) configuration, the energy levels of the photosensitizer need to match the conduction band of TiO_2 and the redox potential of the couple for effective electronic injection and dye regeneration, respectively. The photocurrent generated in the solar cells is associated with the light harvesting capabilities of the dye, the positioning of its frontier energy levels and the recombination kinetics at the TiO_2/dye/electrolyte interface (as also demonstrated in chapter 3) [2,3].

Dai P. *et al.* reported organic dyes based on dithienopyrrole (DTP) and bis(amine) electron-donating units to investigate their effect in DSSCs. In their findings, DTP is a promising terminal electron donor with several attractive properties such as an increased maximum molar absorption coefficients and extended absorption bands, strong charge transfer interactions and allowed application of cobalt electrolytes [4].

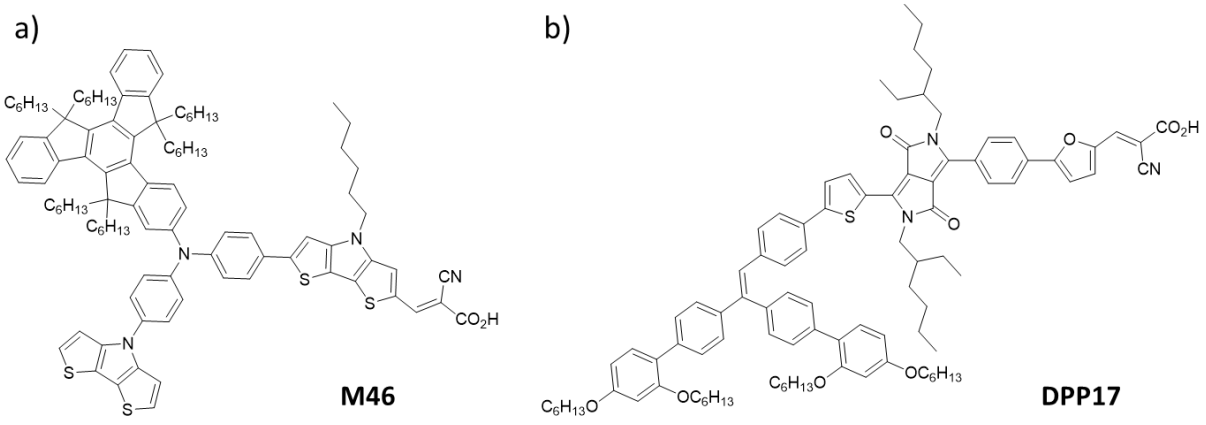

*Figure 4.1 : Chemical structures a) **M46** and b) **DPP17** based on dithienopyrrole (DTP) and on diketopyrrolopyrrole (DPP), respectively.*

Grätzel *et al.* employed electron-donating amine with a thiophene unit connecting it to the diketopyrrolopyrrole (DPP) chromophore to facilitate electronic communication within the molecule. They also applied the standard *para*-hexyloxytriphenyl amine and indoline-based donors with varying steric bulkiness for the implementation of cobalt-based redox shuttle. An increased conjugation in the indoline donors resulted in a better absorption in the visible region with an increased molar extinction coefficient in this region up to ~65,000 $M^{-1}cm^{-1}$. This led to increased light harvesting efficiency hence a power conversion efficiency exceeding 10% in **DPP17**-based devices using cobalt tris-bipyridyl complex $[Co(bpy)_3]^{3+/2+}$ electrolyte [5]. Other donor group moieties disclosed for donor-pi-acceptor dyes are based on phenothiazine and carbazole units [6–8].

The impact of electron donor moiety on performances was also unravelled for **RK** dyes as shown in Fig. 4.2 below.

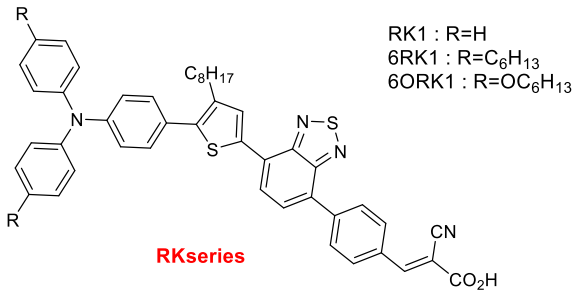

Figure 4.2 : Example of metal-free organic sensitizers designed and synthesized in our group.

With the aim to tune the absorption spectrum and improve the solubility of **RK1**, electron donor modifications were employed by replacing R above with either an alkyl or an alkoxy chain giving **6RK1** or **6ORK1**, respectively. These substitutions were associated with a

bathochromic shift of the ICT band resulting in improved PV performances surpassing 10% efficiency barrier [9].

On the other hand, a strong electron-withdrawing group as an acceptor to facilitate the push-pull effect is also desirable. The effectiveness of the acceptor moiety defines the electron transfer from the donor, tunes the energy levels and modulates the absorption spectra resulting in improved photovoltaic (PV) performance in devices. Several electron-accepting groups have been applied and reported in the DSSCs community. Examples include benzothiadiazole [10–12], benzoxadiazole [13], quinoxaline [14,15], isoindigo [16–18] just to name a few.

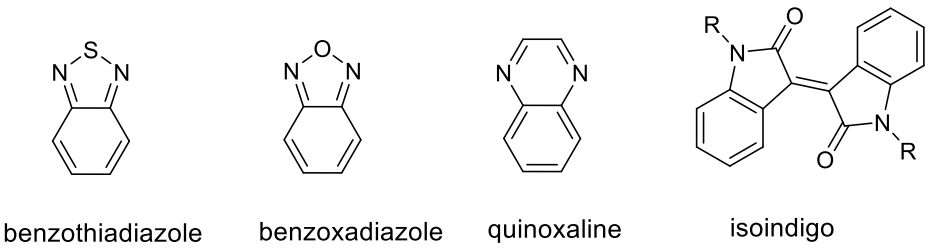

Figure 4.3 : Examples of electron-withdrawing groups applied in photosensitizers.

Benzothiadiazole moiety has been introduced in classical organic dyes in our group. In the work we reported in 2020, we designed dyes coded **YKP-88**, **YKP-137**, **DJ-214**, **MG-207** and **MG-214**, all bearing a benzothiadiazole moiety. The dyes differ from the substitution of the electron-donating TPA unit or from the spacer group close to the anchoring function.

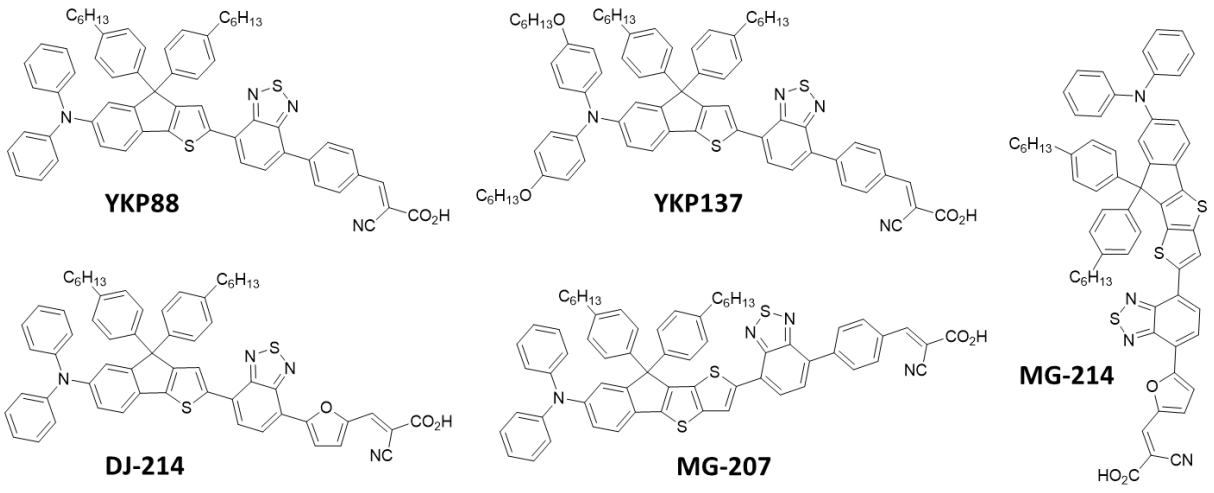

Figure 4.4 : Chemical structures of photosensitizers reported in our group bearing benzothiadiazole moiety.

The benzothiadiazole unit is connected to a benzene ring in **YKP-88** and **YKP-137** with the later possessing two hexyloxy chains on the electron-donating part resulting in a 28 nm

bathochromic shift in its internal charge transfer (ICT) band. **DJ-214**, **MG-207** and **MG-214** have a furan, a benzene and a furan attached to the benzothiadiazole moiety towards the anchoring function. **MG-207** and **MG-214** have a thienothiophene unit at the π-bridge. The thiophene in **DJ-214** was swapped for a thienothiophene unit in **MG-214** resulting in not only only a +52 nm red shift but also an intense hyperchromic shift with varying photovoltaic performances. This work demonstrates the impact of donor and acceptor moieties on the optoelectronic, energy level determination, absorption and photovoltaic properties of classical organic dyes designed for solar cells. These properties allowed for the application of various electrolytes leading to efficiencies close to 10% in iodine-based electrolyte and up to 7.5% in ionic liquid-based electrolytes and up to 5% with cobalt-based electrolytes. The variations resulted in a pallette of colours ranging from pink to violet-blue hues [12].

The electrolyte is a key component in DSSCs that allows for the conductance of charges between the positive and the negative electrode. So far, I have worked with the I_3^-/I^- redox couple and found the optimum conditions for photochromic solar cells. The main drawback with this redox couple is the limited photovoltage that can hardly surpass 0.8 V due to V_{oc} dependence on the TiO_2 band edge level with reference to couple's redox potential. Efforts to improve the photovoltages of photochromic solar cells by changing the surface dipole moment through additives e.g. *tert*-butylpyridine, was accompanied by poor performances from the low J_{sc}. This is due to the close energy level of our dyes' lowest unoccupied molecular orbitals to the TiO_2 conduction band (CB). Photoanode treatments in the previous chapter increased slightly the V_{oc}'s but averaged at ~540 mV. In addition, the average visible transmittance (AVT) in the non-activated and activated states of photochromic DSSCs is negatively impacted by the iodine-based electrolyte that shows competitive absorption in the UV-vis range [19] leading in some cases to lower dyes' activation. The questions are,

- Can these design principles to improve the performances of DSSCs based on classical organic dyes be transferred to photochromic organic dyes?
- Can we increase the V_{oc}'s of photochromic DSSCs by using new redox couples whose the potential is lower?
- Can we make more transparent cells by designing low visible light absorption electrolytes?

In this respect, we have done chemical modifications on the best performing photochromic dyes **NPI** and **NP2** with the goal to either alter the energy levels for the application of new redox couples or improve molar absorptivities thus increasing the photocurrent generated. I have classified these modifications into two i.e. electron donor function and electron acceptor function modifications.

4.1.2 Electron Donor modifications

I have briefly outlined above the impact on the donor modification when classical organic photosensitizers are applied in dye solar cells. Our team has also laid a foundation on modifications and their PV impacts in devices. In this section, I will focus on two sub-divisions i.e. **QH138** and **JoLi135** which are dyes synthesized and characterized by previous members of our team postdoc Dr. Quentin Huaulmé and Dr. Liotier Johan, respectively. The second sub-division shall focus on dyes using a completely modified donor-unit synthesized by currently a 2nd year PhD student, Samuel Fauvel, based on carbazole moiety termed **SF** family. The goal of this study is to understand how the modifications of the donating unit impacts the photochromic behaviour and the different photovoltaic parameters and the performance in solar cells. I will also discuss the compatibility of these modifications with various electrolytes.

4.1.2.1 **JoLi135** and **QH138**

These two photosensitizers have inspirations drawn from **NP2** dye. I fabricated devices based on these dyes, first with an iodine-based redox couple and then replaced with cobalt-based metal complex and TEMPO/TEMPO$^+$ redox couples. The chemical structures of the 3 dyes are as shown below,

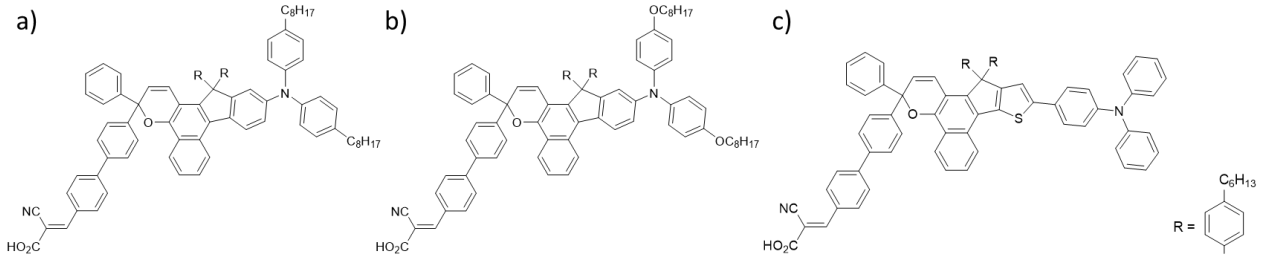

*Figure 4.5 : Molecular structures of a) **NP2** b) **JoLi 135** and c) **QH138** photochromic dyes in their closed form configurations.*

NP2 was chosen to allow for comparison and deduction of structure-property relationships. The structural difference between **NP2** and **JoLi 135** is the presence of C_8 alkoxy chains on the periphery in the later instead of C_8 alkyl chains in the former. The impact of such modification

is well documented in the literature on classical dyes (**D35** dye) [20] including by our group (**YKP-137**) [12].

Wang *et. al* designed and synthesized triphenylamine (TPA) dyes coded (**WR1-5**) featuring a thiophene and a benzene as pi-conjugated spacer with the donating unit and their influence on photovoltaic properties. In their findings, the positioning of the thiophene and benzene with respect to the TPA donor unit can influence various electro-optical properties such as the molar extinction coefficients and the maximum absorption peaks [21]. Other works also reported the use of thiophene π-spacers to increase electronic communication within the photosensitizer thus extending conjugation [22]. Therefore, in **QH138**, the goal is to increase the electron-donating property via insertion of an electron-rich thiophene and a phenyl ring at the indeno-fused position with respect to **NP2** thus improving the optoelectronic properties.

Consequently, the donor modifications resulted in the following changes in the optical properties.

4.1.2.1.1 Optical Characterizations and photochromic properties in solution

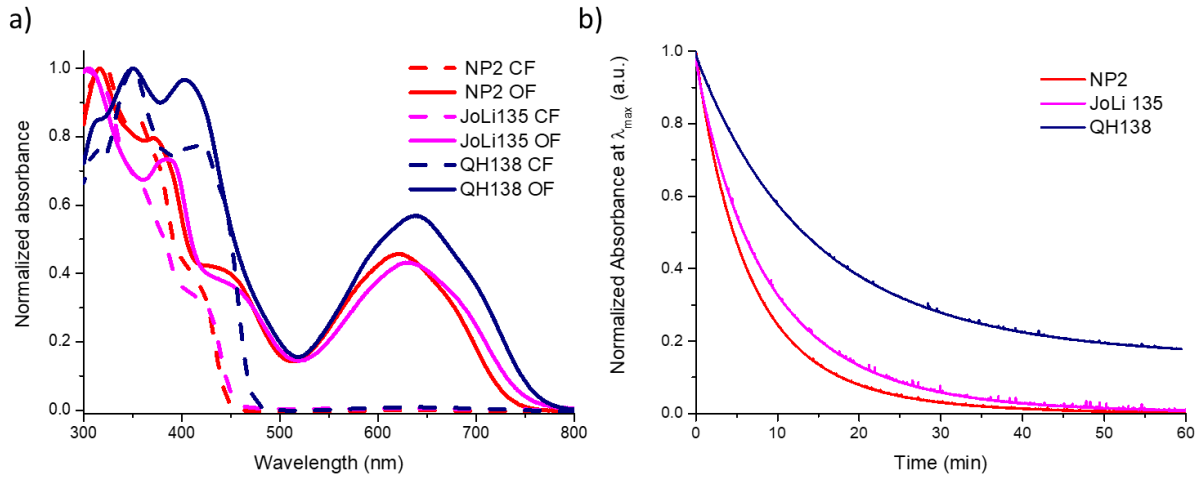

*Figure 4.6 : a) Normalized absorption spectra of **NP2**, **JoLi 135** and **QH138** in toluene solution (10^{-5} M, 25°C) in the dark (dotted lines – closed forms) and under continuous light (solid lines – opened forms). b) Discolouration kinetics of **NP2**, **JoLi 135** and **QH138** after irradiation until the photostationary state (PSS) and registered in the dark.*

From the Figure 4.6, we can see that **NP2** and **JoLi 135** have comparable absorption spectra in their closed forms. Slight differences are observed in their opened forms spectra showing a small red shift. However, **QH138** shows observable differences both in its closed and opened forms absorption spectra. The absorption spectrum of the CF is shifted towards the visible

range. The ICT band of the OF shows a hyperchromic effect with respect to **NP2** and **JoLi 135** with an A_{eq} at 0.67. The extracted optical values are as shown in the table below.

*Table 4.1 : The optical parameters of **NP2**, **JoLi 135** and **QH138**.*

Dye	λ_{max} CF (nm)	λ_{onset} CF (nm)	λ_{max} OF (nm)	λ_{onset} OF (nm)	ΔE_{opt} OF (eV)	A_{eq}	k (s^{-1})
NP2	320	450	620	730	1.70	0.38	2.3×10^{-3}
JoLi 135	306	450	630	750	1.65	0.32	1.7×10^{-3}
QH138	350	470	638	760	1.63	0.67	9.9×10^{-4}

The table above shows the variations in the ICT band where **NP2** dye shows an onset of this band at 730 nm, red-shifted extension by 20 nm upon substitution by an alkoxy chain in **JoLi 135** and by a further 10 nm in the case of **QH138**. In comparison to **NP2**, **JoLi 135** shows a slightly faster discolouration constant whereas that of **QH138** is slower by one order of magnitude, which also explains the high colourability of this dye.

4.1.2.1.2 Energy level determination

For application of these dyes in solar cells, the energetic positions were determined to check if they match DSSC components. The experimentally determined HOMO and LUMO levels (from cyclic voltammetry) are as shown in the diagram below.

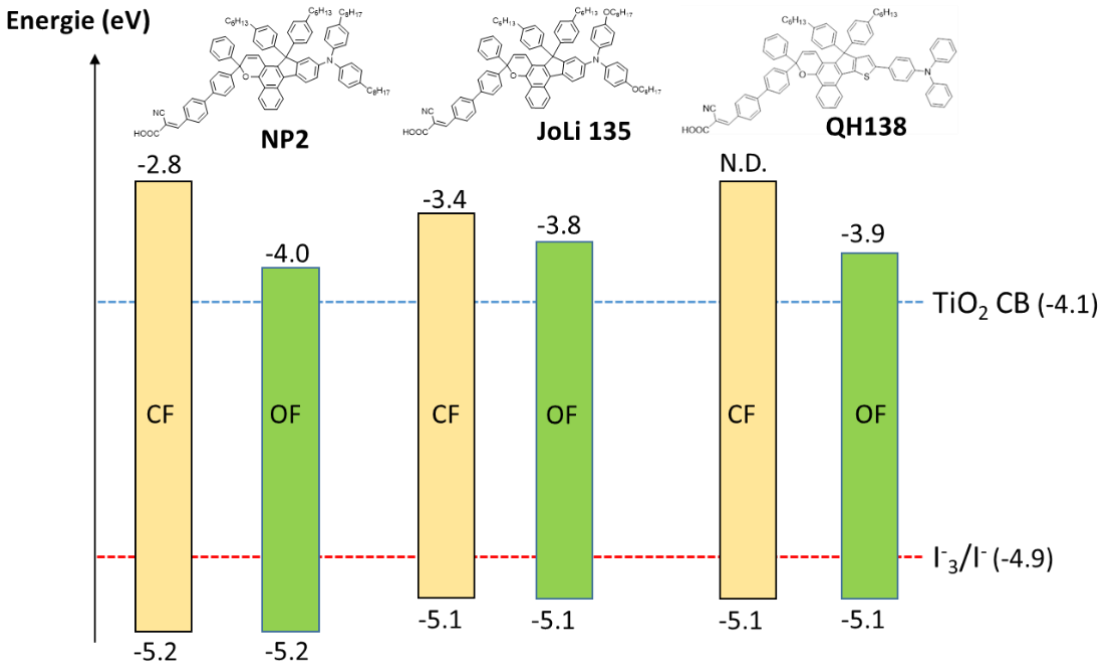

*Figure 4.7 : Energy level diagram for **NP2**, **JoLi 135** and **QH138** dyes as determined by cyclic voltammetry in their closed (CF) and opened (OF) forms. (DCM, $tBAPF_6$, at 25 °C for the CFs and 0 °C for OF, 100 $mV.s^{-1}$).*

From the data above, all the dyes, irrespective of their configuration, seem to be suitable for application in DSSC layout because the energy levels match for effective operation. The HOMO levels for both the CFs and OFs seem less impacted by the nature of electron-donating unit but the thermodynamic cascade remains favourable for regeneration by the I_3^-/I^- redox couple. However, the LUMO levels show some differences. For example, the CFs of **NP2** and **JoLi 135** have a difference of 0.6 eV. Upon isomerization, the OFs of these dyes have a 0.2 eV difference. This suggesting that a better electronic injection into TiO_2 under operational conditions can be expected with **JoLi 135**. **QH138** also shows quasi-similar LUMO compared to **NP2**.

4.1.2.1.3 Devices characterization and photovoltaic performances

After the optoelectronic characterizations, these dyes were implemented in a DSSC set-up and new redox mediators were tested. First, iodine-based electrolyte was applied to make comparison with the state-of-the-art photochromic **NP2**-based DSSC.

4.1.2.1.3.1 Iodine-based electrolyte

The optimized home-based iodine electrolyte for photochromic DSSCs was used and the result is as shown below.

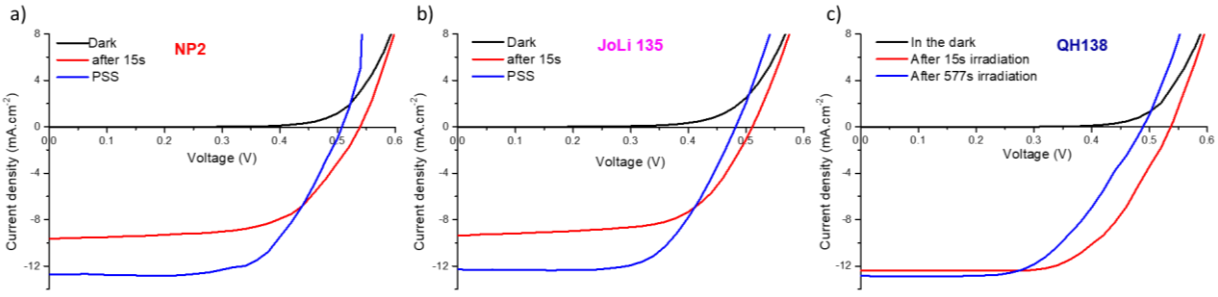

*Figure 4.8 : J(V) curves of a) **NP2**, b) **JoLi 135** and c) **QH138** dye solar cells with opaque electrodes (13+3 µm) and dye:5CDCA ratio where the dark curve in under dark, red curve is the first irradiation and the blue curve at the PSS/after a given time under standard global AM 1.5 solar conditions.*

The statistics were performed on three opaque solar cells and the results are as shown in the table below.

*Table 4.2 : The photovoltaic performances of **NP2**, **JoLi 135**, with statistics based on 3 cells, and **QH138** based on 2 devices.*

Dye	J_{sc} (mA.cm^{-2})	V_{oc} (V)	FF	PCE (%)
NP2	12.74 (13.55 ± 0.67)	0.503 (0.491 ± 0.009)	0.649 (0.620 ± 0.020)	4.16 (4.12 ± 0.04)
JoLi 135	12.29 (12.31 ± 0.02)	0.482 (0.486 ± 0.004)	0.637 (0.630 ± 0.007)	3.78 (3.77 ± 0.00)
QH138	12.84 (13.08 ± 0.23)	0.488 (0.468 ± 0.020)	0.571 (0.555 ± 0.016)	3.58 (3.40 ± 0.18)

The photochromic behaviour of all dyes DSSCs are similar i.e. the photocurrent increases as a function of irradiation time until they reach the PSS accompanied by a V_{oc} drop. The PV parameters of **JoLi 135** are J_{sc}=12.29 mA cm^{-2}, V_{oc}=482 mV, FF=0.64 and PCE=3.78% whereas **NP2** has a J_{sc}=12.74 mA cm^{-2}, V_{oc}=503 mV, FF=0.65 and PCE=4.16% with the difference between them being the donor unit. The photogenerated current in **JoLi 135** is lower compared to reference **NP2**-based device despite the higher $\Delta G_{injection}$ as shown by the energy diagram (Fig. 4.7 above). However, the $\Delta G_{regeneration}$ is lower suggesting a retarded dye regeneration process.

On the other hand, **QH138** shows a ‘‘reverse behaviour’’ : this means that the performance at the PSS is lower than the performance measured right after the start of the irradiation. Notably, the V_{oc} drop takes precedence on the J_{sc} increase thus leading to lower PCE loss with irradiation time. The PV parameters of **QH138** after the first irradiation are J_{sc}=12.38 mA cm^{-2}, V_{oc}=536 mV, FF=0.62 and PCE=4.14% and after 10 minutes the J_{sc}=12.84 mA cm^{-2}, V_{oc}=488 mV, FF=0.57 and PCE=3.58%. This result indicates that the J_{sc} increase is <1 mA cm^{-2} and a V_{oc} decrease magnitude at 50 mV in 10 minutes. The question is, why does the intense absorption of **QH138** not result in improved J_{sc}? Is there increased recombination with **QH138** dye? To understand the photovoltaic characteristics of these dyes’ devices, I carried out a small-signal perturbation study to deduce structure-function relationship.

4.1.2.1.3.1.1 Impedance Spectroscopy

The EIS studies were performed for **JoLi 135** and **QH138** –based devices of the cells in the dark and under illumination at the photostationary states as shown below,

4.1.2.1.3.1.2 **JoLi 135**

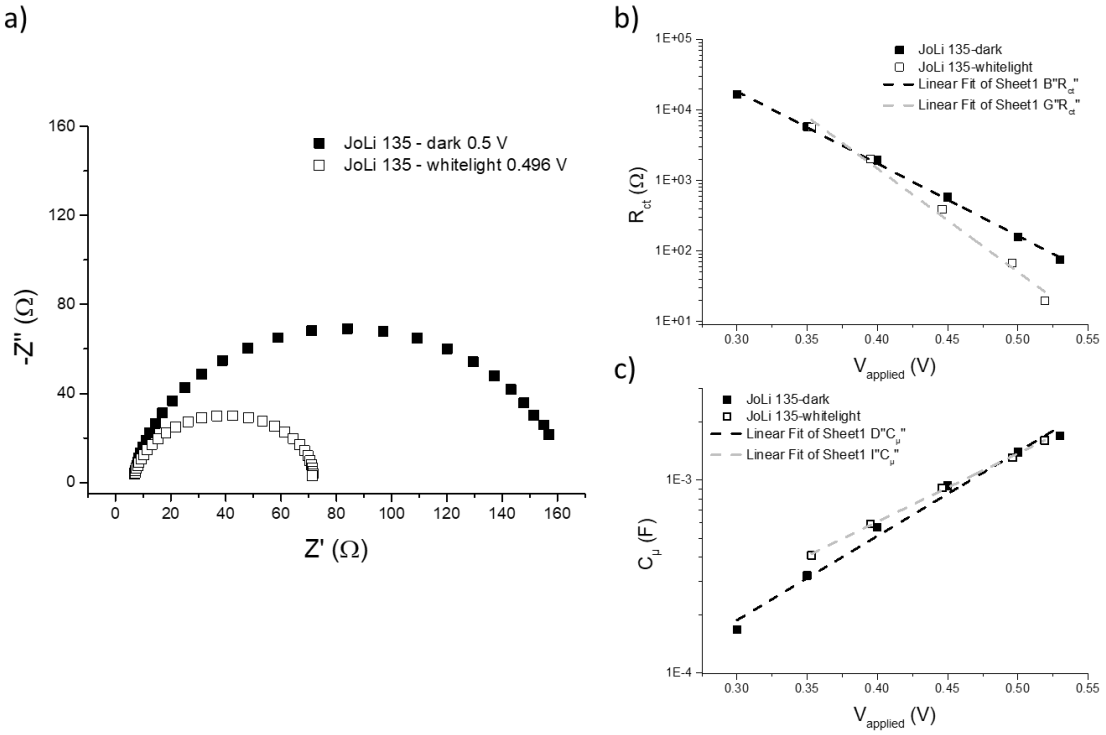

*Figure 4.9 : a) Nyquists plots of **JoLi 135**-based solar cell before and after activation under different illumination conditions, b) recombination resistances as a function of d.c. voltage in the dark or open circuit voltage under white light irradiation, and c) chemical capacitances after fitting to an equivalent circuit.*

The Nyquists plots in Fig. 4.9 a) of **JoLi 135** –based devices using iodine electrolyte demonstrates a classical behaviour of dye solar cells demonstrating a shrink in the recombination arc as a function of irradiation conditions. In Fig. 4.9b) the recombination slopes change from the dark to white light illumination generating the open form isomers. The recombination parameter, β, increases from 0.61 in the dark to 0.88 under operating conditions. The chemical capacitances at the different applied potentials or V_{oc} are comparable and lie on the same line. Such a behaviour in the chemical capacitance element suggests that the band edge of the metal oxide does not shift as a function of photochromism.

To investigate the impact of the alkoxy chain in place of the hydrophobic alkyl chains as in **NP2**-based device, I compared the capacitive behaviour of the two systems.

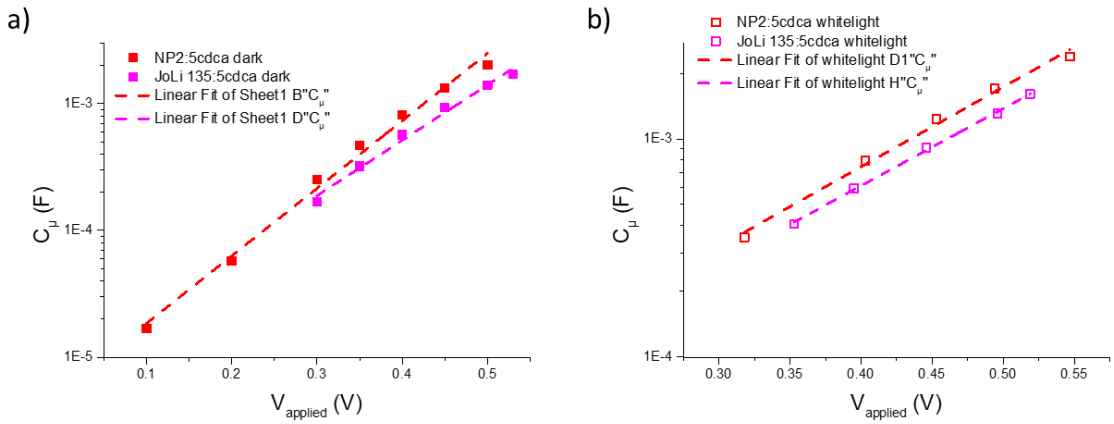

*Figure 4.10 : Comparison of the chemical capacitances of the **NP2** and **JoLi 135** –based devices under the different illumination conditions.*

The capacitance versus the device voltage above demonstrates an exponential dependence on the open-circuit voltages according to the exponentially distributed trap states in the metal oxide and there seem to be slight differences. The capacitance values in **NP2**-based cells are higher than **JoLi 135** ones at all d.c. voltages in the dark and the V_{oc}'s under white illuminations. The plots are parallel to each other suggesting a possible band edge shift in between the systems [23]. I corrected these shifts through displacement to deduce structure-function relationship at the same electron density and the nature of recombination compared as shown below.

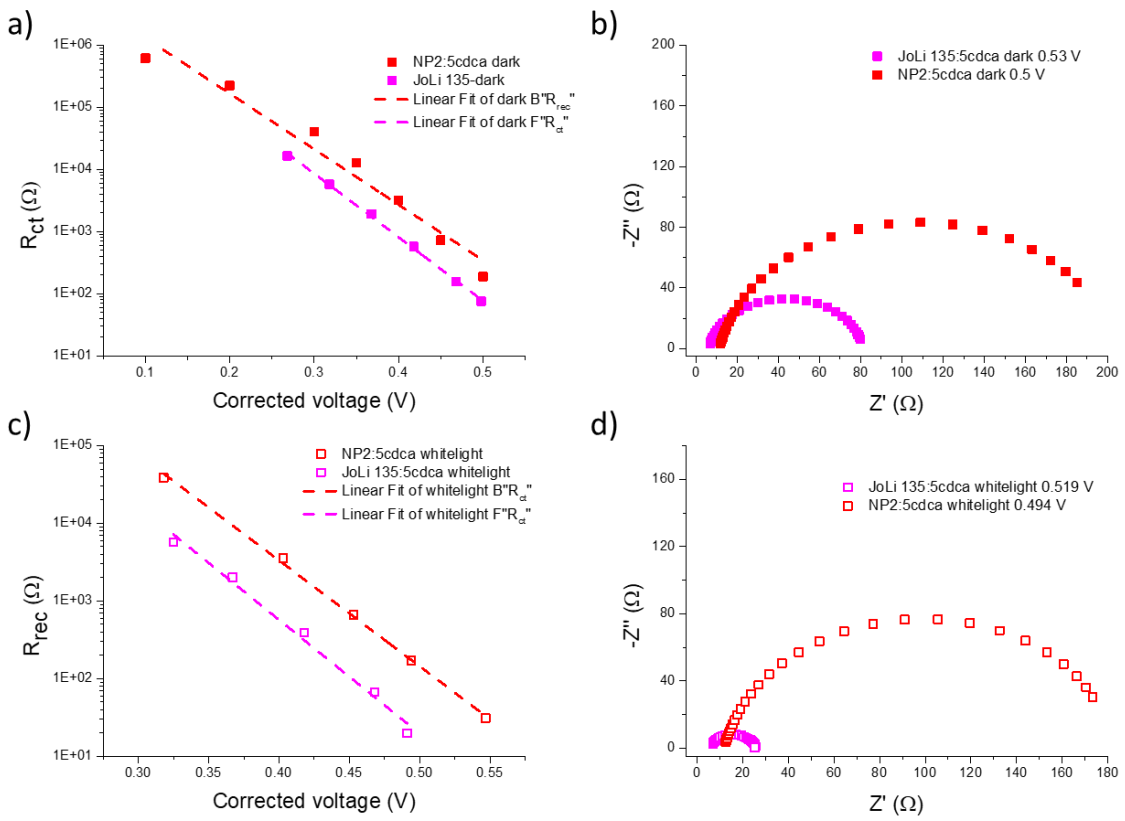

Figure 4.11 : a) and b) charge transfer resistance in the dark, c) and d) recombination resistance under illumination at the corrected voltages with their corresponding Nyquist plots.

The recombination resistance of the **NP2**-based cell is higher than the **JoLi 135**-based cell irrespective of the irradiation conditions. The replacement of alkyl tails with alkoxy ones increases recombination rate in photochromic DSSCs. The diameter of the recombination arc is larger in **NP2**-devices than in **JoLi 135** ones and even more upon surface activation of the dyes. This behaviour is not the one that we expected when we designed **JoLi 135**, based on the literature data of classical dyes, the alkoxy groups usually benefit to the performances by lowering the recombination process.

In summary, the design principles laid for classical photosensitizers that incorporate long alkoxy chains as a method to enhance molar extinction coefficients and suppress recombination [24] are not transferrable to novel photochromic dyes.

4.1.2.1.3.1.3 **QH138**

The EIS study is as follows,

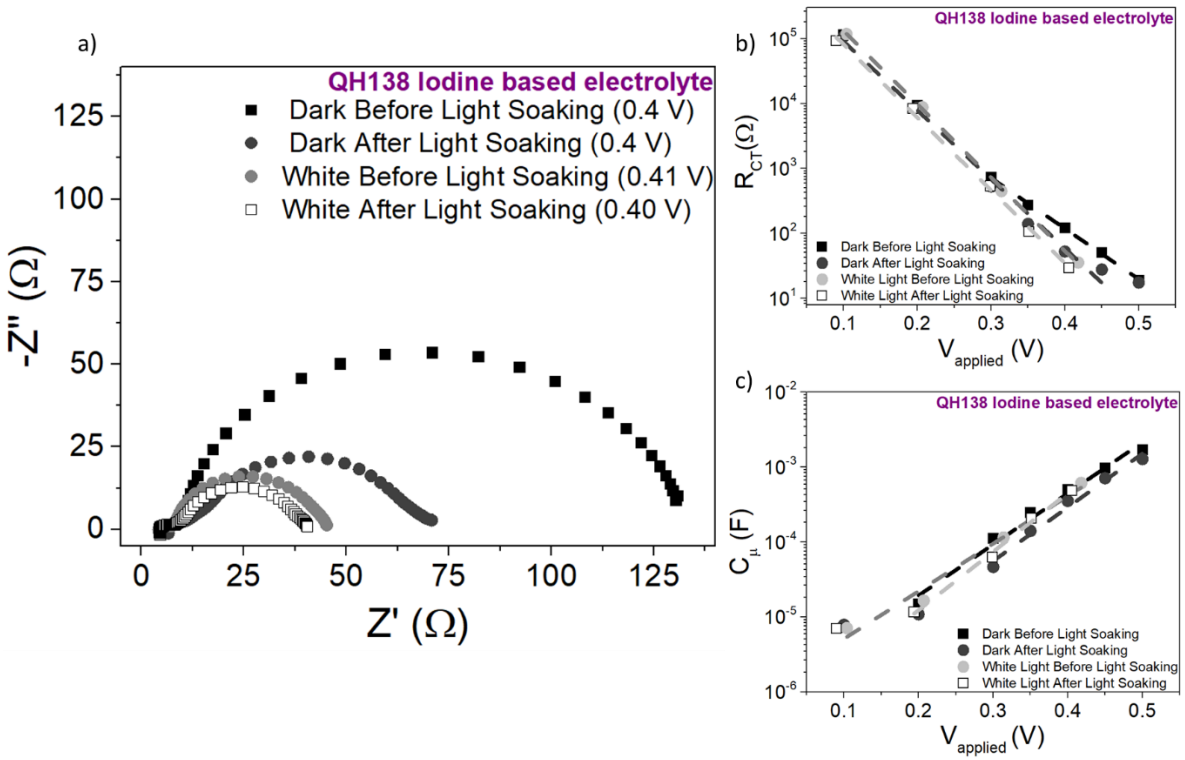

*Figure 4.12 : a) Nyquists plots of **QH138**-based solar cell before and after activation under different illumination conditions, b) the corresponding charge transfer resistances and c) their respective chemical capacitances.*

From Fig. 4.12a above, the diameter of the semicircle giving the first approximation of the charge transfer resistance decreases by nearly 3-fold upon exposure to illumination. Given that the dye induces no CB shift upon isomerization as shown in Fig. 4.12c, the huge V_{oc} loss could be linked to the accelerated recombination kinetics. The continual loss of the V_{oc} is observed in the Nyquist plot where the dark impedance performed on the fully activated cell is compared with its white impedance counterpart. In both scenarios, there is a decrease in the recombination arc. More investigations to separate transport and recombination limitations on such molecules - containing a thiophene/furan (electron-rich moiety) - are required as this behaviour seems typical.

A similar analysis was performed with reference to **NP2**, the impedance spectroscopy analysis is as shown below.

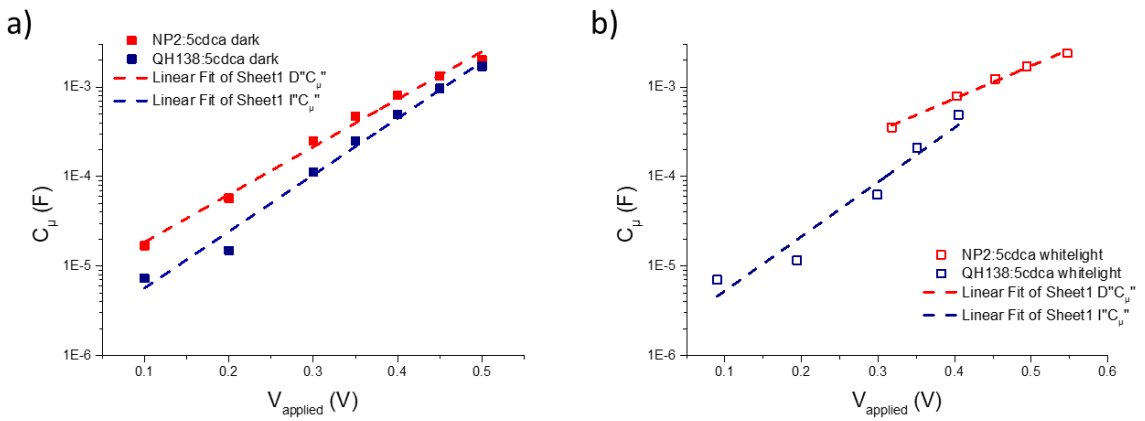

*Figure 4.13 : Comparison of the chemical capacitances of **NP2**- and **QH138** –based devices.*

The electron density in the conduction band of **NP2**-based devices is higher than that of **QH138** ones. There is also a CB shift in between the dyes. The recombination slope of **QH138**-device does not change much as a function of irradiation conditions. The β values changes from 0.56 in the closed form to 0.67 at the photostationary state under irradiation. To compare the recombination behaviour with the reference **NP2**, I made voltage correction and plotted the recombination resistances as below.

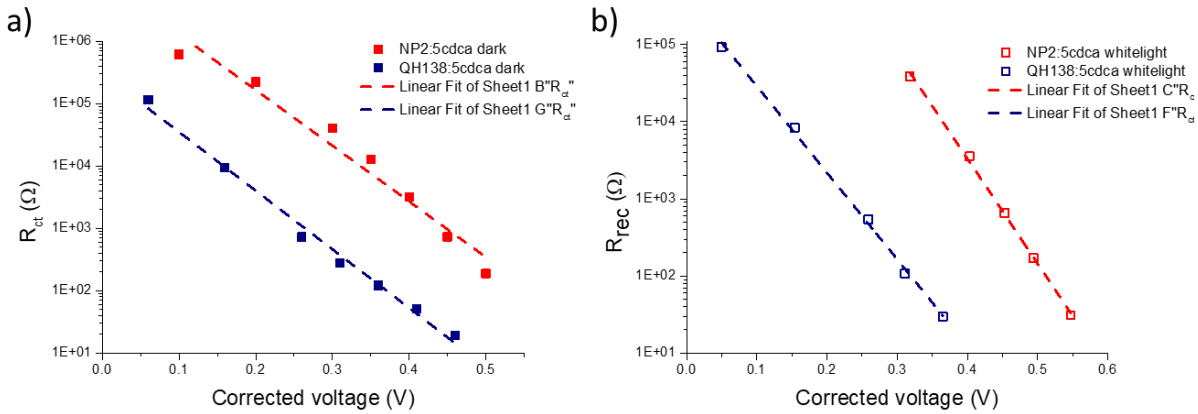

Figure 4.14 : Recombination resistances at the corrected voltages a) in the dark and b) under whitelight irradiation.

The plots above, show same behaviour as observed in **JoLi 135** devices with reference to **NP2** ones. The recombination resistance of **NP2**-based device is higher than **QH138** and **JoLi 135** ones irrespective of the irradiation conditions. This suggests that, eventhough the replacement of the hydrophobic alkyl chains with alkoxy chains and addition of a thiophene between the indeno-fused and the TPA moieties are good strategies to improve the absorption properties, they increase the recombination a lot hence lower photovoltaic performances.

4.1.2.1.3.2 Metal-based complex electrolyte

One objective of this study in which we focused on modification of the donor unit was to assess the compatibility of the dyes with redox mediators, alternative to iodine triiodide redox couple. The dyes were implemented in solar cells with a cobalt-based complex ($Co^{3+/2+}$) as the redox couple designed and synthesized by Postdoc José-Maria ANDRES CASTAN and the molecular structure is reported below.

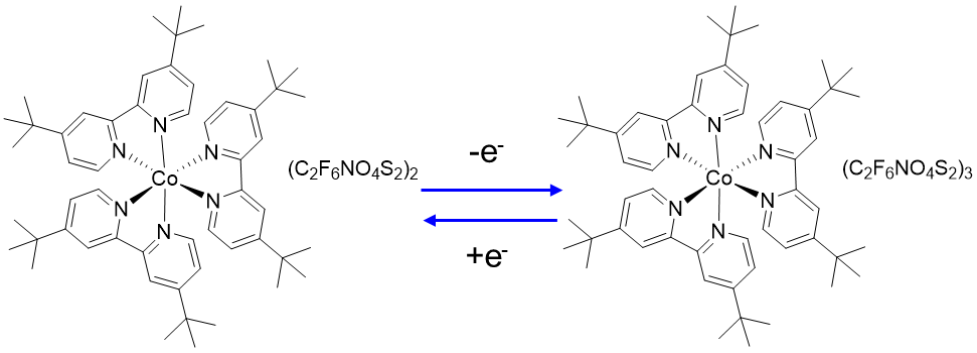

Figure 4.15 : Cobalt tris(4,4'-tert-butyl-2,2'-bipyridine), [Co(t-Bu$_2$bpy)$_3$]$^{3+/2+}$-based redox couple.

The electrolyte that I designed consists of 0.1 M [Co(t-Bu$_2$dpy)$_3$]$^{2+}$, 0.033 M [Co(t-Bu$_2$dpy)$_3$]$^{3+}$ and 0.1 M LiTFSI in acetonitrile. This electrolyte was first tested with classical mesoporous (13+3 µm) mesoporous electrodes but the performances were generally low with J_{sc}=3.04 mA cm^{-2}, V_{oc}=557 mV, FF=0.64 and PCE=1.09% based on **QH138**. Although the J_{sc} was low hence PCE, the photovoltage was slightly improved. The redox potential of [Co(t-Bu$_2$dpy)$_3$]$^{3+/2+}$ is at -4.99 eV [25] which is not far from the classic I_3^-/I^- couple. One suggestion to improve the current density was to improve the porosity of the photoanode. Stéphanie Narbey, an employee at Solaronix, designed these electrodes by preparing a TiO_2 paste mixed with polystyrene marbles in the ratio 1:1 (% wt). During calcination step (at 500 °C), the marbles melt leaving behind a porous TiO_2 substrate. These electrodes were analysed by imaging via the scanning electron microscopy (SEM) as shown below.

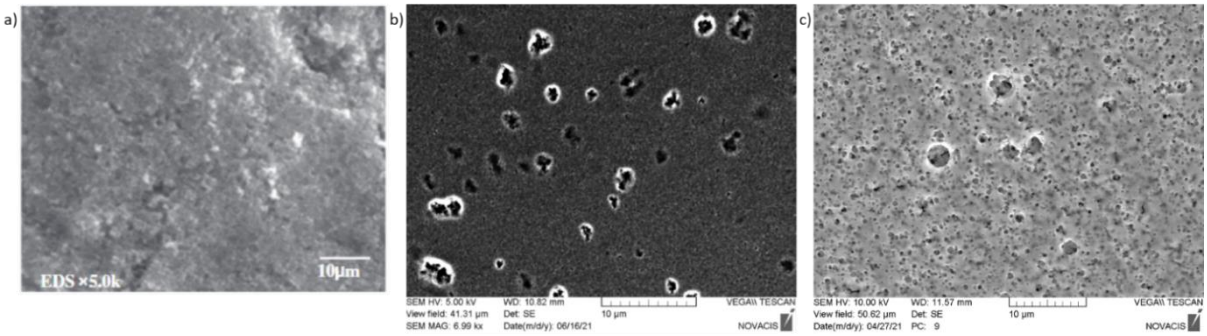

Figure 4.16 : SEM images of the photoanode surface of a) classic meosporous electrodes b) electrode with pores of 180 nm diameter and c) with around 300 nm diameter.

The photochromic dyes above were then sensitized on a 6 µm mesoscopic TiO_2 photoanodes with high porosity (300 nm diameter) adapted to work with such bulky redox couple and sandwiched with Pt-coated counter electrodes. The modified electrodes were employed to allow for permitivity and mobility of the cobalt-based redox couple. The above electrolyte was filled in between the electrodes and characterized under 1 Sun conditions.

This is the first time that we develop and use Cobalt-based electrolytes in the lab, therefore, it is important to learn more about how this electrolyte performs with reference molecules including **RK1**, a non photochromic dye. When **RK1** is implemented in a DSSC using the $Co^{3+/2+}$ couple, the PV parameters are as follows J_{sc}=6.45 mA cm^{-2}, V_{oc}=606 mV, FF=0.61 and PCE=2.39%. The current-voltage responses with photochromic dyes are as below.

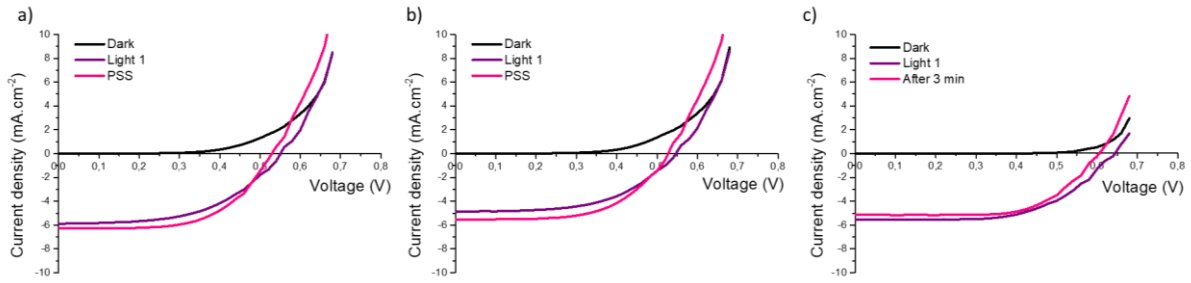

*Figure 4.17 : Current-voltage curves of a) **NP2**, b) **JoLi 135** and c) **QH138** using Co-based electrolyte.*

Dye	Jsc (mA.cm^{-2})	Voc (V)	FF	PCE (%)
NP2	5.53(5.09 ± 0.331)	528 (530 ± 0.002)	0.584 (0.573 ± 0.012)	1.70 (1.55 ± 0.124)
JoLi 135	6.28(6.29 ± 0.007)	529 (530 ± 0.001)	0.587 (0.580 ± 0.006)	1.95 (1.94 ± 0.015)
QH138	5.54 (5.21 ± 0.334)	644 (624 ± 0.020)	0.582 (0.568 ± 0.014)	2.08 (1.85 ± 0.225)

*Table 4.3 : The PV parameters of **NP2**, **JoLi 135**, and **QH138** with Co-based complex as the redox couple. Highly porous electrodes were used with 300 nm pores.*

For all dyes, there is a V_{oc} drop as a function of irradiation with slightly improved photovoltages in comparison to their iodine counterparts. **NP2**-based cells show low performance due to low J_{sc} despite the 'well-positioned' HOMO for favourable $\Delta_{regeneration}$ with respect to the others calls for more investigation. Both **NP2** and **JoLi 135** show the expected photochromic behaviour, increase in J_{sc} and drop of V_{oc}, unlike **QH138** with both J_{sc} and V_{oc} decreasing. The V_{oc} obtained with **QH138** is the highest ever obtained with our photochromic solar cells at 644 mV. We have further investigated both the non-photochromic **RK1** and the peculiar **QH138**-based cells to understand its working by EIS.

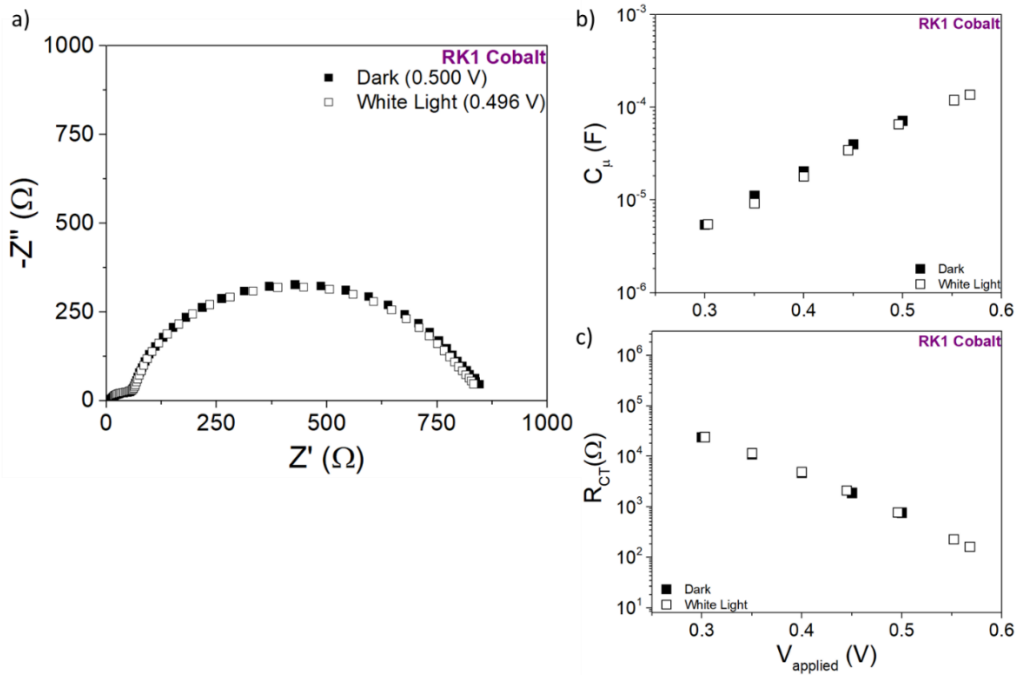

*Figure 4.18 : EIS Analysis of a non-photochromic **RK1**-based cells with a Co-based electrolyte.*

What we observe from Fig. 4.18 a) and c) is that the recombination arc does not change with irradiation conditions. This is a radically different behaviour compared to iodine based electrolytes. This could possibly be that the recombination behaviour is unaltered. This makes sense given the bulkiness of the redox couple in question making it difficult to approach the TiO_2 surface and recombine with electrons. The CB does not shift with this dye.

When an analysis with a **QH138** photochromic dye was carried out, the following response was recorded.

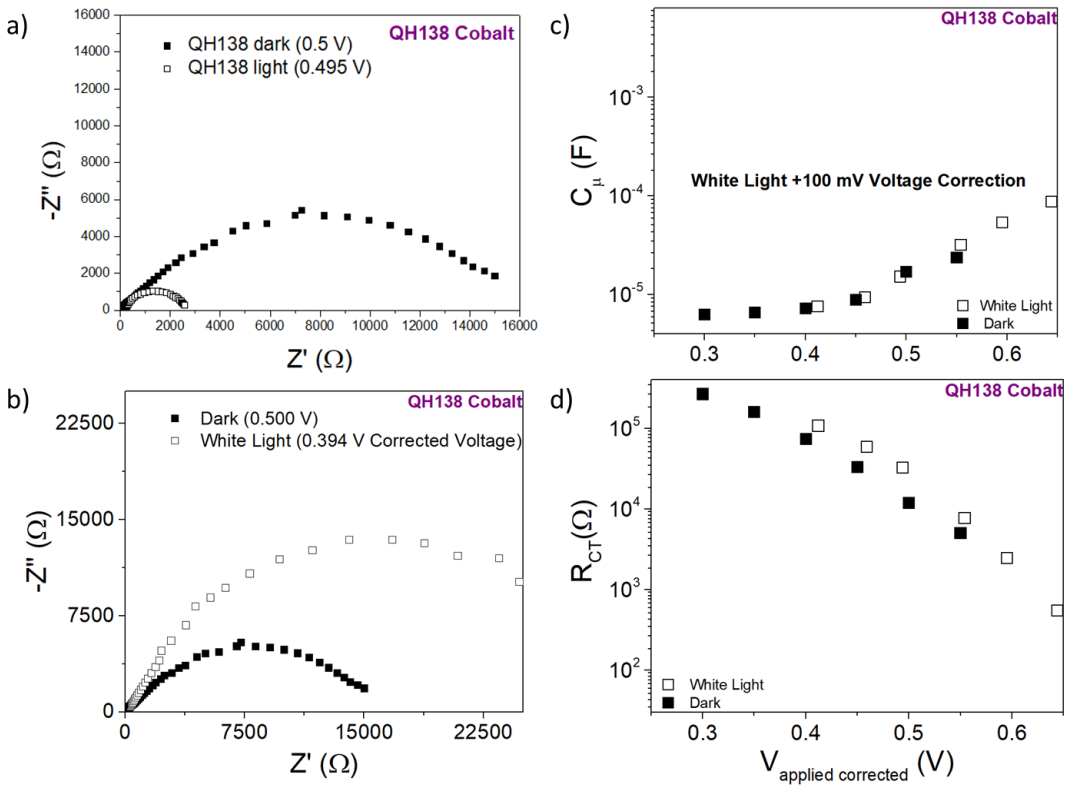

*Figure 4.19 : EIS Analysis of a photochromic dye **QH138** with a Co-based electrolyte.*

From Fig. 4.19 a) the recombination arc decreases to a greater extent when exposed to whitelight irradiation at the operating conditions. As shown in Fig. 4.19 c), we performed a voltage correction in order to make a correlation at the same electron density at the quasi-Fermi level. A 100 mV bandshift is observed indicated by the two parallel capacitance plots. When the recombination resistance plots are done at the corrected voltage, there is an increase in the R_{ct} upon irradiation meaning less recombination. This could explain the improved V_{oc} >640 mV with Co-based electrolyte compared to <500 mV with its iodine counterpart given that their redox potentials are comparable (see illustration below). This result is very encouraging taking into account the limited experience of our lab in the fabrication of solar cells containing cobalt-based electrolytes.

To realise more efficient Co-based photochromic cells, new complexes are desirable since their redox properties are determined by the ligands, to improve the $\Delta G_{regeneration}$ and hence the J_{sc}. Another strategy to further enhance the V_{oc} could be to add alkyl chains on the TPA unit born by **QH138**.

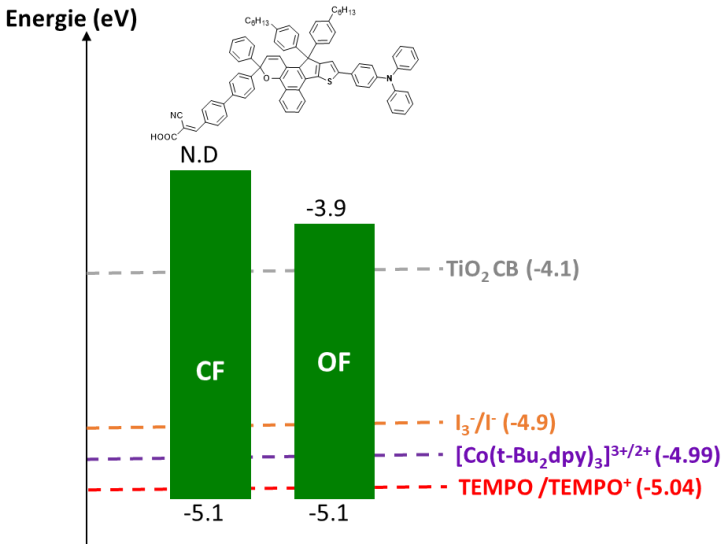

*Figure 4.20 : Illustration of the energy level positioning of **QH138** with the different redox mediators.*

4.1.2.1.3.3 TEMPO/TEMPO+

Given the toxicity and volatility nature of acetonitrile-based electrolytes, the use of environmental-friendly such as water-based electrolytes is desirable. TEMPO is capable of dissolving in water and also lead to highly transparent devices. TEMPO-based electrolyte was chosen due to its non-toxicity and ability to dissolve in an aqueous electrolyte. In addition, its high positive redox potential (0.71 V vs. NHE) results in remarkable photovoltages (>950 mV) leading to a 4.3% efficiency when applied with a hydrophobic **LEG4** photosensitizer [26]. TEMPO has also been applied in DSSCs in a mixed electrolyte with Cobalt-based redox couple to form a tandem redox system resulting in improved efficiencies via improved regeneration dynamics [27]. We have therefore tried TEMPO/TEMPO$^+$ (BF^-_4) redox couple both in an aqueous (water) and non-aqueous (acetonitrile) solvent.

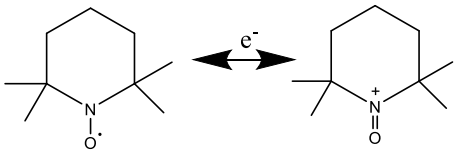

Figure 4.21 : TEMPO/TEMPO$^+$ based redox couple.

Our first attempt in water on **QH138**-based cells was unsuccessful giving PV parameters as follows J_{sc}=0.52 mA cm^{-2}, V_{oc}=647 mV, FF=0.89 and PCE=0.30% possibly due to the more positive potential in aqueous electrolytes that do not match for regeneration [26]. We therefore replaced water with acetonitrile and Dr. Johan Liotier developed a Machine Learning program to help with optimization. With the right design of experiments (DoE) for multiple variables it

is possible, using Python program, to obtain the optimum conditions. The TEMPO/TEMPO$^+$ redox couple contains [TEMPO] (0.1, 0.2, 0.3 M), [TEMPO$^+$], [LiI] (0, 0.5, 1 M) and LiTFSI (0, 0.5, 1 M). Given the 4 parameters, the different possible combinations are 4^4, meaning 256 experiments, which is cumbersome and that is why the DoE is crucial. There are several ways to sample the points as shown below with permission from ACS [28].

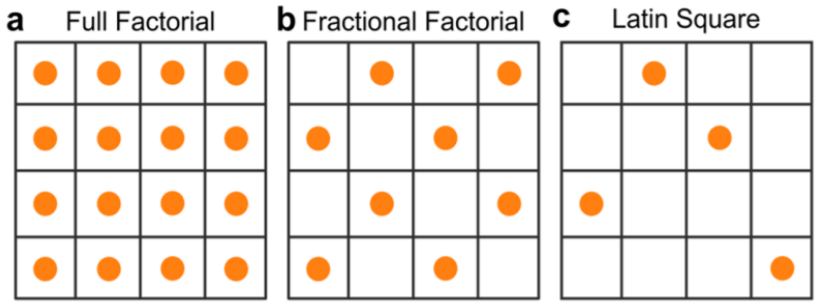

The fractional factorial was employed and the impact of each component was analyzed by ANOVA as shown below.

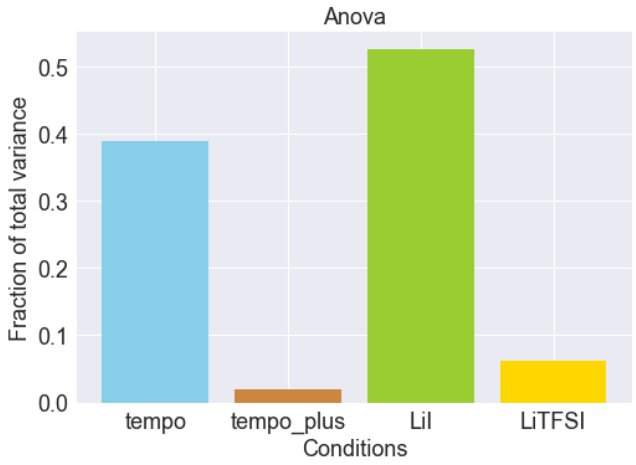

From this statistical analysis, we found out that the TEMPO and LiI have a great impact on the performance of the cells, LiTFSI moderate influence and TEMPO$^+$ the least.

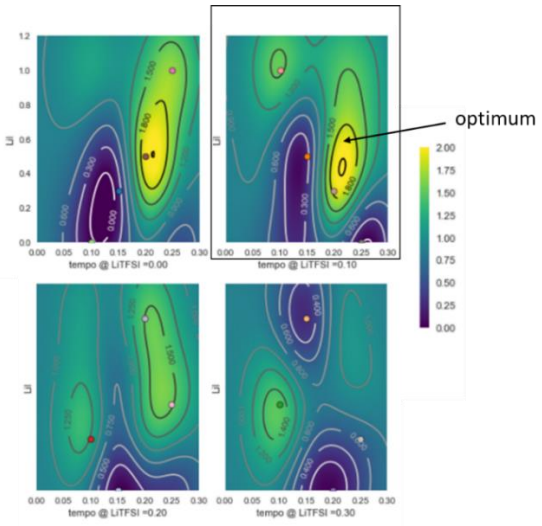

The optimum parameters for the TEMPO/TEMPO$^+$-based electrolyte were found to be [TEMPO] 0.215 M, [TEMPO$^+$] 0.1 M, [LiI] 0.44 M, and [LiTFSI] 0.1 M. The optimized PV performance for the best cell was J_{sc}=6.87 mA cm^{-2}, V_{oc}= 651 mV, FF=0.77 and PCE=3.46% on the first irradiation.

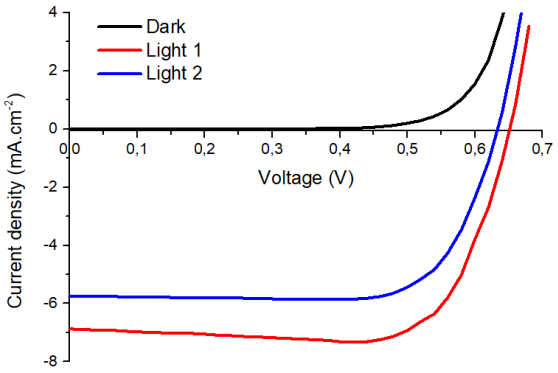

*Figure 4.22 : Best performing **QH138**-based cell with TEMPO/TEMPO$^+$ redox couple.*

The performances deteriorate as a function of irradiation. To get more insights on such behaviour, an EIS study was conducted and the results are presented below.

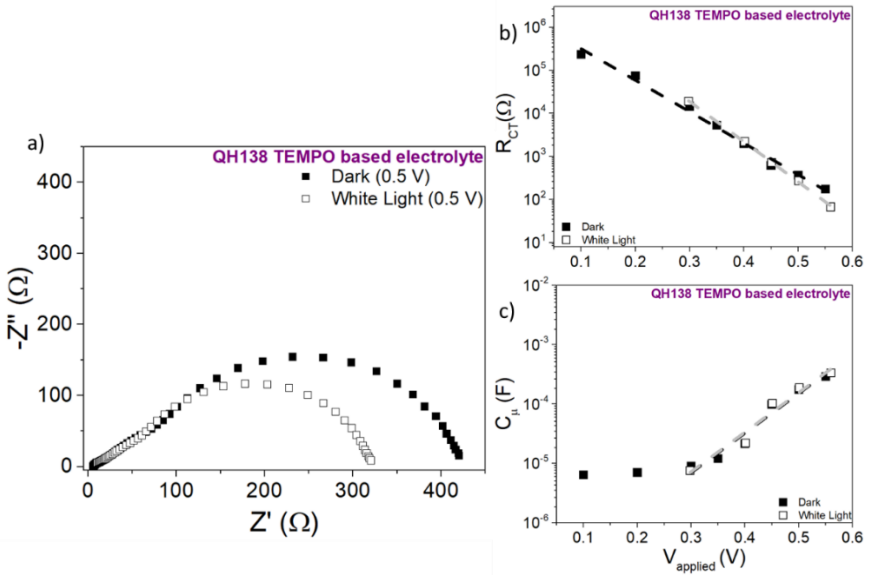

*Figure 4.23 : EIS analysis of **QH138**-based cell with TEMPO/TEMPO⁺ redox couple.*

The Nyquist plot in Fig. 4.23 a) above shows a characteristic linear shape in the high frequency region (100 MHz – 10 Hz) with a slope of 1, represents a 45° transmission line under both irradiation conditions suggesting slow transport which is generally simulated through a transmission line model. Below the 10 Hz frequency, a semi-circle is observed in this low-frequency domain representing the charge transfer resistances and the Faradaic reactions occuring on the TiO_2 surface. The recombination arc decreases as a function of irradiation meaning the recombination increases under operation conditions, which is obvious in DSSCs. The extracted resistance parameters show two different behaviours as a function of the applied voltage at the open-circuit conditions i.e. <0.4 V and >0.4 V and calls for further investigations. Similar behaviour is observed in the capacitance plots withing the same ranges. Below 0.4 V, there is a flat capacitance which could mean absence of regeneration or simply the geometric capacitance at the interface. Beyond the 0.4 V, the capacitance in the dark and under illumination fall on the same line, which suggests that there is no CB shift upon changes on the dye's conformation with irradiation.

To correlate the EIS results to performance of TEMPO/TEMPO⁺-based cells, whose performance deteriorates in a matter of hours, a simple three-electrode cyclic voltammetry (CV) was done to register the oxidation and reduction waves on the Pt-coated DSSC counter electrode immersed in an adapted DSSC electrolyte and the results are as reported below. An Ag/Ag^+ reference electrode and a Pt working electrodes were used.

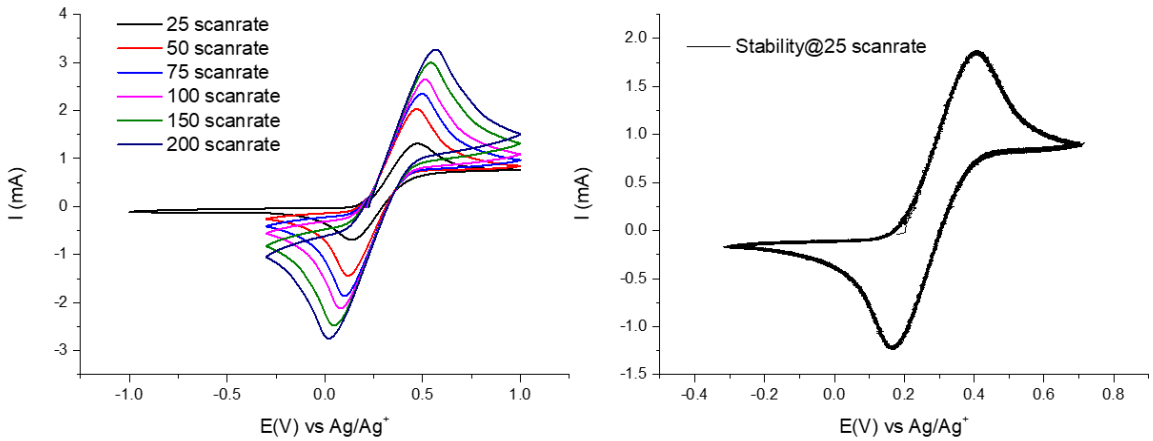

Figure 4.24 : Cyclic voltammogram for a TEMPO/TEMPO⁺ -based electrolyte at different scanrates and at repeated 25 mV/s scanrate cycles.

From the CV experiment above, the electrolyte seems stable although it fails to explain the quick TEMPO degradation when incorporated in solar cells. Dr. Johan Liotier repeated similar experiments with individual electrolyte components in their low concentrations and finally the cocktail electrolyte and the most-affected parameter is LiI that degrades at a faster rate leading to poor stabilities. The cyclic voltammogram is as shown below.

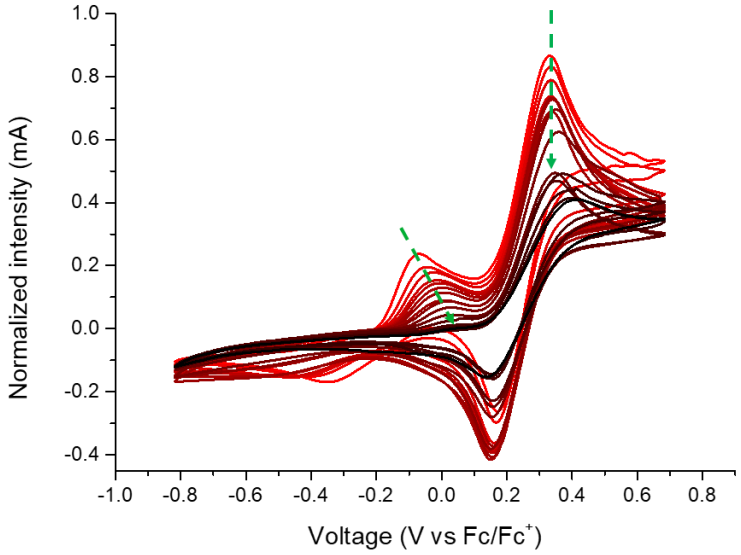

Figure 4.25 : Stability measurement of the cocktail TEMPO-based electrolyte performed after every 20 cycles in a total of 300 cycles using cyclic voltammetry. (Conditions : ACN, $tBAPF_6$, 25°C, 100 $mV.s^{-1}$.)

The measurements shown in the figure above shows 15 successive sweeps that were conducted on a TEMPO-based electrolyte after every 20 cycles with a scanrate of 100 $mV.s^{-1}$ up to 300 cycles. The electrochemical window under which these measurements were performed is between -0.8 V vs Fc/Fc^+ and +0.7 V vs Fc/Fc^+. The oxidation peak corresponding to the I_3^-/I^- couple disappears as a fuction of time whereas that related to oxidation of TEMPO

into $TEMPO^+$ decreases in its intensity with time. Given the degradation of this electrolyte after 300 cycles, could help us explain their PV performance loss in devices where several of these cycles occur under operation.

4.1.2.2 Study of carbazole derivatives as donor unit in photochromic dyes– **SF** family

Carbazole is a chemical group that is now becoming more and more popular for the preparations of molecules applicable in optoelectronic devices [29,30]. Carbazole-based dyes are molecules possessing a fused TPA donor unit. Brunner K. et al demonstrated that the HOMO level of carbazole derivatives can be engineered through substitutions at the phenyl rings and at the nitrogen affecting the spectroscopical and electrochemical properties relevant for OLEDs [31]. Other works have also reported on the improvement of electron-donating abilities of carbazole-based donors via introduction of carbazolyl or tert-butyl groups [30,32]. Carbazole-based dyes have also demonstrated compatibility with Cobalt-based redox shuttle leading to enhanced photovoltages yielding a power conversion efficiency of 9% [33].

Keeping all this in mind while improving π conjugation, Samuel Fauvel (PhD student) developed this class of molecules to tune the photochromic response, stability and efficiency of the devices based on the **NP2** dye structure. Thus, the **SF** dyes have the following carbazole-based donor structural representations expected to influence performance in devices [34].

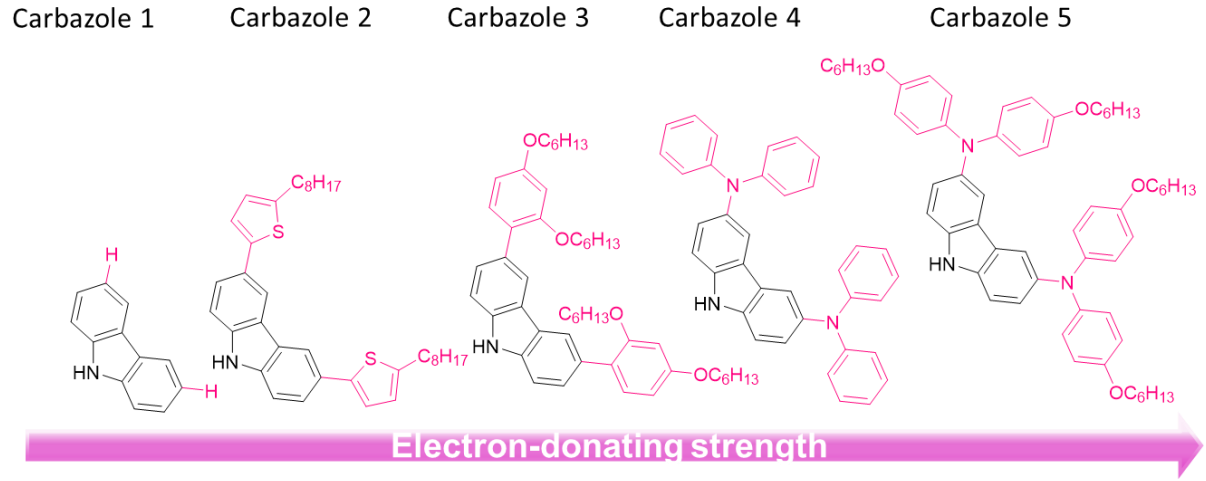

Figure 4.26 : The anticipated donor-strength trend as analyzed from the literature [32].

These donor substitutions linked to a naphthopyran photochromic core and a phenyl-cyano-acrylic anchoring group, as in **NP2**, give **SF1**, **SF2**, **SF3**, **SF4** and **SF5** termed SF family as shown below.

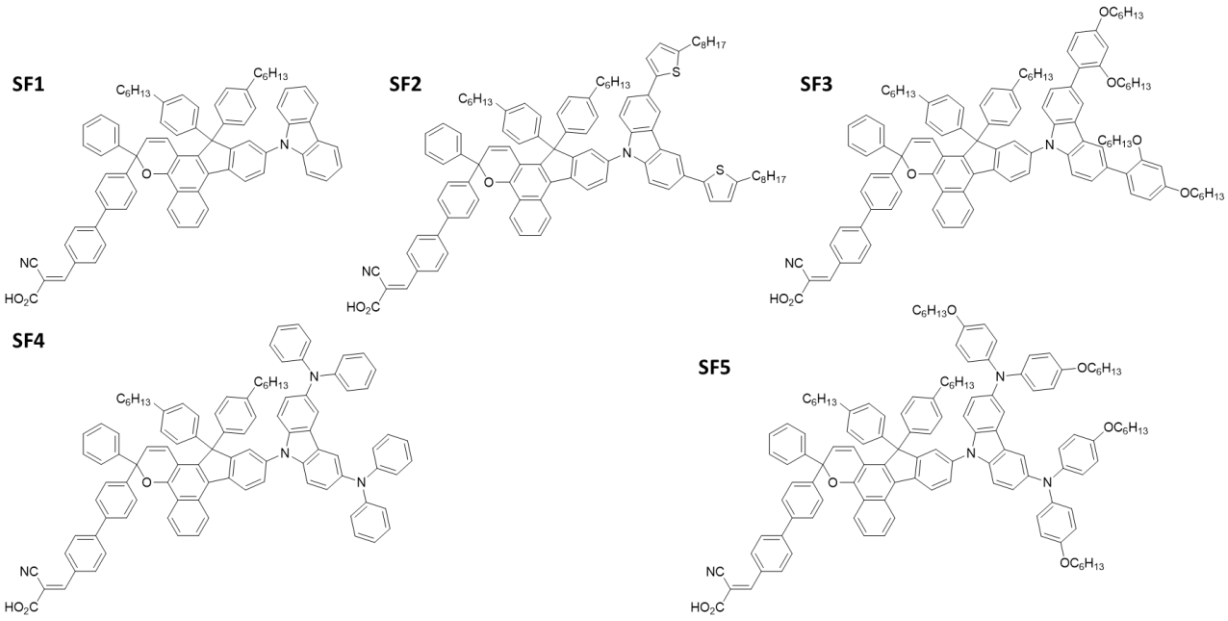

*Figure 4.27 : The chemical structures of the **SF** family.*

Other than the expected increase in the electron-donating property from **SF1** to **SF5**, the bulkiness increases in this order. These photochromic dyes were characterized by Samuel Fauvel optoelectronically to assess both their optical and electronic properties for application in DSSCs.

4.1.2.2.1 Optical properties

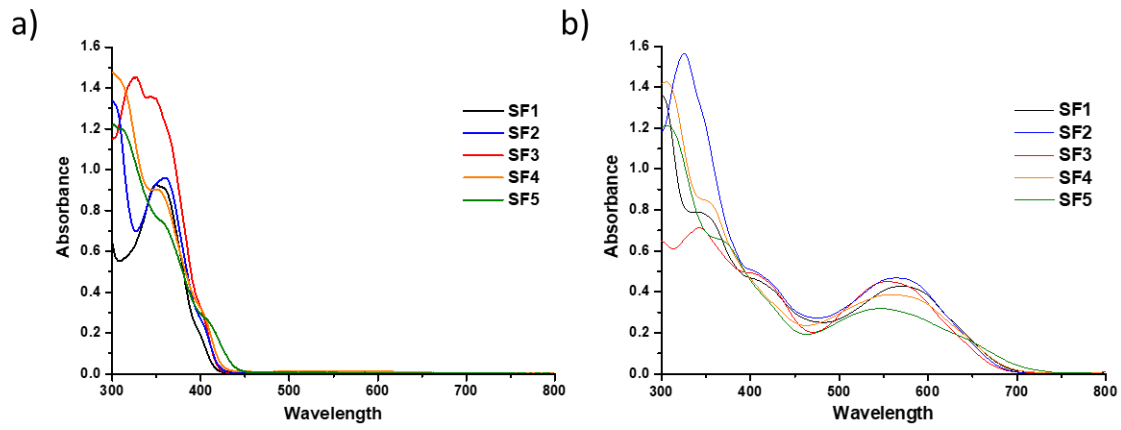

Figure 4.28 : Absorption spectra for the SF family a) in the dark and b) under irradiation. Conditions : 25°C, 2 × 10^{-5} M in toluene under Xenon lamp 200W 300-600 nm irradiation.

There are slight and major differences in the closed and open forms of the SF family and the parameters are as shown in the table below.

Table 4.4 : Showing optical parameters of the carbazole-based SF family of dyes (2 × 10^{-5} M in toluene at 25°C).

Dye	λ_{max} CF (nm)	λ_{onset} CF (nm)	λ_{max} OF (nm)	λ_{onset} OF (nm)	ΔE_{opt} OF (eV)	Discoloration constant, *k* (s^{-1})
SF1	349	416	554	675	1.84	4.14×10^{-3}
SF2	325	421	565	681	1.82	4.22×10^{-3}
SF3	300	418	571	687	1.79	3.72×10^{-3}
SF4	301	424	557	692	1.79	4.96×10^{-3}
SF5	302	439	546	717	1.73	3.75×10^{-3}

From the table above, all dyes have their λ_{onset}s <440 nm in the closed forms. Upon irradiation, different absorption intensities are observed within this family as a function of the electron-donating property. Thus, slight differences are observed in the OFs with the λ_{onset}s extended further into the red from **SF1** to **SF5**. As a result, the optical band gap decreases which means that the energy cost of promoting electrons from the dyes' HOMO to LUMO is lower thus supporting our ealier hypothesis on electron-donating strength.

4.1.2.2.2 Energy-level determination

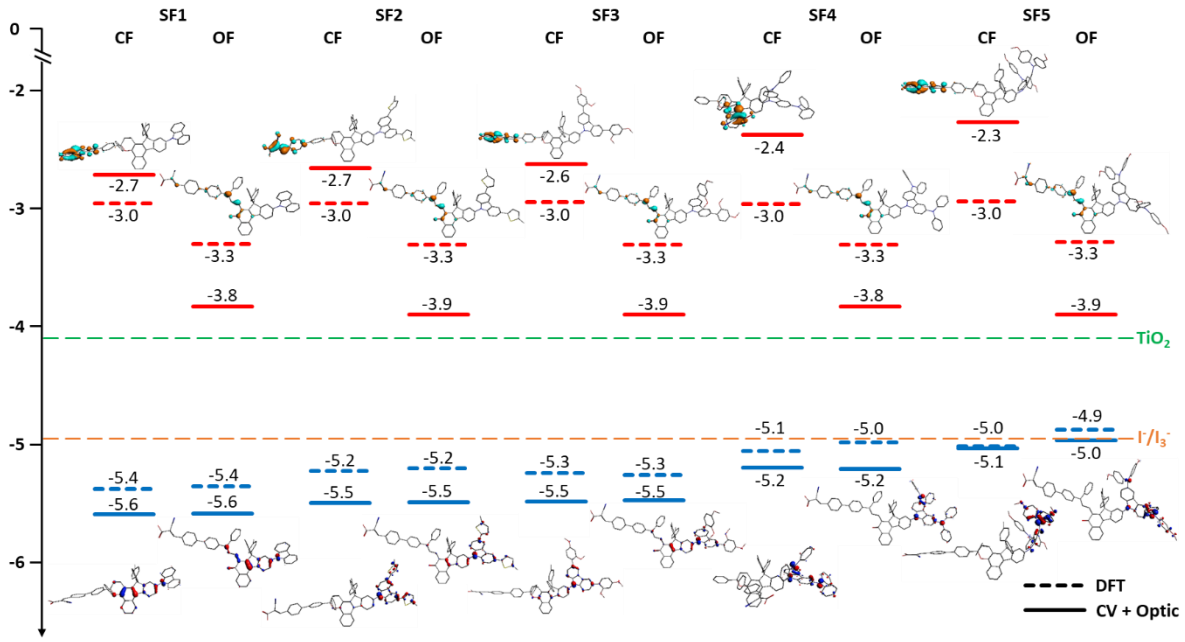

*Figure 4.29 : Frontier orbitals of the **SF** family determined experimetally and theoretically.*

The modulation of the electron-donating strength of the different carbazole units has a direct effect of the HOMO levels that were strongly impacted. Indeed, the HOMO levels are located

between -5.6 and -5.0 eV with **SF1** possessing the lowest HOMO level and increases progressively to the highest in **SF5** with the bulkiest donor. Among the **SF** family of dyes, **SF4** frontier orbitals demonstrate the highest potential differences (~0.3 eV) with reference to the TiO_2 and I_3^-/I^- redox potential hinting a favourable electronic injection and regeneration, respectively. DFT result shows a HOMO level localized on the π-system and partially on the donor in **SF1**, good distribution on the donor part and π-spacer in **SF2** and **SF3**, and only on the donor moiety in **SF4** and **SF5**. The CFs of all dyes show a LUMO localized on the cyanoacrylic acceptor unit whereas their corresponding OFs show LUMOs extending into the π-spacer is all cases. The localization and positioning of frontier orbitals are favourable for electronic injection and regeneration in a DSSC configuration.

4.1.2.2.3 Devices fabrication

The performance of these dyes was evaluated in a DSSC layout using the home-based electrolyte prepared and optimized for naphthopyran-based dyes. Due to the bulkiness of these dyes, they were applied with and without CDCA coadsorbants to assess the impact of the bulky substituents on the carbazole donor unit. The results are as summarized in the table below.

*Table 4.5 : Photovoltaic performances of the **SF** family without and with (in bold) CDCA coadsorbant.*

Dye : CDCA ratio	**J_{sc} (mA cm^{-2})**	**V_{oc} (V)**	**FF**	**PCE (%)**
SF1 :0CDCA	2.47	0.52	0.68	0.87
SF1 :10CDCA	**2.78**	**0.48**	**0.67**	**0.89**
SF2 :0CDCA	5.41	0.45	0.68	1.68
SF2 :10CDCA	**5.24**	**0.47**	**0.67**	**1.67**
SF3 :0CDCA	4.29	0.48	0.66	1.36
SF3 :10CDCA	**4.27**	**0.52**	**0.74**	**1.63**
SF4 :0CDCA	8.14	0.51	0.68	2.81
SF4 :10CDCA	**7.93**	**0.52**	**0.73**	**3.04**
SF5 :0CDCA	2.38	0.29	0.44	0.30
SF5 :10CDCA	**2.32**	**0.22**	**0.43**	**0.21**

Generally, the current density is less influenced by CDCA coadsorption due to the bulkiness of carbazole-based dyes. On the other hand, the V_{oc} does not follow a particular trend. In **SF1** and **SF5** –based devices, the photovoltage is higher with 0 CDCA than with 10 CDCA ratio. This suggests that their dyes' structure is sufficient to cushion the TiO_2 surface from the I_3^- scavengers. **SF2**, **SF3** and **SF4** –based cells have lower V_{oc}s in the absence of CDCA as to those with. The photochromic behaviour in solar cells was evaluated and demonstrated in the *J(V)* curves below.

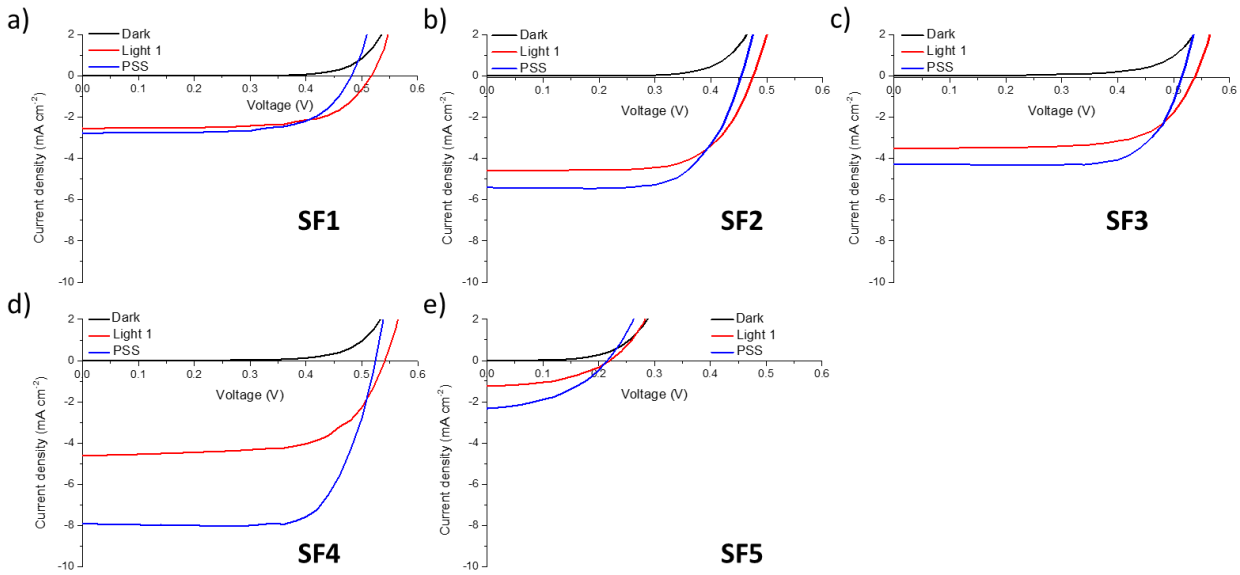

*Figure 4.30 : J(V) curves of **SF1-SF5** family with black curve showing the response in the dark (black curve), after first irradiation in 15s (red curve) and at the PSS (blue curve) under A.M. 1.5 Sun based on opaque (13+3 µm) photoanodes.*

The figure above shows that the behaviour of **SF** family resembles that of naphthopyran-based photochromes i.e. there is an increase in the J_{sc} associated with increased opened form molecules on the TiO_2 surface. The V_{oc} drop could be associated to the enhanced recombination kinetics with the dye's isomerization [1]. For all dyes, the photochromic behaviour is transferred from that in solution to the metal oxide surface. In terms of the photovoltaic (PV) performance, **SF4** is promising registering power conversion efficiencies >3% due to a sufficient driving force for electronic injection into TiO_2 CB and the dye regeneration observed in the optoelectronic characterization. **SF5** has the lowest PV performance because of low J_{sc} and V_{oc}. The hypothesis to such poor J_{sc} (2.32 mA cm^{-2}) and low V_{oc} (0.22 V) at the PSS is that fewer molecules are adsorbed due to extreme bulkiness and increased recombination, respectively. To answer these questions, dye-loading experiments need to be carried out for the former and small signal perturbation study for the latter.

4.1.2.2.4 Impedance spectroscopy measurements

The recombination and trap distribution parameters extracted after fitting the Nyquists plots to an –RC– element are as listed in the table below.

Table 4.6 : α and β parameters obtained from fittings to Equations exposed in chapter 1 and 2 involving chemical capacitances and recombination resistances.

Dye : 10 CDCA	**α**		**β**	
	In the dark	Under whitelight	In the dark	Under whitelight
SF1	0.23	0.22	0.76	0.92
SF2	0.25	0.24	0.61	0.71
SF3	0.28	0.25	0.48	0.80
SF4	0.26	0.24	0.55	0.76
SF5	0.33	0.35	0.60	0.75

All the trap distribution parameters lie within the range reported for DSSCs of 0.15-0.35. The recombination parameter various from one dye to another. For all dyes, the β parameter lies within values observed in DSSCs (0.5 – 0.8) irrespective of the conformation except in **SF1**-based dyes. This could suggest that the increased bulkiness in carbazole photochromic dyes helps in decelerating the recombination kinetics as compared to first generation photochromic DSSCs [1]. In **SF1**-based devices, the recombination parameter increases to 0.92 suggesting that the recombination kinetics is slightly higher in this case although it does not change much with respect to dark conditions. The chemical capacitances, C_{μ}, of the **SF** family are as shown below.

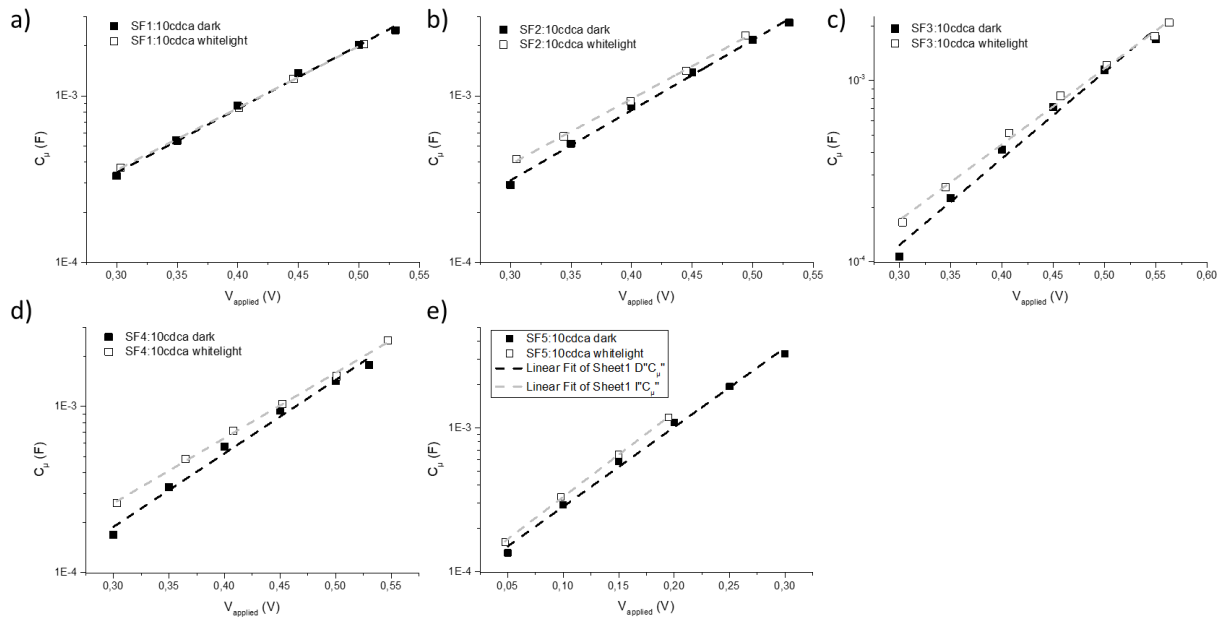

*Figure 4.31 : Chemical capacitances of the **SF**-family after fitting to a simple –RC- elements.*

The C_μ values of **SF1**-based devices remain constant in the dark and under irradiation suggesting a lack of band edge shift. However, with increased carbazole bulkiness we observe parallel capacitance plots which suggests possible band edge shifts with the surface isomerization of **SF2**-**SF5**.

To investigate the influence of carbazole bulkiness and its interplay between PV performance and photochromism, comparison was made at the same electron concentration as shown below.

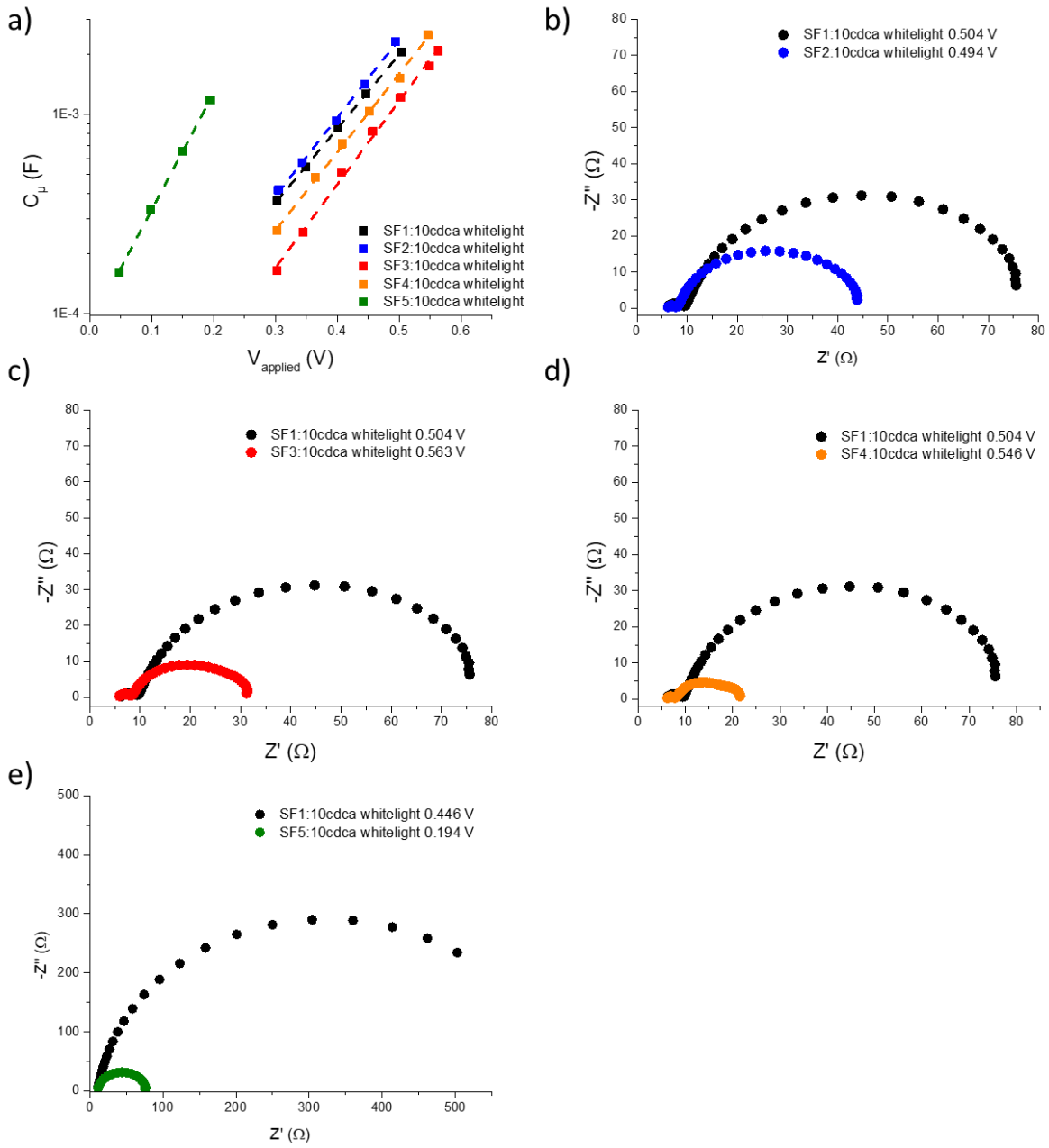

*Figure 4.32 : a) Comparison of the chemical capacitances of **SF** family, b), c) and d) Nyquists plots at the corrected voltages among the **SF** family at the corrected voltages under operating conditions.*

The capacitance plots show the differences within the **SF** family. The CB level are localized differently. At the corrected voltages, the Nyquist plot of **SF1**-based solar cell shows the largest recombination resistance within the **SF** family. This suggests that the increased bulkiness results in decreased recombination by creating pathways for I_3^- to recombine with electron in TiO_2 CB during isomerization.

In summary, eventhough carbazole-based donor units have been applied in classical sensistizers to improve both the optical and photovoltaic performances in DSSCs, these

structural design principles cannot be fully transferred to photochromic DSSCs. Indeed, the bulkiness led to improved PV performances as in **SF4**-based cells but further bulkiness in **SF5** resulted in poor performances and increased recombination.

4.1.3 Acceptor function

Until now, I have demonstrated the application of photochromic dyes in solar cells based on diphenyl-naphthopyran unit. I have deduced structure-property relationships through **NP**series and donor group modifications via **SF**series. In this sub-section, I will present two dyes synthesized and characterized by Dr. Johan Liotier. In these dyes, based on reference **NPI** dye, he substituted a phenyl ring in **NPI** by a thiophene and a furan to form **NPI-ThPh** and **NPI-FuPh** photochromic dyes, respectively. The goal is to improve the open form absorption properties of these photochromes in solution and immobilize them on a TiO_2 substrate leading to an improvement in the J_{sc} and hence the power conversion efficiency. The chemical structures are as shown below,

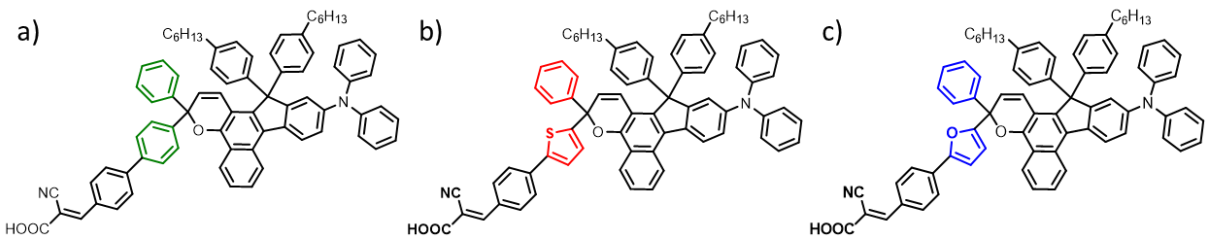

*Figure 4.33 : Chemical structures of the closed forms of a) **NPI**, b) **NPI-ThPh**, and c) **NPI-FuPh** photochromic dyes and their PV summary.*

When these dyes were dissolved in solution, the following colouration was portrayed.

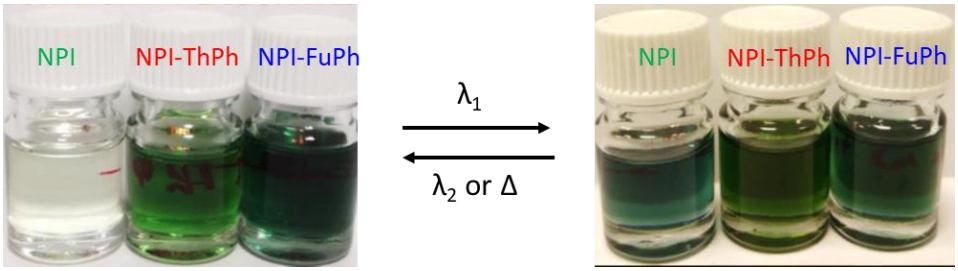

Figure 4.34 : On the left, is the colouration the dyes observed in the dark, closed forms, and on the right, under irradiation at the photostationary state.

The optical properties of the closed and opened forms were determined as shown in the figure below.

4.1.3.1 Optical characterizations

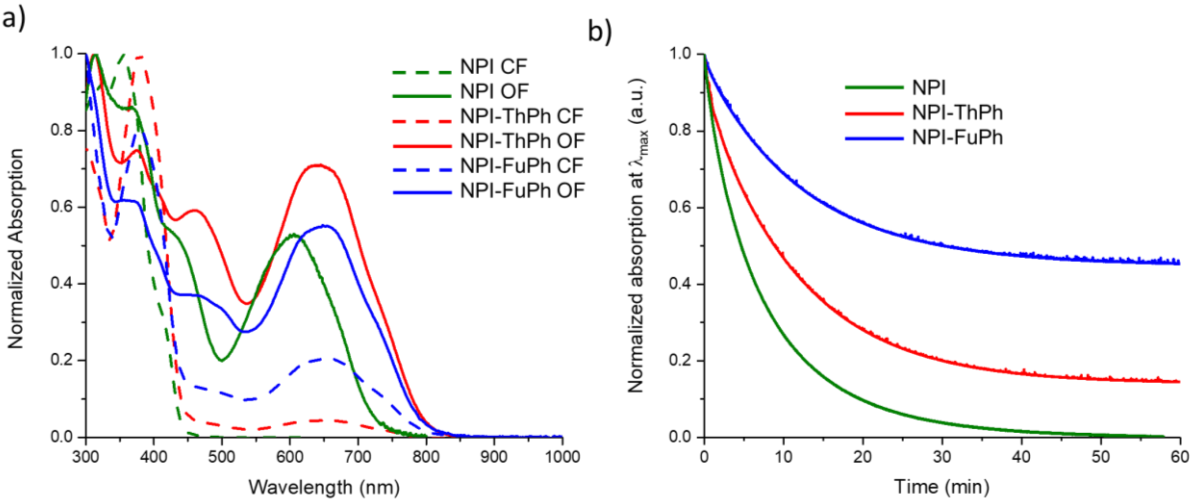

*Figure 4.35 : a) Absorption spectra of **NPI**, **NPI-ThPh**, and **NPI-FuPh** dyes in closed forms (dotted) and open forms (solid lines). b) Decoloration kinetics in solution. (Conditions : in toluene, 2x10^{-5} M, 25 °C, irradiation : 200 W, 300-600 nm).*

The new compounds show photochromic behaviour in solution upon irradiation that result in the C-O bond cleavage of the pyranic unit thus giving open forms showing deep green hue for **NPI-ThPh** and dark green (black) for **NPI-FuPh**. The spectra in the dark for **NPI-ThPh** and **NPI-FuPh** show absorption in the visible range unlike **NPI**. This suggests the presence of stable open form isomers. Under irradiation, the generated OF isomers show a bathochromic shift of the λ_{max} by 37 nm and 50 nm for **NPI-ThPh** and **NPI-FuPh** with respect to **NPI**, respectively, and a hyperchromic shift in the case of **NPI-ThPh**.

The optical parameters are as listed in the table below.

Table 4.7 : Optical parameters of the dyes where ΔE_{opt} OF is the optical bandgap of the opened form, A_{eq} is the absorption intensity at the PSS, A_∞ is the absorption obtained after a long time discolouration and k is the kinetic constant of the monoexponential modeling of the fading process.

Dye	λ_{max} CF (nm)	λ_{onset} CF (nm)	λ_{max} OF (nm)	λ_{onset} OF (nm)	ΔE_{opt} OF (eV)	A_{eq}	A_∞	k (s^{-1})
NPI	318	450	605	728	1.70	0.38	0	2.08×10^{-3}
NPI-ThPh	378	450	642	798	1.55	0.97	0.14	1.45×10^{-3}
NPI-FuPh	380	450	655	800	1.55	0.49	0.22	1.31×10^{-3}

The decolouration kinetic constants demonstrate that the replacement of the benzene in **NPI** by a thiophene and a furan in **NPI-ThPh** and **NPI-FuPh**, respectively, stabilizes more the open forms thus retarding the ring closure process. More studies were conducted by Dr. Johan

Liotier through a DFT calculation to understand this process and found that their CC isomers are more stabilized as compared to that of **NPI**.

These modifications in **NPI** photochrome resulting in a red-shifted absorption spectra is coherent with observations in classical dyes [35,36]. In conventional photosensitizers, this red-shift led to improved power conversion efficiencies. The question is, will this transfer the same effect to photochromic DSSCs? First, let's check whether their energy levels match in a DSSC configuration.

4.1.3.2 Energie level determination

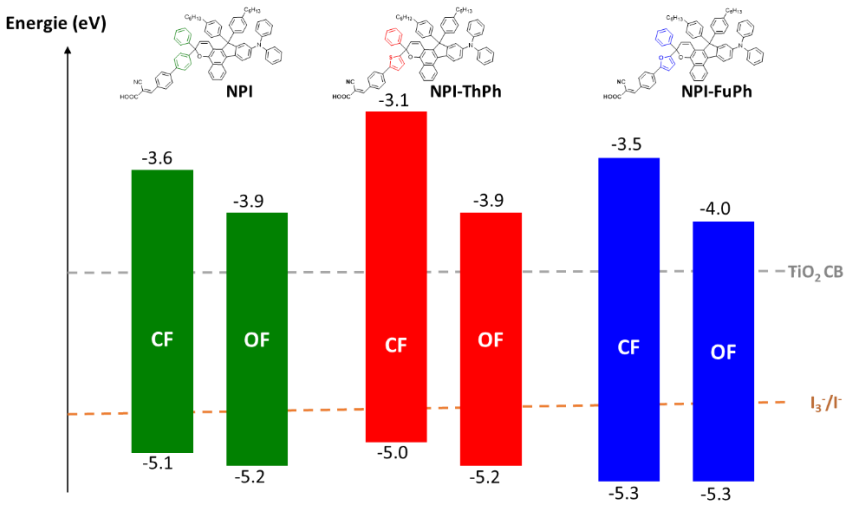

*Figure 4.36 : Experimentally determined energy levels of **NPI**, **NPI-ThPh** and **NPI-FuPh** dyes.*

The frontier orbitals were found to match well in a DSSC framework. Therefore, I made solar cells based on these dyes and their performances are as shown in the *J(V)* curves and summarized in the table below.

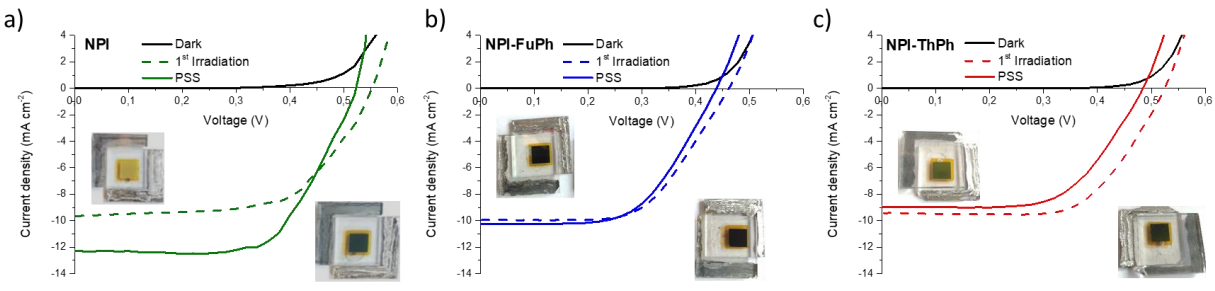

*Figure 4.37 : The J(V) curves of a) **NPI**- b) **NPI-FuPh** and c) **NPI-ThPh** based solar cells using 13+3 µm opaque photoanodes.*

The statistics of the fabricated devices done on at least 3 solar cells.

*Table 4.8 : The current-voltage characteristics of **NPI**, **NPI-ThPh**, and **NPI-FuPh** based cells where supersripts (1) are the first measurements and (2) at the PSS of the best cells and (3) the average for 3 cells at the PSS.*

Dye	Jsc (mA cm^{-2})	Voc (V)	FF (%)	PCE (%)
NPI	9.66^{1} 12.29^{2} $(12.14 \pm 0.11)^{3}$	0.552^{1} 0.523^{2} $(0.521 \pm 0.007)^{3}$	61.5^{1} 64.8^{2} $(65.4 \pm 0.9)^{3}$	3.28^{1} 4.16^{2} $(4.13 \pm 0.02)^{3}$
NPI-ThPh	9.44^{1} 8.97^{2} $(9.38 \pm 0.36)^{3}$	0.525^{1} 0.484^{2} $(0.454 \pm 0.026)^{3}$	64.6^{1} 61.4^{2} $(61.6 \pm 0.8)^{3}$	3.20^{1} 2.66^{2} $(2.62 \pm 0.04)^{3}$
NPI-FuPh	9.94^{1} 10.23^{2} $(9.91 \pm 0.32)^{3}$	0.462^{1} 0.439^{2} $(0.441 \pm 0.011)^{3}$	58.9^{1} 58.4^{2} $(58.7 \pm 0.6)^{3}$	2.71^{1} 2.61^{2} $(2.56 \pm 0.05)^{3}$

Both the photochromic and the PV behaviour of **NPI-FuPh** and **NPI-ThPh** were found to be completely different from **NPI**. First is their colouration and decolouration process. The solar cells appear coloured even before exposure to sunlight and the decoloration process is long as observed in solution. Secondly, the PCEs decrease with irradiation in comparison to **NPI**. For instance, a small J_{sc} increase is detected in **NPI-FuTh** device followed by a huge V_{oc} loss. On the other hand, both the J_{sc} and the V_{oc} in **NPI-ThPh** –based devices decreases as a function of irradiation time. As a result, a routine EIS tool was employed to unravel this behaviour as shown below.

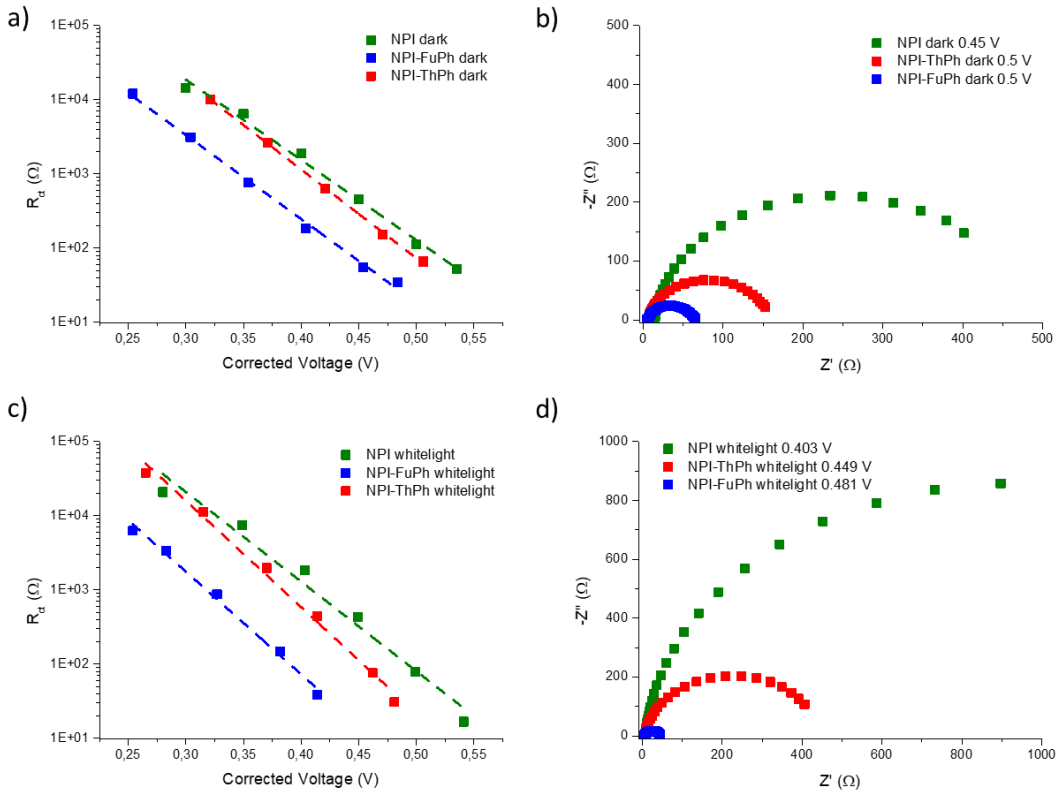

*Figure 4.38 : EIS study of **NPI**, **NPI-ThPh**, and **NPI-FuTh** -based solar cells a) and b) in the dark and c) and d) after light activation at the PSS. On the left, the recombination resistances at the corrected voltages and on the right their respective Nyquists plots.*

The recombination resistances were plotted at the corrected voltages to deduce the chemical structure-property relationship. From this study, the evolution of recombination resistances with voltage is similar under all irradiation conditions. **NPI** registers the highest recombination resistances i.e. lowest recombination followed by **NPI-ThPh** and lastly **NPI-FuPh**. This behaviour is in agreement with the observed decreasing performances from **NPI** to **NPI-ThPh** and finally **NPI-FuPh** in cells.

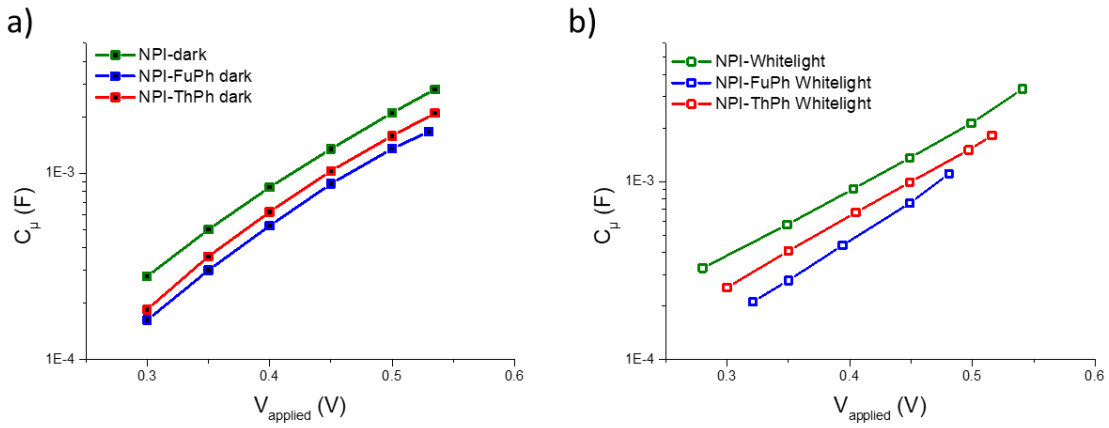

Figure 4.39 : Chemical capacitance after fitting the Nyquists data of solar cells under different irradiation conditions.

From the plots above, we can conclude that there are possible band edge shifts in between the dyes given the dependence of the photovoltage on the CB and the redox potential [37,38]. Indeed, under the operating conditions, we observe negative bandshifts of 35 and 67 mV in **NPI-ThPh** and **NPI-FuPh**, respectively, with reference to **NPI**-based device.

In conclusion, the substitution of electron-rich groups at this position of the photochromes is not a good strategy to attain higher PCEs due to increased recombination. This work was published in Solar RRL journal in 2021 (https://doi.org/10.1002/solr.202100929).

The strategy to vary the spacer connecting the anchoring function to the π-spacer is powerful in classical dyes to improve performances. This study shows that swapping a phenyl by a furan or a thiophene close to the pyran ring is bad in photochromic dyes. However, further investigations are needed to assess if the introduction of electron-rich moieties on the acceptor-function of photochromic dyes would be of benefit to the performances.

In this section, I have investigated two modifications i.e. either a donating group : a thiopheneclose to the anchoring function or a benzothiadiazole (BTD), a strong electron withdrawing group, as a π-spacer.

Such dyes include a thiophene and BTD group incorporated closer to the cyanoacrylic group than **NPI-ThPh** based on **NP2** structure termed **NP2-Th** (**SF7**) and **NP2-BTD** (**SF9**), respectively.

4.1.4 NP2-Th and NP2-BTD

These photochromes have their chemical structures as shown below.

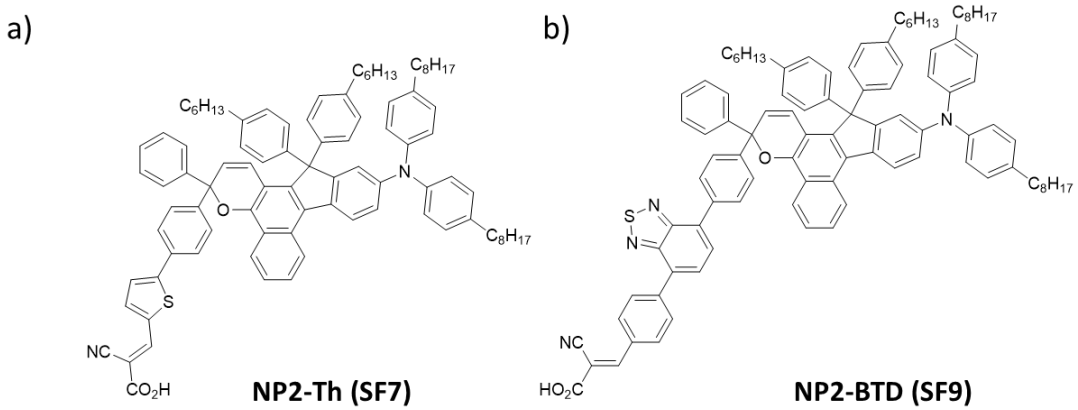

*Figure 4.40 : **NP2**-like acceptor modifications where a) is based on a thiophene labelled **NP2-Th** (**SF7**) and b) is based on a benzothiadiazole known as **NP2-BTD** (**SF9**).*

The above molecules have been synthesized by Samuel Fauvel and their optical properties determined are partly as shown below.

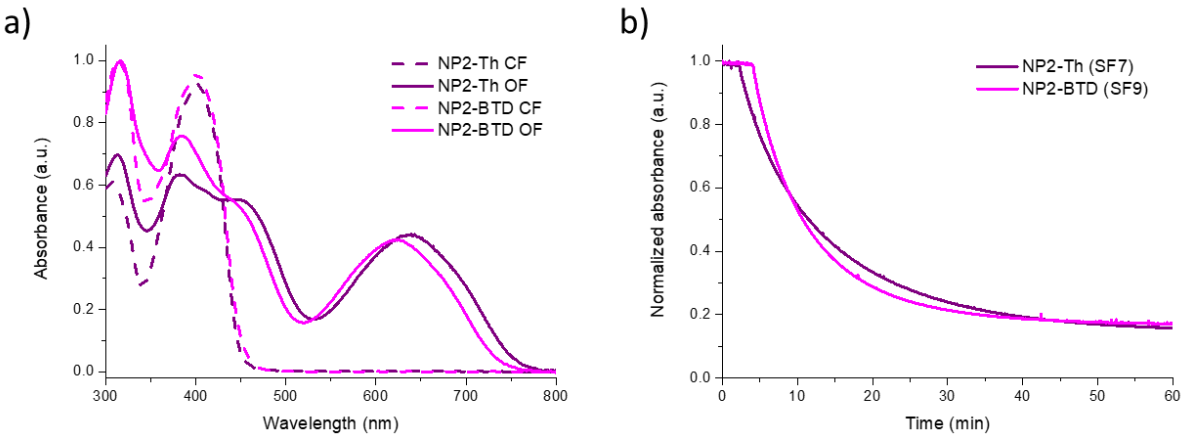

*Figure 4.41 : a) UV-Vis absorption spectra of **NP2-Th** (**SF7**) and **NP2-BTD** (**SF9**) in their closed forms (dotted lines) and their opened forms after irradiation (solid lines). b) The discolouration kinetics of the 2 dyes after irradiation until the photostationary state and registered in the dark at the λ_{max} of the ICT bands of the opened forms.*

From the curves above, the closed forms of the **NP2-Th** (**SF7**) and **NP2-BTD** (**SF9**) have their maxima at 313 nm and 403 nm, respectively, whereas that of **NP2** as ealier reported is at 320 nm. Upon irradiation, the internal charge transfer band is observed accompanied with a green colouration of the solution showing a maxima of this band at 622 nm and 639 nm for **NP2-Th** (**SF7**) and **NP2-BTD** (**SF9**), respectively, whereas that of **NP2** is at 620 nm. This marks a slight bathochromic shift with respect to **NP2** dye suggesting that the fabricated devices will harvest more low-energetic photons. On the other hand, as shown in Fig. 4.41 b), the fading kinetics registered and fitted to a monoexponential decay equation has a constant, *k*, of 3.25×10^{-3} s^{-1} and 2.199×10^{-3} s^{-1} for **NP2-Th** (**SF7**) and **NP2-BTD** (**SF9**), respectively, against 2.3×10^{-3} s^{-1}. **NP2-BTD** (**SF9**) and **NP2** have comparable ring-closure kinetics whereas that of **NP2-Th** (**SF7**) is slightly faster. However, both **NP2-Th** (**SF7**) and **NP2-BTD** (**SF9**) show comparable residual absorbance unlike near absence in **NP2**, suggesting the generation of stable open form isomers with addition of electron-rich groups (as observed in **NPI-ThPh** and **NPI-FuPh**). This calls for further investigations.

Eventhough energy-level determination is still underway, I applied them in a DSSC layout and the PV performances reported are as shown in the table below.

*Table 4.9 : The photovoltaic performance of the 3 dyes and the statistics based on 3 cells for **NP2** and **NP2-Th** (**SF7**) and 2 devices for **NP2-BTD** (**SF9**).*

Dye : 5cdca	J_{sc} (mAcm^{-2})	V_{oc} (V)	FF	PCE (%)
NP2	12.74 (13.55 ± 0.67)	0.503 (0.491 ± 0.009)	0.649 (0.620 ± 0.020)	4.16 (4.12 ± 0.04)
NP2-Th (SF7)	14.70 (14.59 ± 0.30)	0.494 (0.487 ± 0.006)	0.579 (0.580 ± 0.000)	4.21 (4.12 ± 0.08)
NP2-BTD (SF9)	10.53 (10.36 ± 0.16)	0.495 (0.493 ± 0.002)	0.641 (0.647 ± 0.006)	3.34 (3.31 ± 0.03)

The most promising among the 3 dyes listed above is **NP2-Th** (**SF7**) giving an efficiency up to 4.21%. The slightly improved performance is due to an increased J_{sc}. These are preliminary results and more investigations are required to unveil the impact of positioning and localization of electron-rich moieties such as thiophene which had a lower photovoltaic performance in the previous sub-section. This is the best result reported based on a single photochromic dye DSSC and a good point to conclude and hence perspectives to my PhD project.

4.2 Conclusion

To conclude in this chapter, I have investigated several families of dyes. I have investigated the impact of electron-rich groups on either the electron-donating part or the acceptor part through chemical engineering. I have deduced important structure-function relationships. The introduction of alkoxy groups, as in **JoLi 135** photochromic dye, does not have similar effect on **NP** dyes as it has on classical dyes. The introduction of carbazole donors with varying bulkiness has an impact on the electron donating strength leading to shifts in the HOMO energy level positioning. This is important because it can allow for the application of new redox couples such as Co-based ones that can result in highly efficient photochromic DSSCs. I have also been the first to develop and study in detail Cobalt-based electrolytes in the lab and they work with photochromic dyes! We have also observed that the design rules stipulated for classical organic photosensitizers such as the incorporation of thiophene and furan as in **NPI-ThPh** and **NPI-FuPh**, respectively, result in increased molar absorptivities, yes, but result in increased recombination. However, with proper design as in **NP2-Th** (**SF7**) can lead to

decent cell performances if well optimized and lead to a power conversion efficiency beyond its current **4.21%** which is promising. Finally, I would like to thank the work of different chemists in the team (Dr. Johan Liotier, Dr. Quentin Huaulmé and Samuel Fauvel), through which I have been able to explore different families and build the basement on how to design photochromic dyes for DSSCs.

4.3 References

1. Huaulmé, Q. *et al.* Photochromic dye-sensitized solar cells with light-driven adjustable optical transmission and power conversion efficiency. *Nat Energy* **5**, 468–477 (2020).
2. Xu, M. *et al.* Electrical and photophysical analyses on the impacts of arylamine electron donors in cyclopentadithiophene dye-sensitized solar cells. *Energy Environ. Sci.* **4**, 4735 (2011).
3. Tian, H. *et al.* Effect of different electron donating groups on the performance of dye-sensitized solar cells. *Dyes and Pigments* **84**, 62–68 (2010).
4. Dai, P. *et al.* Influence of the Terminal Electron Donor in D–D–π–A Organic Dye-Sensitized Solar Cells: Dithieno[3,2-b:2′,3′-d]pyrrole versus Bis(amine). *ACS Appl. Mater. Interfaces* **7**, 22436–22447 (2015).
5. Yum, J.-H. *et al.* Blue-Coloured Highly Efficient Dye-Sensitized Solar Cells by Implementing the Diketopyrrolopyrrole Chromophore. *Sci Rep* **3**, 2446 (2013).
6. Srinivas, K. *et al.* D-π-A organic dyes with carbazole as donor for dye-sensitized solar cells. *Synthetic Metals* **161**, 96–105 (2011).
7. Zhu, B., Wu, L., Ye, Q., Gao, J. & Han, L. Asymmetric double donor-π-acceptor dyes based on phenothiazine and carbazole donors for dye-sensitized solar cells. *Tetrahedron* **73**, 6307–6315 (2017).
8. Thongkasee, P. *et al.* Carbazole-Dendrimer-Based Donor–π–Acceptor Type Organic Dyes for Dye-Sensitized Solar Cells: Effect of the Size of the Carbazole Dendritic Donor. *ACS Appl. Mater. Interfaces* **6**, 8212–8222 (2014).
9. Joly, D. *et al.* Metal-free organic sensitizers with narrow absorption in the visible for solar cells exceeding 10% efficiency. *Energy Environ. Sci.* **8**, 2010–2018 (2015).
10. Chen, L. *et al.* 5,6-Bis(octyloxy)benzo[*c*][1,2,5]thiadiazole-Bridged Dyes for Dye-Sensitized Solar Cells with High Open-Circuit Voltage Performance: Benzothiadiazole-Bridged Dyes for Dye-Sensitized Solar Cells. *Eur. J. Org. Chem.* **2013**, 1770–1780 (2013).
11. Zhu, H. *et al.* Insight into Benzothiadiazole Acceptor in D–A–π–A Configuration on Photovoltaic Performances of Dye-Sensitized Solar Cells. *ACS Sustainable Chem. Eng.* **2**, 1026–1034 (2014).

12. Godfroy, M. *et al.* Benzothiadiazole-based photosensitizers for efficient and stable dye-sensitized solar cells and 8.7% efficiency semi-transparent mini-modules. *Sustainable Energy Fuels* **5**, 144–153 (2021).
13. Li, H. *et al.* Co-sensitization of benzoxadiazole based D–A–π–A featured sensitizers: compensating light-harvesting and retarding charge recombination. *J. Mater. Chem. A* **2**, 14649–14657 (2014).
14. Pei, K. *et al.* Constructing High-Efficiency D–A–π–A-Featured Solar Cell Sensitizers: a Promising Building Block of 2,3-Diphenylquinoxaline for Antiaggregation and Photostability. *ACS Appl. Mater. Interfaces* **5**, 4986–4995 (2013).
15. Chang, D. W. *et al.* Novel Quinoxaline-Based Organic Sensitizers for Dye-Sensitized Solar Cells. *Org. Lett.* **13**, 3880–3883 (2011).
16. Aumaitre, C. *et al.* Visible and near-infrared organic photosensitizers comprising isoindigo derivatives as chromophores: synthesis, optoelectronic properties and factors limiting their efficiency in dye solar cells. *J. Mater. Chem. A* **6**, 10074–10084 (2018).
17. Ying, W. *et al.* Series of New D-A-π-A Organic Broadly Absorbing Sensitizers Containing Isoindigo Unit for Highly Efficient Dye-Sensitized Solar Cells. *ACS Appl. Mater. Interfaces* **4**, 4215–4224 (2012).
18. Wang, D. *et al.* Near-infrared absorbing isoindigo sensitizers: Synthesis and performance for dye-sensitized solar cells. *Dyes and Pigments* **112**, 327–334 (2015).
19. Ho, P., Thogiti, S., Lee, Y. H. & Kim, J. H. Discrete photoelectrodes with dyes having different absorption wavelengths for efficient cobalt-based tandem dye-sensitised solar cells. *Sci Rep* **7**, 2272 (2017).
20. Saygili, Y. *et al.* Effect of Coordination Sphere Geometry of Copper Redox Mediators on Regeneration and Recombination Behavior in Dye-Sensitized Solar Cell Applications. *ACS Appl. Energy Mater.* **1**, 4950–4962 (2018).
21. Wang, S. *et al.* Influence of thiophene and benzene unit in triphenylamine dyes on the performance of dye-sensitized solar cells. *Synthetic Metals* **168**, 1–8 (2013).
22. Al-Faouri, T. *et al.* Exploring Structure-Property Relationships in a Bio-Inspired Family of Bipodal and Electronically-Coupled Bistriphenylamine Dyes for Dye-Sensitized Solar Cell Applications. *Molecules* **25**, 2260 (2020).
23. Pourjafari, D. *et al.* Brookite-Based Dye-Sensitized Solar Cells: Influence of Morphology and Surface Chemistry on Cell Performance. *J. Phys. Chem. C* **122**, 14277–14288 (2018).

24. Chen, J. *et al.* The effect of different alkyl chains on the photovoltaic performance of D–π–A porphyrin-sensitized solar cells. *New J. Chem.* **39**, 3736–3746 (2015).
25. Hamann, T. W. The end of iodide? Cobalt complex redox shuttles in DSSCs. *Dalton Trans.* **41**, 3111–3115 (2012).
26. Yang, W., Söderberg, M., Eriksson, A. I. K. & Boschloo, G. Efficient aqueous dye-sensitized solar cell electrolytes based on a TEMPO/$TEMPO^+$ redox couple. *RSC Adv.* **5**, 26706–26709 (2015).
27. Cong, J., Hao, Y., Boschloo, G. & Kloo, L. Electrolytes Based on TEMPO-Co Tandem Redox Systems Outperform Single Redox Systems in Dye-sensitized Solar Cells. *ChemSusChem* **8**, 264–268 (2015).
28. Cao, B. *et al.* How To Optimize Materials and Devices via Design of Experiments and Machine Learning: Demonstration Using Organic Photovoltaics. *ACS Nano* **12**, 7434–7444 (2018).
29. El-Shafei, A., Hussain, M., Atiq, A., Islam, A. & Han, L. A novel carbazole-based dye outperformed the benchmark dye N719 for high efficiency dye-sensitized solar cells (DSSCs). *J. Mater. Chem.* **22**, 24048 (2012).
30. Lee, W., Cho, N., Kwon, J., Ko, J. & Hong, J.-I. New Organic Dye Based on a 3,6-Disubstituted Carbazole Donor for Efficient Dye-Sensitized Solar Cells. *Chem. Asian J.* **7**, 343–350 (2012).
31. Brunner, K. *et al.* Carbazole Compounds as Host Materials for Triplet Emitters in Organic Light-Emitting Diodes: Tuning the HOMO Level without Influencing the Triplet Energy in Small Molecules. *J. Am. Chem. Soc.* **126**, 6035–6042 (2004).
32. Teng, C. *et al.* Tuning the HOMO Energy Levels of Organic Dyes for Dye-Sensitized Solar Cells Based on Br^-/Br_3^- Electrolytes. *Chem. Eur. J.* **16**, 13127–13138 (2010).
33. Soni, S. S. *et al.* Improved molecular architecture of D–π–A carbazole dyes: 9% PCE with a cobalt redox shuttle in dye sensitized solar cells. *J. Mater. Chem. A* **3**, 21664–21671 (2015).
34. Yang, J. *et al.* Influence of the Donor Size in D–π–A Organic Dyes for Dye-Sensitized Solar Cells. *J. Am. Chem. Soc.* **136**, 5722–5730 (2014).
35. Cariello, M. *et al.* An investigation of the roles furan *versus* thiophene π-bridges play in donor–π-acceptor porphyrin based DSSCs. *Dalton Trans.* **47**, 6549–6556 (2018).
36. Cao, H. & Rupar, P. A. Recent Advances in Conjugated Furans. *Chem. Eur. J.* **23**, 14670–14675 (2017).

37. Guillén, E., Peter, L. M. & Anta, J. A. Electron Transport and Recombination in ZnO-Based Dye-Sensitized Solar Cells. *J. Phys. Chem. C* **115**, 22622–22632 (2011).
38. Raga, S. R., Barea, E. M. & Fabregat-Santiago, F. Analysis of the Origin of Open Circuit Voltage in Dye Solar Cells. *J. Phys. Chem. Lett.* **3**, 1629–1634 (2012).

CHAPTER 5 : General Conclusion and Perspectives

5.1 General Conclusion and Perspectives

As a recap of this work, I have understood the working of dye-sensitized solar cells (DSSCs) using classical organic dyes. In Chapter 1, I laid foundation knowledge on DSSCs, how to incorporate dyes and hence project PISCO. 1n Chapter 2, I swapped the classical organic dye for a photochromic dyes in DSSC-layout forming photo-chromo-voltaics based on platinum counter electrodes. Consequently, the resulting solar cells can simultaneously generate electricity and self-adapt their colour with irradiation intensity thus making them achieve high transparency under low-light (59%) and low transparency (27%) upon full activation. Among the first generation photochromic cells, **NPI** emerged as the champion dye surpassing the 4% efficiency barrier. Despite an increased current density generation, I discovered an abnormal behaviour where our new photochromic devices lost their photovoltages with irradiation time. Thanks to impedance spectroscopy technique, the detrimental processes are unravelled whereby the surface isomerization results in an accelerated recombination kinetics.

Thanks to these findings, we applied a strategy in Chapter 3 common in the DSSC community. With the help of chemists, structural modifications were done either on the photochromic core or on the electron-donating TPA unit. Chemical modifications of **NPI** gave rise to **NP**series photochromes from which structure-function relationships were established leading to nearly 4.20% in power conversion efficiencies (PCEs) using **NP2** dye. Not only was the PCE improved, the decolouration kinetics was greatly improved by adding bulky substituents on the photochromic core as in the case for **NP5** and **NP6**. Addition of bulky substituents on the TPA electron-donating part, as in **NP6**, led to improved photovoltages due to surface passivation. In a particular case of **NP3**, with bis C_6 chains, showed no V_{oc} drop when incorporated in devices suggesting that the addition of buky substituents on the bridge is a good strategy to protect the semi-conductor from the triiodide. Lastly, photoanode electrode treatments with hydrazine and oleic-acid post-treatment have allowed **NP2**-based devices to reach 4.90% in efficiency, which is the record for this class of devices.

Finally, molecular substitutions on either the electron-donating unit or the electron-acceptor moiety results in varying optical properties allowing for the application of new redox couples translating to variations in device performance as observed in Chapter 4. From this work, we can see that the new photochromic dyes can work with Cobalt-based and TEMPO –based electrolytes (the first ever trial). Also, the design principles established for classical organic

dyes to improve photovoltaic performances in DSSCs cannot be fully transferred to the new photochromic photosensitizers. All the devices presented so far in this work are based on platinum counter electrodes.

As a face and way forward for this work, the objectives henceforth would be,

- To increase the optical transparency of the devices and
- To increase the photovoltaic performances and lower the cost for application.

In this regard and the experienced acquired, I have initiated projects that could be interesting for the future of this work. Therefore, I have replaced the classical platinum with a conducting polymer and introduced new small molecules either in the electrolyte or on the photoanode surface to improve the performances as shown in the sections below.

5.2 Perspectives

5.2.1 Use of Conducting polymers as counter material

DSSCs are famous for the cheap fabrication units. However, when platinum is used as the counter electrode material, very high temperatures are used in their manufacturing limiting largescale production. Platinum is also rare and expensive metal [1]. As part of preliminary results, I have investigated the use of conducting polymers as cathode material as already reported in literature [2]. Poly(3,4-ethylenedioxythiophene) -Polystyrene sulfonate (PEDOT-PSS), is well-known and commercially available polymer, here I prepared PEDOT stabilized with different counter-anions such as trifluoromethanesulfonate CF_3SO_3- (OTf) and poly(styrenesulfonate) (PSS) and I incorporated it as the counter material.

I prepared these polymers from solutions via polymerization during deposition using materials and procedure as reported by Gueye *et. al* [3].

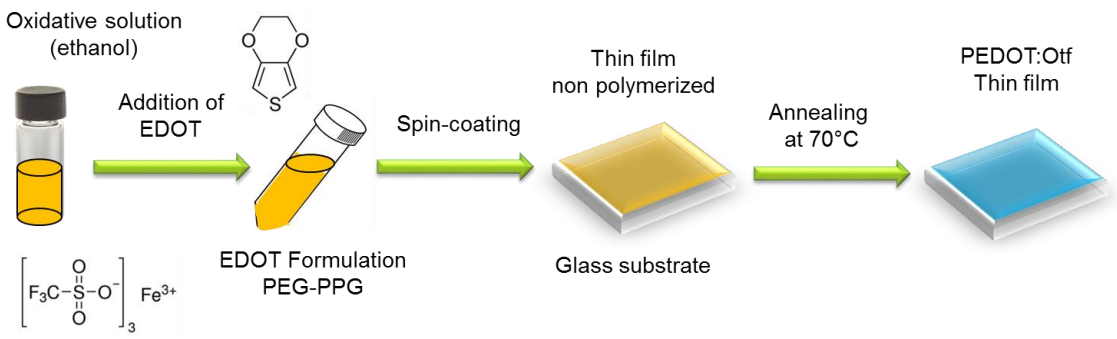

Figure 5.1 : Preparation of conducting polymer counter electrodes according to Gueye et. al [3].

5.2.2 Application on classical RK1 dye and NP2 photochromic dye

The drilled coated counter electrodes were applied in devices using classic **RK1** photosensitizer and **NP2** photochromic dye. **RK1** was included as a reference to assess the quality of the counter electrodes with a well known system. The result of the solar cells using PEDOT:OTf cathodes is as shown below.

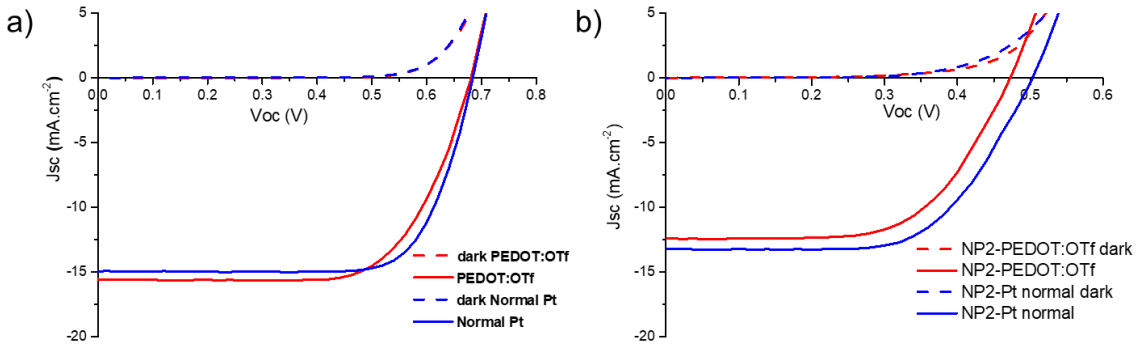

*Figure 5.2 : J(V) characterization of the devices based on a) **RK1**-dye and b) **NP2**-dye using conducting polymers.*

The photovoltaic parameters are as summarized in the table below.

*Table 5.1 : The photovoltaic parameters when classical **RK1** dye and **NP2** dye were applied with conducting polymers. The statistics for **NP2**-based cells are based on 3 opaque (13 +3 µm) devices for each.*

Counter Electrodes	**J_{sc} (mA.cm^{-2})**	**V_{oc} (V)**	**FF**	**PCE (%)**
RK1 PEDOT:OTf	15.58	0.681	0.685	7.27
RK1 Pt only	14.94	0.684	0.745	7.62
NP2 PEDOT:OTf	12.42 (12.16 ± 0.33)	0.472 (0.472 ± 0.001)	0.617 (0.621 ± 0.003)	3.62 (3.57 ± 0.06)
NP2 Pt only	12.74 (13.55 ± 0.67)	0.503 (0.491 ± 0.009)	0.649 (0.620 ± 0.020)	4.16 (4.12 ± 0.04)

This result is good given that it is the first example of PEDOT electrodes ever applied in our STEP lab. The conducting polymers also work well with our photochromic dyes thus providing a new direction towards more transparent devices.

5.2.3 New electrolyte additives (TPAA)

Electrolye additives have been used to improve performances in DSSCs [4,5]. Boschloo G. *et. al* reported in 2016 on a small electron donor in a cobalt complex electrolyte that significantly improved the overall efficiency of devices. In their work, they proposed a solution for cobalt-

based DSSCs by improving the driving force for the dye regeneration while at the same time slowing down the recombination processes. They demonstrated that by introducing an intermediary step via the TPAA, which has reversible electrochemical properties, can form a good redox tandem with cobalt thus accelerating dye regeneration kinetics via an electron cascade process. Under AM 1.5 conditions, using **LEG4** dye, they attained a 25% improvement in the efficiencies [6]. The chemical structure is as shown below.

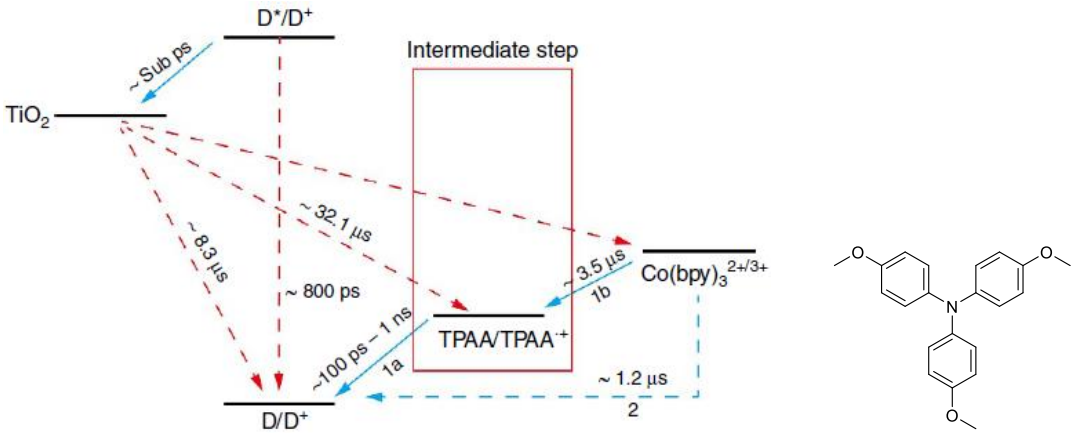

Figure 5.3 : Energy diagram showing an intermediate TPAA via path 1 and the normal Co electrolyte path 2 (with permission from [6]). (On the right side) Chemical structure of TPAA molecule.

Thanks to Samuel Fauvel who helped in synthesizing this molecule. In this respect, I have envisioned the application of this redox species for application with photochromic dyes as shown in the summary below.

$Dye^{+} + TPAA \longrightarrow Dye + TPAA^{\cdot+}$

$TPAA^{\cdot+} + 3I^{-} \longrightarrow TPAA + I_3^{-}$

However, for application in a DSSC layout with photochromic dyes, the energy levels should match in the dye regeneration electron cascade. I identified that the only photochromic dyes that could be potentially applied are the **SF** family due to their low-lying HOMO levels as shown below.

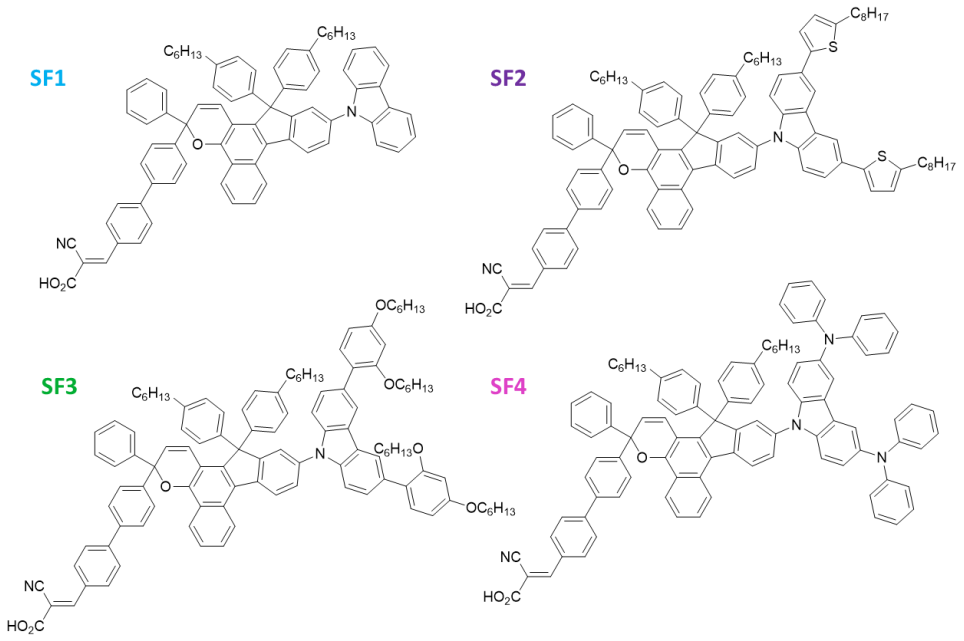

*Figure 5.4 : Chemical structures of the **SF** family dyes.*

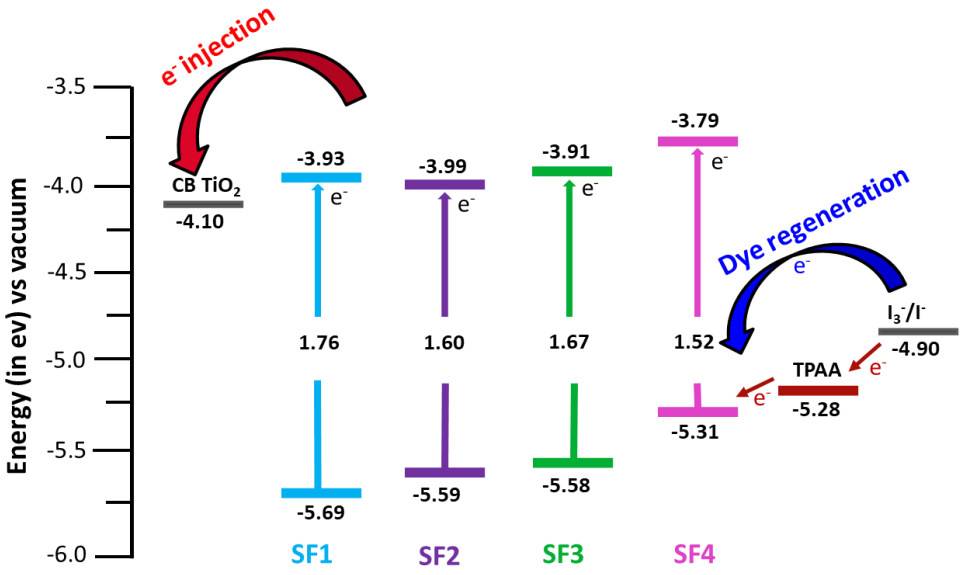

*Figure 5.5 : Analysis of the **SF** family energetics for the application of TPAA-based additives.*

I started by implementing **SF4** since it has the best photovoltaic performance within its family despite the close proximity of its HOMO level to the redox potential of TPAA additive. Unfortunately, compared to **SF4** performance with home-based electrolyte with PV parameters as (J_{sc}=7.93 mA.cm^{-2}, V_{oc}=524 V, FF=0.73 and PCE=3.04%), the addition of 0.1 M TPAA into this electrolyte gave (J_{sc}=9.05 mA.cm^{-2}, V_{oc}=522 V, FF=0.61 and PCE=2.86%). Of course the J_{sc} was slightly improved by 1 mA.cm^{-2}, the V_{oc} seems less affected but a drop in the fill factor led to lower performance. The probable explanation is that the energy levels are not well aligned for a good electron cascade.

I then tested with the other dyes i.e. **SF1**, **SF2** and **SF3** whose HOMO levels seem to be correctly placed and the result is as demonstrated in the table below.

*Table 5.2 : Photovoltaic parameters of the **SF** family showing the impact of TPAA additive with statistics done on at least 3 opaque (13 +3 µm) electrodes. The values in red shows the improvement attained with TPAA additive.*

DSSC type	J_{sc} (mA.cm^{-2})	V_{oc} (V)	FF	PCE (%)
SF1	2.78	0.482	0.667	0.89
SF1 + TPAA	5.32 (4.95 ± 0.54)	0.478 (0.477 ± 0.006)	0.572 (0.608 ± 0.057)	1.45 (1.42 ± 0.05)
SF2	5.24	0.474	0.67	1.67
SF2 + TPAA	7.31 (7.33 ± 0.02)	0.506 (0.500 ± 0.006)	0.63 (0.619 ± 0.015)	2.35 (2.27 ± 0.07)
SF3	4.35	0.527	0.72	1.65
SF3 + TPAA	6.89	0.544	0.61	2.29

Indeed, the impact of TPAA additive in the electrolyte is clear. For instance, in **SF1** there is nearly ~100% increase in the J_{sc}, the V_{oc} is almost constant leading to >60% increase in the PCE with respect to a device without TPAA i.e. from 0.89% up to 1.45%. In **SF2**, we have a 2 mA.cm^{-2} increase in the J_{sc}, 30 mV photovoltage gain leading to a 40% increase in the power conversion efficiency giving 2.35% overall efficiency. In **SF3** we have >2 mA.cm^{-2} J_{sc} increase accompanied with a slight V_{oc} increase leading to a 38% increase in the PCE thus reaching 2.29%.

These preliminary results demonstrate a strong impact of the additives and are promising for high performance photochromic DSSCs. This work is in progress and recently we had an intern from Italy, Diego Mirani, whose goal was to introduce different substitution on the TPAA. Future work should focus on improving the solubility of such additives in the electrolyte solution and a better understanding in devices is also required.

5.3 References

1. Hunt, B. Availability of the Platinum Metals. *Platinum Metals Rev.* **13**, 126–138 (1969).
2. Idígoras, J. *et al.* Highly efficient flexible cathodes for dye sensitized solar cells to complement Pt@TCO coatings. *J. Mater. Chem. A* **2**, 3175–3181 (2014).
3. Gueye, M. N. *et al.* Structure and Dopant Engineering in PEDOT Thin Films: Practical Tools for a Dramatic Conductivity Enhancement. *Chem. Mater.* **28**, 3462–3468 (2016).
4. Stergiopoulos, T., Rozi, E., Karagianni, C.-S. & Falaras, P. Influence of electrolyte co-additives on the performance of dye-sensitized solar cells. *Nanoscale Res Lett* **6**, 307 (2011).
5. Bella, F., Sacco, A., Pugliese, D., Laurenti, M. & Bianco, S. Additives and salts for dye-sensitized solar cells electrolytes: what is the best choice? *Journal of Power Sources* **264**, 333–343 (2014).
6. Hao, Y. *et al.* A small electron donor in cobalt complex electrolyte significantly improves efficiency in dye-sensitized solar cells. *Nat Commun* **7**, 13934 (2016).

Resume

Over the past decades, dye-sensitized solar cells (DSSCs), amidst other thin-film technologies, have captured interests from academia and industry thanks to their low production costs, decent stability in applications, high efficiency and their tunable optoelectronic properties. A DSSC layout comprises a photosensitizer immobilized on a semi-conductor, a redox couple (usually I_3^-/I^-) and a Pt-coated cathode. Among these components, the photosensitizer allows for the fabrication of chromatic and semi-transparent solar cells which are appealing candidates in the Building Integrated PhotoVoltaics (BIPV) industry.

Nevertheless, for application as windows in BIPV, transparency and efficiency have to be optimized. Among the different approaches reported recently in that field, the use of NIR-photosensitizers allowed to reach an impressive transparency in the visible up to 76% but lead to sacrificing efficiencies. Another approach consists in developing semi-transparent solar cells with visible light-absorbing dyes but the optical transmission in that case is fixed during manufacturing and a compromise has to be found between efficiency and transparency.

Our group has made efforts to reconcile these properties by replacing classical photosensitizers with organic photochromes. We have developed a new class of DSSCs with dynamic optical properties, capable to self-adapt their transparency levels and energy production as a function of daylight. During this PhD I will also report on the development of photochromic solar cells registering efficiencies exceeding 4.3%. I will comment on the structure-property relationships and photochromism-photovoltaic interplay for this class of molecules. Thanks to the better understanding of the interfacial processes, we have achieved photochromic solar cells with close to 5% efficiency.

Résumé

Au cours des dernières décennies, les cellules solaires à colorant (DSSC), parmi d'autres technologies à couches minces, ont suscité l'intérêt du monde universitaire et de l'industrie grâce à leurs faibles coûts de production, leur stabilité décente dans les applications, leur rendement élevé et leurs propriétés optoélectroniques accordables. Une disposition DSSC comprend un photosensibilisateur immobilisé sur un semi-conducteur, un couple redox (généralement I_3^-/I^-) et une cathode revêtue de Pt. Parmi ces composants, le photosensibilisateur permet la fabrication de cellules solaires chromatiques et semi-transparentes qui sont des candidats attrayants dans l'industrie du photovoltaïque intégré au bâtiment (BIPV).

Néanmoins, pour une application en tant que fenêtres dans le BIPV, la transparence et l'efficacité doivent être optimisées. Parmi les différentes approches rapportées récemment dans ce domaine, l'utilisation de photosensibilisateurs NIR a permis d'atteindre une transparence impressionnante dans le visible jusqu'à 76% mais conduit à sacrifier les efficacités. Une autre approche consiste à développer des cellules solaires semi-transparentes avec des colorants absorbant la lumière visible mais la transmission optique dans ce cas est fixée lors de la fabrication et un compromis doit être trouvé entre efficacité et transparence.

Notre groupe s'est efforcé de concilier ces propriétés en remplaçant les photosensibilisateurs classiques par des photochromes organiques. Nous avons développé une nouvelle classe de DSSC aux propriétés optiques dynamiques, capables d'auto-adapter leurs niveaux de transparence et leur production d'énergie en fonction de la lumière du jour. Au cours de cette thèse, je rendrai également compte du développement de cellules solaires photochromiques enregistrant des rendements supérieurs à 4,3%. Je commenterai les relations structure-propriété et l'interaction photochromisme-photovoltaïque pour cette classe de molécules. Grâce à une meilleure compréhension des processus interfaciaux, nous avons réalisé des cellules solaires photochromiques avec un rendement proche de 5 %.